A Quasi-Dimensional Spark Ignition Two Stroke Engine Model

by

Daniel Lewis

A Doctoral Thesis

Submitted in partial fulfilment of the
requirements for the award of Doctor of
Philosophy of Loughborough University

2013

Despite challenges with poor emissions and fuel economy, gasoline two stroke engines continue to be developed for a number of applications. The primary reasons for the choice of a gasoline two stroke engine includes its low cost, mechanical simplicity and high specific power output. Some applications for the gasoline two stroke engine include small capacity motorcycles and scooters, off road recreational vehicles, hand held power tools and unmanned aerial vehicles.

New technologies, which are already mature in four stroke engines, are now being applied to two stroke engines. Such technologies include direct fuel injection, electronic engine management and exhaust gas after treatment. To implement these new technologies computation models are being continuously developed to improve the design process of engines. Multi-dimensional computational fluid dynamics modelling is now commonly applied to engine research and development, it is a powerful tool that can give great insight into the thermofluid working of an engine. Multi-dimensional tools are however computationally expensive and quasi-dimensional modelling methods are often better suited for the analysis of an engine, for example in transient engine simulation.

This thesis reports the development of a new quasi-dimensional combustion model for a loop scavenged two stroke engine. The model differs from other quasi-dimensional models available in the literature as it accounts for a bulk motion of the flame front due to the tumble motion created by the loop scavenge process. In this study the tumble motion is modelled as an ellipsoid vortex and the size of the vortex is defined by the combustion chamber height and a limiting elliptical aspect ratio. The limiting aspect ratio has been observed in experimental square piston compression machines and optical engines. The new model also accounts for a wrinkled flame brush thickness and its effects on the interaction between flame front and combustion chamber.

The new combustion model has been validated against experimental engine tests in which the flame front propagation was measured using ionization probes. The probes were able determine the flame front shape, the bulk movement of the flame front due to tumble and also the wrinkled flame brush thickness.

I would first like to thank my supervisors Dr Andrew Clark and Mr Paul King for their encouragement in starting and completing this work, for sharing their knowledge and words of wisdom in the many meetings and discussions throughout my postgraduate years.

I would also like to thank Loughborough University for allowing me to use the engine and vehicle laboratory facilities. Thanks are also due to the technicians in the laboratories for their help during the experimental period of this project.

Finally I must give thanks to both my parents and acknowledgement to my father, David Hamer Lewis, for guiding me in my early learning years and pointing me in the direction of science and engineering which has provided me with years of entertainment as a hobby and a means to earn a living.

Table of Contents

Nomenclature

English letters

a	Ellipsoid dimension, x direction (m)
A_{sq}	Squish area (m^2)
A_f	Flame front area (m^2)
A_{wall}	Cylinder wall area (m^2)
b	Ellipsoid dimension, y direction (m)
B	Cylinder bore diameter (m)
c	Ellipsoid dimension, z direction (m)
c_d	Closure coefficient for eddy viscosity
c_h	Integral scale calibration constant, based on clearance height
c_{ign}	Ignition delay constant
c_{kin}	Calibration constant for scavenge jet turbulence
c_l	Integral scale calibration constant
c_{Lmax}	Calibration constant for flame brush thickness
c_p	Specific heat constant at constant pressure (J/kg.K)
c_{RIFF}	Constant for Reactant Islands Fractal Flame
c_{sp}	Calibration constant for scavenge jet velocity
c_v	Specific heat constant at constant volume (J/kg.K)
c_β	Calibration constant for turbulence generated by shear
c_ε	Calibration constant for turbulence dissipation

C_m	Constant for reference laminar burning velocity
C_2	Constant for reference laminar burning velocity
Da	Damkohler number
D_L	Fractal dimension coefficient for Santavicca equation
D_T	Fractal dimension coefficient for Santavicca equation
D_3	Fractal dimension
e_u	Specific internal energy, unburned gas (J/kg)
e_b	Specific internal energy, burned gas (J/kg)
E	Internal energy (J/kg)
f_D	Fraction of products consumed as islands
f_W	Fraction of products consumed at wrinkled flame front
G	Radius of gyration (m)
h	Specific enthalpy (J/kg)
h_c	Combustion chamber clearance height (m)
h_{fg}	Enthalpy of vaporisation (J/kg)
h_p	Port height (m)
I	Moment of inertia
k	Turbulent kinetic energy (J/kg)
k_{in}	Kinetic energy of inlet jet (J/kg)
k_j	Turbulent kinetic energy of inlet jet (J/kg.s)
k_{sh}	Turbulent kinetic energy generated vortex shear (J/s)

k_{sq}	Kinetic energy due to squish (J/s)
k_{th}	Thermal conductivity (W/m.K)
k_{tum}	Turbulent kinetic energy generated by mass leaving vortex (J/s)
KE	Kinetic energy (J)
Ka	Karlovitz number
Ka_{δ}	Karlovitz number for chemical reaction zone thickness
l	Integral length scale (m)
l_f	Laminar flame thickness (m)
l_{ph}	Preheat flame thickness (m)
L_{max}	Fractal outer cut off (m)
L_{min}	Fractal inner cut off (m)
L_{RIFF}	Fractal brush thickness for Reactant Islands Fractal Flamelets (m)
l_{δ}	Chemical reaction zone thickness (m)
m	Mass (kg)
m_f	Mass of fuel (kg)
m_{in}	Mass entering cylinder (kg)
m_{out}	Mass exiting cylinder (kg)
m_{sq}	Mass moved due to squish (kg)
m_{tum}	Mass of tumble vortex (kg)
m_x	Mass fraction burned (kg)
Nu	Nusselt number

p	Pressure (N/m^2)
Q_b	Heat transfer from burned zone (J)
Q_{ht}	Heat transfer (J)
Q_{vap}	Heat loss due to latent heat of evaporation (J)
Q_R	Heat release due to combustion (J)
Q_u	Heat transfer from unburned zone (J)
r_f	Flame front radius (m)
r_{elp}	Radius on ellipsoid surface (m)
Re	Reynolds number
Re_T	Turbulent Reynolds number
S_{ij}	Strain rate tensor
S_C	Combined burning velocity, wrinkled flame and reactant islands (m/s)
S_D	Reactant island burning velocity (m/s)
S_L	Laminar burning velocity (m/s)
S_{L0}	Reference laminar burning velocity (m/s)
S_T	Turbulent burning velocity (m/s)
S_W	Wrinkled flame front burning velocity (m/s)
t	Time (s)
T	Temperature (K)
T_{ad}	Adiabatic flame temperature (K)
T_{del}	Ignition delay (s)

T_{in}	Torque addition due to flow entering cylinder (Nm)
T_{out}	Torque removed due to flow leaving cylinder (Nm)
T_{sh}	Torque due shear stress (Nm)
T_{wall}	Cylinder wall temperature (K)
u	Instantaneous velocity (m/s)
$\bar{u}$	Time averaged velocity (m/s)
u_{ref}	Reference velocity (m/s)
u_t	Tangential velocity (m/s)
u'	Fluctuating velocity (m/s)
u'_{rms}	Turbulence intensity (m/s)
u_{sq}	Velocity due to squish (m/s)
u_P	Piston velocity (m/s)
U	Mean velocity (m/s)
V	Volume (m^3)
V_c	Volume, clearance (m^3)
V_{cyl}	Instantaneous cylinder volume (m^3)
V_s	Swept volume (m^3)
V_w	Wrinkled flame brush volume (m^3)
w	Exponential wall function
W	Work done
x_b	Mass burn fraction

x_{egr}	Trapped exhaust residual
x_f	Flame offset (m)
X_C	Mean reactant island diameter (m)
x	Orthogonal coordinate system
y	Orthogonal coordinate system
z	Orthogonal coordinate system

Greek letters

α	Constant for laminar burning velocity
β	Constant for laminar burning velocity
γ	Ratio of specific heats
λ	Taylor length scale
δ	Ratio of reaction zone to laminar flame thickness
ε	Turbulent dissipation
η	Kolmogorov length scale
θ	Crank angle position (degrees)
θ_{ign}	Ignition timing (degrees)
θ_{exh}	Exhaust timing (degrees)
ν	Kinematic viscosity
ν_t	Eddy viscosity
Π	Gas purity

ρ	Density (kg/m^3)
τ_{flame}	Characteristic flame time (s)
τ_D	Characteristic burn up time of reactant island (s)
τ_{flow}	Characteristic turbulent flow time (s)
τ_{ij}	Stress tensor
τ_{ij}^R	Turbulent shear stress
τ_w	Characteristic reaction time in the wrinkled flame front (s)
τ_λ	Taylor time scale (s)
τ_η	Kolmogorov time scale (s)
υ_η	Kolmogorov velocity scale
ϕ	Equivalence ratio
ϕ_m	Reference burning velocity parameter
Ω	Angular momentum (kg.m^2/s)
ω	Angular velocity (radians/s)

Subscripts

b	Burned zone
in	Entering cylinder
out	Leaving cylinder
sq	Squish
tum	Tumble

u	Unburned zone
θ	Crank angle (degrees)
0	Reference condition

Abbreviations

ATDC	After Top Dead Centre
BMEP	Brake Mean Effective Pressure
BSFC	Brake Specific Fuel Consumption
BTDC	Before Top Dead Centre
CAD	Computer Aided Design
CFD	Computational Fluid Dynamics
CNG	Compressed Natural Gas
DNS	Direct Numerical Simulation
EBU	Eddy Break Up
ECU	Engine Control Unit
EGR	Exhaust Gas Residual
HCCI	Homogeneous Charge Compression Ignition
IMEP	Indicated Mean Effective Pressure
LDV	Laser Doppler Velocimetry
LES	Large Eddy Simulation
LPG	Liquid Petroleum Gas

MOC	Method of Characteristics
PIV	Particle Image Velocimetry
RANS	Reynolds Averaged Navier Stokes
RIFF	Reactant Islands and Fractal Flamelets
RMS	Root Mean Square
SCAI	Stratified Charge Auto Ignition
SCSI	Stratified Charge Spark Ignition
TDC	Top Dead Centre
UAV	Unmanned Aerial Vehicle

1 Introduction

The loop scavenged, crankcase pump, gasoline two stroke engine has been a popular power plant for small capacity motorcycles and scooters for many years. The primary reasons for its use in these applications include its size, specific power, low parts count, ease of maintenance and manufacturing cost. In recent years there has been a decline in the use of two stroke engines for road use generally due to more stringent legislation for vehicle emissions. However, small capacity two stroke motorcycles and scooters are still popular in developing countries, due to their cost of manufacture and simple construction. Many of the technologies established with four stroke engines are now being applied to two stroke engines including electronic engine management (ECU), direct fuel injection and exhaust gas after treatment, catalytic converters. Two stroke engines are still often found in off road recreational vehicles such as snow mobiles and outboard motors for water craft, in these applications new technologies are also being developed in order to reduce emissions. To implement new technologies into two stroke engine design will require engine simulation tools that can accurately predict the thermodynamic processes of the engine. These simulation tools will improve the design process and reduce the need for experimental development. Of the different thermodynamic and fluid mechanic processes of an engine the combustion process is probably the most complex involving turbulent fluid motion, exothermic chemical reactions and heat transfer. Small capacity gasoline two stroke engines generally use a homogeneous premixed combustion process, although stratified charge combustion has been investigated. Different analytical methods have been developed for modelling premixed combustion in piston engines. The most complex analytical methods involve three dimensional Computational Fluid Dynamic codes (CFD) to calculate the fluid mechanic and thermodynamic properties in the engine cylinder with respect to both time and space. The simplest method for modelling the combustion process in an engine is a zero dimensional model using a predefined heat release rate, usually known as a Wiebe model. Between these two extremes is a class of modelling known as quasi-dimensional. Two zone quasi-dimensional combustion models are able to predict the progress of combustion in both time and space based on simplified assumptions for the shape of the flame front and its interaction with the combustion chamber geometry. Quasi-dimensional combustion models

usually assume a spherical flame front that propagates radially outward from the spark plug. The rate of flame propagation in premixed combustion is known to be enhanced by turbulence and hence quasi-dimensional models often include a sub model for turbulence.

Although simple in their construction, when compared to four stroke engines, two stroke engines can be more complex with respect to their fluid dynamic operation. Two stroke engines are often designed with exhaust systems that utilise pressure wave action to improve delivery ratio and trapping efficiency. Pressure waves propagate along the exhaust duct at rate which is a function of the acoustic velocity of the local gas which is dependent upon gas temperature. The temperature of the gas in the exhaust system is largely dependent upon the combustion process and hence the delivery ratio and trapping efficiency will also depend on the combustion process. The rate of progress of combustion, or the flame propagation, is governed by a number of parameters including air/fuel ratio, ignition timing, in-cylinder pressure, gas temperature, in-cylinder turbulence and the amount of residual exhaust gas. As an engine control strategy ignition timing and air/fuel ratio may be varied at different engine speed and load conditions to improve delivery ratio, trapping efficiency and overall performance. To design such control strategy will require a whole engine simulation tool that includes both a combustion model and pressure wave model for the exhaust duct.

Numerical methods for whole engine simulation have been around for many decades and have evolved both in terms of complexity and accuracy in that time. One of the simplest of the simulation methods is referred to as filling and emptying models, in these models the engine cylinders are connected to finite fixed volumes which represent the engines manifolds and ducts. The filling and emptying models do not account for the pressure wave motion in the engines ducts. Multidimensional CFD methods can be used for whole engine modelling, including the cylinder, inlet and exhaust ducts, but are often prohibitively expensive in computational terms. A compromise between these two methods is to use a quasi-dimensional model for the combustion process and a one dimensional gas dynamic code for the exhaust duct.

1.1 Research Objectives

Because of the importance of the interaction between the combustion event, exhaust duct gas dynamics, delivery ratio and trapping efficiency of a two stroke engine there is a need for a whole engine simulation tool that includes a combustion model and exhaust gas dynamics. The combustion model needs to account for the parameters that influence flame propagation and heat release, which includes in-cylinder motion/turbulence, combustion chamber and flame front interaction, air/fuel ratio, trapped exhaust residuals, cylinder pressure and temperature. The purpose of this study is to develop a quasi-dimensional two zone combustion model for a two stroke engine that fits within a whole engine simulation code. The prime research objectives include;

- To develop a phenomenological model for predicting both the bulk flow motion and in-cylinder turbulence in a loop scavenged two stroke engine
- To develop a two zone quasi-dimensional combustion model that accounts for the tumble motion in a two stroke engine.
- The turbulence and combustion models will be applied to different combustion chamber geometries.
- Determine heat release and pressure rise using a turbulent combustion model which takes into account the in-cylinder turbulence and movement of the flame due to bulk flow motion.
- To determine heat release rate from cylinder pressure measurements taken from a test engine running at different speeds and throttle positions.
- To measure the bulk flow movement of the flame during combustion and compare measured flame movement with predictions.
- To evaluate the flame front shape by monitoring flame front propagation in a test engine operating at various loads and speeds.
- To define and measure a wrinkled flame brush thickness based on a statistical mean combustion event.

1.2 Thesis Outline

This thesis is made up of nine chapters. This first chapter has given a brief overview of the project and its aims.

The second chapter of this thesis gives a literature review of current and recent research areas on two stroke engine development. A review is given of some of the combustion models available in the open literature which have been used for premixed combustion and also phenomenological models for in-cylinder flow motion and turbulence. A brief review of some of the experimental methods used to monitor the flow motion and flame propagation in engine cylinders is also given.

In Chapter 3 a description is given of how a tumble flow motion is generated in the cylinder of a loop scavenged two stroke engine during the scavenge process. Details are given for a phenomenological model developed in this study to define the formation of a tumble vortex. The angular velocity of the vortex increases due to mass entering the cylinder and reduces due to viscous shear effects. A review of some recent measurements and CFD simulations of the tumble motion in engines is given. Details are also given for a turbulence model and how the tumble vortex generates small scale turbulent kinetic energy due to viscous shear. The levels and scales of turbulence predicted by the turbulence model will be required for the combustion model.

In Chapter 4 laminar and turbulent flame propagation is discussed and some of the mechanisms that lead to an enhanced turbulent flame speed, including mass entrainment and flame front wrinkling. Flame regime diagrams and the non-dimensional scales that influence flame structure are introduced. An ignition delay is defined, early flame kernel growth described and a method used to characterise the end of burn period is discussed. Wrinkled flame front scales are discussed and a wrinkled flame brush thickness is defined, also the interaction between the combustion chamber walls and the wrinkled flame brush is explained.

In Chapter 5 the details of the thermodynamic model used in the current work are given. Both single and two zone thermodynamic models are used to determine that state of the

cylinder during the complete engine cycle. The two zone model is used during the combustion process when a burned zone is present.

In Chapter 6 a brief outline of a whole engine simulation model is given. The combustion model developed here is intended to be used with a whole engine simulation that includes gas dynamic effects.

In Chapter 7 the details of the experimental set up in which tests on a single cylinder two stroke scooter were carried out are described. The scooter was mounted on a chassis dynamometer and tests carried out at various speeds and throttle positions. Details of the instrumentation used in the tests are given, including in-cylinder pressure measurement and ionization probes used to monitor the progress of the flame front. Results from the tests are discussed including how the data from the ionization probes is analysed to determine flame front arrival, flame propagation speed and wrinkled flame brush thickness.

In Chapter 8 results from the quasi-dimensional combustion model are presented including in-cylinder tumble motion, turbulence, flame movement, mass burn fraction and cylinder pressure. The model results are also compared to the engine test data.

The final chapter, nine, concludes this study outlining some of the important findings and the contributions from the current work. Suggestions are also given for further work and development for quasi-dimensional combustion models.

2 Two Stroke Engines

Applications for two stroke engines are numerous and engine size varies from very small to very large. This work will concentrate on the smaller engines for which the normal applications include small capacity motorcycles and scooters, marine outboard motors, hand held power tools such as chain saws, snow mobiles, recreational vehicles and small aircraft. Various methods and tools have been developed over the years for the design and development of internal combustion engines and new tools are constantly being developed to further improve the efficiency of engines. In the following sections is a brief overview of some of the recent research work carried out on two stroke engines followed by a review of whole engine modelling and then combustion modelling techniques.

Figure 2-2 below shows a schematic of a simple loop scavenged two stroke engine, in this example the inlet port is controlled by the piston skirt, other types of crankcase scavenged engines have used reed valves or disc valves to control the inlet port. When the inlet port is controlled by the piston skirt the port timings are symmetrical about TDC and BDC, Figure 2-1 below shows a timing diagram for a piston ported two stroke engine.

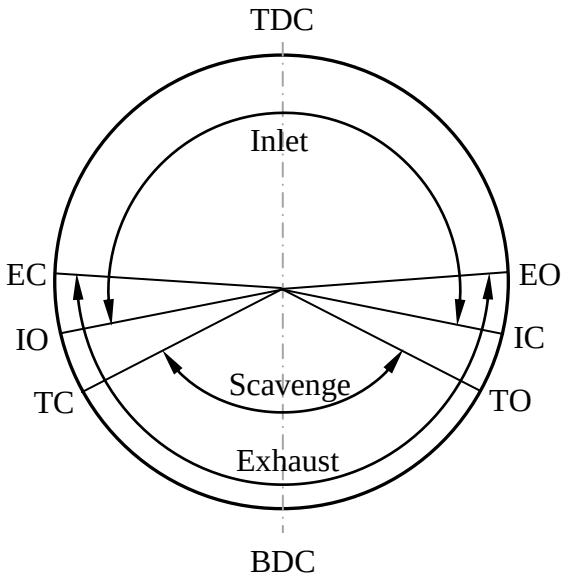

Figure 2-1, Symmetrical port timimg events

In the operation of a crankcase scavenged two stroke engine as the piston moves upwards the pressure in the crankcase reduces, then as the piston skirt uncovers the inlet port fresh charge is drawn into the crankcase due to the pressure difference between atmosphere and the crankcase. On the downward piston stroke the inlet port is closed by the piston skirt and the fresh charge in the crankcase is compressed. The pressure difference between the crankcase and cylinder moves the fresh charge from the crankcase to the cylinder via transfer ports in the cylinder wall. The transfer ports and exhaust port in the cylinder wall are controlled by the piston crown. On the following upward stroke of the piston after the transfer and exhaust ports are closed the fresh charge in the cylinder is compressed and the just prior to TDC the fresh charge is ignited by a spark plug and the combustion process begins. In the preceding cycle description no account was given of gas dynamics, however Figure 2-2 shows an engine with an exhaust duct designed to use pressure wave motion to produce a low pressure at the exhaust manifold near BDC, this low pressure will then enhance the flow of exhaust gas out from the cylinder. Just prior to the exhaust port closing the pressure wave motion in the exhaust duct will produce an increased pressure at the exhaust manifold which will help prevent the loss of fresh charge from the cylinder into the exhaust duct.

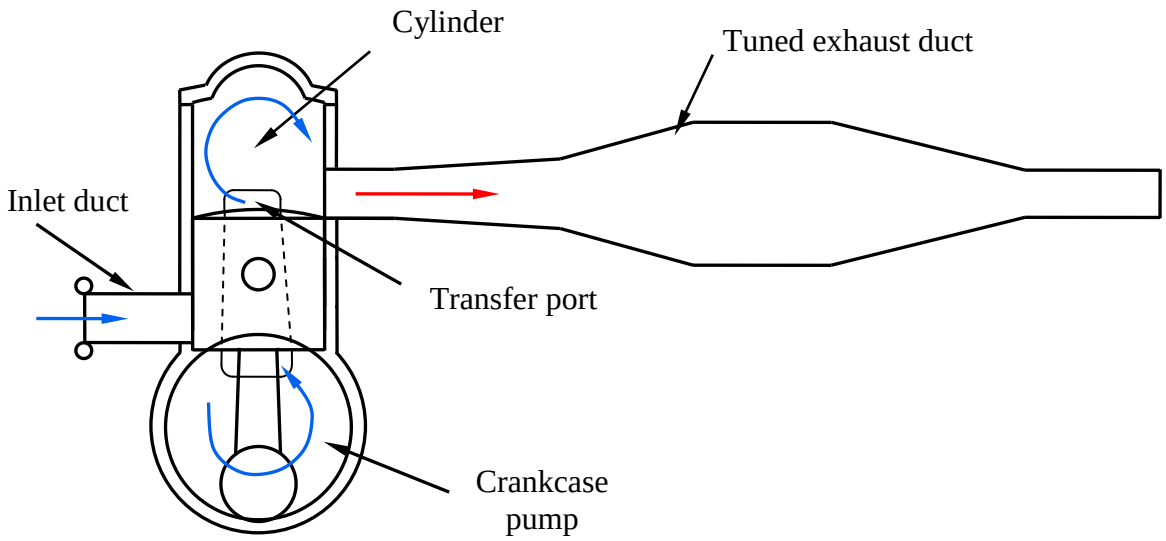

Figure 2-2, Piston ported two stroke engine

2.1 Two Stroke Engine Applications

2.1.1 Small Capacity Motorcycle and Scooters

Motorcycles powered by two stroke engines were popular up to the 1980s, primarily due to their high specific power and low cost. Today due to increased emission regulations, the two stroke engine is now restricted to the smallest of two wheeled vehicles, 50 cc scooters and motorcycles. Heng et al. (2009) note the popularity of small capacity motor cycles in developing countries, due to their low cost and mechanical simplicity. In their publication they reported results of tests on a 120 cc two stroke engine with gaseous fuel direct injection. The engine used was typical of that found in south east Asia. The most significant source of emissions from a loop scavenged two stroke engine fitted with a carburettor are unburned hydrocarbons. During the scavenging process on a carburetted two stroke engine a mixture of fuel and air enters the cylinder whilst at the same time exhaust leaves the cylinder through the exhaust port. As the fresh mixture enters the cylinder whilst the exhaust port is open there is always likely to be some amount of fresh mixture passing straight through cylinder and into the exhaust port. The loss of fuel to the exhaust during the scavenging process may be eliminated by scavenging the cylinder by air alone and then injecting the fuel directly into cylinder after the exhaust port has closed. A number of studies have been published on fuel injection strategies, including a comparison of 50 cc two stroke and four stroke engines conducted by Hirz et al. (2004). The comparison included four different four stroke engines and four two stroke engines. Three of the two stroke engines used carburettors and one used air assisted direct injection. Two of the four stroke engines used carburettors and two used fuel injection. One of the four stroke engines was supercharged, where the crankcase served as the supercharger in a similar way as the crankcase is used as the scavenge pump for a two stroke engine. The two stroke engines were homologated to the Euro II emissions standards, European Union Directive 2002/51/EC, which amends Directive 97/24/EC. The directive specifies a Type 1 test transient drive cycle, ECE 47, which includes eight accelerations and decelerations over an 896 second duration. The first 448 seconds is a warm up cycle and for Euro II homologation the emissions are recorded for the last 448 seconds only, for Euro III homologation the emissions are recorded for the entire test. With the warm up phase included in the drive cycle the carburetted two stroke engines will be unlikely to meet emissions regulations. However in the conclusion to work it was stated that “Two stroke

engines with direct injection systems are able to fulfil the requirements of future emissions regulations based on cold start...". Further to the work of Hirz et al. (2004) a comparison was made between 50 cc two stroke and four stroke engines by Kirchberger et al. (2007). This study included two different four stroke engines and two different two stroke engines. Both four stroke engines were manifold fuel injected, the first normally aspirated and the second supercharged. The first two stroke engine used low pressure direct injection with the injector positioned in the cylinder wall such that it could inject above or below the piston crown. When injecting below the crown the fuel entered directly into the crankcase. The second two stroke engine used manifold injection upstream of the crankcase reed valve. For emissions comparison each of the engines was tested to the Euro III homologation standard, the manifold injected two stroke engine failed this test. However the direct injected two stroke engine passed this test with hydrocarbon emissions approximately 10% greater than the four stroke engines. A cost analysis was performed in which the production cost of a two stroke engine was at least 30% less than a four stroke. In terms of power output (un-restricted) the worst performer is the naturally aspirated four stroke at 3.0 kW, whilst the supercharged four stroke engine produces 4.15 kW, the direct injected two stroke 4.35 kW and the manifold injected two stroke 4.5 kW. Although not discussed in the publication, diagrams of the engines did indicate that the four stroke supercharged engine was significantly larger than the two strokes, mostly due to the valve gear and it is fair to assume that the mass of the four stroke engines would be significantly greater than the two strokes.

The emissions performance of a two stroke engine designed with two different injection modes was reported by Winkler et al. (2006). The engine used in the study was typical of a loop scavenged two stroke engine in that it had two main transfer ports, two auxiliary ports and a boost port situated opposite the exhaust port. A fuel injector was positioned in the crankcase with its spray aimed into the cylinder via the boost port. Two strategies for injection timing may then be used, the first injects during transfer port open period which produces a stratified charge in the cylinder. The second strategy injects during the upward stroke of the piston when the transfer ports are closed and the injected fuel enters into the crankcase. The fuel injected into the crankcase has greater time to mix with the air and then subsequently enters the cylinder as a homogeneous charge during the following downward stroke of the piston. Significant improvements in emissions were achieved and when

coupled with catalyst exhaust after treatment and the CO emissions were comparable with four stroke engines. Tests on a loop scavenged engine with indirect fuel injection were conducted by Oswald et al. (2010) in which fuel could be injected above or below the piston crown for either a homogeneous or stratified mixture. In direct injection mode the unburned hydrocarbon emissions are between 50 and 75% better than a carburetted two stroke engine. Brake specific fuel consumption of the direct injection engine was better than an equivalent carburetted four stroke engine.

A recent study of a direct injection two stroke engine was conducted by Heng et al. (2009) in which Liquid Petroleum Gas (LPG) was used as the fuel. The LPG fuel is normally stored in a pressurised fuel tank at between 400 and 1500 kPa. Because the fuel is stored at high pressure, low pressure fuel injection technology may be used without the need for fuel pumps and associated hardware. The pressurised fuel tank leads to a potential low cost fuel injection system. Their work however showed that fuel injection after exhaust port closure was limited by the ratio of fuel pressure to cylinder pressure and that poor fuel mixing results when injecting after exhaust port closure.

Tests and analyses were carried out on a two stroke engine running on gasoline and Compressed Natural Gas (CNG) by Bozza et al. (2011). The aim of the using CNG is to reduce emissions, primarily CO_2 emissions due to the hydrogen carbon ratio of the fuel. A carburettor is used to mix fuel in the inlet manifold when running on gasoline and when running on CNG the gas is injected into the inlet manifold. As the fuel, in both cases, is mixed before entering the cylinder there is still the potential for the direct loss of unburned fuel during the scavenge process. In the analysis both 1D and 3D combustion modelling methods were used and results from both methods show a good correlation with experimental results. Initial results show an improvement on Brake Specific Fuel Consumptions (BSFC) when fuelled on CNG.

2.1.2 Homogeneous Charge Compression Ignition

A significant amount of research work has gone into Homogeneous Charge Compression Ignition (HCCI) engines in the recent past in an attempt to reduce emissions. HCCI engines

often use residual exhaust gas to increase the temperature of the fresh charge towards its auto ignition temperature. With respect to HCCI, the two stroke engine has an advantage in that the exhaust port closes at the start of the compression stroke which leaves less time for the residual gas to cool. A small two stroke engine with low operating power requirements and using HCCI was investigated by Wijesinghe and Hong (2007). The engine used in their experiments operated with a butterfly valve in the exhaust duct to control the amount of trapped exhaust residuals in the cylinder rather than using an external Exhaust Gas Recirculation (EGR) loop to inject exhaust gas into the inlet manifold. The operating regime for HCCI was shown to be limited to between approximately 2000 and 3200 rpm and also between Brake Mean Effective Pressures (BMEP) of 160 and 250 kPa. To further the operating range of the two stroke engine Wijesinghe and Hong (2010) used spark ignition to assist the auto ignition combustion process, this increased the BMEP to 320 kPa and reduced cycle to cycle variation. A potential strategy for future two stroke engines is to run in HCCI mode at part load then in Spark Ignition (SI) mode at high load, Nishida et al. (2009) used this approach in a concept two stroke engine to good effect. The two stroke engine used in their experiments was a 250 cc engine with air assisted direct injection. The engine was designed to operate in SI mode at high load, HCCI mode in the low to mid load range, Stratified Charge Spark Ignition (SCSI) at idle and Stratified Charge Auto Ignition (SCAI) between idle and low load. The results of engine tests were compared with a four stroke 125 cc engine which showed improvements in specific fuel consumptions and NOx emissions whilst producing similar hydrocarbon emissions. They also indicated a potential downsizing of 30% compared to the four stroke engine.

A two stroke research engine with variable compression which is clearly aimed at automotive use was described by Turner et al. (2010). One of the reasons for choosing a two stroke engine for this research study was the lack of poppet valves in the cylinder head which made it easier to incorporate a variable compression combustion chamber. The research work was aimed at developing a two stroke engine to work with HCCI, although a spark plug is retained and hence may be operated in spark assisted auto ignition or normal spark ignition mode.

2.1.3 Snow Mobiles and Recreational Vehicles

Off road recreational vehicles often use two stroke engines due to their high specific power. Snow mobiles, in particular, use larger capacity two stroke engines compared to two wheel vehicles used on roads, often two cylinder engines between 500 and 800 cc displacement. Gasoline Direct Injection (GDI) has been developed for such high performance two stroke engines in order to reduce unburned hydrocarbon emissions and improve fuel efficiency. At Graz University of Technology, Austria, a number of studies have been conducted on this type of engine using 3D CFD including a whole engine model generated by Shmidt et al. (2004) which included a single cylinder, crankcase, transfer ports and exhaust system. The model was used to analyse different injection parameters including pressure, timing and direction relative to the cylinder axis. In their publication they noted that it was important to include the gas dynamics of the exhaust system in order to correctly model the gas exchange process. The engine uses a reed valve in the inlet system although the opening and closing of the reed valve was not included in the CFD model, instead a variable mass flow boundary condition was applied at the reed valve location. The mass flow for the reed valve was determined using a 1D engine simulation model. The combustion process was also analysed with 3D CFD using Eddy Break Up (EBU) and coherent flame models, these are phenomenological models in which the smallest scales of turbulence and structure of the flame are not resolved. With this simplified CFD approach to combustion modelling the whole engine model was still too large, in terms of computation time. A smaller computational mesh was used for the combustion model which was only solved during the closed cycle. At the start of the closed cycle the flow regime in the combustion model was defined as an initial boundary condition taking data from the whole engine model. In this approach to combustion modelling three levels of model were required, a 1D model to provide boundary conditions for a 3D whole engine model which then provides boundary conditions for the 3D combustion model. In the conclusions of their work they noted that the use of direct injection to reduce the loss of unburned fuel during the scavenging process would require an injection pressure greater than 12MPa. Injection pressures of 17MPa to 18MPa may be required for late injection in order to achieve reasonable fuel air mixing. Further work using CFD analysis on the same engine was carried out by Schmidt et al. (2007) to investigate modifications to the transfer ports and the effects on mixture

preparation. Stratified charge direct injection on a similar engine was experimented with by Johnson and Bravon (2008) as a means to improve fuel consumption at low loads. In stratified combustion mode improvements were only seen below 4000 rpm and 10% throttle position.

The ability of simpler 1D engine simulation techniques to accurately predict the performance characteristics of a two stroke engine has been demonstrated by Schoegl et al. (2010). In this work a similar two cylinder engine to that used in Schmidt's work was analysed using 1D engine simulation with a zero-dimensional Wiebe for combustion. Jajcevic et al. (2008) used a coupled 1D/3D modelling approach to reduce computer time, the exhaust system was modelled with a 1D gas dynamic code whilst the cylinder was modelled in 3D.

2.1.4 Small Power Plant

Small hand held power tools such as chain saws, leaf blowers, circular saws etc. are often powered by small two stroke engines. The main reasons for the choice of two stroke engine are its high specific power output relative to its weight as well as its low cost. A further advantage when compared to a four stroke engine is that it does not require an oil sump for hydrodynamic bearings and the engine can operate in any orientation, providing a pulse type carburettor is used rather than a traditional float chamber carburettor.

Research work has been conducted the University of Karlsruhe, Germany, on small power plant engines. Beck et al. (2006) investigated the combustion process of a 64 cc two stroke engine using fibre optics to detect the arrival of the propagating flame front at a number of positions around the cylinder head. Results from the fibre optic probes show that "the flame propagation is nearly symmetric around the cylinder axis". Further investigation work was carried out on the 64 cc engine by Beck et al. (2008) using ionization probes in the cylinder head and optical fibres mounted in the spark plug. Although the flame propagation could be detected by the probes no clear conclusion could be given for the flame front shape or movement. Pre-ignition and early flame propagation in a small 30 cc two stroke engine was studied by Schreer et al. (2009) using a number of pressure sensors and optical fibres fitted to the cylinder head. The signals from the optical fibres and pressure sensors were used to

identify the location of early flame propagation and pressure rise. The turbulent flame propagation was not evaluated on statistical mean basis over a number of cycles and the cycle by cycle early flame propagation did not appear to have a preferred direction. Gegg et al. (2010) used fibre optic endoscopes to monitor the ignition plasma formation and early flame development in a 64 cc engine. Ionization probes were also used which showed that for a single cycle the flame moved towards the exhaust port. The gas velocities in the region of the spark plug gap of a 70 cc engine were measured by Bertsch et al. (2011) using Laser Doppler Anemometry (LDA). The engine was motored up to 9000 rpm at full and part throttle. The peak velocity measured did not occur at the fastest engine speed, but at 7000 rpm where a velocity of just over 60 m/s was measured towards the end of the scavenge period. The direction of the maximum velocity was normal to the spark plug axis and this velocity reduced to 10 m/s at TDC.

2.1.5 Unmanned Aerial Vehicles

Two stroke engines may be used to power small aircraft, which can range from model aircraft to larger Unmanned Aerial Vehicles (UAVs) for military use. Research on two stroke engines used to power UAVs for military use has been carried out to investigate the use of JP-8 “heavy” fuel with the aim of achieving a single-fuel initiative. The lubricant qualities of JP-8 fuel with added oil were investigated by Lee et al. (2011) and compared with gasoline mixed with oil.

Tests on a spark ignition two stroke engine designed to run on JP-8 were carried out by La et al. (2012). The engine used air assisted direct injection which injects an air fuel mixture at sonic velocity to help atomise and vaporise the fuel. The purpose of the tests was to correlate a 1D whole engine simulation which will then be used to design performance improvements.

Researchers from the UFA State Aviation Technical University, Russia, Enikeev et al. (2011) published measured and whole engine simulation results for a four cylinder 800 cc two stroke engine. The simulation was made using a one-dimensional whole engine simulation model with a Wiebe combustion model.

2.1.6 Automotive

During the 1980s the automotive industry developed two stroke research engines intended for use in passenger vehicles, Fansler and Drake (2009) give an account of the development work conducted by General Motors at this time. More recently Orbital of Australia conducted high mileage tests on a fleet of cars fitted with three cylinder two stroke engines. Shawcross et al. (2000) reported the results of the study including emissions testing over the life cycle of a number of engines, the durability of the engines and driver impressions of the vehicle, in general the results were positive. The durability and maintainability of the vehicles was tested with some the vehicles exceeding more than 100 000 miles. The vehicle used in the study was a Ford Festiva in which the four stroke 1.3 litre engine was replaced with a two stroke engine. It was pointed out that although the engine was approximately 10% smaller it produced 19% more power. The two stroke engine used air assisted direct injection with an air/fuel ratio as high as 60/1, at idle. Its direct injection stratified charge contributed to good fuel consumption and emissions.

2.2 Whole Engine Simulation

Modelling of the internal combustion engine, with respect to its fluid mechanics and thermodynamics may be conducted at differing levels of complexity. Although most of the thermodynamic work is carried out in the cylinder it is important to model the delivery of air to the cylinder and removal of exhaust from the cylinder through the engine manifolds, ducts and plenums. The simplest level of engine modelling is often referred to as filling and emptying models (Winterbone and Pearson, 1999), these models use fixed volumes to represent the engines inlet and exhaust ducts which cannot account for the pressure wave motion in the ducts. As two stroke engines often use exhaust systems designed to use pressure wave motion to improve the gas exchange process the filling and emptying modelling approach is the least appropriate. The next level of engine modelling accounts for the travelling pressure waves in the manifolds and ducts using one dimensional techniques, these methods will be discussed in more detail in the following section. The most complex engine modelling technique uses multi-dimensional CFD codes, these methods produce the most detailed information on a spatial scale for the fluid mechanics and thermodynamics in

the engine. Examples of 3D CFD whole engine models applied to two stroke engines can be found in Schmidt et al. (2007) and Jajcevic et al. (2010). 3D CFD methods are, however, often computational prohibitive as a design tool. As a compromise aimed at reducing computer time coupled hybrid models using all the above methods may also be used.

2.2.1 One Dimensional Gas Dynamic Engine Models

Engine models using wave action methods to predict the gas dynamic flow within the engine manifolds have been described by Horlock and Winterbone (1986). The text describes how the Method Of Characteristics (MOC) are solved graphically and also describe Rolland Benson's methods to solve the methods of characteristics on a digital computer. The MOC was applied to whole engine models which include the boundary conditions to the manifolds such as cylinder valves, pipe junctions, branches etc. and also covered other engine hardware such as turbochargers and compressors.

An alternative method to MOC for the calculation of unsteady gas dynamics in one dimensional ducts was developed by Blair (1991) at Queens University Belfast, referred to here as the GPB method. The GPB method is based on a mesh space interpolation procedure in which each of the engines ducts is divided into a number of finite volume cells or mesh spaces. Within each space it is assumed that the pressure amplitude of both the rightward and leftward propagating waves varies linearly. The GPB method monitors the individual mesh space gas composition and the transport of gases between adjacent mesh spaces. This is particularly important in the two stroke engine because a mixture of unburned and burned gases will occupy the exhaust duct in different ratios along the length of the duct. Towards the end of the scavenging process the composition of gas at the entry to the exhaust duct will be similar the cylinder contents, which will be mostly fresh charge. With a tuned exhaust duct it is common to have a reverse flow of gas from the exhaust duct into the cylinder just prior to the exhaust port closing which can produce a supercharging effect. Blair (1996) published a detailed description on two stroke whole engine modelling including gas dynamics, cylinder scavenging and a combustion model based on the Wiebe approach. In his publication he presented test and simulation results for a number of small two stroke

engines including a 125 cc motorcycle engine. Some examples of the necessary Wiebe parameters and burn durations were given.

Other methods of 1D finite volume gas dynamic modelling have been developed including work at the Polytechnic University of Milan, Italy, where a whole engine simulation code has been developed, known as GASDYN. The method uses a Lax Wendroff scheme for solving the gas dynamics in engine ducts. Onarati et al. (2004) used the whole engine simulation code to model a 90 second transient drive cycle of a four stroke engine including exhaust catalyst warm up to predict emissions.

At the University of Napoli, Italy, a finite volume 1D code has been developed for gas dynamic ducts incorporated into whole engine simulation models. The whole engine simulation code known as DIME and its 1D gas dynamic code has been reported by Bozza et al. (1995) who used the code to model a 198 cc two stroke engine. The combustion process of the engine simulation was modelled with a two zone fractal approach, which is discussed in more detail in Section 2.3.3. Cylinder scavenging is modelled with a perfect mixing model which was recognised as a potential short fall in the whole engine simulation. The same code was used by Bozza and Gimelli (2004) to model a 50 cc two stroke engine again with a fractal combustion model but this time with an improved model for scavenging.

A two-step Lax-Wendroff method for calculating the gas dynamics in engine ducts has been applied to an air assisted direct injection two stroke engine and reported by Payri et al. (2001). In their simulation they used 1D modelling for inlet and engine ducts and 3D CFD to simulate the scavenging process.

2.2.2 Applications for 1D Engine Modelling

Before choosing an engine modelling technique it must first be decided how much detail is required for an acceptable solution. Modelling every detail of the thermodynamics of an engine at the smallest scale is not practical. One dimensional modelling may be preferable to multi-dimensional modelling for a number of applications, for example if a large number of design iterations on basic engine geometry such as bore, stroke, compression ratio, port timings etc. are required. Another example where one dimensional modelling might be

preferable to multi-dimensional is when a large number of engine cycles need to be solved for a particular engine design such as a transient drive cycle analysis.

A transient engine simulation developed by Baruah (1990) was coupled to a simple vehicle model which included the engine, clutch, gearbox, axle gear and wheels. Gas dynamics in the engine manifolds were accounted for using the method of characteristics. A two zone combustion model was included which assumes the propagating flame is spherical. The turbulent flame speed is a function of the laminar flame speed and engine speed which varies linearly with engine speed. Only a simple step throttle acceleration and deceleration cycle was tested over a 6.5 second time period. The model could be used to qualitatively predict emissions from a dynamically operated engine, but It was stated that "extensive vehicle testing is required to calibrate the model accurately." indicating that the model is not totally predictive.

A coupled vehicle/engine simulation of a four cylinder, four stroke engine was described by Onarati et al. (2004). The coupled model was generated using GASDYN, introduced above, which takes account of the gas dynamic effects in the engines inlet and exhaust ducts. The engine model also included a multi-zone fractal combustion model. The simulation was used to calculate exhaust emissions during start up and the initial 90 seconds of running. During the 90 second transient drive cycle approximately 1000 engine cycles were solved. Chemical reactions within the exhaust system and catalytic converter were also included in the model in order to predict tail pipe emissions. The vehicle model accounted for the vehicle mass, the moment of inertia of the engine and wheels and transmission.

A two zone combustion model was included in a transient engine simulation by Lafossas et al. (2005) and used for a simulation of a four cylinder, four stroke, turbocharged, direct injected spark ignition engine. In the turbulent combustion model the turbulent kinetic energy is related to the engine speed and a characteristic tumble number which in turn was related to engine volumetric efficiency. Unlike other quasi-dimensional models, the flame was assumed to be a complete sphere centred in the combustion chamber until the flame diameter is equal to the combustion chamber height after which the flame front is assumed to be cylindrical. The turbulent flame velocity was calculated as a function of turbulence intensity, integral scale length and eddy viscosity. The whole engine model includes ducts,

turbocharger, heat exchanger and other elements and is generated using IFP engine library in the AMESim environment. Just the inlet manifold pressure was reported for the transient simulation although this did show a good correlation with test results, transient results from the combustion simulation or exhaust were not presented.

2.3 Combustion Modelling

A number of methods have been developed for modelling the combustion process in a piston engine, the simplest methods involve zero-dimensional models and the most complex methods use multi-dimensional CFD models. Between these two extremes there is a level of modelling known as quasi-dimensional modelling. The following sections give a short description for zero-dimensional and multi-dimensional modelling, then follows a more detailed review of some of the quasi-dimensional models available in the literature.

2.3.1 Zero-Dimensional Combustion Modelling

Zero-dimensional models use a pre-defined heat release rate which usually takes the form of an S shape curve or sigmoid curve, known as a Wiebe model. The constants that define the Wiebe model may be defined taking into account the in-cylinder conditions just prior to the combustion event. An example of a Wiebe for small two stroke engines was developed by Galindo et al. (2011). They produced expressions to calculate the Wiebe model constants for a 50 cc and 125 cc engines based on the in-cylinder density, mean piston speed, trapped residuals and ignition timing. However important parameters not included in the determination of the Wiebe constants were air/fuel ratio and combustion chamber geometry.

2.3.2 Multi-Dimensional Combustion Modelling

In multi-dimensional combustion modelling the cylinder is descretised into a large number of small volumes, normally referred to as a mesh. For CFD analysis to solve the turbulent chemical reacting flow at the scale of the inner structure of the flame an extremely fine mesh will be required, mesh spacing could be of the order of 0.001 mm. CFD analysis where the

small scale structure is resolved is known as Direct Numerical Simulation (DNS). Poinsot and Veynante (2005) give an example of DNS for a turbulent flame at atmospheric pressure in a 5 mm^3 box which requires 1-2 million grid points to solve. CFD analysis of combustion in an engine cylinder using DNS would be computationally prohibitive due to the refined mesh required, so other methods which do not resolve the small scale flow structure have been developed. Reynolds Averaged Navier Stokes (RANS) is a CFD method that does not analytically solve the turbulent flow structure, rather mean values of the flow field are calculated and a sub grid scale model is used for turbulence. Combustion analysis using RANS CFD will require a further sub grid model to account for the turbulent flame structure. One example of a phenomenological flame structure model used with RANS is the EBU model. Large Eddy Simulation (LES) CFD is an analysis method which is less demanding, computationally, than DNS but resolves the turbulent flow field at large scales, and then the smaller scales of turbulence are accounted for with sub grid models. As with RANS a further sub model is required to account for the flame structure when using LES, the EBU model has been modified for use with LES and other models are available.

2.3.3 Quasi-Dimensional Combustion Modelling

The quasi-dimensional modelling approach takes into account the combustion chamber and flame front geometry using a simple assumption based on a spherical flame front. Many quasi-dimensional models are made up of two zones, burned and unburned gas. The two zones are separated by a flame front which is usually assumed to be infinitely thin and propagates radially outward from the spark plug. The rate at which the flame propagates depends upon a number of parameters including turbulence and flame structure. Different ways have been used to define the flame structure for homogenous premixed combustion in piston engines, the two most common methods are based on either an eddy entrainment model or flame wrinkling. Based on either entrainment or wrinkling a definition of turbulence is required for a quasi-dimensional model to determine turbulent flame propagation. A number of quasi-dimensional models have been developed which are available in the literature, a brief summary of some of these models, based on either the eddy entrainment or flame wrinkling, is given below.

Eddy Entrainment

Blizard and Keck (1974) developed a turbulent entrainment model for a propagating flame front. It is assumed that once the turbulent eddies are entrained by the flame front the flame propagates along the highly diffusive boundaries between the eddies and that the eddy burns inward at the laminar burning velocity. The size of the turbulent eddies was based on the inlet valve lift and compression ratio. Tabaczynski et al. (1977) developed the turbulent entrainment model further by introducing the Taylor scale of turbulence. A homogeneous and isotropic turbulent structure was assumed where the dissipative vortex tubes are at the Kolmogorov scale and separated at the Taylor scale consistent with Tennekes (1968). It is assumed that the flame propagates along the Kolmogorov scale vortex tubes. Tabaczynski et al. (1980) defined the propagation rate along the vortex tubes as the sum of the laminar burning velocity and the turbulence intensity.

A two zone combustion model has been developed for a four stroke engine and reported by Polous and Heywood (1983). The model uses the eddy entrainment concept originally proposed by Blizard and Keck (1974) for the flame structure. A simple energy cascade model for turbulence was incorporated which was originally developed by Hossien Mansouri et al. (1982) for a diesel engine. Kinetic energy enters the cylinder with mass and velocity of the fresh charge, the kinetic energy produces turbulent kinetic energy which is subsequently dissipated.

A turbulent eddy entrainment model was proposed by Chen and Veshagh (1992), which included an early flame kernel development model which defined the early turbulent flame propagation. When the flame radius is much smaller than the integral scale the flame speed will be unaffected by the turbulence. They also note that the turbulent flame speed is characterised by the ratio of flame size to the integral scale. Once the flame radius is greater than the integral scale the flame propagation is fully developed.

An assessment of available turbulent combustion models was carried out by Agarwal et al. (1998). In the assessment both single zone and two zone turbulence models using k-ε and energy cascade approach were included. The turbulence models were used with an eddy entrainment combustion model. The study used a simple filling and emptying engine model

with the combustion model. The energy cascade method for modelling turbulence was taken from Hossein Mansouri et al. (1982), whilst the single zone k-ε model was taken from Ramos (1989) and the two zone k-ε model was taken from Borgnakke (1980). Each of the four models use calibration constants and these were defined using tests on a 1.9 litre four cylinder four stroke engine at medium load. With the calibration constants set at one speed and load a quantitative test for each of the models is made by comparing model predictions with test results for other engine loads. The two zone k-ε model performed the best and in general all the two zone turbulence models performed better than the single zone models. For medium load and high load conditions the peak pressures predicted by all the combustion models were all within 5% of the measure peak pressures.

A quasi-dimensional combustion model was incorporated into a transient whole engine simulation of a turbocharged spark ignition engine by Filipi (1991). The combustion model is based on the eddy entrainment model of Blizard and Keck (1974), the turbulence model used was taken from Hossein Mansouri et al. (1982), Polous and Heywood (1983). Gas dynamics were not included in the simulation, rather a simple filling and emptying approach was used to model the effects of the engine manifolds. In the whole engine simulation a number of other features were also modelled including a turbocharger and its waste gate and engine friction effects. In the paper the authors emphasise a need to model a large number of mechanisms, thermo-fluid and mechanical in order to be able to define engine performance.

The eddy entrainment model of Blizard and Keck (1974) has been applied to a two stroke engine by Reid (1993). A k-ε turbulence model is used to predict the turbulent intensity taking into account squish clearance and piston motion. The interaction between the flame front and combustion chamber walls is determined by assuming a spherical flame front whilst the combustion chamber surface is defined by a large number of points in cylindrical polar coordinate system and stored in a look up table. By determining which points lie within the flame front the surface areas and volumes can be found. The model was applied to both a simple disc combustion chamber and a typical squish type combustion chamber. Although the model was able to be predict quite well the mass fraction burned and heat release rate for the plane disc combustion chamber the predictions for the squish chamber

are less encouraging. The predicted and measured heat releases from the squish combustion chamber are shown below in Figure 2-3. In the conclusion to his work Reid noted that the poor correlation of predicted heat release in the latter half of the combustion process was attributed to difficulties in modelling the flame front as it propagates through the squish band.

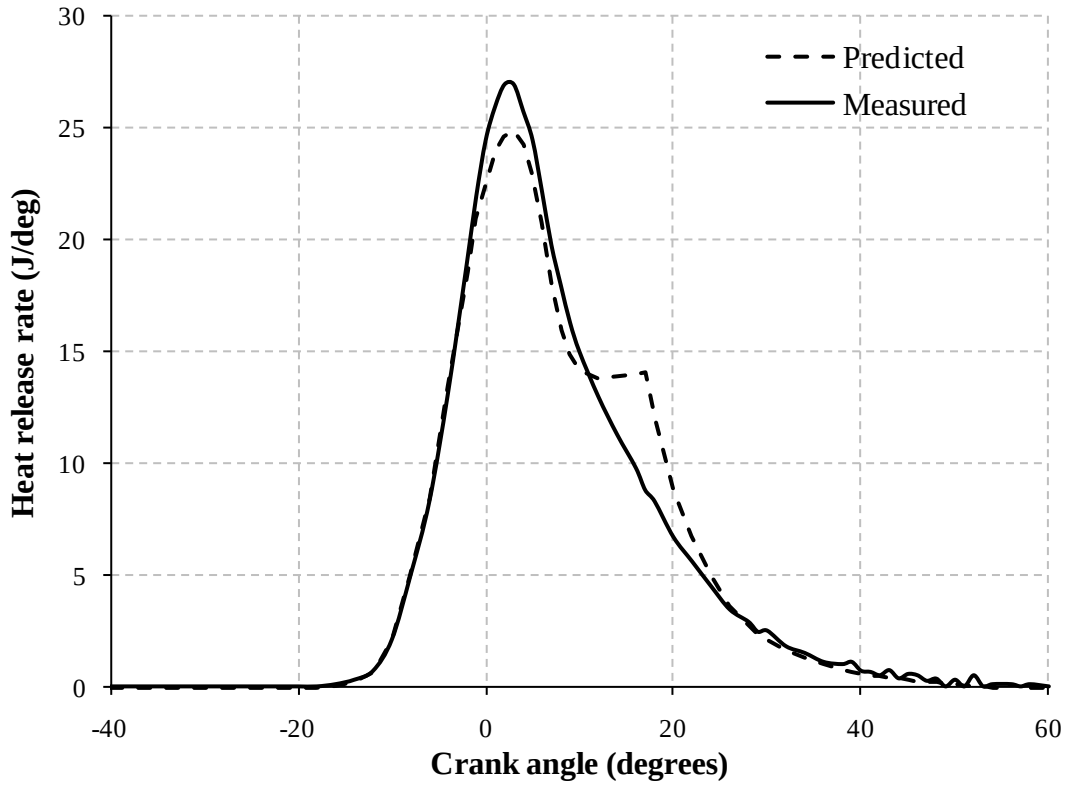

Figure 2-3, Heat release rate at 3000 rpm and full throttle for a squish combustion chamber adapted from Reid (1993)

A combustion model based on the mass entrainment flame structure of Tabaczynski et al. (1977) and the turbulent energy cascade model of Poulos and Heywood (1983) was applied to a four stroke engine and reported by Lee and Filipi (2011). The turbulence model was modified using an additional constant to account for a charge motion control valve which is situated upstream of the inlet valve and used to enhance cylinder turbulence. The combustion model was integrated with the commercial whole engine simulation code

Ricardo Wave. The whole engine model then accounts for gas dynamics in the manifolds and ducts from the engine air filter to exhaust tail pipe.

It is generally assumed that in-cylinder turbulence increases linearly with engine speed and taking this into account combustion models have been developed with turbulence defined as a function of mean piston speed rather than using an energy cascade model or k-ε model. This approach was used by Verhelst and Sierens (2007) who assumed that the turbulence intensity is defined as a function of mean piston speed up to TDC and then decays linearly after TDC. The model was applied to an engine fuelled with hydrogen. They also suggest in their publication that 3D CFD modelling techniques are more suitable to research and development work on simpler combustion models which may then be used to develop engine simulation tools.

The eddy entrainment model was used by Ma et al. (2008) to investigate the use of hydrogen enriched compressed natural gas in a four stroke turbocharged engine. The model was assessed against engine tests and the results were reported as being satisfying.

An eddy entrainment combustion model was developed for a small two stroke engine by Hunzinger et al. (2006), once again the assumption is made that the flame propagates spherically outward from the spark plug. The burned and unburned zones are separated by the infinitely thin flame front. The flame front area is calculated by interpolating between look up tables generate using CAD software. For turbulence a value for the turbulent kinetic energy was defined at exhaust port closure based on the mean piston speed, delivery ratio and cylinder geometry. During the closed cycle further turbulent kinetic energy is generated due to compression and also turbulent kinetic energy is lost due to viscous dissipation. The results of the simulation show a very steep rise in turbulence intensity towards the end of combustion, which may not be accurate.

An eddy entrainment model was used to investigate cycle by cycle variation in a single cylinder two stroke research engine by Abdi Aghdam et al. (2007) at Leeds University. A different method was used to determine the entrainment velocity which took into account the proximity of the flame front with the combustion chamber walls and also the elapsed time from ignition. The same combustion model was integrated into a whole engine simulation,

using the commercial code GT Power, and applied to a four valve four stroke production engine.

Flame Wrinkling

Rather than the eddy entrainment model a combustion model which assumes the flame front to be a single thin wrinkled surface in which the surface area is defined by fractal geometry was proposed by Gouldin (1987). The flame front proceeds at the local laminar burning velocity and the enhanced turbulent burning rate is due to the increased surface area of the flame front caused by wrinkling. The increase in surface area due to wrinkling is defined by fractal geometry.

A quasi-dimensional combustion model using the fractal approach for flame wrinkling has been developed for a four stroke engine by Matthews and Chin (1991). The in-cylinder turbulence intensity and integral length scale were defined by the turbulence model taken from Poulos and Heywood (1983). The nominal flame is again assumed to be spherical and propagate from the spark plug electrodes.

A two zone fractal combustion model has been developed by Bozza et al. (1995) and applied to a 198 cc two stroke engine. Later Bozza and Gimelli (2004) applied the fractal model to a 50 cc two stroke engine with a squish combustion chamber. In the latter work a turbulence model taken from Poulos and Heywood (1983) was incorporated. The flame front geometry was defined using CAD geometry to generate look up tables which are then interpolated between during the simulation. In their publication the turbulent flame front area has been plotted against crank angle and shows a similar profile to the heat release curve generated by Read (1993), Figure 2-3. As the heat release is a function of the flame front area it may then be assumed that Bozza's fractal model will have the same issue with heat release rate that Read showed. Bozza et al. (2005) also applied the fractal combustion model to a four stroke engine.

Eddy Entrainment versus Flame Wrinkling

The eddy entrainment model was initially developed nearly forty years ago and has been recently applied, with reasonable success, to both four and two stroke engines, Ma et al. (2008) and Hunzinger et al. (2006). Experimental methods used to observe flame fronts inside engines, including laser sheet imaging, have also seen significant development over the last three decades. A number of researchers including Mantzaras et al. (1988), Hicks et al. (1994), Gillespie et al. (2000), Yoshiyama et al. (2001) and Verhelst and Sheppard (2009) have all shown, by laser sheet imaging, that the flame front is a highly convoluted and wrinkled surface. However, experimental observation using laser sheet imaging has not shown significant evidence of eddy entrainment, and subsequent consumption, as being the predominant mechanism for premixed turbulent combustion. In conclusion it is assumed in this work that the flame wrinkling better models turbulent flame structure than does eddy entrainment.

2.3.4 In-Cylinder Bulk Flow Motion

Whilst most quasi-dimensional models use the assumption that the flame front remains centred at the spark plug location, bulk flow motion in the cylinder may be able to advect the flame away from the spark plug. In piston engines in-cylinder bulk flow motion can usually be defined as swirl or tumble. A swirl bulk flow motion rotates around the axis of the cylinder whilst a tumble motion rotates about an axis normal to the cylinder axis. Phenomenological models have been developed to predict in-cylinder motion for both swirl and tumble.

A simple model for predicting the swirl motion in a two valve four stroke engine was developed by Borgnakka et al. (1981). The model was based on the conservation of angular momentum of the cylinder contents and where momentum is added to the cylinder by the fresh charge entering through the inlet port. A k-ε model was included for turbulence.

A phenomenological model for in-cylinder tumble motion was developed by Benjamin (1992) and further developed to include a k-ε turbulence model by Benjamin (1993). The model calculates the tumble motion based on the conservation of angular momentum, taking

into account turbulent shear stresses which reduce the tumble motion. The model was developed for just the compression process in a simple disc combustion chamber. The model was further developed by Achuth and Mehta (2001) to include the inlet stroke of a four stroke engine and the momentum added to the tumble motion due to the fresh charge entering the cylinder through the inlet port. A comparison was made between the Achuth and Mehta phenomenological model with a 3D CFD analysis by Ramajo et al. (2007). The comparison considered two variations of pent roof combustion chamber. One of the pent roof combustion chambers used a conventional port whilst the other used a port designed to promote a tumble flow. The angular momentum of the tumble flow calculated by both the phenomenological and CFD models have been compared and it was shown that for the conventional port that the tumble motion generated during the intake stroke gave a reasonable correlation. The tumble momentum, however, decayed significantly faster in the zero-dimensional model than the CFD analysis from the late in the induction stroke. For the tumble port configuration the phenomenological model under predicted the CFD results during the inlet stroke and the CFD results show a larger tumble momentum until late in the compression stroke. Generally poor correlation was seen between the two methods.

A phenomenological model to predict the tumble motion and turbulence in a four stroke engine was presented by Dai et al. (1996). Once again the calculation for tumble velocity is based on the conservation of angular momentum, where momentum is added through the inlet port and momentum is lost due to viscous shear. A simple one equation model is used for the calculation of turbulent kinetic energy which includes a term for the turbulent energy generated by shear due to the tumble motion.

A quasi-dimensional combustion model which included a prediction for tumble motion based on the conservation of momentum was reported by Watanabe et al. (2010). An energy cascade model similar to that proposed by Hossein Mansouri et al. (1982) is used to determine turbulence where kinetic energy lost from the tumble motion becomes a gain in turbulent kinetic energy. A further term is added which accounts for turbulence generated by compression. Heat release in the combustion model was based on the Wiebe approach.

Other Turbulent Combustion Models

A simple approach to determining the turbulent flame propagation without referring to flame structure was used by Tsai (1994). The turbulent flame speed is determined by multiplying the laminar burning velocity by a flame factor which is based on engine speed, the flame factor being derived empirically. Tsai included the two zone combustion model into a whole engine simulation model for a two stroke engine with an exhaust system designed to use pressure wave motion to improve performance.

2.4 Experimental Methods Used in Engine Combustion Research

A variety of methods to monitor and measure the progress of combustion in an engine cylinder have been developed. The single most common device is a cylinder pressure transducer, although capable of determining the rate of heat release and mass fraction burned it is unable to provide information on flame location and structure. Optical engines provide the ability to observe in-cylinder flow motion and flame propagation in an engine. Today many systems of lasers and high speed digital cameras are used with optical engines, however they are limited in engine speed. Recently Rimmer et al. (2009) published high speed particle image velicimetry results for a four stroke engine operating at 1500 rpm, 750 combustion events per minute. The engine used in this study operates at up to 10,000 combustion events per minute. Optical engines with a large field of visual access are purpose built research engines and require a significant investment to procure.

A method of gaining optical access to an engine combustion chamber using production hardware rather than manufacturing an optical research engine is to use optical fibres. A modified spark plug with eight optical fibres added was used by Beck et al. (2008) to investigate the early flame progress in a 64 cc two stroke engine. As the optical fibres are included in the spark plug no modifications are required to the production cylinder head. However during tests fouling of the optical fibres did occur.

Ionization Probes

In this work an existing engine will be used for test and validation so the instrumentation used to monitor the progress of the flame front is required to fit within existing hardware.

To monitor the flame front propagation and the bulk flow motion of the burned zone ionization probes have been fitted into the cylinder heads of piston engines. Ionization probes have been used for several decades to investigate the combustion process, they offer an economical way to measure the progress of the flame front with minimum interference to the in-cylinder flow motion.

Ionization probes have been proved capable of monitoring the propagation of a turbulent flame front in high speed engines. Pfeffer et al. (2002) used twelve ionization probes to monitor the flame front propagation in a high speed, pent roof, tumble, four stroke engine. The cylinder head was modified by drilling and inserting ionization probes, four close to the spark plug (8 mm radius) and eight close to the cylinder wall. The ionization probes at the outer edges of the combustion chamber had to be designed to operate in a tight squish zone. The engine was operated at speeds up to 17,000 rpm and the signals from the probes were used to produce flame propagation contour plots which indicate the shape of the flame front. Flame speeds in excess of 120 m/s were also measured. In another example twenty five ionization probes were fitted in the cylinder head of a high speed four valve engine used by Kato et al. (2007). The engine was operated at speeds up to 16000 rpm and the probes were able to monitor the flame propagation speeds of up to approximately 180 m/s.

A simple method of fitting ionization probes to an engine without significant modification to the engine is to insert the probes in a replacement head gasket. Witze (1989), Meyer et al. (1993), Nicholson and Witze (1993), Witze (1994), Salvat et al. (1994), Hadjiconstantinou and Heywood (1995) have all included ionization probes in the head gasket of four stroke engines. Witze (1994) used a two zone spherical flame front combustion model to compare predicted flame front position with measured flame arrival times at ionization probes. It was shown that by monitoring the evolution of the spherical flame it would be possible to discern the in-cylinder bulk flow motion. Much work has been done on four stroke engines using ionization probes embedded within the head gasket by Russ et al. (1997) who used a four

stroke engine configured to produce both swirl and tumble motion. Eight ionization probes were placed in the head gasket and these were able to show that the flame moved towards the exhaust port in the tumble configuration but stayed more central in the swirl configuration. The advantage of the head gasket approach is that no modifications to the cylinder head are required however a disadvantage is that the flame arrival times are only determined at the cylinder wall.

An advantage of the two stroke engine used in this work is that there are no poppet valves in the cylinder head which allows more room for ionization probes to be fitted to the existing cylinder head by drilling. Different researchers have constructed ionization probes in different sizes and configurations. A simple method for producing an ionization probe is to use a spark plug with the side electrode removed, an approach used by Arrigoni et al. (1973), Reid (1993), Vressner et al. (2004) and James et al. (2010).

Two different approaches have been used in the design of bespoke ionization probes, the first approach uses two wires in close proximity which form the anode and cathode of the ionization probe. The second approach uses a single wire for the electrode and then the combustion chamber is used as an earth. The second approach was used by Blizard and Keck (1974) who inserted five ion probes into the cylinder head of a two valve four stroke engine, three near the cylinder wall and two approximately half way between spark plug and the cylinder wall. The ionization probes were used to validate a two zone eddy entrainment combustion model for an engine with a plane disc type combustion chamber. The ionization probes were made using 0.81 mm (0.032 in) diameter nickel wire in a ceramic tube. The two wire approach was used by Ohigashi et al. (1971) and Hamamoto et al. (1996) who installed two separate wires into fixed volume combustion chambers. The two wires were insulated from the combustion chamber walls by either PTFE or ceramic tubes.

Ionization probes have been continually developed to monitor the propagation of a flame front in engines and recently as many as 80 ionization probes were used in a four stroke pent roof combustion chamber by Tanaka et al. (2009).

Ionization probes and fibre optics were used in a small capacity two stroke engine running up to 9000 rpm by Beck et al. (2008). As well as ionization probes fitted specifically for test purposes the spark plug was also used as an ionization probe.

2.5 Concluding Remarks

Despite challenges with poor emissions, loop scavenged two stroke engines continue to be used in a number of applications including small capacity motor cycles and scooters, off road recreational vehicles, hand held power tools and UAVs. To address the issue of poor emissions new technologies, many of which are currently in used on four stroke engines, are being applied to two stroke engines. In order to improve the design process and reduce the need for experimental development new computational design tools are continually being developed. Perhaps the most complex process in an engine is the combustion process and in this work a combustion model will be developed for a loop scavenged two stroke engine. The combustion model will be incorporated into a whole engine simulation which includes pressure wave motion in the exhaust duct. The model will be validated against engine tests using ionization probes to monitor the progress of the flame front.

3 In-Cylinder Flow and Turbulence

The rate of combustion in a piston engine is significantly influenced by the levels and scales of turbulence in the cylinder. Turbulence might be described as a three dimensional random motion of fluid with a broad spectrum of velocities and length scales. A fluid motion that is not turbulent would be referred to as laminar and the transition from a laminar to a turbulent fluid motion occurs at a Reynolds number of approximately 2000, the Reynolds number being the ratio of inertia and viscous forces. The flow inside the cylinder of a running engine will always be turbulent. An instantaneous velocity vector at a point location in the cylinder may be divided into two components, a mean velocity and a turbulent velocity, Figure 3-1 below show schematically the concept of mean and fluctuating velocity. The mean velocity will vary periodically with a frequency consistent with the engine speed. The turbulent velocity will fluctuate about the mean velocity. The mean velocity represents a bulk flow or large scale motion in the cylinder which is usually referred to as either swirl or tumble.

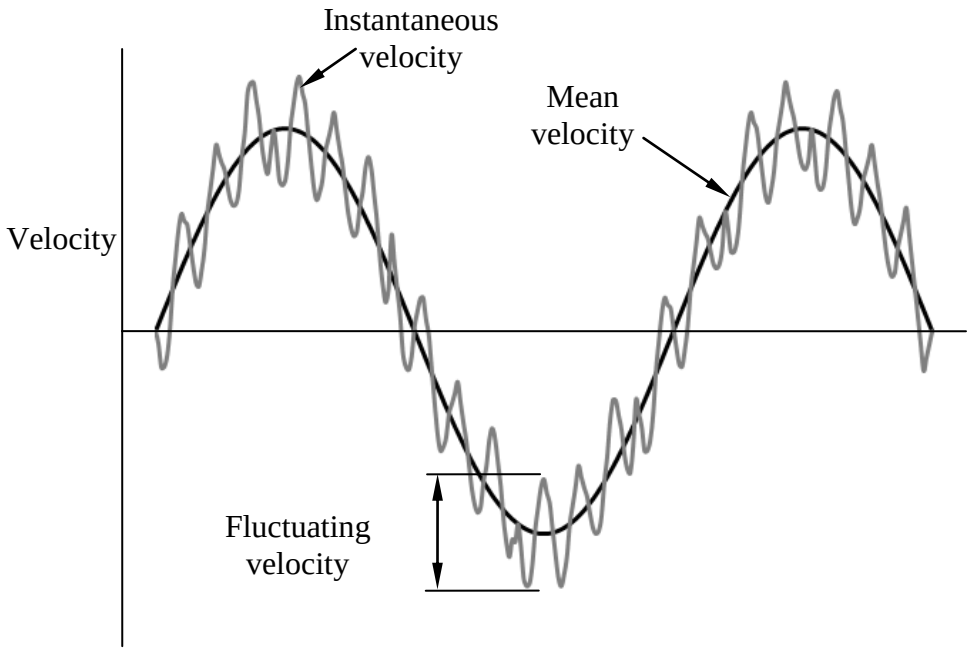

Figure 3-1, Instantaneous, mean and fluctuating velocities

3.1 Two Stroke Scavenging and In-Cylinder Flow Motion

The bulk flow motion in a piston engine is generated during the gas exchange period and two stroke engines may use either swirl or tumble depending on the engine and port layout. One example of swirl used in a two stroke engine is a uniflow scavenged engine in which the fresh charge enters the cylinder through ports in the cylinder wall that are open when the piston is near BDC. The cylinder wall ports are arranged to generate a tangential velocity component in the cylinder. The fresh charge fills the cylinder from the bottom whilst the exhaust exits through poppet valves in the cylinder head. A typical example of a two stroke engine using a tumble motion is a loop scavenged or Schnurle ported engine. In the loop scavenged engine fresh charge enters the cylinder through ports in the cylinder wall that are open near BDC, the fresh charge then travels towards the cylinder wall on one side of the cylinder whilst exhaust exits through an exhaust port on the opposite side of cylinder wall. The tumble motion should be repeatable and predictable and will persist after the completion of the scavenge process. The correct level of tumble is important in a loop scavenged engine as excessive tumble may lead to an increase in mixing between the fresh charge and exhaust gases. Increased mixing during the scavenge process will tend to increase the amount of residual exhaust trapped in the cylinder after exhaust port closes.

The engine considered in this study is a loop scavenged two stroke engine with transfer ports arranged symmetric about a plane which passes through the axis of the cylinder and the centre of the exhaust port. The jets of fresh charge entering the cylinder should collide at the plane of symmetry, or tumble plane, and then be directed towards the cylinder wall opposite the exhaust port. Figure 3-2 shows a diagram looking into the cylinder from the cylinder head, there are four transfer ports, two main, two auxiliary and one exhaust port. The arrows in Figure 3-2 show the direction of flow of fresh charge exiting the transfer ports and exhaust gas leaving the cylinder through the exhaust port.

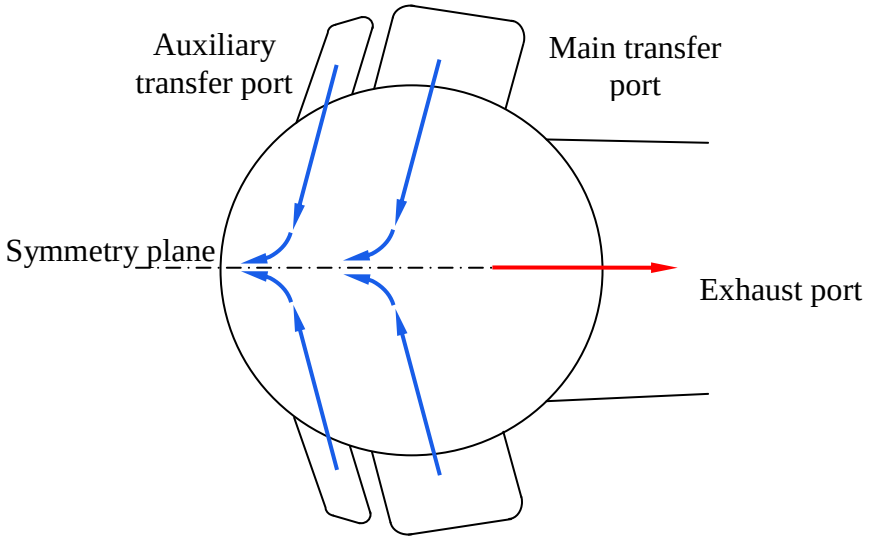

Figure 3-2, Scavenge flow view looking into the cylinder

Two stroke spark ignition engines are often designed with squish combustion chambers, Figure 3-3 below shows a side view of such a combustion chamber and cylinder, sectioned through the tumble plane. The spark plug is normally positioned on the tumble plane and in the centre of the combustion bowl as shown. Also shown is the fresh charge entering the cylinder and creating the scavenge loop. The flow through the exhaust port depends both on the cylinder pressure and the pressure in the exhaust manifold. A two stroke engine with an exhaust system designed to use pressure wave motion to improve trapping efficiency may produce a reverse flow from the exhaust duct into the cylinder just prior to the port closing.

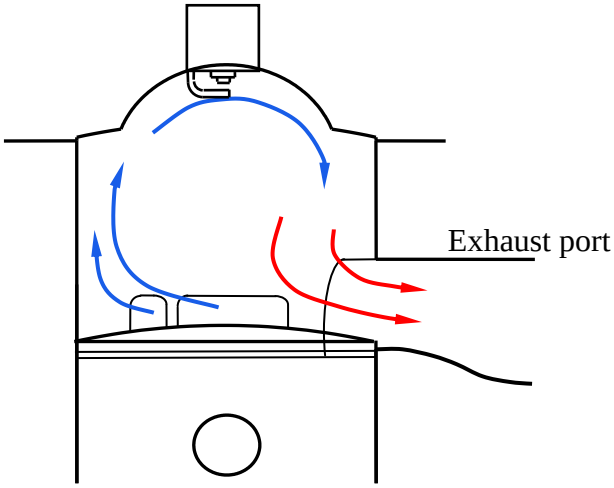

Figure 3-3, Loop scavenge flow

After the transfer and exhaust ports have closed and the compression stroke begins the tumble vortex, generated during the gas exchange period, is compressed as the piston moves closer to the cylinder head. The compressed residual tumble vortex will form an elliptical profile as shown below in Figure 3-4. The tumbling vortex persists during compression until near TDC when the tumble vortex will break down into smaller scale turbulence.

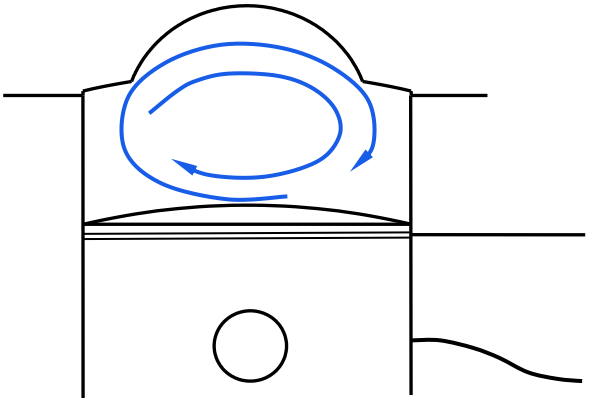

Figure 3-4, Elliptical tumble vortex

A number of researchers have studied the scavenging flow and tumbling motion in loop scavenged engines including Fansler and French (1992) who used Laser Doppler Velocimetry (LDV) to measure the velocity vectors in a motored two stroke engine. The engine in the study was loop scavenged with a bore of 84 mm, stroke of 72 mm and fitted with a disc type combustion chamber. The results of their experiments show the tumble motion produced during the scavenge process and that it persists into the closed cycle but is destroyed around 30° BTDC. Amsden et al. (1992) used the KIVA-3 CFD code to model the tumble flow of the engine used by Fansler and French in their experiments, the KIVA-3 code was used with a standard k-ε model for turbulence. The results of the CFD analysis appear to overestimate the amount of tumble at 30° BTDC when compared to the experimental results.

CFD results images, Fig 6 from Moriyoshi et al (1999), removed for copyright reasons

Figure 3-5, Tumbling vortex in a two stroke engine operating at full throttle and 6000 rpm taken from Moriyoshi et al. (1999)

A multi-dimensional CFD simulation of a loop scavenged two stroke engine with a bore of 71.3 mm and stroke of 65 mm was conducted by Moriyoshi et al. (1999). The commercial

code FLUENT, also using a k-ε turbulence model, was used in the analysis. Velocity vectors from that analysis, at an engine speed of 6000 rpm and full throttle, are shown above in Figure 3-5. The velocity vector plots clearly show the tumble vortex generated during the scavenge period which persist during compression.

Ahmadi-Befrui et al. (1989) conducted a multi-dimensional CFD analysis of a 250 cc loop scavenged two stroke engine with a bore of 67.5 mm, stroke of 69 mm and fitted with a squish combustion chamber. The results show the formation of the scavenge loop during the scavenge process and that the tumble motion persists during the compression stroke. It was stated that the tumble motion persists "until near TDC (ie around CA=320°) when the tumbling motion breaks up". In their velocity vector plots some amount of tumble motion can still be seen inside the combustion bowl at 20° BTDC, whilst in the squish region there is a radial flow towards the centre of the cylinder. A study of the flow motion in a 50 cc two stroke engine using CFD with k-ε model for turbulence was carried out by Yu et al. (1997). The engine analysed used a squish combustion chamber that was similar to that analysed by Moriyoshi et al. (1999). The analysis was conducted at 6000 rpm and the maximum tumble velocity just after exhaust port closing was 39 m/s and at TDC there was still reasonable tumble velocity of 16.3 m/s.

A multi-dimensional CFD analysis of the scavenging and compression cycle of a two stroke cylinder was carried out by Tsui and Cheng (1994). The engine has a bore of 74 mm, stroke of 75 mm and the combustion chamber was a simple disc type. From the results of their analysis, after the transfer ports have closed, they describe the in-cylinder motion as "the single tumbling vortex dominates the flow structure...". Tsui and Cheng (1995) extended their analysis to consider the effects of a domed cylinder head on the in-cylinder flow. Five different cylinder heads were analysed each with the same compression ratio but with differing curvature radius on the top of the combustion chamber. As the radii on the top of the combustion chamber reduces the height of the chamber increases. The effect of increasing the height of the chamber increases the turbulence, but also delays the position of peak turbulence intensity to closer to TDC. It is considered here that the delay in the peak intensity value is due to the breakdown of the tumble vortex occurring later in compression stroke.

3.2 Mean Flow Model

Both experimental and CFD analysis results have shown that a tumble motion is generated during the transfer period due to the fresh charge entering the cylinder. The fresh charge is directed by the transfer ports to generate a loop scavenge flow and the available data also shows that the tumble motion persists during the compression stroke. During the compression process the tumble vortex will lose its momentum primarily due to viscous shear between the vortex and the cylinder walls. As the tumble vortex looses momentum turbulence is generated in a shear layer between the vortex and cylinder walls. As the in-cylinder turbulence will influence the speed of the flame propagation a combustion model will require an estimate for the turbulent kinetic energy in the cylinder. Although most of the tumble momentum will be lost by TDC any amount of tumble motion that is present after the time of ignition will advect the flame front and burned mass away from the spark plug. The assumption is made in the present study that the flame front is spherical and propagates radially outward from the centre of the burned zone which originates at the spark plug. As the flame front propagates through the combustion chamber the area of the flame front will be restricted by its interaction with the combustion chamber walls. Both the flame radius and flame centre location will define the interaction between flame front and chamber walls. An estimate for the flame front area will be required for the combustion model in order to determine the heat release rate. The quasi-dimensional combustion model developed in this study will use a phenomenological model for the tumble motion which will be able to predict the generation of the tumble motion due to the fresh charge entering the cylinder and loss of tumble motion due to viscous shear. As viscous shear caused by the tumble vortex generates turbulence the tumble model is also required to predict the production of turbulence, due to tumble vortex, in order to determine the turbulent flame propagation rate.

3.2.1 Tumble Generation

The tumble vortex generated during the scavenge period rotates about an axis normal to the cylinder axis with the centre of the vortex being approximately at the middle of the cylinder chamber height. The vortex rotates with an angular velocity ω and an angular momentum Ω. As the fresh charge enters the cylinder, with velocity and mass, momentum is added to the

tumble vortex. The rate at which momentum is added to the vortex may be defined as a torque and the rate at which the tumble momentum is lost due to viscous shear may also be defined as a torque.

A phenomenological model to predict tumble motion in an engine during closed cycle compression has been developed by Benjamin (1992) for a plane disc type combustion chamber. The model was further developed by Benjamin (1993) to include the k-ε turbulence model of Borgnakke et al. (1981) such that a turbulent viscosity could be calculated. The turbulent viscosity is then used to determine turbulent shear stresses which will act to reduce the tumble motion. The model was based on the conservation of angular momentum of the total cylinder contents and equations were formulated to integrate the tumble moment of inertia for the entire disc combustion chamber. The rate of change of angular momentum was expressed as,

$$\frac{d\Omega}{dt} = -T_{sh} \tag{3.1}$$

Where T_{sh} is the torque applied to the vortex due to viscous shear.

The model was further developed by Achuth and Mehta (2001) to include the inlet stroke of a four stroke engine to account for the torque addition to the tumble motion due to the fresh charge entering the cylinder through the inlet port. The model included geometry variables to account for a pent roof combustion chamber when calculating the inlet torque. However the same equations as used in Benjamin's disc combustion chamber model were used to calculate the angular momentum and viscous shear. The change in angular momentum was given as,

$$\frac{d\Omega}{dt} = \dot{m}_{in} U_{in} h - T_{sh} \tag{3.2}$$

Where m_{in} is the mass entering the cylinder, U_{in} is the velocity of the jet entering the cylinder and h is the distance between the jet of fresh charge and the centre of the tumble vortex. Achuth and Mehta included pent roof and valve geometry when calculating h.

A similar approach to Benjamin (1993) and Achuth and Mehta (2001) will be used in the phenomenological model developed in this work but here the momentum is confined to the mass of an ellipsoid vortex rather than the mass of the complete cylinder. The distance, h, between the centre of the tumble vortex and the fresh charge entering the cylinder is simply taken as half the chamber height. An additional term is added to account for the loss of angular moment due to mass exiting the cylinder through the exhaust port and a further term is included to account for a reverse flow of gas through the exhaust port prior to the port closing.

The sum rate of change of the tumble momentum due to the mass entering, viscous shear stresses and the mass exiting the cylinder during the open cycle is given by,

$$\frac{d\Omega}{d\theta} = I\dot{\omega} = T_{in} - T_{sh} - T_{out} \tag{3.3}$$

The torque added to the tumble motion due to the fresh charge entering the cylinder is

$$T_{in} = c_{sp}\dot{m}_{in}U_{in}h \tag{3.4}$$

Where U_{in} is the velocity of the jet and c_{sp} is an adjustable model constant which accounts for the fact that not all the fresh charge entering the cylinder is converted to angular momentum. Further details of how c_{sp} may be calibrated is given is Section 8.1. The fresh charge does not enter directly in the plane of rotation and also the jets collide at the tumble plane, as shown in Figure 3-2. The value of c_{sp} would be expected to be a function of the cylinder and port geometry and would remain constant for a particular engine geometry. A list of all the model constants used in the tumble and turbulence model are given in Table 8-1 for a 50 cc two stroke engine and also Table 8-2 for a 200 cc two stroke engine which was used in the experimental phase of this work.

The change in angular momentum due to mass leaving the cylinder is the product of the mass specific angular momentum and mass leaving the cylinder, given as

$$T_{out} = \frac{\Omega}{m_{tum}} \dot{m}_{out} \tag{3.5}$$

As already mentioned, two stroke engines often use exhaust systems which utilise pressure wave motion to reverse the flow through the exhaust port just prior to the exhaust port closing. In the event of a reverse flow through the exhaust port further momentum will be added to the tumble vortex due to the reverse flow, then,

$$T_{out} = \dot{m}_{out} U_{out} h \tag{3.6}$$

Note that in the case of a reverse flow $\dot{m}_{out}$ and U_{out} are both negative which produces a positive T_{out}.

3.2.2 Solid Body Approximation

The scavenging process was briefly described in Section 3.1, a number of jets of fresh charge enter the bottom of the cylinder and collide before forming the scavenge loop. A complex 3D flow field is formed during the scavenge period which will not be resolved by the quasi-dimensional model, rather an engineering approximation is used. The assumption made is that the bulk flow motion of the cylinder contents rotates as a solid body. If the clearance height in the cylinder was equal to the cylinder bore then the rotating solid body would approximate to a sphere, when the clearance height is less than the bore the rotating body becomes an ellipsoid shape. With the solid body approximation the angular momentum of the tumble vortex is defined as

$$\Omega = I\omega \tag{3.7}$$

Where I is the moment of inertia of the solid body given by,

$$I = m_{tum} G^2 \tag{3.8}$$

The mass of the tumbling vortex is m_{tum} and G is the radius of gyration, which for an ellipsoid is given by Rothbart and Brown (2006).

$$G = \sqrt{\frac{1}{5}(a^2 + b^2)} \tag{3.9}$$

The ellipsoid will have three axis's, *x*, *y* and *z*, as shown below in Figure 3-6. The *x* axis represents the width of the combustion chamber, the *y* axis is the height of the chamber and the *z* axis is the axis of rotation of the tumble vortex. The ellipsoid will have three dimensions, *a* in the *x* direction which will be half the bore dimension near BDC, *b* in the *y* direction which is defined by half the chamber height and *c* in the *z* direction which will be half the bore dimension. Not shown in Figure 3-6 is the c dimension in the z direction which is the axis of rotation for the tumble motion.

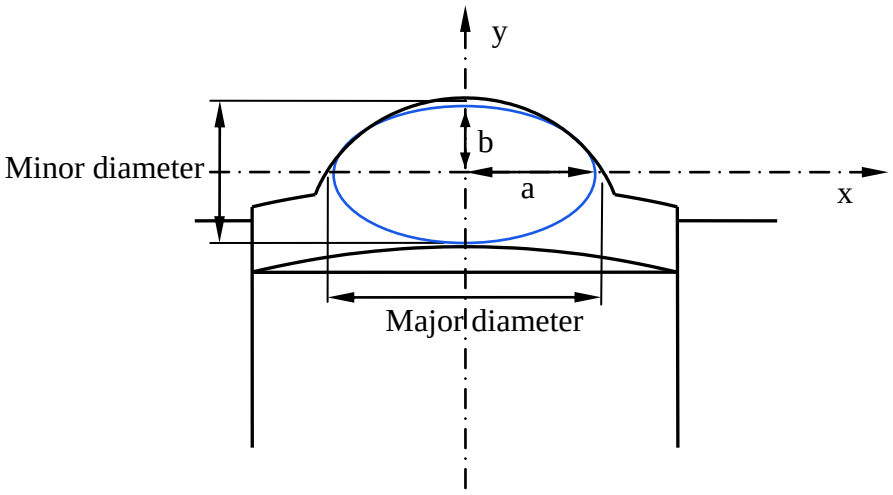

Figure 3-6, Tumble vortex ellipse dimensions and coordinate system

3.2.3 Elliptical Vortex Aspect Ratio

As the piston travels towards TDC the tumbling vortex is compressed and the aspect ratio of the elliptical shape will increase prior to the vortex breaking down into smaller scale turbulence. The aspect ratio of the elliptical profile is defined as the ratio of the major and minor diameters. Initially the major diameter of the elliptical profile is defined by the cylinder bore and the minor diameter as the chamber height. The nomenclature for the ellipse dimensions and coordinate system was shown in Figure 3-6. There will however be a limit to the aspect ratio for a tumbling vortex.

An investigation on the development of a tumble vortex in a square piston compression machine was conducted by Mark et al. (1997), the vortex structure was described as a quasi solid body rotation and there was a "break down" of the tumble motion into turbulence near TDC. The compression machine used a rectangular port which was the width of the cylinder head, rather than poppet valves, in order to generate a near two dimensional flow structure. The compression chamber had large windows for optical access to allow for laser techniques, LDV and PIV, to be used to record the flow structure in the cylinder. Tumble ratios were calculated using velocity measurements taken at different radial distances from the centre of rotation and it was found that the tumble ratio decreased with increasing radius, this indicates that the assumption of solid body rotation is not wholly correct. As the piston approached the cylinder head and the aspect ratio of combustion chamber becomes flatter and an elliptical tumble motion was observed. Flow separation occurs on the piston face, a similar separation might be expected on the cylinder head, although this was not in the field of the PIV measurements. As the height of the combustion chamber further reduces the extent of the rigid body tumble motion reduces to just the centre of the chamber. The results display how the major diameter of the elliptical vortex is limited by the chamber height. This separation and loss of tumble structure as the piston approaches the top of the chamber characterises the breakdown of tumble.

The square piston compression machine used by Marc et al. (1997) was analysed by Roy and Penven (1998) using CFD with both a k-ε model and Reynolds Stress Model (RSM) for turbulence. There were significant differences between the results of the two turbulence models with the RSM model better replicating test data. The RSM results clearly show an

elliptical vortex with an aspect ratio of approximately 2.1 when chamber width/height ratio is four, Figure 3-7 below shows velocity vector plots from the RSM results at two different piston positions. Boree et al. (1999) published results from LDV measurements taken from the same square piston compression machine which show that the tumble velocity reduces quickly at around 65° BTDC, indicating the breakdown of the tumble vortex. At 65° BTDC the chamber aspect ratio is ~2.5. Results from PIV experiments used in the work of Boree et al. (1999) also show that early in the compression cycle the major diameter of the vortex is close to the bore dimension. Tumbling vortex is compressed into an elliptical shape in which the minor diameter is close to the chamber height and the ellipse aspect ratio is approximately two.

CFD results images, Fig 5 from Roy and Penven (1998), removed for copyright reasons

Figure 3-7, CFD results using RSM for a square piston compression machine showing the elliptical vortex, Roy and Penven (1998)

Compression of the tumbling vortex has also been observed in optical engines using laser techniques by different researchers. Fansler and French (1992) used LDV techniques to measure the flow in a two stroke loop scavenged engine with a plane disc type cylinder head. The results show the spin up of the tumbling vortex up to around 65° BTDC but by about 30° BTDC most of the tumble vortex had broken down. 3D CFD analysis, with a k-ε model for turbulence, was used by Khalighi et al. (1995) and predicted that a tumbling elliptical vortex will remain present in a four stroke pent roof combustion chamber up to 30° BTDC. The piston of the engine had a slight concave crown and the combustion chamber also has a squish band. Velocity vector plots in the work of Khalighi et al. (1995) show an elliptical

vortex aspect ratio of approximately 2.4. In-cylinder flow motion of four valve four stroke engine was measured using PIV techniques by Li et al. (2002) who noted that the tumbling vortex has broken down by 50° BTDC. The height of the pent roof combustion chamber appears smaller than the engine analysed by Khalighi et al. (1995), also the piston appears flat and there is a smaller squish area, which result in a larger chamber aspect ratio towards TDC. The smaller chamber height will produce a larger vortex aspect ratio earlier in the compression stroke and this may be why the tumble vortex breaks down earlier. It was also noted that the tumble vortex centre moved away from the cylinder axis and towards the exhaust valves.

The tumble model in the present work will have an ellipsoid vortex which is centred on the cylinder axis and at the middle of the chamber height with its minor diameter defined by the chamber height. Initially the major diameter of the vortex will be defined as the cylinder bore, however as the vortex is compressed the aspect ratio will increase but will be limited to a value defined in the present work as 2.5. Hence at a certain piston position both the major and minor diameters of the vortex will be defined as a function of the chamber height. The diameter of the ellipsoid across the axis of rotation is not controlled by an aspect ratio and so may be as large as the bore diameter. Two combustion chamber profiles are considered in this work, a squish and a plane disc type combustion chamber. The majority of homogeneous charge spark ignition two stroke engines use squish combustion chambers. Plane disc type combustion chambers are often used in research engines and will be used in this work for comparison. Both the disc and squish combustion chambers are shown below in Figure 3-8, note that the plane disc type combustion chamber has a slight curvature on the cylinder head, this is to match the curvature on the production standard piston.

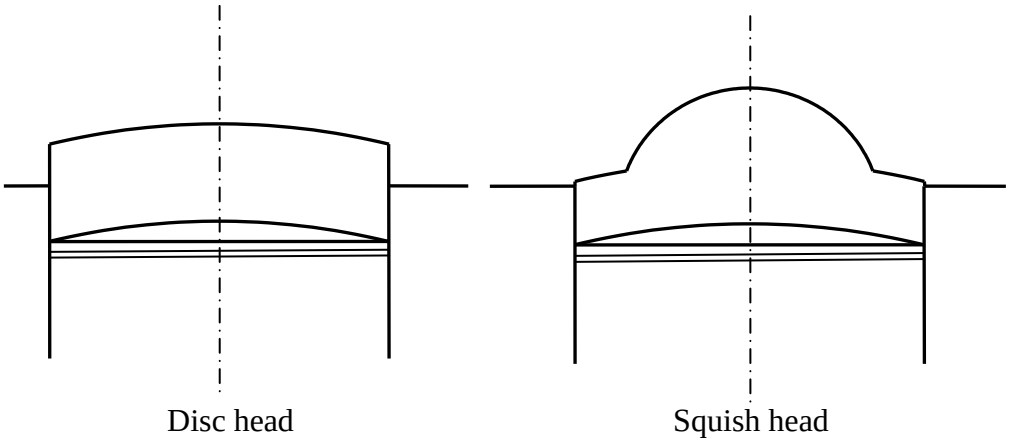

Figure 3-8 , Disc and squish combustion chamber geometries

An ellipsoid vortex is shown schematically in the simple disc type combustion chamber in Figure 3-9, the aspect ratio of the vortex is restricted to 2.5 and the major diameter of the vortex is smaller than the cylinder bore diameter. For the plane disc head the tumbling vortex will be confined by the dimensions of the cylinder bore and chamber height, with the added restriction of the limiting aspect ratio of the ellipse. The ellipsoid diameter in the direction of the axis of rotation will be set by the bore diameter.

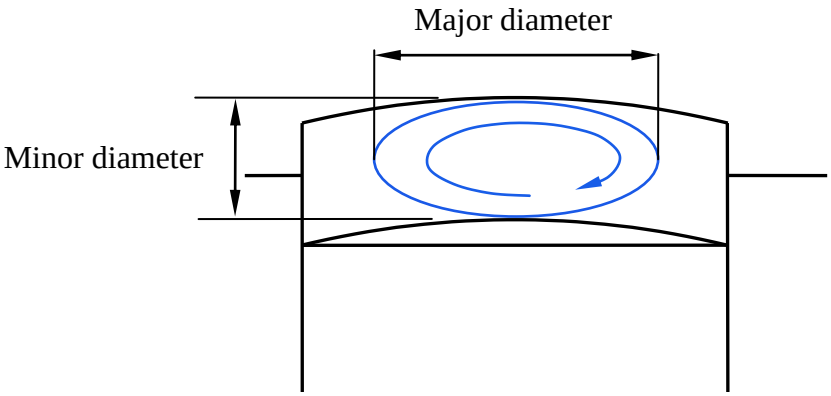

Figure 3-9, Tumble vortex ellipse dimensions

In the case of a squish combustion chamber the tumbling vortex will be compressed into the combustion bowl and hence the major diameter of the ellipse becomes controlled by the squish combustion chamber. At BDC the major diameter of the vortex will be defined by the cylinder bore dimension, then as the piston approaches TDC the tumbling vortex will be compressed into the combustion bowl. The concept of the tumbling vortex being compressed into the combustion bowl is shown below in Figure 3-10. The assumption is made that when the height below the squish area is less than twice the bowl height then the major diameter of the vortex reduces linearly from the bore diameter to the squish diameter. As the vortex is compressed into the squish combustion chamber the major diameter and the diameter in the direction of the axis of rotation will be equal and the vortex becomes a spheroid shape which is an ellipsoid with two of its dimensions equal.

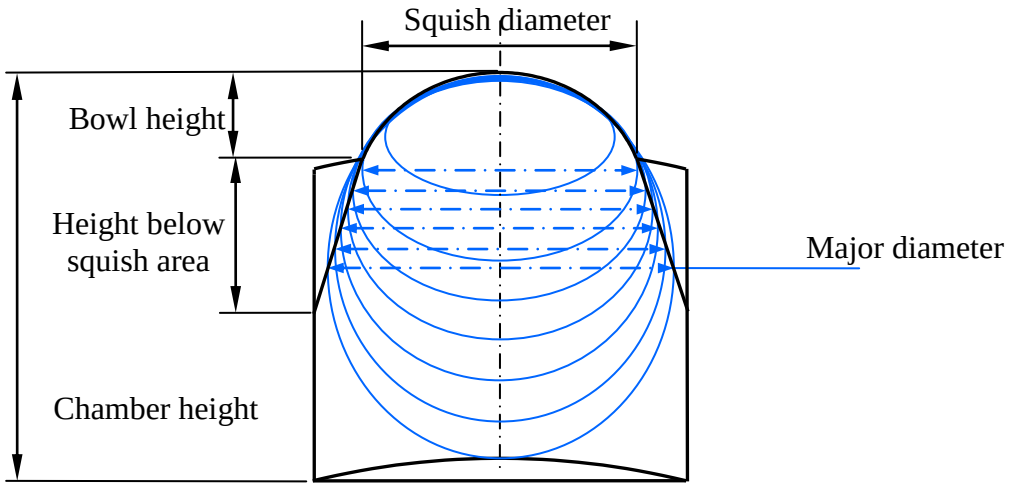

Figure 3-10, Major diameter of vortex reduces linearly from bore to squish diameter during compression

When the minor diameter is less than twice the height of combustion bowl, then the major diameter of the spheroid is controlled by the combustion bowl profile radius, Figure 3-11 below shows the major diameter controlled by the bowl profile radius. The aspect ratio limit is still imposed on the vortex and if the limit is reached the vortex becomes an ellipsoid with

its minor diameter controlled by the chamber height and the major diameter controlled by an aspect ratio of 2.5 and the chamber height. The diameter in the direction of the axis of rotation is controlled by the combustion bowl profile.

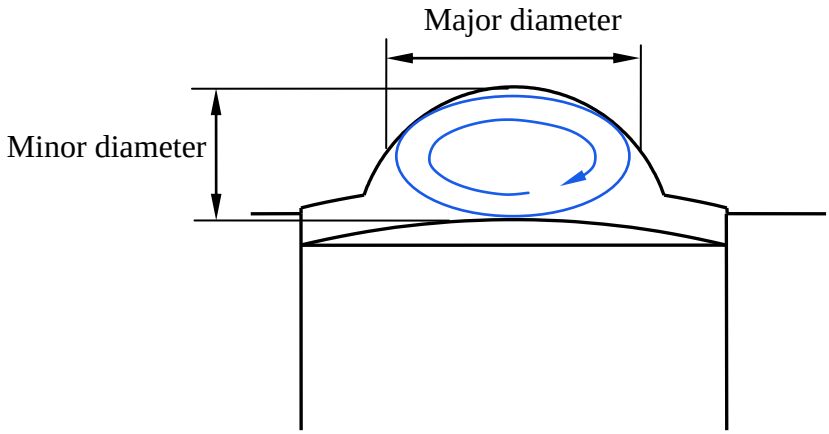

Figure 3-11, Major diameter of vortex controlled by combustion bowl profile radius

3.2.4 Tumble Energy Loss Due to Mass Transfer

The volume of the ellipsoid is calculated from the equation,

$$V_{tum} = \frac{4}{3}\pi abc \tag{3.10}$$

The mass of the ellipsoid is calculated from its volume and the in-cylinder gas density. The mass of the tumbling vortex will always be less than the total mass of the cylinder. As the piston approaches TDC the dimension b of the tumble vortex becomes controlled by the limiting aspect ratio of the ellipsoid. When the ellipsoid dimensions become controlled by its aspect ratio, during compression, the mass of the tumble vortex will reduce. As the mass of the vortex reduces the mass that leaves the tumble vortex joins the cylinder mass outside the of the tumble vortex, which is assumed to have no bulk flow motion. As the mass of the tumble vortex reduces the kinetic energy of the tumble vortex due to its angular momentum will also reduce, at the same rate.

The kinetic energy KE of the tumble vortex is given by,

$$KE = I\frac{\omega^2}{2} \tag{3.11}$$

Where I is given by Equation (3.8)

It is assumed that the kinetic energy of the mass leaving the tumble vortex joins the rest of the cylinder as turbulent kinetic energy, k, hence the change in tumble vortex kinetic energy ΔKE is equal to the change in turbulent energy Δk of the cylinder contents.

$$\Delta KE = KE.\frac{\Delta m_{tum}}{m_{tum}} = \Delta k \tag{3.12}$$

3.2.5 Tumble Momentum Loss Due to Viscous Shear

The tumble vortex rotates with an angular velocity ω. At the surface of the combustion chamber the fluid velocity will be zero, a no slip condition. At some distance away from the chamber wall surface the fluid velocity will be unaffected by the surface, free stream velocity. Between the chamber surface and the free stream velocity there will be a shear layer with a velocity gradient. The shear stress is proportional to the velocity gradient and acts against the fluid motion. The tumble vortex may not contain the complete mass of the cylinder contents, when the tumble mass is less than the cylinder mass the mass outside of the tumble vortex is assumed to have no large scale flow motion, zero velocity. At the surface of the vortex there will be a velocity gradient which produces a viscous shear stress. For a laminar flow Newton's law of viscosity is given by Equation (3.13), taken from Davidson (2007).

$$\tau_{ij} = \rho\nu\left[\frac{\partial u_i}{\partial x_j} + \frac{\partial u_j}{\partial x_i}\right] \tag{3.13}$$

For a simple one dimension shear flow Equation (3.13) becomes

$$\tau_{ij} = \rho\nu\frac{\partial u_x}{\partial y} \tag{3.14}$$

In turbulent flows further stresses are generated due to the fluctuating velocities in the flow, the stresses due to the fluctuating velocities are known as turbulent Reynolds stress, τ_{ij}^R. Turbulence increases the transport of momentum through the thickness of the shear layer. Analogous to Newton's law of viscosity the turbulent shear stress can be defined by replacing the kinematic viscosity with a turbulent viscosity. The turbulent viscosity will be greater and independent of the kinematic viscosity.

Energy is transported from the tumble vortex to turbulent kinetic energy via the shear stresses at the surface of the vortex. To account for the effects of turbulence a simple engineering model based on an eddy viscosity, or Boussinesq approximation, is used where the molecular viscosity in Equation (3.14) is replaced with and eddy viscosity, ν_t

$$\tau_{xy}^R = \rho\nu_t\frac{\partial \bar{u}_x}{\partial y} \tag{3.15}$$

Where $\bar{u}_x$ is the time averaged velocity. It is the turbulent Reynolds stress that is responsible for transferring energy from the mean flow to the turbulence. The eddy viscosity is based on the turbulent kinetic energy and a length scale, from Wilcox (2006),

$$\nu_t = c_d\sqrt{k}.l \tag{3.16}$$

Where c_d is a closure coefficient typically with a value of 0.09, as used by both Borgnakke et al. (1981) and Poulos and Heywood (1983).

The product of the turbulent shear stress and the ellipsoid surface area generates a force on the surface of the vortex which acts to reduce the momentum of the vortex. A torque which

reduces the tumble momentum is given by the force on the surface of the vortex multiplied by the radius at which the force acts, this is modelled approximately as,

$$T_{sh} = \int c_{sh} r_{elp} \rho \nu_t \frac{u_t}{l} A_v \tag{3.17}$$

Where u_t is the tangential velocity, it is assumed that the velocity gradient at the surface of the vortex occurs across a thickness dimension equivalent to the integral scale of turbulence, l, c_{sh} is a calibration constant and r_{elp} is the distance between the vortex surface and the axis of rotation, A_v represents the vortex surface area.

To determine the total torque due to the viscous shear over the surface of the vortex, the vortex surface is divided in a number of smaller discrete surfaces. The ellipsoid surface has three planes of symmetry and only a 1/8 segment may be considered when summing the shear at the surface. The $1/8^{th}$ segment is sub-divided into 19^2 quadrilateral surface elements, Figure 3-12 shows a single surface element on the ellipsoid.

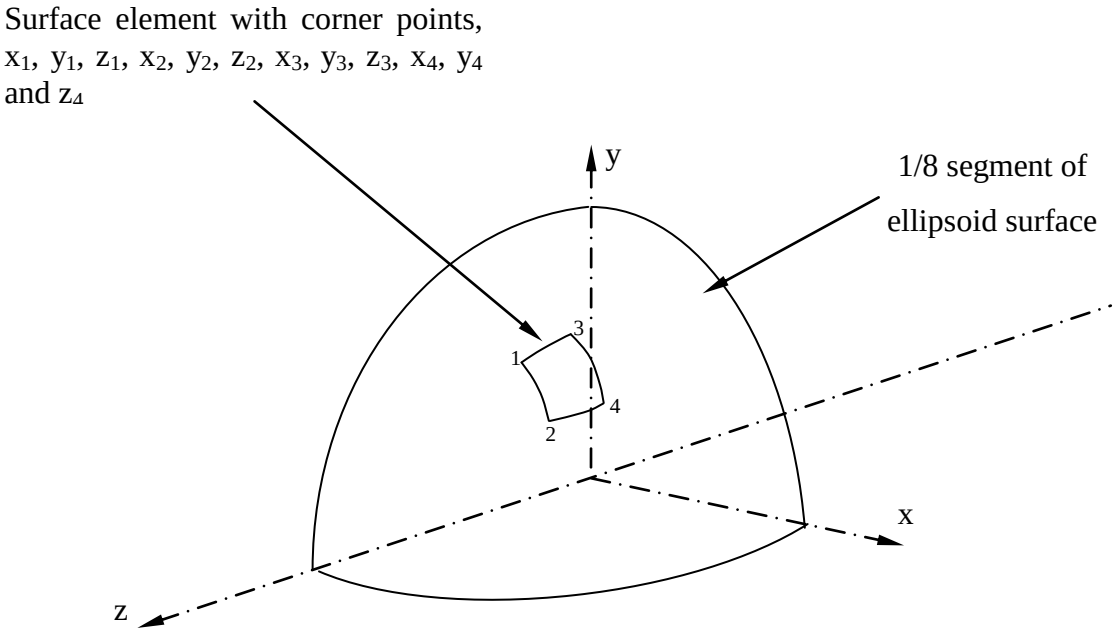

Figure 3-12, Surface element on ellipsoid

The surface element corner points are defined in the Cartesian coordinate system by the equation for an ellipsoid,

$$\frac{x^2}{a^2}+\frac{y^2}{b^2}+\frac{z^2}{c^2}=1 \tag{3.18}$$

The area of a quadrilateral element may be found by dividing the surface element into two triangles where the area of a triangle is given by,

$$A=\sqrt{s(s-i)(s-j)(s-k)} \tag{3.19}$$

$$\text{Where } s=\frac{i+j+k}{2} \tag{3.20}$$

Where i, j and k are the lengths of the sides of a triangle, the length of the sides can be found from the corner points,

$$i=\sqrt{(x_1-x_2)^2+(y_1-y_2)^2+(z_1-z_2)^2} \tag{3.21}$$

The total ellipsoid surface area is found from the sum of surface element areas and checked against an area calculated from a Knud Thomsen formula taken from Ersoy (2010),

$$A_{tum}=4\pi\left[\frac{a^p b^p+a^p c^p+b^p c^p}{3}\right]^{1/p} \tag{3.22}$$

Where a, b and c are the ellipsoid dimensions and p is an approximation constant taken as 1.6075.

The averaged radius from the surface element to the axis of rotation, r_{elp}, is given by,

$$r_{elp} = \frac{\sqrt{x_1^2 + y_1^2} + \sqrt{x_2^2 + y_2^2} + \sqrt{x_3^2 + y_3^2} + \sqrt{x_4^2 + y_4^2}}{4} \quad (3.23)$$

A schematic of the tumble vortex with the tumble velocity and length scale used in Equation (3.17) is shown in Figure 3-13. The velocity gradient across the height of the tumble vortex is due to the local velocity being a product of the angular velocity and radius. If the vortex rotates as a solid body shear stresses are not generated in the vortex, it is only at the surface of the vortex that the turbulent shear stress is generated. It is assumed that there is a shear layer at the surface of the vortex which has a thickness equal to the integral scale.

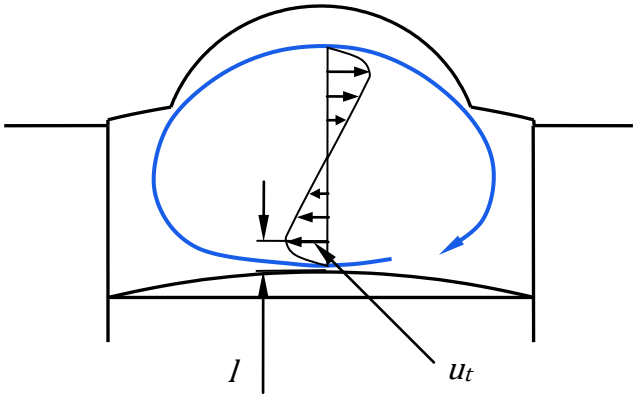

Figure 3-13, Tumble velocity gradient

3.2.6 Calculation Method for Angular Velocity

During an engine simulation the conditions in the cylinder are calculated on a step by step basis, each step being approximately 0.5° crank angle. All the conditions are known at the beginning of a new step, θ, conditions at the end of the step, θ+1, must be calculated. For the angular velocity of the tumble vortex the following procedure is used.

- At the start of the calculation the angular velocity ω_θ is known, calculated from the previous step. The chamber height changes and the new ellipsoid dimensions, radius of gyration and moment of inertia are calculated based on a constant tumble

mass. Then a new angular velocity is calculated based on the conservation of angular momentum but with a new radius of gyration, using Equations (3.7) to (3.9).

$$\omega_{\theta+1} = \omega_{\theta}\left(\frac{G_{\theta}}{G_{\theta+1}}\right)^{2} \tag{3.24}$$

- As discussed in Section 3.2.4 mass may be lost from the tumble vortex during compression due to the limiting aspect ratio of the ellipsoid vortex. In this situation the calculation for the new angular velocity is carried out in two steps. In the first step it is assumed that mass is lost from the tumble vortex, but that density and angular velocity remain constant, Figure 3-14 below shows the concept of the first step in the calculation.

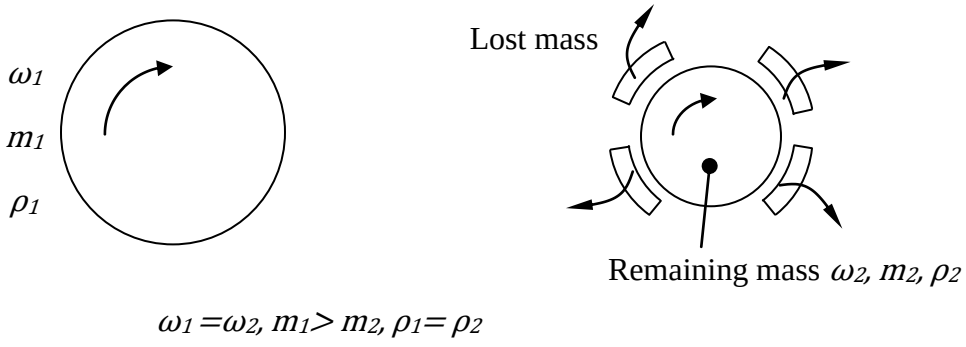

Figure 3-14, Tumble mass lost at constant density

- As the mass of the ellipsoid vortex reduces so too will the tumble kinetic energy. If the tumble vortex loses mass at constant density then the volume of the vortex reduces proportional to the mass loss and the dimensions of the vortex will reduce by the cube root of the mass also the radius of gyration,

$$G_2 = \left(\frac{m_2}{m_1}\right)^{1/3} G_1 \tag{3.25}$$

Then the new moment of inertia is

$$\Omega_2 = \omega_2 m_2 \left[\left(\frac{m_2}{m_1}\right)^{1/3} G_1\right] \tag{3.26}$$

- In the second step of the calculation the vortex is compressed to a smaller size but with constant mass and inertia.

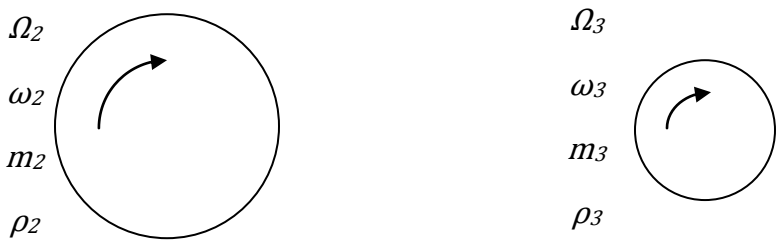

$\Omega_2 = \Omega_3,\ \omega_2 < \omega_3,\ m_2 = m_3,\ \rho_2 < \rho_3$

Figure 3-15, Tumble vortex compressed at constant inertia

The new radius of gyration is based on combustion chamber geometry then,

$$\omega_3 = \omega_2 \left(\frac{G_2}{G_3}\right)^2 \tag{3.27}$$

Incorporating Equation (3.25) into (3.27)

$$\omega_3 = \omega_1 \left\{ \left[\left(\frac{m_3}{m_1}\right)^{1/3} G_1\right]^2 \Big/ G_3^2 \right\} \tag{3.28}$$

Rewriting Equation (3.28) in terms of crank angle

$$\omega_{\theta+1} = \omega_{\theta} \left\{ \left[\left(\frac{m_{\theta+1}}{m_{\theta}} \right)^{1/3} G_{\theta} \right]^2 \Big/ G_{\theta+1}^2 \right\} \tag{3.29}$$

- The new angular velocity is modified to account for the fresh charge entering the cylinder and viscous shear,

$$\omega_{\theta+1} = \omega_{\theta+1} + \left(\frac{T_{in} - T_{sh} - T_{out}}{I_{\theta+1}} \right) dt \tag{3.30}$$

And then a new kinetic energy for the tumble vortex is calculated,

$$KE_{\theta+1} = \frac{1}{2} I_{\theta+1} \omega_{\theta+1}^2 \tag{3.31}$$

3.2.7 Burned Zone Offset

During the early stage of the combustion process the tumble vortex will advect the burned zone away from the spark plug, how far will depend upon the tumble velocity and the size of the tumble vortex. Figure 3-16 below shows the semi-spherical burned zone advected from the spark plug by the tumble vortex, the flame offset, x_f, is the distance measured in the x direction between the cylinder axis and the centre of the semi-spherical burned zone.

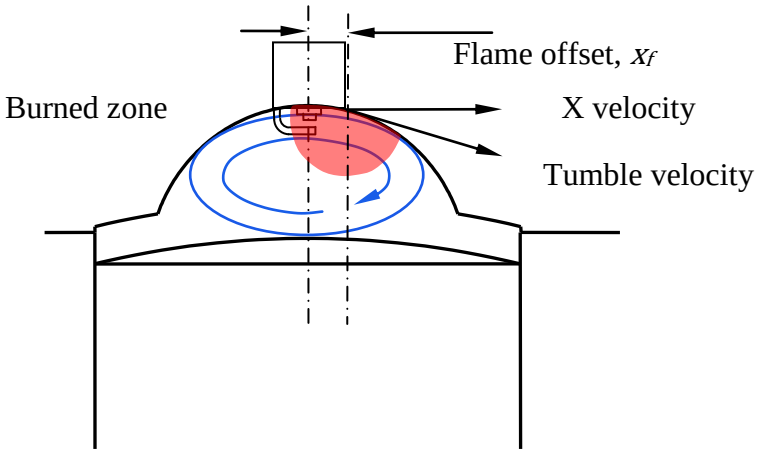

Figure 3-16, Flame front movement due to tumble motion

An incremental offset of the burned zone in the x direction is determined from the velocity in the x direction at the centre of the burned zone and the length of the time step. Figure 3-17 below shows two sections in the elliptical vortex, if the mass flow rate through section x-x is equal to the mass flow through section y-y and if density is uniform then for continuity the flow velocity through section y-y must be greater than the velocity through x-x.

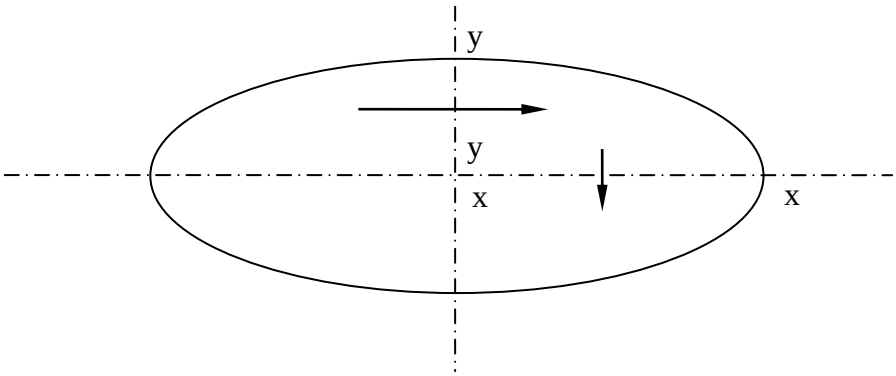

Figure 3-17, Variation in vortex velocity

In order to calculate the velocity in the x direction at a position offset from the cylinder axis, first the tangential velocity at the offset location must be determined. The tangential velocity is calculated from a reference velocity. The reference velocity is based on a tangential velocity of a circle with an area equivalent to an ellipse area with the vortex major and minor diameters, the radius of an equivalent circle is then,

$$r_{eq} = \sqrt{ab} \tag{3.32}$$

Then the reference velocity is calculated from the vortex angular velocity,

$$u_{ref} = \omega r_{eq} \tag{3.33}$$

Once a reference velocity has been determined and with known vortex dimensions and initial flame offset the tumble velocity at any point on the surface of the vortex may be calculated, Figure 3-18 below shows the tangential and x direction velocity components at a point x, y on the ellipse

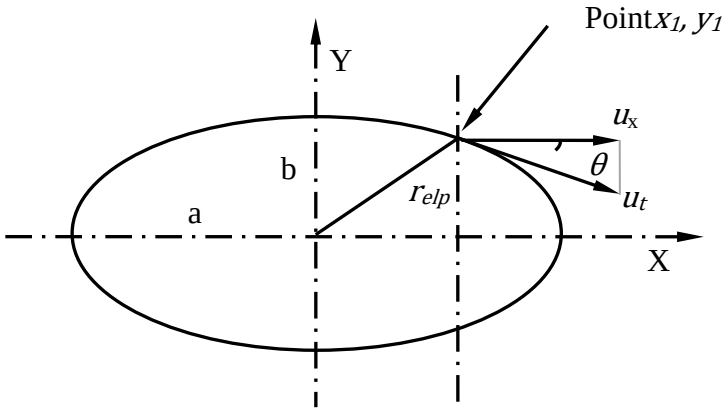

Figure 3-18, Tangential velocity at vortex surface

The equation for the geometry of an ellipse is given by,

$$\frac{x^2}{a^2}+\frac{y^2}{b^2}=1 \tag{3.34}$$

Taking $x_1$as the flame offset Equation (3.34) can then be rearranged for y_1

$$y_1=\sqrt{1-\frac{x_1^2}{a^2}}.b \tag{3.35}$$

The effective radius to point x_1, y_1 is then

$$r_{elp}=\sqrt{x_1^2+y_1^2} \tag{3.36}$$

The tangential velocity at the point x_1,y_1 is calculated taking into account mass continuity and the reference velocity,

$$u_t=\sqrt{\frac{r_{eq}}{r_{elp}}}u_{ref} \tag{3.37}$$

The differential of Equation (3.35) is

$$\frac{dy}{dx}=-b\frac{x}{a^2}\frac{1}{\sqrt{1-{x^2}/{a^2}}} \tag{3.38}$$

The angle θ in Figure 3-18 can be found from

$$\tan\theta=\frac{dy}{dx}=-b\frac{x}{a^2}\frac{1}{\sqrt{1-{x^2}/{a^2}}} \tag{3.39}$$

Then the velocity in the x direction at point x_1,y_1 can be calculated as

$$u_x = \cos\theta\, u_t \tag{3.40}$$

The new flame offset is then calculated

$$x_{f\theta+1} = x_{f\theta} + u_x dt \tag{3.41}$$

3.3 Turbulence Model

The normal operating speed of the engine considered in this study is 7000 – 10,000 rpm. At such speeds for complete combustion to occur the burning velocity in the cylinder would have to be many times greater than the laminar burning velocity. It is well known that it is the turbulent motion in the engine cylinder that is responsible for increasing the rate at which the fuel and air mixture burns. As mentioned at the beginning of this chapter the fluid velocity measured at a point in the cylinder will have a mean and fluctuating component. The fluctuating velocity is a characteristic of the turbulent flow motion and is due to flow structures on a smaller scale than the tumble vortex. The differences between the instantaneous, fluctuating and mean velocities were shown schematically in Figure 3-1. The instantaneous velocity is denoted as u, the mean velocity as U and the fluctuating velocity u'. In order to quantify turbulence statistical methods are usually used. As the fluctuating velocity alternates about zero the mean of the alternating velocity becomes zero, in order to give the fluctuating velocity a statistical magnitude the Root Mean Square (RMS) of the fluctuating velocity is used as a measure of turbulence. The RMS of the fluctuating velocity is used here to define the turbulence intensity.

$$u'_{rms} = \sqrt{\overline{u'^2}} \tag{3.42}$$

The turbulence intensity represents a characteristic turnover velocity of the integral scale eddy. For homogeneous isotropic turbulence the turbulent kinetic energy is related to the intensity (Wilcox 2006).

$$u'_{rms} = \sqrt{\frac{2k}{3}} \tag{3.43}$$

Both the scales and magnitude of turbulence will influence the turbulent burning velocity.

Different models have been developed to determine turbulent kinetic energy, k, and the rate of turbulence dissipation, ε, inside an engine cylinder. Borgnakki (1981), Reid (1993) and Benjamin (1993) have used a two equation k-ε turbulence model whilst Polous and Heywood (1983) have used a one equation model. Two equations models may be described as complete (Wilcox) as they produce a solution for the turbulent energy and length scale, however one equation models are incomplete and the length scale must be defined. In this work a simpler one equation model will be used.

3.3.1 Energy Cascade

The turbulence in the cylinder may be thought of as a large number of rotating eddies of varying sizes and angular velocities. The size of the largest of these eddies, for internal flows, will be of the order of the scale of the geometry containing the turbulent flow. For the in-cylinder flow the largest scale will be the tumble motion which is discussed in Section 3.2. Smaller scale turbulence in engines is generated by a number of different mechanisms, which include turbulent jets entering the cylinder during the scavenge period and shear stresses at the surface of the tumble vortex. Figure 3-19 below shows a turbulent jet of fresh charge entering the cylinder with integral scale eddies the size of the transfer port height. Turbulent eddies are being continually generated by the shear stress in the tumble vortex and turbulent kinetic energy is produced at the expense of the tumble vortex kinetic energy. Squish combustion chambers produce turbulence near TDC due to the movement of gas

from a squish area around the circumference of the combustion chamber into the main combustion chamber.

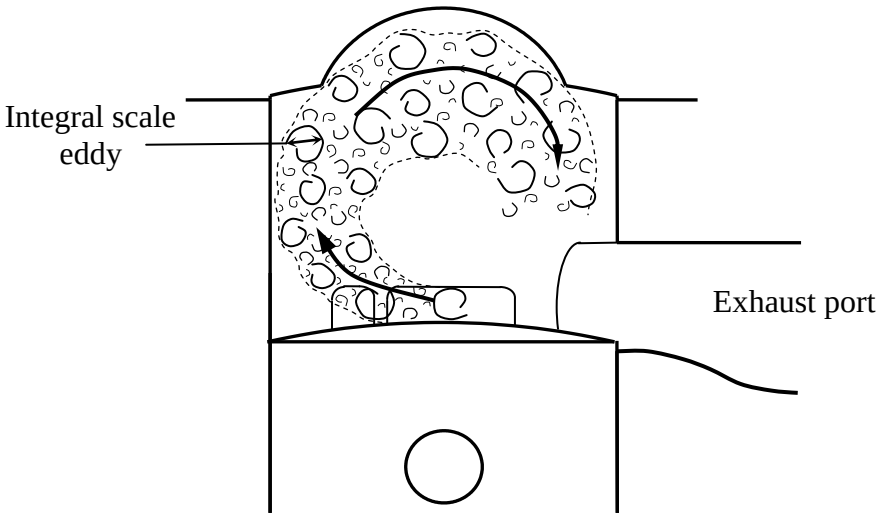

Figure 3-19, Turbulent jet entering the cylinder

Instabilities in the turbulent eddies cause them to breakdown into smaller eddies which in turn breakdown into still smaller eddies. Infinitely small scales are prevented by viscosity effects which dissipate small scale energy into heat, the smallest scale of eddy is known as the Kolmogorov scale. As the turbulence breaks down into smaller and smaller eddies it can be said that the kinetic energy of the tumble vortex cascades down through the smaller and smaller turbulent eddies to be dissipated at the Kolmogorov scale.

3.3.2 Integral Scale Eddies

An important scale in the turbulent flow field is known as the integral scale, which defines a scale of eddies that contain much of the turbulent kinetic energy. It is the integral scale eddies that are most effective in the transport of heat and momentum. In order to define or measure the integral scale a two point correlation can be used in which a velocity component is measured at two points separated by a distance r, at a coincident time. If the location of the second point is moved relative to the first then a correlation between the two velocities

can be plotted against distance, Figure 3-20 shows such a graph. The integral scale is defined as (Peters 2006),

$$l(t) = \int_0^\infty f(r,t)dr \tag{3.44}$$

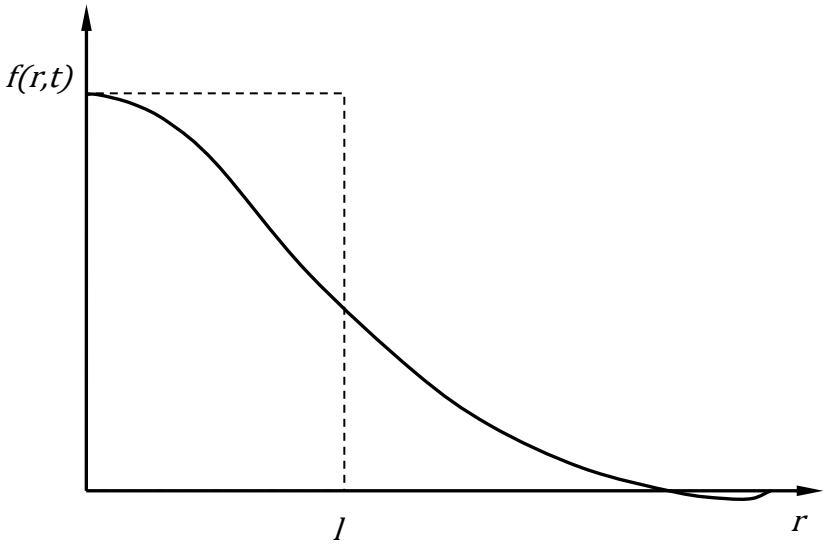

Figure 3-20, Two point auto correlation

Integral length scales have been measured based on single point velocity measurements where the autocorrelation is based on time, the length scale being equal to the product of the mean fluid velocity and the autocorrelation time scale. The single point measurement technique was referred to as an indirect measurement by Fraser et al. (1986) and in engines where the turbulence is non-stationary and where turbulence intensity levels may be as large as or larger than the mean velocity then single point measurements may not be valid.

If values for the turbulence intensity and integral length scale can be defined then a turbulent Reynolds number may be defined as,

$$Re_T = \frac{u'_{rms} l}{\nu} \tag{3.45}$$

3.3.3 Turbulent Spectrum

For a turbulent flow which has a defined integral scale if the turbulent Reynolds number increases then the smallest scale at which the turbulent energy dissipates reduces. Hence as the turbulent Reynolds number increases so too will the spectrum of turbulent eddies increase. The energy cascade was introduced in Section 3.3.1 which described how energy is transferred down from the integral scale through a spectrum of turbulent eddy scales. It is common in turbulence literature to represent the spectrum of energy in the cascade in terms of wave numbers, κ, which may be thought of as the inverse of the eddy length scale. The range of turbulent eddies produces a distributed spectrum of kinetic energy $E(\kappa)$. Following Komogorov's universal equilibrium theory (Wilcox 2006) there is a range of eddies where the energy depends only upon the wave number and dissipation. An expression is given for the energy density per unit wave number,

$$E(\kappa) = c_\kappa \varepsilon^{2/3} \kappa^{-5/3} \tag{3.46}$$

Where c_κ is the Kolmogorov constant. This is often referred to as the $\kappa^{-5/3}$ law for kinetic energy and the range of eddies in which this applies is known as the inertia sub range. Figure 3-21 below shows a schematic of the -5/3 law with the inertia sub range, also shown is the viscous sub range which represents the scale at which turbulence energy is dissipated due to viscous effects. The greatest levels of energy are at and around the integral scale, as shown.

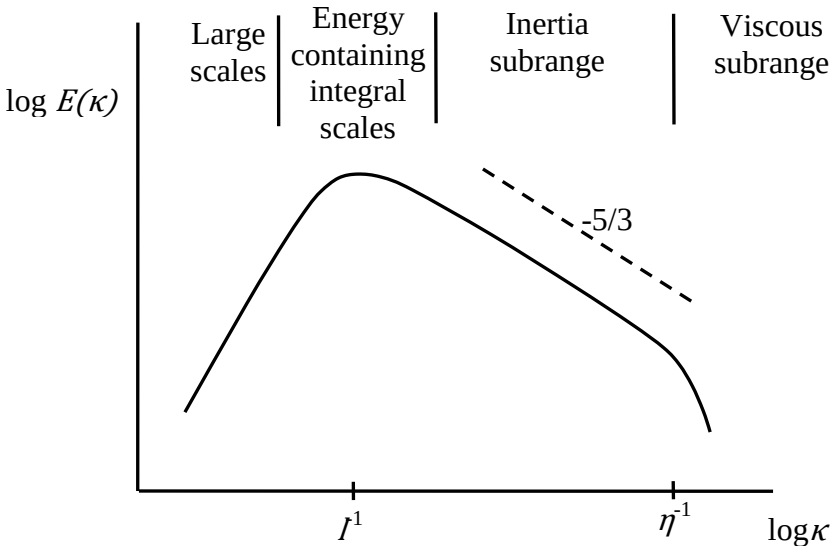

Figure 3-21, Turbulent energy spectrum adapted from Wilcox (2006)

The $\kappa^{-5/3}$ law has been observed in engine flows, Peterson and Ghandi (2010) used planar laser induced fluorescence to observe the turbulent flow in a four valve four stroke motored engine. The engine was motored at 600 and 1200 rpm. From their measurements in a view field 15.2 mm by 19.5 mm they were able to determine the energy spectrum and a scalar dissipation spectrum at scales as small as the viscous sub range.

3.3.4 Turbulent Energy Production

Turbulent Scavenge Jets

During the scavenge period high velocity jets enter the cylinder. The large velocity gradient between the jet and port opening creates a turbulent shear stress which in turn leads to the production of turbulent kinetic energy. The exact details of the 3D interaction between the scavenge jets and the port opening are unknown, however the jet velocity and mass flow are calculated. The approach used by Borgnakke et al. (1981) to account for the turbulence

entering the cylinder will be used here to calculate for the turbulent production due to the scavenge jets,

$$k_j = \frac{\dot{m}_{in}}{m}(k_{in} - k) \tag{3.47}$$

Where k_j is the mass specific turbulent kinetic energy entering the cylinder, $k_{in} = (c_{kin}u_{in})^2$ and c_{kin} is a calibration constant, Bornakke set the calibration constant at 0.4 and the same will be done here.

Tumble Vortex Shear

Between the tumble vortex and the combustion chamber walls there will be a shear layer. For a laminar flow applying Newton's law of viscosity the shear stress in the flow is defined as, taken from Davidson (2007),

$$\tau_{ij} = \rho\nu\left[\frac{\partial u_i}{\partial x_j} + \frac{\partial u_j}{\partial x_i}\right] \tag{3.48}$$

The strain rate tensor for the fluid is defined as

$$S_{ij} = \frac{1}{2}\left[\frac{\partial u_i}{\partial x_j} + \frac{\partial u_j}{\partial x_i}\right] \tag{3.49}$$

Then Equations (3.48) and (3.49) can be combined to give,

$$\tau_{ij} = 2\rho\nu S_{ij} \tag{3.50}$$

The rate of work done due to the shear stress per unit volume is

$$\frac{\partial}{\partial x_j}\left[u_i \tau_{ij}\right] = \frac{\partial \tau_{ij}}{\partial x_j} u_i + \tau_{ij} \frac{\partial u_i}{\partial x_j} \tag{3.51}$$

The second term on the right hand side of the equation represents the change of internal energy due to viscous shear, which may be written as

$$\tau_{ij} \frac{\partial u_i}{\partial x_j} = \frac{1}{2}\left[\tau_{ij} + \tau_{ji}\right] \frac{\partial u_i}{\partial x_j} = \frac{1}{2}\left[\frac{\partial u_i}{\partial x_j} + \frac{\partial u_j}{\partial x_i}\right] = \tau_{ij} S_{ij} \tag{3.52}$$

The gain in internal energy may be determined from the above equations except that the shear stress is replaced with the turbulent shear stress and the molecular viscosity with the eddy viscosity, then

$$\tau_{ij}^R \bar{S}_{ij} = \tau_{ij}^R . \frac{\tau_{ij}^R}{2\rho \nu_t} \tag{3.53}$$

For a simple shear flow

$$\tau_{ij}^R = \rho \nu_t \frac{\partial \bar{u}_x}{\partial y} \tag{3.54}$$

Combining equations (3.53) and (3.54)

$$\tau_{ij}^R \bar{S}_{ij} = \frac{\rho \nu_t}{2}\left[\frac{\partial \bar{u}_x}{\partial y}\right]^2 \tag{3.55}$$

Equation (3.55) represents the turbulent kinetic energy produced per unit volume. The exact velocity gradient in the shear flow is not known and is simply taken as the ellipsoid surface velocity divided by the integral scale. The absolute production of turbulent kinetic energy due to the shear stress at the surface of the vortex is then modelled as,

$$k_{sh} = c_\beta \rho \nu_t \left[\frac{u_t}{l}\right]^2 Al \tag{3.56}$$

In Equation (3.56) the tangential velocity u_t and the area A are taken from the surface element calculations defined in Section 3.2.5. The turbulent kinetic energy generated by shear is calculated for each surface element and then summed for the total ellipsoid vortex.

Squish Combustion Chamber

Squish combustion chambers are often used in gasoline two stroke engines to generate further turbulent kinetic energy near TDC. Figure 3-22 below shows a squish combustion chamber divided into two volumes, the squish volume and the main volume. As the piston approaches TDC fresh charge in the squish volume is pushed into the main combustion chamber with a velocity and mass. It is assumed that the kinetic energy due to the mass and velocity of the charge moving from the squish volume to main volume is all converted to turbulent kinetic energy, the absolute turbulent kinetic energy generated by squish is then,

$$k_{sq} = \frac{1}{2}\dot{m}_{sq} u_{sq}^2 \tag{3.57}$$

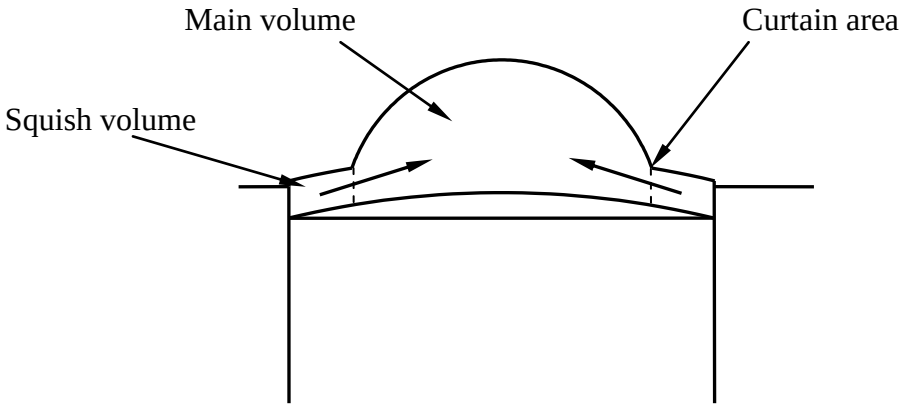

Figure 3-22, Squish velocity

The method for calculating the squish velocity is taken from Blair (1996). The calculation is conducted over a time step, at the start of the time step the pressure, temperature and hence density in the two volumes are equal, therefore the ratio of mass to volume for the squish volume, main volume or total cylinder volume are all equal.

If $V_{t,\theta}$, m_t, $V_{sq,\theta}$ and $m_{sq,\theta}$ are the total cylinder volume, total cylinder mass, squish volume and squish mass at crank angle θ then the squish mass can be found from

$$m_{sq,\theta} = m_t \frac{V_{sq,\theta}}{V_{t,\theta}} \tag{3.58}$$

During the time step the piston moves an incremental distance which will change both the squish and main volumes. At the end of the time step the density is again assumed to be common for both the squish and main volumes, the mass in the squish volume must then change,

$$dm_{sq} = m_{sq,\theta} - m_{sq,\theta+1} = m_t \left[\frac{V_{sq,\theta}}{V_{t,\theta}} - \frac{V_{sq,\theta+1}}{V_{t,\theta+1}}\right] \tag{3.59}$$

The curtain area shown in Figure 3-22 defines the area, A_{sq}, through which the displaced mass from the squish volume must pass. The squish velocity is then found from the continuity equation.

$$u_{sq} = \frac{dm_{sq}}{dt}\frac{1}{\rho A_{sq,\theta+1}} = \frac{V_{t,\theta+1}}{A_{sq,\theta+1}}\left[\frac{V_{sq,\theta}}{V_{t,\theta}} - \frac{V_{sq,\theta+1}}{V_{t,\theta+1}}\right]\frac{1}{dt} \tag{3.60}$$

Mass Loss From Tumble Vortex

As defined in Section 3.2.4 when the mass of the tumble vortex reduces due to a limit on the size of the ellipsoid dimensions then kinetic energy leaves the tumble vortex and becomes turbulent kinetic energy, k_{tum} gives the absolute gain in turbulent kinetic energy.

$$k_{tum} = \dot{m}_{tum} KE \tag{3.61}$$

Compression

A two equation model for turbulence in a two stroke engine was used by Reid (1993), the equation for the production of turbulent kinetic energy included a term for isotropic compression or expansion and will be used in the present turbulent model.

$$\frac{dk}{dt} = \frac{2}{3} k \frac{\dot{\rho}}{\rho} \tag{3.62}$$

k Equation for Turbulence Production

In this work a simple one equation model for turbulence will be used, the sum of the above turbulent production terms Equations (3.47), (3.56), (3.57), (3.61) and (3.62) gives the turbulent kinetic energy equation as,

$$\frac{dk}{dt} = \frac{2}{3} k \frac{\dot{\rho}}{\rho} + \frac{k_{sh}}{m} + \frac{k_{sq}}{m} + \frac{k_{tum}}{m} + \frac{\dot{m_{in}}}{m} (k_{in} - k) - \varepsilon \tag{3.63}$$

The last term of the equation ε is the turbulence dissipation term.

3.3.5 Turbulence Dissipation

In a steady state turbulent energy cascade the production of turbulence will be equal to the viscous dissipation of energy at the smallest scale. An estimate for the dissipation rate is taken from Tennekes and Lumley (1974). The assumption is made that the rate at which energy passes from the integral scale to the smaller eddies is proportional to the inverse of the integral time scale. The characteristic time scale of an integral scale eddy, or turnover time, can be defined as the eddy size divided by its characteristic velocity. The characteristic velocity is taken as the root mean square of the fluctuating velocity or turbulence intensity,

therefore the characteristic time scale $= {}^{l}/_{u'_{rms}}$. The amount of energy passed down to the smaller eddies is assumed to be proportional to the characteristic velocity squared $(u'_{rms})^2$ then the rate of energy supply is $\approx \frac{u'_{rms}}{l}.(u'_{rms})^2$, if the rate of energy supplied is equal to the rate of dissipation then,

$$\varepsilon = \frac{(u'_{rms})^3}{l} \tag{3.64}$$

The dissipation can also be defined from turbulent kinetic energy, using an adjustable model constant c_ε

$$\varepsilon = \frac{c_\varepsilon k^{3/2}}{l} \tag{3.65}$$

Note that viscous dissipation may be defined without the fluid viscosity, it is dictated by the inviscid behaviour of the turbulent flow. The turbulent energy cascades down to successively smaller eddies. The size of the small scale eddies is then defined by the rate at which they receive energy and the molecular viscosity of the fluid. The scale at which kinetic energy is dissipated by viscous effects is known as the Kolmogorov scale, η, defined by

$$\eta \equiv (\nu^3/\varepsilon)^{1/4} \tag{3.66}$$

The time scale of the Kolmogorov scale eddy is given by

$$\tau_\eta \equiv (\nu/\varepsilon)^{1/2} \tag{3.67}$$

And the Kolmogorov velocity scale is given by

$$v_\eta \equiv (\nu\varepsilon)^{1/4} \tag{3.68}$$

Tennekes and Lumley (1974) noted that for steady homogeneous pure shear flow the rate of production of turbulent energy will be equal to the rate of viscous dissipation. However in most flows production and dissipation do not balance.

3.3.6 Turbulent Scales

As stated in the beginning of Section 3.3 the one equation turbulence model, as used in this work, requires an integral length scale to be defined. For internal flows the integral scale of turbulence is often taken as a length scale of the enclosed volume. In the case of an engine cylinder the integral scale may be taken as either the cylinder bore or height dimension. However, during the inlet stroke in a four stroke engine or the scavenge period in a two stroke engine jets of fresh charge enter the cylinder through valves or ports. The turbulent jets enter the cylinder generating turbulent eddies which will be a size similar to the valve or port height. After the ports or valves close and the compression stroke begins the existing eddies will be compressed. In the turbulent model developed here separate methods are used to determine the integral scale for the open and closed cycles.

Integral Scales During Open Cycle

An overview of turbulent motion in a four stroke engine was given by Reynolds (1980), in which it was stated that in-cylinder turbulence is generated during the inlet stroke where a conical jet of fresh charge enters the cylinder. The turbulent eddies that enter the cylinder are of a scale of approximately the width of the conical jet, but the turbulent eddies increase in size as the jet flow widens. A large scale circulation is formed, swirl or tumble, within the cylinder which will be a size determined by the cylinder geometry. The large scale circulation continually breaks down into turbulent eddies of smaller and smaller size, with

the smaller eddies tending to be more isotropic and universal in character. Integral scales were quoted as being of the order of 10 mm.

Measured Integral Scales During Open Cycle

A number of researchers have attempted to measure the integral scale in four stroke engines during the induction stroke, Rouland et al. (1997) used particle image velocimetry to monitor the flow structure in a four stroke engine with a bore and stroke of 88 mm and 82 mm respectively. The engine used a four valve pent roof combustion chamber with the inlet ports restricted to enhance tumble motion whilst achieving a volumetric efficiency of 0.35. Their tests were conducted with the engine motored at 2000 rpm and a filtering technique was used to separate the bulk tumble flow motion from smaller scale turbulent motions. With the piston at 120° ATDC the PIV results show that the "characteristic size eddies" are of the order of 9 mm whilst the maximum valve lift was 9.8 mm. Planar laser induced fluorescence methods were used by Peterson and Ghandhi (2010) to investigate a two dimensional flow field in the cylinder of a four stroke engine during the intake stroke, the bore size was 86 mm and the stroke 94.6 mm. Integral length scales were determined by an autocorrelation method which produced scales of between 3.03 and 7.95 mm over a range of operating conditions between 600 and 1200 rpm and varying inlet manifold pressures. All the measurements were taken at 240° BTDC at which point the valve lift was given as 4.66 mm. Particle image velocimetry was used by Li et al (2002) to record a two dimensional velocity field in a single cylinder optical engine with a bore of 80 mm and stroke of 89 mm. The engine was motored at 1200 rpm. The cylinder head was a four valve pent roof type with one of its inlet ports blanked in order to produce swirl and with a maximum valve lift of 9 mm. Measurements were taken on a plane 12 mm below the cylinder head and in order to compute ensemble averaged velocities 120 PIV images were captured over consecutive engine cycles each at 60° BTDC. Fluctuating velocities were separated into two parts, low frequency and high frequency, and the assumption was made that low frequency fluctuations were due to cyclic variation whilst high frequency fluctuations were due to in-cylinder turbulence. Integral length scales were calculated based

on a spatial autocorrelation function which resulted in integral scales between approximately 6 and 10 mm which is consistent with valve lift.

Experiments were carried out on an engine cylinder model by Ishima et al. (2008), the extent of the model included the head but not the piston and crank assembly, the model has a cylinder of 75 mm bore and 100 mm in length. Air was drawn through the model by the use of external blower whilst one or two inlet valves were held open with a lift of 8 mm, hence simulating the inlet stroke. Integral length scales were determined from spatial correlation coefficients and measured integral scales were approximately 4 mm, half the valve lift, from both single and two valve operation.

It would appear that the integral length scale is more influenced by the valve lift than the cylinder dimensions during the inlet stroke.

Modelled Integral Scale During Open Cycle

Measurements from engines and flow rig models indicate that the integral length scale during the open cycle is of a similar order to valve lift rather than cylinder geometry. In the present work the integral scale during the transfer period will be defined by the transfer port height. During the scavenging process it is assumed that turbulent eddies enter the cylinder with a length scale that is proportional to the height of the transfer port. As the transfer port height is constantly varying the size of eddies entering the cylinder will vary. It is assumed that the eddies mix instantly in the cylinder and a mass averaged eddy size is used to define the turbulence integral length scale in the cylinder. The following defines the mass averaged integral scale length during scavenging,

$$l_{\theta+1} = (l_\theta m_\theta) + \left(h_p m_{in}\right) - (l_\theta m_{out}) \tag{3.69}$$

Where h_p is the instantaneous port height

Measured Integral Scale During Closed Cycle

Laser Doppler velocimetry was used to measure a two point spatial correlation for the turbulent integral scale in a two stroke engine by Fraser et al. (1986). The engine had a bore of 82.6 mm and stroke 114.3 mm and was motored at 600 rpm with air supplied by an external compressor. A disc style combustion chamber gave a compression ratio of eight and a clearance height of 12.1 mm. Direct measurement of turbulent integral length scale was achieved by making simultaneous velocity measurements at two locations within the laser crossing. Measurement results between 40 BTDC and 20 ATDC show that the integral length scale is compressed and reaches a minimum of 2.2 mm about ten degrees before TDC, the length scale then increases after TDC. Bulk flow motion and turbulence were measured by Obokata et al. (1987) in a 123 cc two stroke engine, with a bore of 56 mm and stroke of 50 mm. The engine was fitted with a wedge style combustion chamber with optical access and LDA was used to determine an integral scale of 3 mm around TDC. Hong and Tarng (1998) used LDV two point correlation method to measure the integral length scales in the cylinder of a four stroke engine with a bore of 41 mm and a stroke of 51 mm. Tests were conducted motoring the engine at 500 rpm and they also used 3D CFD analysis to calculate the integral scale. Figure 3-23 below shows that during compression the integral scale reduces and that at TDC, 180°, the scale is approximately 50% of the value at inlet valve closure.

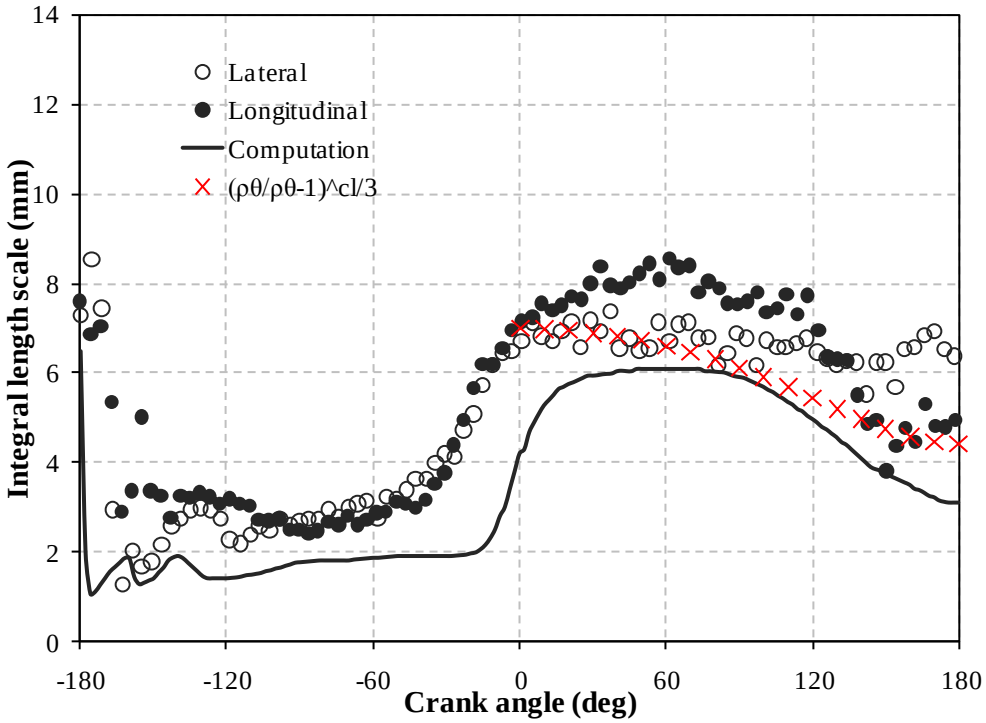

Figure 3-23, Integral length scale in a four stroke engine motored at 500 rpm adapted from Hong and Tarng (1998)

Particle image velocimetry was used to record two dimensional velocity fields in a single cylinder four stroke research engine by Reuss et al. (1989). The engine has a bore of 98.4 mm, stroke of 108 mm, compression ratio of eight and a clearance height of 15 mm. The engine was operated at 600 rpm and measurements at 12° ATDC produced integral length scales of approximately 2 mm.

Laser Doppler anemometry was used to measure flow velocities in the cylinder of a large four stroke engine with a bore of 120.65 mm and stroke of 140 mm running at 700 rpm and reported by Klingmann and Johansson (1999). Simultaneous velocity measurements were made at two locations from which the integral scale of turbulence is determined. The integral length scale was shown to be approximately 60% of the clearance height, Figure 3-24 below shows the measured integral scale near TDC.

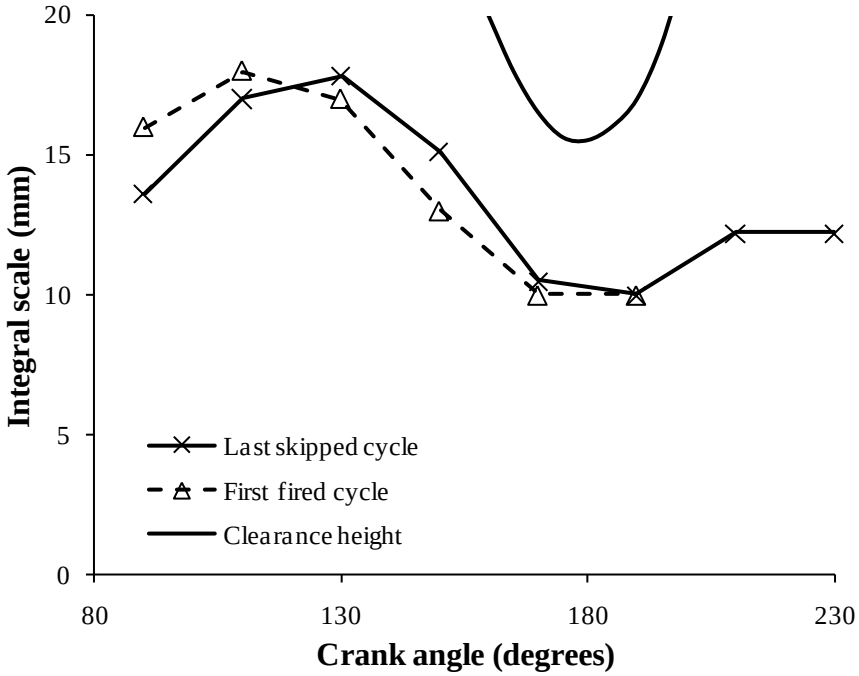

Figure 3-24, Integral scale measured in four stroke engine operating at 700 rpm adapted from Klingmann and Johansson (1999)

The flow structure in a four stroke tumble engine using two inlet and one exhaust valve was investigated by Li et al. (2004) using particle image velocimetry. Measurements of flow velocities, in two vertical planes and one horizontal, were made during the intake and compression stroke under motored conditions. Integral scales measured during compression up to approximately 50° BTDC were between 4 and 9 mm, the head clearance was 15 mm.

Modelled Integral Scale During Closed Cycle

Measurements indicate that turbulent integral scale in engines reduces as the piston approaches TDC and that at TDC the scale is approximately half the clearance height in the combustion chamber. Phenomenological combustion models developed by other researchers have used methods to define the integral scale based on the combustion chamber height. Poulos and Heywood (1983) used a one equation model for turbulence and related integral scale to the instantaneous cylinder height during the compression stroke, an additional

restriction was included such that the integral scale could not exceed half the bore dimension. Bozza et al. (2005) define the integral scale as between 20% and 80% the clearance height. Other models have included other parameters to determine the integral scale including Hunzinger et al. (2006) who relate the integral scale to the transfer port height and also the turbulent kinetic energy in a two stroke engine,

$$l = c_l h_{p,max} \sqrt{k_{EC}/k} \tag{3.70}$$

Where $h_{p,max}$ is the maximum transfer port height, k_{EC} is the turbulent energy at exhaust port closing and c_l is model constant. Then during combustion the integral scale varies as cube root function of the density,

$$l = l_{st} \left(\frac{\rho_{u,st}}{\rho_u} \right)^{1/3} \tag{3.71}$$

Where l_{st} is the integral scale at the spark time $\rho_{u,st}$ is the unburned density at spark time. A further restriction is included such that the integral scale cannot exceed 25% of the clearance height. Watanabe et al. (2010) base the integral scale on a function of the bore diameter at inlet valve closure in a four stroke engine. It is then assumed that the scale reduces during compression as a function of the cube root of the cylinder volume. In this study two mechanisms will be used to define the integral scale during the closed cycle, the first assumes that the integral scale is compressed at a rate proportional to the cube root of the density change and the second mechanism restricts the integral scale to a function of the clearance height. For the first mechanism the integral length scale during the closed cycle is calculated from the following,

$$l_{\theta+1} = l_\theta (\rho_\theta / \rho_{\theta+1})^{1/3} \tag{3.72}$$

In Figure 3-23 integral scales calculated using Equation (3.72) have been included, shown as crosses for comparison to test data. As the piston approaches TDC if the integral scale exceeds a certain fraction of the clearance height then the following restriction is imposed

$$l_\theta = c_h h_c \tag{3.73}$$

Where c_h is a calibration constant which has been set at 0.5.

3.3.7 Turbulence Isotropy

For the phenomenological turbulence model used in this work the assumption is made that turbulence in the cylinder is isotropic and homogeneous. Test and simulation methods have been used to evaluate the three dimensional structure of turbulence in engine cylinders, results from which may be used to assess the isotropic assumption. Laser Doppler velocimetry was used by Dimopoulos and Boulouchos (1997) to examine the turbulent flow field in a four stroke engine. Three orthogonal velocity components were measured at seven locations. It was noted in their conclusion that turbulence was neither homogeneous nor isotropic, however during the compression stroke the fluctuating intensities became more isotropic and homogeneous. A CFD analysis, using a k-ε model for turbulence was compared with experiments by Amsden et al. (1992). The experiments used laser Doppler anemometry to measure in-cylinder flow velocities of a loop scavenged two stroke engine. Results from their experiments showed that after 270° ATDC the fluctuation intensity was nearly isotropic.

Fraser and Bracco (1989) used a LDV two point velocity correlations, in tangential and axial directions, to evaluate integral length scales in a two stroke engine with optical access. They compared results from their engine test, averaged between 330 and 370 crank angle degrees ATDC, with other engine tests and also classical round-rod grid turbulence. It was concluded that the degree of anisotropy for the turbulence intensity was greater than grid turbulence but of the same order.

4 Flame Structure and Combustion Modelling

The combustion model developed in this work is based on a turbulent homogeneous premixed flame which is ignited by a single spark plug located in the centre of the combustion chamber. The flame then propagates spherically at a rate determined by the combustion model. The laminar burning velocities of typical fuels used in piston engines are relatively slow compared to the speed of the engine, complete combustion would be unlikely if the combustion progressed at the laminar speed. The flow field in a running engine will however always be turbulent and it is the turbulence that promotes the burning velocity due to its ability to transport heat and mass faster than by molecular diffusion alone. Turbulence may be used to increase the speed of the flame propagation, however excessive turbulence may lead to flame extinction.

Propagation of a turbulent premixed flame is dependent upon both by the chemical reaction rate and the turbulent motion of the fluid. In order to characterise a turbulent premixed flame structure a number of velocity and length scales are used. Figure 4-1 below shows a turbulent wrinkled flame front and some of the velocity and length scales.

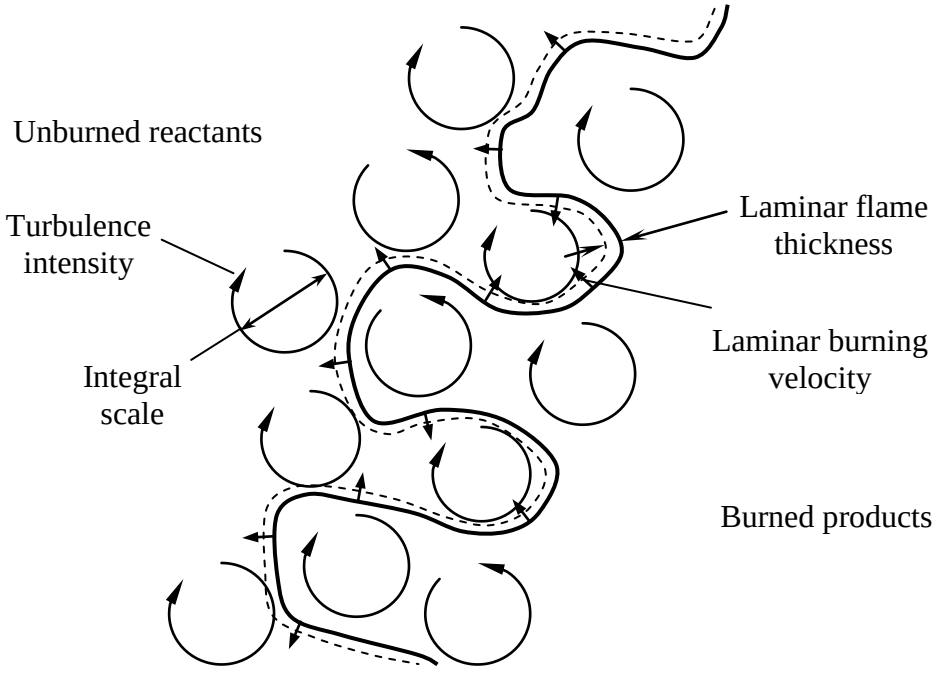

Figure 4-1, Wrinkled flame front

The turbulent intensity and integral length scale were described in the last chapter, the laminar flame thickness and burning velocity will be described in the next section.

4.1 Laminar Premixed Flame

In laminar premixed combustion the flame front propagates normal to the flame front. In a number of turbulent premixed combustion models the laminar flame structure is assumed to be unaffected by the turbulence. Therefore to analyse such turbulent combustion systems details of the laminar flame are required, including the flame thickness and burning velocity. Parameters that will influence the ability of the turbulence to modify the laminar flame structure are the scale of the turbulent eddies relative to the flame thickness and the characteristic velocity of the turbulent eddies relative to the laminar flame velocity.

4.1.1 Laminar Flame Structure

For a definition of the laminar flame thickness a description of the laminar flame structure is required, Figure 4-2 below shows the flame structure where reactants flow from left to right. The flame can be divided into three zones, the preheat zone, the reaction zone and the oxidation zone. In the preheat zone, heat from the reaction zone raises the temperature of the reactants to their ignition temperature. Once the reactants reach their auto ignition temperature, in the reaction zone, fast exothermic chemical reactions raise the temperature further. In the oxidation zone slower chemical reactions occur such as the oxidation of CO to CO_2 occur and the final products are formed.

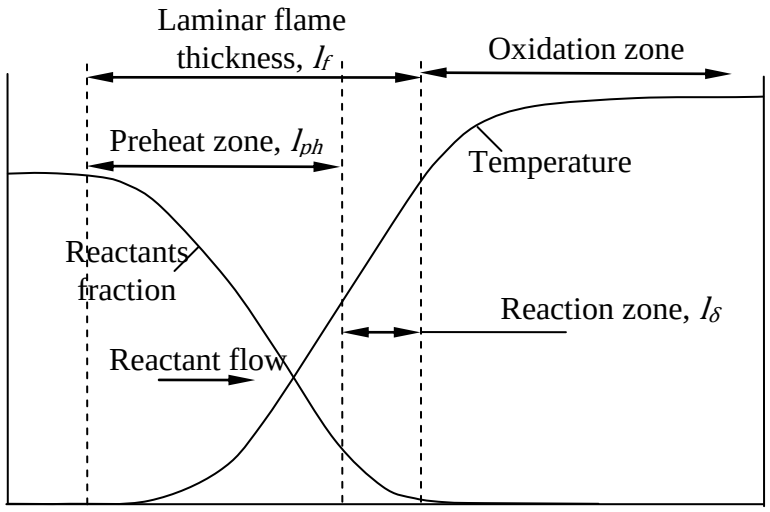

Figure 4-2, Laminar flame structure adapted from Turns (2000), Peters (2006) and Cant and Mastorakos (2008)

4.1.2 Laminar Flame Thickness

For the purpose of characterising the turbulent flame structure an estimate of the laminar thickness is required. An expression for the laminar flame thickness, l_{ph}, is taken from Heywood (1988) which is,

$$l_{ph} = \frac{4.6 k_{th}}{\left(c_p \rho S_L\right)_u} \tag{4.1}$$

Where k_{th} is the thermal conductivity, c_p the specific heat capacity, ρ density and the laminar burning velocity is S_L, which are all calculated at the preheat zone conditions. To calculate the preheat zone, in this work, values for the thermal conductivity are taken from tabulated data published by Incropera et al. (2006). The relationship between the flame thickness shown in Figure 4-2, l_f, and the reaction zone thickness, l_δ, for a stoichiometric methane flame at atmospheric pressure has been given by Peters (2006),

$$l_\delta = \delta l_f \tag{4.2}$$

Where δ is approximately 0.1 at atmospheric pressure. In this work Equation (4-1) will be used to define the laminar flame thickness.

The thickness of a laminar stoichimetric methane-air flame was measured at approximately 0.9 mm by Clarke and Hargrave (2009) at atmospheric conditions. As pressure increases the flame thickness reduces and at a pressure of 30 atmospheres δ in Equation (4.2) will reduce to 0.03, Peters (2006).

4.1.3 Laminar Burning Velocity

The burning velocity is defined as the velocity at which unburned mixture is consumed by the flame front. In laminar flow or quiescent conditions the flame front will be flat and normal to the flow of reactants. Metghalachi and Keck (1982) carried out tests with a combustion bomb to determine the burning velocities at various pressures and temperatures of methanol, isooctane and a reference fuel, RMFD 303. The properties for the reference fuel, RMFD 303, were given as 88.3 MON, 101.4 RON, density as 765 kg/m^3, molecular formula $C_{7.8}H_{2.214}$ and molecular weight 106.9 as kmol/kg. A simple power law was used to define laminar burning velocity

$$S_L = S_{L0}\left(\frac{T_u}{T_0}\right)^{\alpha}\left(\frac{P}{P_0}\right)^{\beta}\left(1 - 2.1x_{egr}\right) \tag{4.3}$$

Where T_u is the unburned gas temperature, P is the pressure, T_0, P_0 and S_{L0} are temperature, pressure and laminar burning velocity at a reference condition and x_{egr} is the residual mass fraction. The values for α an β were considered to be independent of the fuel type and were defined as,

$$\alpha = 2.18 - 0.8(\phi - 1) \tag{4.4}$$

$$\beta = -0.16 + 0.22(\phi - 1) \tag{4.5}$$

The dependence of the reference burning velocity with respect to fuel air equivalence ratio ϕ is shown below Figure 4-3. The data in the graph is for the reference burning velocity at 298k and 1 bar, however it should be noted that the graph points for RMFD 303 are extrapolated from data at temperatures between 300 and 360k. A second order curve fit for RMFD 303 is also plotted in Figure 4-3 which is given by the equation,

$$S_{L0} = C_m + C_2(\phi - \phi_m)^2 \tag{4.6}$$

Where the parameters C_m and C_2 are 0.3558 and -1.4045 m/s respectively and ϕ_m is taken as 1.13 for RMFD 303.

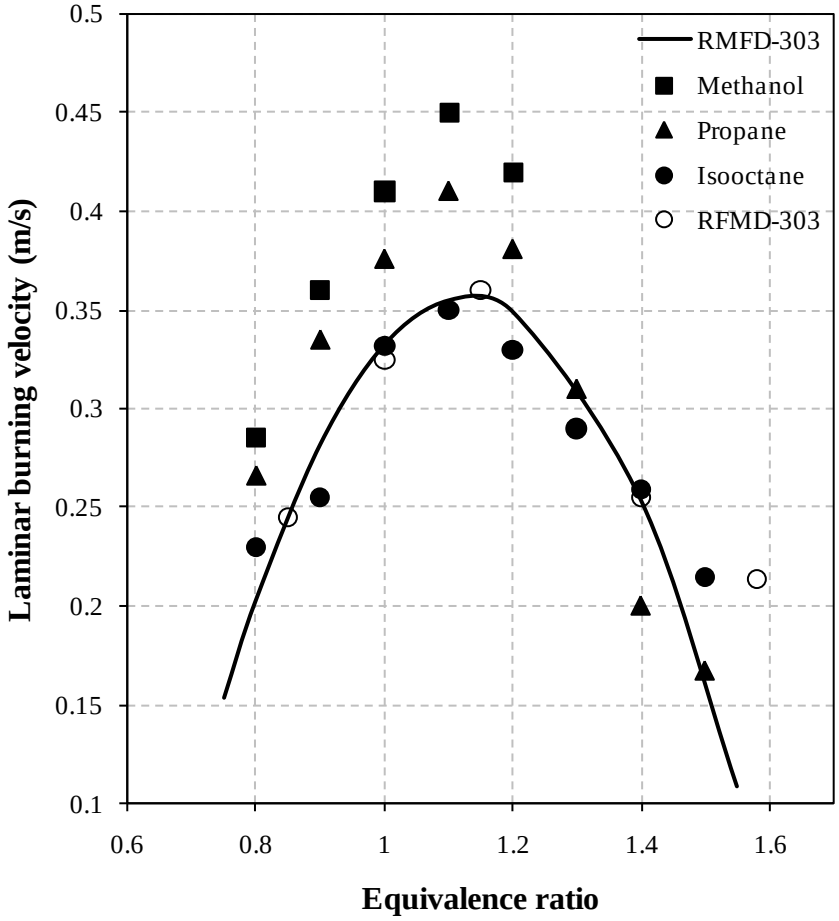

Figure 4-3, Laminar burning velocity for RFMD 303 adapted from Rhodes and Keck (1985)

Using the same combustion bomb Rhodes and Keck (1985) extended the work of Metghalachi and Keck for two reference fuels RMFD 302 and RMFD 303 which are similar to gasoline. New expressions were derived for the constants α and β used in Equation (4.3), for RMFD 303,

$$\alpha = 2.4 - 0.271\phi^{3.51} \tag{4.7}$$

$$\beta = -0.357 + 0.14\phi^{2.77} \tag{4.8}$$

Independent of equivalence ratio the amount of burned gas residuals will reduce the burning velocity. Rhodes and Keck simulated residual burned gas in the combustion bomb experiments by using mixture of 80% nitrogen and 20% carbon dioxide to evaluate the effects of residual gases on burning velocity. Figure 4-4 below shows the extent to which the residual fraction reduces burning velocity. The effect of residual fraction on burning velocity can be correlated by the expression,

$$S_{L,0} = S_L(1 - 2.06x_{egr}^{0.773}) \tag{4.9}$$

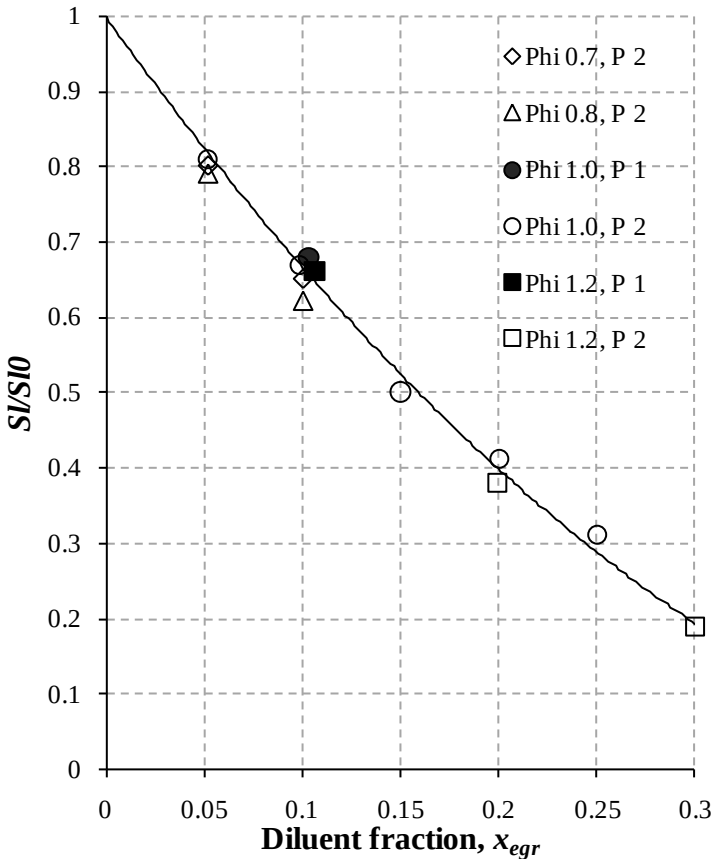

Figure 4-4, Burning velocity adjustment for dilution fraction, adapted from Rhodes and Keck (1985)

4.2 Flame Regime Diagrams

The structure of a turbulent flame is largely dependent on the turbulent flow field and the chemical reaction rate. Flame regime diagrams may used to characterise turbulent premixed flame structures, based on the velocity and length scales of the turbulent flow and laminar flame. Two such regime diagrams are the Damkholer and the modified Borghi regime diagrams.

4.2.1 Damkholer Flame Regime Diagram

A non-dimensional parameter often used to characterise flames is the Damkholer number, Da, which defines the relationship between turbulent eddy turnover time and characteristic flame reaction time.

$$Da = \frac{\tau_{flow}}{\tau_{flame}} \tag{4.10}$$

Where τ_{flow} is the turbulent eddy turnover time defined as $\tau_{flow} \equiv {}^{l}/_{u'_{rms}}$ with l being the turbulence integral length scale and u_{rms}' the turbulent intensity. Characteristic flame time is defined as $\tau_{flame} \equiv {}^{l_f}/_{S_L}$. Where l_f is the laminar flame thickness and S_L is the laminar burning velocity. Abraham et al. (1985) used a regime diagram with Damkohler number as the vertical axis and turbulent Reynolds number for the horizontal axis. The turbulent Reynolds number was defined in Section 3.3.2 by Equation (3.45). Figure 4-5 below shows a flame regime diagram based on the Damkholer number, two flame regimes known as reaction sheets and distributed reactions have been identified on the diagram.

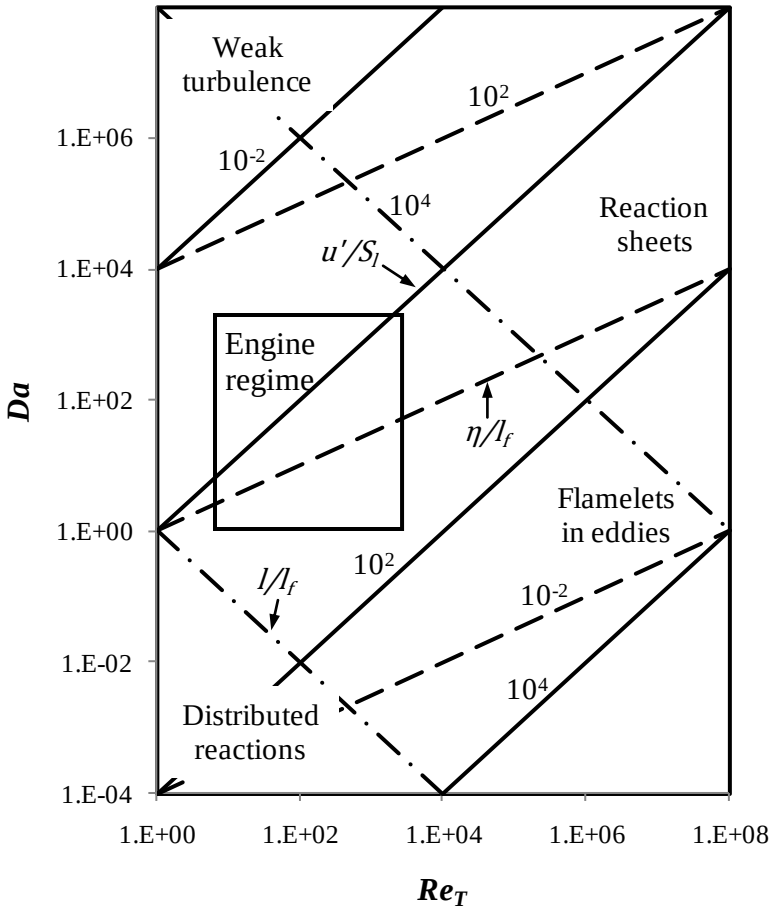

Figure 4-5, Flame regime diagram adapted from Abraham et al. (1985)

Distributed Reaction Regime

When the turbulence integral scale is smaller than the laminar flame thickness, $l/l_f < 1$, the turbulent eddies are able to stir the laminar flame front which leads to the transport of heat and mass within the flame and may lead to distributed reactions. Turns (2000) notes that achieving the small integral scale and large u'_{rms} may be difficult and states that "it is not clear that a flame can be sustained" in this regime.

The location of the boundaries for distributed reactions and reaction sheets is not precisely defined and it is unlikely that a single boundary between the two regimes exist.

Reaction Sheets Regime

In the reaction sheet regime, at large Damkholer numbers, the chemical reaction time is short relative to the turbulence time scale and the turbulence has little effect on the reaction rate in the flame. The turbulence is, however, able to advect the flame front causing it to wrinkle. The reaction zone may be a single continuous wrinkled sheet and the enhanced burning velocity is then simply a function of the increased surface area of the flame front due to wrinkling. With increasing turbulence the reaction zone may become highly convoluted, folded with multiple connected reaction sheets. If the turbulence is sufficient then adjacent reaction sheets may collide and "cut off" pockets of unburned gas and produce multiple reaction sheets. As turbulence levels increase small islands of unburned mixture may be seen behind the flame front in what is considered to be the burned zone, also small islands of burned mixture may be seen ahead of the flame front in what is considered the unburned zone. The convoluted flame front is referred to as a wrinkled laminar flame regime and the Kolmogrov scale of turbulence is larger than the thickness of the laminar flame, that is

$$\eta / l_f > 1$$

For the reaction sheets regime Turns (2000) suggests that Damkohler numbers are approximately 500 for $Re_T \approx 100$, and that the turbulence intensity u'_{rms} is the same order of magnitude as the laminar flame speed S_L.

Flamelets in Eddies Regime

A further regime known as flamelets in eddies was included in the Damkholer regime diagram by Turns (2000). This regime is below the line defined by Kolmogorov scale being equal to the flame thickness and here the smallest turbulence scales are able to enter and mix the laminar preheat zone. This regime requires a high level of turbulence and moderate Damkohler numbers. The reaction zone is made up of parcels of unburned gas surrounded by hot burned gas. The speed at which the flame front proceeds is defined by the rate at which the parcels of unburned gas are broken down to a size small enough that the unburned parcel temperature will increase to its ignition temperature and for combustion reaction to

occur. With this regime the turbulent flame propagation is determined by turbulent mixing rather than chemical reaction time, the flame structure is shown schematically below in Figure 4-6. The concept is similar to the eddy break up model of Blizard and Keck (1974).

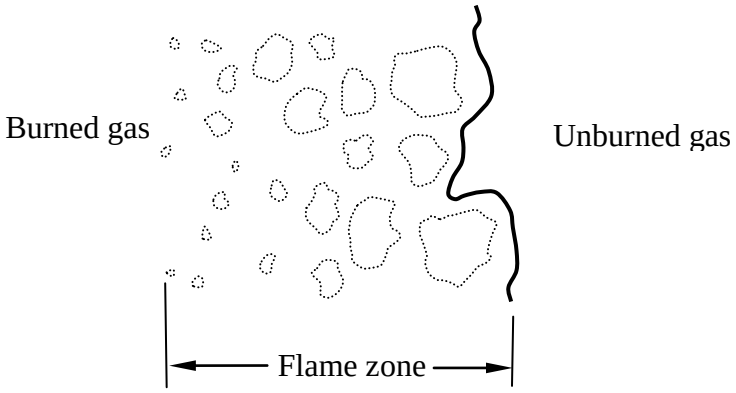

Figure 4-6, Flamelet in eddies regime adapted from Turns (2000)

4.2.2 Modified Borghi Diagram

A different flame structure regime diagram has been used by Peters (1986), a modified Borghi diagram, which is shown below Figure 4-7. A further non-dimensional parameter used to characterise flames is the Karlovitz number which relates characteristic flame time to the Kolmogorov eddy turnover time, τ_η

$$Ka = \frac{\tau_{flame}}{\tau_\eta} = \frac{l_f^2}{\eta^2} \tag{4.11}$$

The vertical scale of the diagram is the ratio of turbulence intensity to laminar burning velocity, whilst the horizontal scale is the ratio of the integral scale to laminar flame thickness. The diagram is divided into three main regimes defined by the Damkholer and Karlovitz numbers. Above Da=1 is the well stirred reactor, which is not relevant to piston engines. Between Da=1 and Ka=1 is a distributed reaction regime, where the Karlovitz number is greater than one and the smallest turbulent eddies are small enough to enter the

laminar flame structure preheat zone, but not the reaction zone. Below $Ka=1$ is the flamelet regime and this regime is further sub divided by the line $u'_{rms}=S_L$. Above the $u'_{rms}=S_L$ line the turbulent eddy velocity is greater that the laminar burning velocity and the flame front may become convoluted and folded to a point where multiple reaction sheets are formed. Below the $u'_{rms}=S_L$ line the front is likely to be characterised by a single wrinkled flame front.

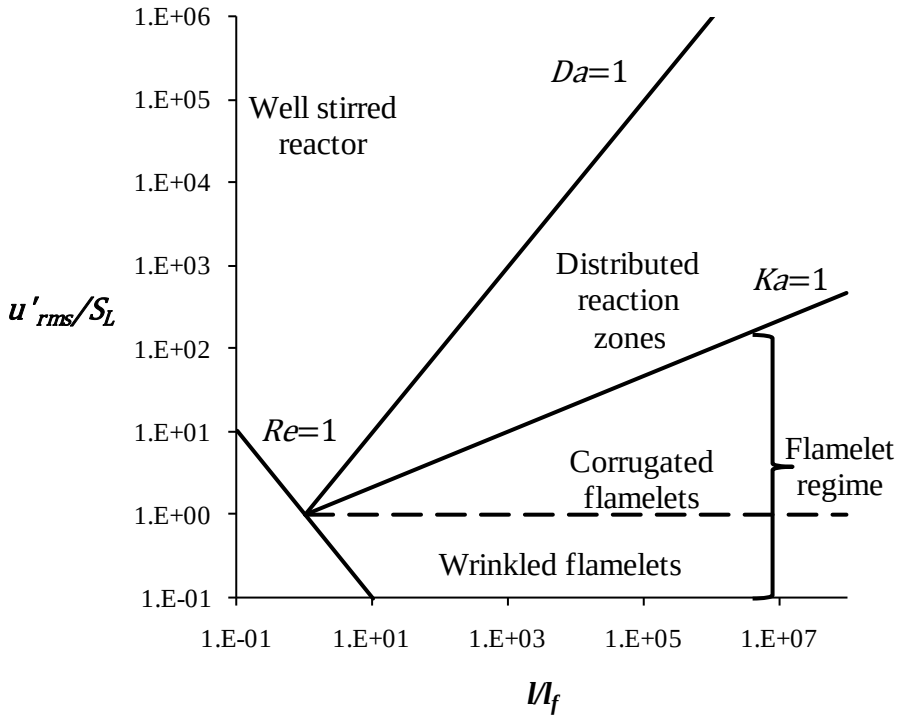

Figure 4-7, Flame regime diagram adapted from Peters (1986)

A further modification of the Borghi regime diagram was presented by Peters (1999) in which a regime referred to as thin reaction zones was added, shown in Figure 4-8. A second Karlovitz number was introduced based on the chemical reaction zone or the inner layer thickness, l_δ,

$$Ka_\delta = \frac{l_\delta^2}{\eta^2} = \delta^2 Ka \tag{4.12}$$

In the thin reaction regime Komogorov scale eddies are smaller than the flame preheat zone but larger than the reaction zone. The small eddies are able to increase mixing in the preheat zone and able to transport heat and mass from the preheat zone in front of the chemical reaction zone faster than by diffusion alone which will thicken the preheat zone. The eddies, however, not able to enter the chemical reaction zone and hence the reaction zone remains thin.

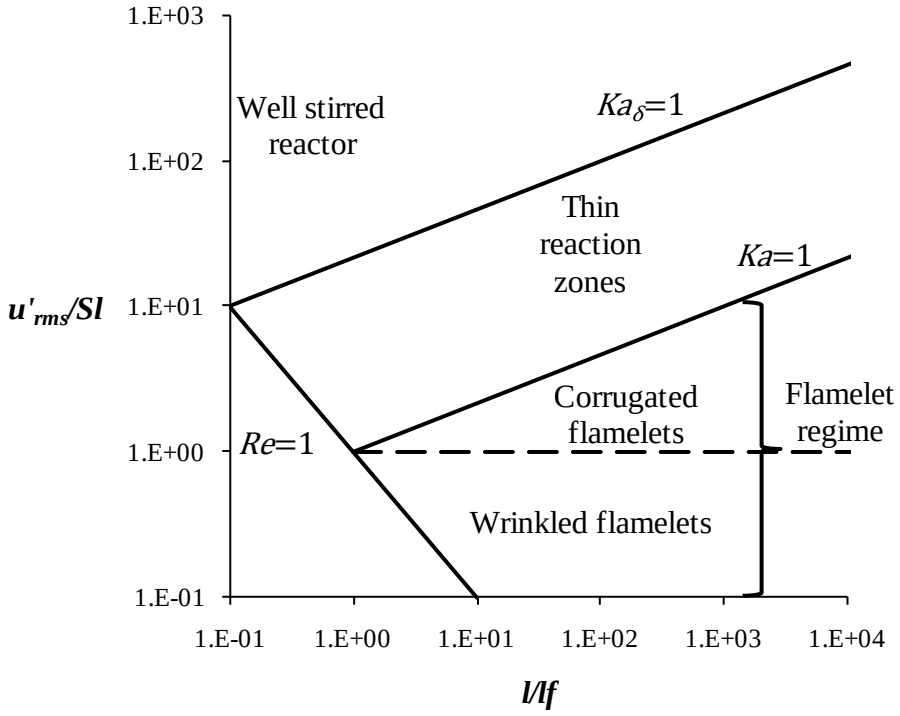

Figure 4-8, Flame regime diagram adapted from Peters (1999)

For flames in the thin reaction zone Gulder (2007) suggests that the flame structure may differ from the simple laminar structure. As turbulence increases the enhanced burning velocity may be influenced by mechanisms other than the increase in surface area due to flame wrinkling. An additional mechanism which enhances burning velocity is one in which

small scale eddies penetrate into the flame front and enhance the transport of heat and mass as described by Peters (1999). Gulder assumed that eddies on the Taylor scale are able to stir the reaction pre-heat zone transporting heat and mass from the reaction zone to the pre-heat and unburned zones.

The temperature rise in the preheat zone was measured by Kortschik et al. (2004) using Rayleigh LaserInduced Pre-dissociative Fluorescence (LIPF) of the OH radical. The 2D temperature field was measured in a low swirl burner with a stabilised flame and measurements were made at differing levels of turbulence intensity. The ratio of intensity to laminar burning velocity varied from 3.5, 9.2 and 18.7. Temperature measurements were averaged over 200 images and temperature profiles generated in a direction normal to the flame front plotted. The temperature profiles are shown below in Figure 4-9. The x axis on the graph is the distance from the flame front where zero on the axis is at a point in the flame where the temperature is equal to 800K. The temperature profile shows that with increasing turbulence the preheat zone increases in temperature. The increase in temperature is attributed to the turbulent transport within the preheat zone.

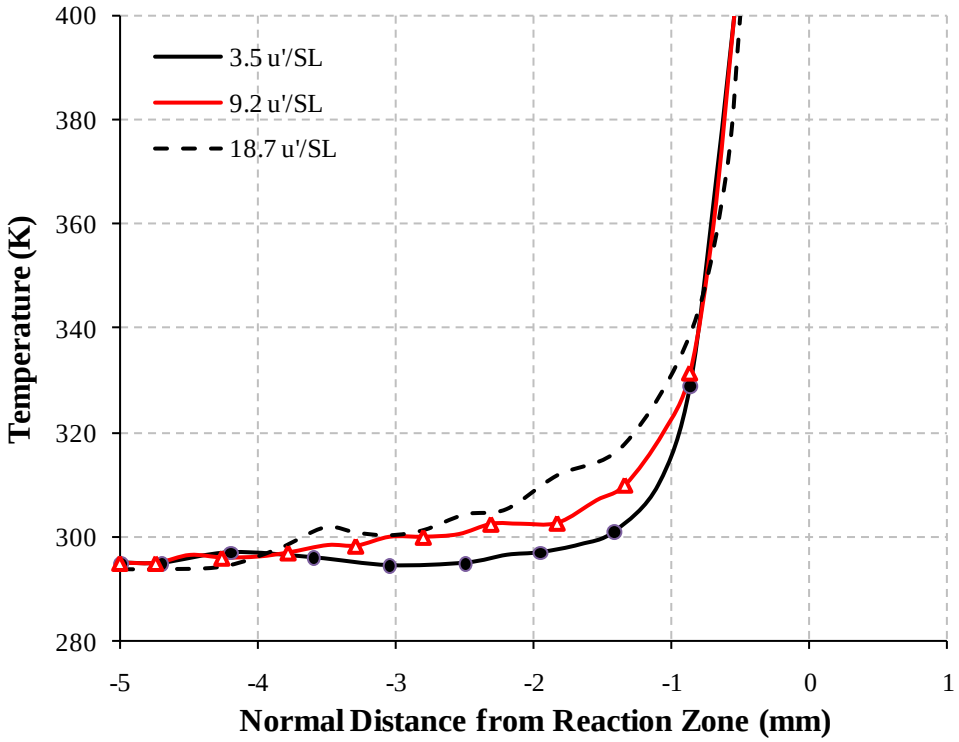

Figure 4-9, Effects of turbulence on preheat zone adapted from Kortschik et al. (2004)

DNS studies have been used to investigate the structure of turbulent premixed combustion and results show that the boundary between the wrinkled flamelet regime and the distributed reaction regime on the modified Borghi diagram may actually occur at $Ka>1$. Poinsot et al. (1996) used DNS results to determine the limit for wrinkled and corrugated flamelet regime as shown in Figure 4-10. The limit for the flamelet regime is consistent with the upper limit of the thin reaction zone regime when the integral scale is at least an order of magnitude larger than the flame thickness.

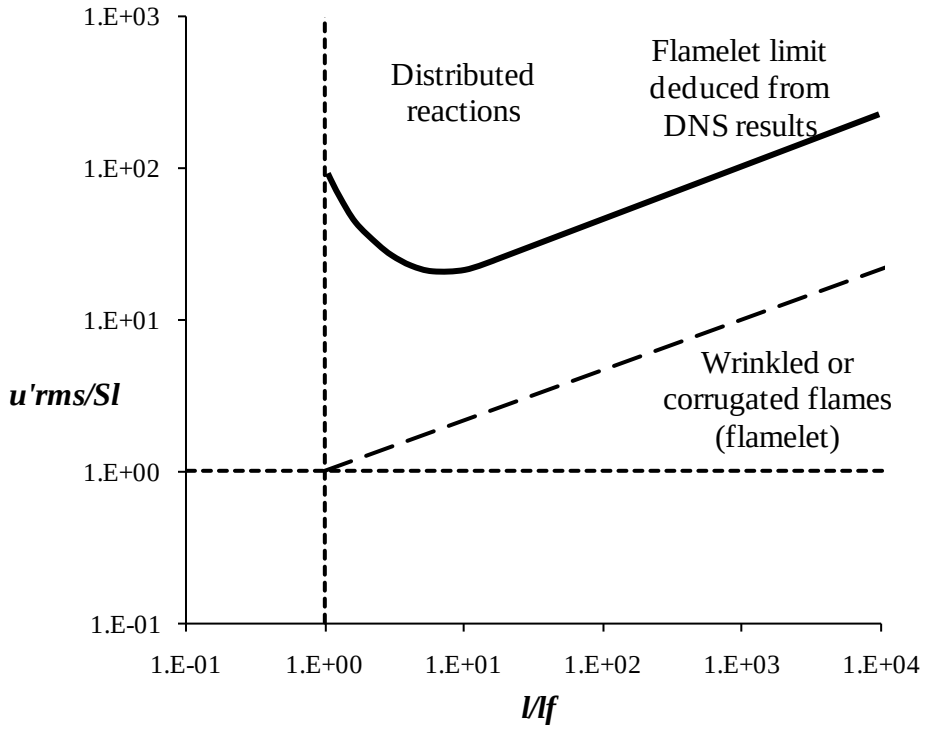

Figure 4-10, Modified Borghi diagram with results from DNS studies adapted from Poinsot (1996)

4.2.3 Flame Front Measurement and Visualization

Flame front visualisation using optical engines has been carried out by multiple researchers, including Baritaud and Green (1986) who used a laser Mie scattering technique at engine speeds between 300 and 1500 rpm. The engine used in their studies had a bore of 76.5 mm

and used a plane disc type combustion chamber with a clearance height of 18 mm. Bulk flow motion was very weak at TDC and turbulence intensity varied linearly with engine speed up to 5.5 m/s at 1500 rpm. They found that the flame front was the least convoluted at 300 rpm and as engine speed increases the flame front becomes more and more convoluted. The range of wrinkling scales also increased with engine speed. The 2D images taken at each engine speed show pockets or peninsulas of unburned gas inside the burned zone. Pockets or islands of unburned gas are disconnected from the main flame front where as peninsulas are distended fingers of unburned gas connected to the main flame front on a separate plane than that of the image. As the engine speed increases the numbers of pockets or peninsulas increase and the size of these vary from a few millimetres to tenths of millimetre.

Tests on a two stroke engine with optical access to the combustion chamber were performed by Hicks et al. (1994). The engine had a bore of 80 mm, stroke of 74 mm and a clearance height of 8 mm. The combustion chamber was a simple disc type and the engine was run at 1500 rpm. The turbulence intensity at TDC was estimated at 1.85 m/s. In their study multi plane laser sheet imaging was used to observe the flame front simultaneously at four separate cylinder heights. At an equivalence ratio of one the results do appear to show islands of unburned charge behind the flame front. However these islands were connected on a different plane and were considered as connected peninsulas. At lean mixtures, equivalence 0.7, isolated islands were observed and these were considered to be consumed after they were entrained.

A sequence of images of an advancing flame front in a combustion bomb were captured by a laser sheet technique and published by Gillespie et al. (2000). The flame front images taken using the laser sheet technique were plotted coincident with images of the flame front outline captured using the Schlierlen technique. The Schlierlen images of the flame front are always bigger than the laser images as the Schlierlen technique takes an image of the whole 3D profile and projects onto 2D plane whilst the laser sheet technique takes an image at one particular 2D plane. In some of the images there appears to be islands of burned products in the unburned zone, however with the highly convoluted 3D flame surface it is likely that the islands are connected to the burned zone on another plane. A scale of wrinkling for a flame

front was quantified by calculating a mean flame radius and then a root mean square value of the difference between actual and mean radii. The same optical two stroke as used by Hicks et al. (1994) but with a central spark plug was used by Gillespie et al. (2000). Images clearly show that the flame front cannot be accurately described as spherical, particularly in the early stages, see Figure 4-11 below. The images were captured using the laser sheet technique and the images between 15.7° and 10.3° and show significant variation in size of the burned zone. The variation in size does not however mean that the mass fraction burned varies significantly, but rather the centre of mass of the burned zone has moved to different locations relative to the laser sheet. Also apparent in some of these images are islands or peninsulas of unburned mixture within the burned zone.

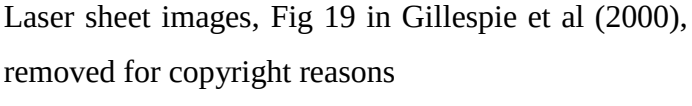

Figure 4-11, Laser sheet images of a flame front in a two stroke engine operating at 1500 rpm taken from Gillespie et al. (2000)

4.2.4 Multi Dimensional Modelling of a Flame Front

Insight into the structure of premixed turbulent combustion may be gained from Direct Numerical Simulation (DNS). DNS is a class of Computational Fluid Dynamics (CFD) which solves, numerically, for all the scales of turbulence involved without having to resort to turbulence models. A review of DNS applied to premixed turbulent combustion was given by Poinsot et al. (1996). Results show that a distended finger may exist in the flame front and such a flame front profile, when inspected with laser sheet imaging, may display this finger as an isolated island. DNS modelling is however limited by the need for an extremely dense computational grid, a typical DNS model may require one to two million grid points for a 5 mm^3 computational zone.

4.3 Combustion Modelling

An engine simulation requires a combustion model to predict the mass fraction burned and the heat release. The heat release rate is dependent on both the area of the flame front and the flame structure. For a quasi-dimensional model the propagating flame front is usually defined as a smooth semi-spherical surface contained by the combustion chamber walls. As discussed in Section 4.2 the flame structure is influenced by the turbulence intensity and the laminar burning velocity. A simple approach to turbulent combustion uses smooth spherical flame front area with a turbulent burning velocity which may be defined as a function of turbulent intensity and laminar burning velocity.

The mass burn rate is given by,

$$\dot{m}_b = \rho_u A S_T \tag{4.13}$$

Where ρ_u is the unburned density, A is the smooth semi spherical flame area and S_T is the turbulent burning velocity.

4.3.1 Burning Velocity Ratio

Turbulent combustion models have been developed based on a Burning Velocity Ratio (BVR) which is defined as the ratio of turbulent and laminar burning velocities. The turbulent burning velocity is that which is enhanced by the in-cylinder turbulence.

$$BVR = \frac{S_T}{S_L} \tag{4.14}$$

Turns (2000) gives examples of combustion models which use BVR that are applicable to the reaction sheet regime. Each of these models relates the turbulent burning velocity to a function of turbulence intensity and the laminar burning velocity.

Damkohler Model

$$S_T/S_L = 1 + u'/S_L \tag{4.15}$$

Clavin and Williams Model

$$S_T/S_L = \left\{0.5\left[1 + (1 + 8Cu'^2/S_L^2)^{1/2}\right]\right\}^{1/2} \tag{4.16}$$

Klimov model

$$S_T/S_L = 3.5(u'/S_L)^{0.7} \tag{4.17}$$

Other turbulent combustion models have been developed which attempt to model details of the flame structure. A critical appraisal of turbulent burning models was given by Andrews et al. (1975). A number of models were reviewed which were divided into two groups, turbulent or molecular transport processes. The models will not be discussed in detail here but a brief description of each group is given.

4.3.2 Turbulent Transport Models

Turbulent transport models maybe subdivided into large and small scale eddy models. In the large eddy model the eddies are assumed to be completely consumed once they reach their spontaneous ignition temperature. Consumed or reacting eddies may move forward of the burned zone due to the turbulent flow where they increase the temperature of other eddies. The movement of eddies acts to broaden the reaction zone. In the small scale eddy model it is assumed that the flame propagation proceeds along the small scale highly dissipative regions between the larger scale turbulent eddies.

An example of the small scale turbulent transport model is the eddy entrainment model originally developed by Blizard and Keck (1974), this was applied to a plane disc shape four stroke combustion chamber. Tabaczynski et al. (1977) and Tabaczynski et al. (1980) further developed the turbulent entrainment model by introducing the Taylor scale of turbulence. The flame is assumed to propagate along highly dissipative vortex tubes which are a thickness of the Kolmogorov scale and have a spacing of the Taylor scale, consistent with Tennekes (1968). A homogeneous and isotropic turbulent structure is assumed and the turbulence intensity varies linearly with engine speed. The turbulent entrainment speed is proportional to the turbulent intensity. The model assumed a spherical flame for which the rate of mass entrained by the propagating flame front was calculated based on a turbulent eddy entrainment rate and the area of the flame front, once entrained the individual eddies on the Taylor scale burn inward at the laminar burning velocity.

The eddy entrainment model has also been used in the two zone quasi-dimensional combustion model for a two stroke engine developed by Reid (1993) and reported by Reid and Douglas (1994). The entrainment model has been used by Poulos and Heywood (1982), Hunzinger et al. (2006) and others.

4.3.3 Molecular Transport Models

The molecular transport models assume that turbulence does not affect the laminar flame structure and that the flame propagation is enhanced by an increase in the flame surface area

caused by turbulence wrinkling the flame front. An example of a combustion model from the molecular transport group is the fractal model.

In the fractal wrinkled flame model it is assumed that there is a single connected flame front and that chemical reactions occur at the laminar burning velocity. The mass burning rate in a quasi-dimensional combustion model which assumes a spherical flame front is then a function of the ratio of wrinkled flame area to the spherical area. The fractal model has been applied to a two stroke engine by Bozze et al. (2005) and has also been used by Kido et al. (1991), Matthews and Chin (1991) and Wu et al. (1993).

4.4 Fractal Model

The combustion model used in this study assumes a laminar wrinkled flame front and uses a fractal geometry approach to define the wrinkled flame area. Fractals have been developed to provide a statistical geometric description of an irregular and contorted surface, Mandlebrot (1982) gives an in depth description of fractal geometry. A succinct explanation of the fractal approach and Mandlebrot's question "How long is the coast of Britain" is given by Gouldin (1987), who applied the fractal geometry approach to combustion modelling. Consider the perimeter of an area in a two dimensional plane which is wrinkled and convoluted, but is one continuous line. The perimeter length around the wrinkled flame front can be defined by a polygon of N sides of equal lengths L. As the length scale L reduces so the perimeter length increases. A characteristic of fractal geometry is that the measured length for the two dimensional perimeter depends on the measurement scale L to a power law dependence L^{1-D}, where D is known as the fractal dimension. For a three dimensional surface of a flame the fractal area follows the law L^{2-D}. For the two dimensional line a D value of one will produce a smooth line, whilst for a three dimensional surface a D value of two will produce a smooth surface. As the length scale L reduces smaller and smaller irregularities are measured and the area increases. If however the smallest scale of irregularity is defined by, for example the Kolmogorov scale, then reducing L below this scale will have no effect on area, this is known as the inner cut off. Similarly there is a outer

cut off beyond which the surface area should become independent of *L.* The inner cut off is defined here as L_{min} and the outer cut off as L_{max}.

In a quasi-dimensional combustion model the burned and unburned zones are separated by an infinitely thin spherical flame front. The actual flame front in the engine is however a highly convoluted and wrinkled shape. The ratio of the wrinkled flame front area to the spherical flame area is defined by the fractal geometry model,

$$Arearatio = \left(\frac{L_{max}}{L_{min}}\right)^{D-2} \tag{4.18}$$

The area ratio may used in a similar way to the burning velocity ratio, the flame is assumed to propagate at the laminar burning velocity and the enhanced burn rate is due to the area ratio,

$$\dot{m}_b = \rho_u S_L A_f \left(\frac{L_{max}}{L_{min}}\right)^{D-2} \tag{4.19}$$

Where A_f is the smooth spherical flame front area.

The correct choice of the fractal dimension and the inner and outer cut offs is necessary for the wrinkled flame surface area to be estimated. The inner and outer scales are generally chosen to represent the minimum and maximum scales of the wrinkled flame front which should be related to the scales of the turbulent flow field.

4.4.1 Outer Cut Off

For the outer cut off Gouldin (1987), Kido et al. (1991) and Bozza et al. (2005) chose the integral scale, whilst Yoshiyama et al. (2001) used the flame radius for the outer cut off. Matthews and Chin (1991) used three different approaches to define the outer cut off scale. The first assumes the instantaneous flame radius is equal to the outer cut off. In the second approach the flame radius is used until the flame radius exceeds the chamber height at which

point the outer cut off is equal to the chamber height. In the third approach the integral scale was used. In the conclusions to their work they state that the third approach was the most accurate over a range of loads.

In this work the outer cut off or the maximum scale of wrinkling will be defined as a wrinkling brush zone thickness, based on an averaged engine cycle. Cycle by cycle variation occurs in spark ignition engines and is, to a large extent, caused by the random behaviour of the turbulent flow field in the cylinder, particularly during early flame development. The combustion model developed in this study will be used to predict the heat release for a nominal or averaged cycle, is not intended to analyse cycle by cycle variation. As such the fractal dimension, inner and outer cut offs, should all be representative of an averaged cycle. Although quasi-dimensional combustion models are usually based on the assumption of a spherical flame front propagating radially outward from the spark plug, observations in optical engines have shown the flame front to be a highly convoluted shape, far from spherical and not exactly centred at the spark plug location. Figure 4-11 shows examples of flame front images taken at the same crank angle positions but for different cycles. The wrinkled flame front is obvious and differences in the shape of the flame front for different cycles can be seen. The concept of a mean flame brush thickness for an averaged cycle is shown schematically in Figure 4-12 below, on the left is a flame front from a single cycle and on the right are a number of individual flame fronts plotted from different cycles at the same crank angle and engine operating conditions. A smooth curve bounding the outer edges of all the flame fronts will approximate to a circle and a smooth curve lying within the burned zone of all the flame fronts will also approximate to a circle. A mean wrinkled flame brush thickness is then defined by the outer and inner circular profiles. In this study the outer cut off of the fractal geometry model is considered to be equivalent to the mean wrinkled flame brush thickness. The shape of the wrinkled flame front is due to the turbulent flow field in the engine cylinder and it is the integral scale eddies that have the most significant amount of energy to wrinkle the flame. It is assumed here that the wrinkled flame brush thickness is a function of the integral scale.

$$L_{max} = c_{Lmax} l \tag{4.20}$$

Where c_{lmax} is a model constant which may be adjusted to calibrate the combustion model with experimental data, this is discussed in Section 8.2.

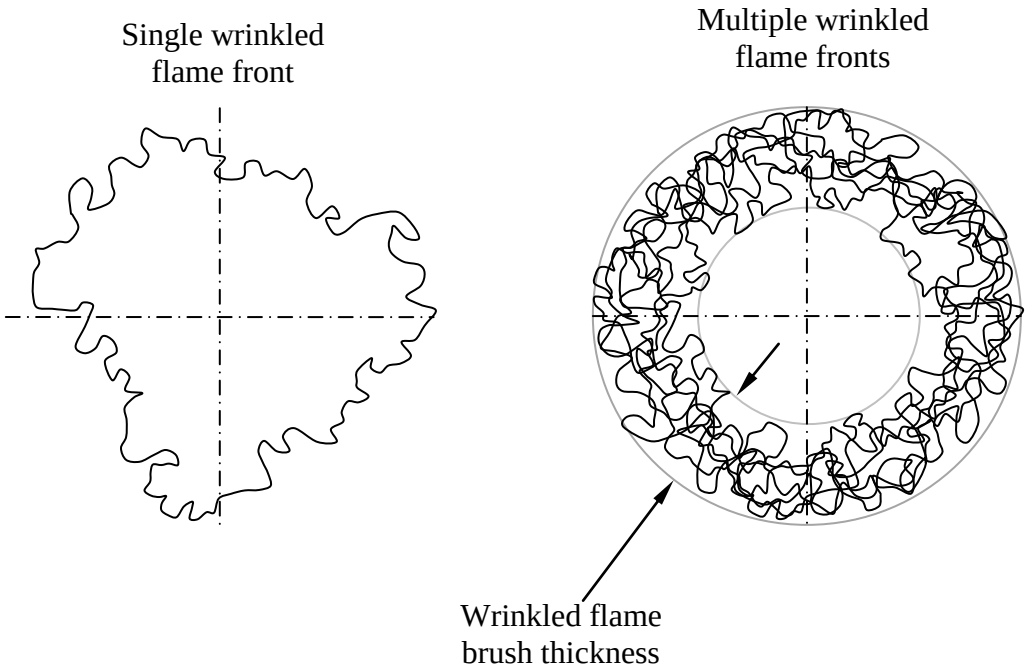

Figure 4-12, Flame front geometry and wrinkled flame brush thickness

4.4.2 Inner Cut Off

As the smallest scale of turbulence is the Kolmogorov scale then the inner cut off should be no smaller than the Kolmogorov scale. Gouldin (1987), Wu et al. (1993), Matthews et al. (1996), Bozza et al. (2005) and Perini et al. (2010) use the Kolmogorov scale as the inner cut off. Kido et al. (1991) calculated the inner cut off based on a function of the laminar flame preheat zone and Kolmogorov scale,

$$L_{min} = \frac{\eta}{\eta + l_{ph}}\eta + \frac{l_{ph}}{\eta + l_{ph}}l_{ph} \tag{4.21}$$

Where η is the Kolmogorov scale and l_{ph} is the preheat zone thickness. With this assumption the minimum wrinkling scale cannot become smaller than the preheat zone

thickness. If the minimum scale of turbulence were to become smaller than the preheat zone then Kido et al. (1991) suggest that the description of the flame structure may become "ambiguous".

Matthews and Chin (1991) used an inner scale equal to the Kolmogorov scale multiplied by 3.55, a value based on burner stabilised flames. Yoshiyama et al. (2001) based the inner cut off on function of the laminar flame preheat zone and a Karlovitz number

$$\frac{L_{min}}{l_{ph}} = 5Ka^{-0.5} \tag{4.22}$$

Where the Karlovitz number is based on the Taylor scale, λ,

$$\mathrm{Ka} = (u'_{rms}/\lambda)\left(l_{ph}/S_L\right) \tag{4.23}$$

Where the Taylor scale is defined as

$$\lambda^2 = \frac{15\nu u^2}{\varepsilon} \tag{4.24}$$

The fractal model used in this study will use an inner cut off equal to the Kolmogorov scale multiplied by 3.55, as used by Matthews and Chin (1991).

4.4.3 Fractal Dimension

The fractal dimension, *D*, in Equation (4.19), defines the degree of wrinkling of the flame front surface. As already mentioned for the value *D*=2 the three dimensional surface becomes smooth, as *D* increases the surface will become more irregular and convoluted, *D*=3 is the upper limit. Gouldin (1987) quotes values for fractal dimensions of 2.35 - 2.4 as those found in clouds whilst values between 2.35 and 2.6 are given for turbulent shear flows. Mantzaras et al. (1988) used laser sheet imaging techniques to record the flame front profile

in an engine with a bore of 82.6 mm, stroke 114.3 mm and compression ratio of 8. The engine tests were conducted at a maximum speed of 2400 rpm at which condition the turbulence intensity was given as 5 m/s. At an equivalence ratio of one and engine speed of 2400 rpm the maximum measure fractal dimension was 2.349. It was pointed out that an upper limit to the fractal dimension had not been reached. A heuristic model for defining the fractal dimension has been given by Santavicca et al. (1990) as,

$$D_3 = D_L \frac{S_L}{u'_{rms} + S_L} + D_T \frac{u'_{rms}}{u'_{rms} + S_L} \tag{4.25}$$

Where D_L is the fractal dimension due to the laminar burning velocity and the first term on the right hand side of Equation (4.25) tends to smooth the surface of the flame front. D_T defines the fractal dimension due to turbulence and the second term acts to increase wrinkling of the flame front, a value of 2.35 was given for D_T and D_L is set to 2.0

Hicks et al. (1994) used laser sheet imaging to determine the fractal dimension of a propagating flame front in a two stroke engine. The degree of flame wrinkling quantified by a number of methods including fractal analysis, simple area ratios and a Power Spectral Density (PSD) technique. They determined the fractal dimension associated with the length of the flame front based on a 2D measuring plane. The fractal dimension increased rapidly after ignition from near unity to approximately 1.35. This indicates that the flame front starts of smooth and laminar at ignition and then the scales of wrinkling increase rapidly to a maximum and then remain constant for the main burn duration.

The predicted results from a fractal combustion model were presented by Yoshiyama et al. (2001) and compared to measured results from constant volume combustion chamber and a spark ignition engine. The dimensions of the fixed volume combustion chamber were similar to the combustion chamber of the spark ignition engine at top dead centre, both have a bore dimension of 85 mm and a similar level of swirl and turbulence intensity. The engine tests were conducted at relatively slow speeds, a maximum of a 1000 rpm. The test engine was driven by an electric motor at constant speed, either methane or propane were used as fuel mixed homogeneously. In both the fixed volume chamber and the engine the turbulence

intensity was less than 1 m/s. In their tests the propagating flame was recorded using laser tomography and the flame boundary and fractal characteristics determined using a circle method. Calculated fractal dimensions were compared with those measured in the fixed combustion chamber and SI engine and shown to correlate well, when the fractal dimensions were plotted against u'/SL there was no correlation, however when the fractal dimension was plotted against $(\rho_u/\rho_0)^2(u'_{rms}/S_L)$ a correlation is seen. A different expression for the fractal dimension was defined which included the unburned density as a variable,

$$D_2 = \frac{1.0}{1 + \left(\rho_u/\rho_0\right)^4 \left(u'_{rms}/S_l\right)^2 /3} + \frac{1.3}{1 + \left(\rho_u/\rho_0\right)^{-4} \left(u'_{rms}/S_l\right)^{-2} /3} \tag{4.26}$$

Kido et al. (1991) use the equation,

$$D_3 = 2 + 0.5exp\left\{\frac{-0.53}{\ln\left(1 + u'_{rms}/S_L\right)}\right\} \tag{4.27}$$

Which shows that the fractal dimension will increase as u'_{rms}/S_L increases.

Matthews and Chin (1991) and Wu et al. (1993) use the expression for the fractal dimension given by Santavicca et al. (1990), Equation (4.25). Bozza et al. (2005) also use the Santavicca equation but with D_L set to 2.05. Verhelst and Sierens (2007) use the Santavicca equation with D_T set to 2.38 and D_L set to 2.0 for a fractal model that calculates an entrainment rate rather than a burning velocity for a hydrogen fuelled engine. The fractal combustion model developed in this study will use Santavicca equation with D_L set at 2.0 and D_T used as a model constant to calibrate the combustion model against engine test data.

4.5 Fractal Model with Entrainment

The laser images from the work of Mantzaras et al. (1988) showed that a flame front had a fractal characteristic and also showed islands of unburned mixture behind the flame front. The explanation for these islands is that the flame front becomes so distorted that the convolutions produce flame fingers or peninsulas on a separate plane to the laser sheer, but the islands are connected to the main flame front. The engine used by Mantzaras operated at a moderate 2500 rpm and generated a turbulence intensity of 5 m/s. If turbulence intensity increases proportional to engine speed then at 10,000 rpm and intensity of 20 m/s there is a greater possibility of generating islands of unburned reactants behind the flame front as the flame front becomes more convoluted. Also as trapped exhaust residuals increase, as might be expected with a two stroke engine at part throttle, the laminar flame velocity reduces which increases the ratio of intensity to laminar flame speed moving the flame structure towards the distributed reaction regime. To account for the possibility of unburned islands modified fractal models have been developed.

4.5.1 Peninsula-Fractal Model

A development of the fractal model was proposed by Matthews et al. (1996), called the peninsula-fractal model. The peninsula-fractal model uses the fractal model developed by Matthews and Chin (1991) and Wu et al. (1993) to account for a mass of reactants burned at a single wrinkled flame front and includes an eddy entrainment model, originally developed by Blizard and Keck (1974), to account for a mass of reactants burned by islands. The entrainment rate was reduced by 50% in the combined model, the value of 50% was chosen arbitrarily and may be treated as a model constant, although a value of 50% yielded good results for two different four stroke engines.

4.5.2 Reactant Islands and Fractal Flamelets

An adaptation of the fractal model was proposed by Kido et al. (1991) and further discussed by Kido and Huang (1993), where the modified model was named the Reactant Islands and Fractal Flamelets (RIFF). The model uses the fractal geometry approach to define a

wrinkled flame front but also assumes that as intensity increases there is an increased chance that pockets of unburned reactants will be entrained by the wrinkled flame front. The unburned pockets or islands are then subsequently consumed. In the RIFF model the outer cut off dimension for the fractal model is taken as the integral scale and the turbulent burning velocity at the wrinkled flame front calculated by the laminar burning velocity and the fractal area ratio. The reactant islands entrained at the flame front are also assumed to have a wrinkled surface with the same fractal geometry as the wrinkled flame front and burn at the same rate. The islands are assumed to be entrained initially at a characteristic size of the integral scale. A schematic of the concept of the reactant islands behind the fractal flame front is shown below Figure 4-13.

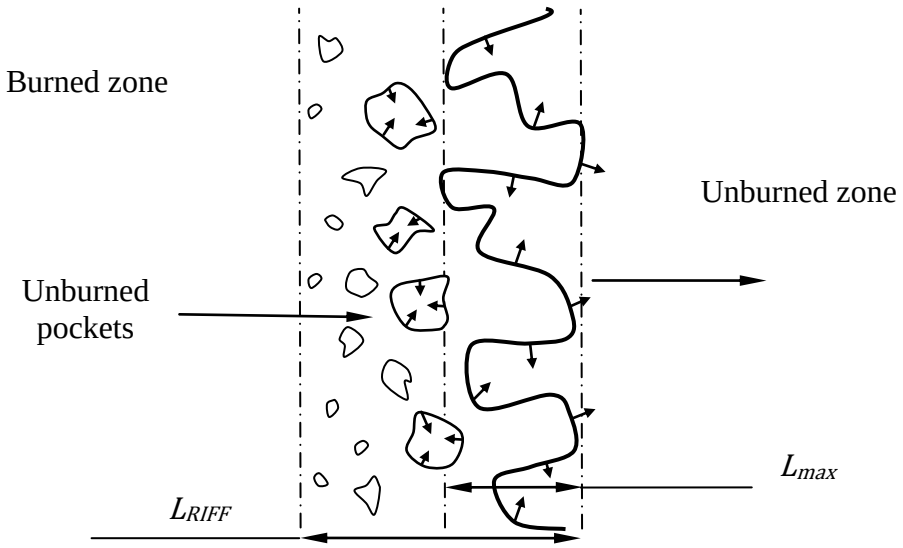

Figure 4-13, Unburned islands behind wrinkled flame front adapted from Kido et al. (1991)

The total mass burn rate will be a function of both the wrinkled flame front and the number of reactant islands. The volume fraction burned at the wrinkled flame front is defined as f_W and the volume fraction burned by islands is defined by f_D. The volume fraction of the reactants consumed as islands is dependent upon the turbulent intensity and laminar burning velocity and is defined by the exponential function,

$$f_D = exp\left(-c_{RIFF}\frac{S_L}{u'}\right) \tag{4.28}$$

Where c_{RIFF} is a calibration constant, determined experimentally as 4.8 by Kido et al. (1991).

In this study a different expression is used to define the mass fraction burned and is an equation similar to the Santavicca equation,

$$f_D = \left[\frac{u'_{rms}}{u'_{rms} + S_L}.\frac{r_f}{(L_{max}/2)}\right]c_{RIFF} \tag{4.29}$$

The second part on the right hand side of Equation (4.29) accounts for the early flame development which is covered in Section 4.7. Once the flame radius is greater than half the wrinkled brush thickness L_{max} Equation (4.29) is replaced with,

$$f_D = \left[\frac{u'_{rms}}{u'_{rms} + S_L}\right]c_{RIFF} \tag{4.30}$$

The characteristic burn up time of an island is

$$\tau_D = {X_C}/{2S_D} \tag{4.31}$$

Where X_C is the mean diameter of the islands and is of the order of the integral scale and S_D is the burning velocity of the islands. The volume fraction of reactants consumed by the wrinkled flame front is then given as,

$$f_W = 1 - f_D \tag{4.32}$$

A characteristic length scale for the flame brush thickness, wrinkled flame front plus islands, is shown in Figure 4-13 labelled as L_{RIFF}.

A modified version of the RIFF model will be used in this study, the outer cut off of the fractal geometry for the wrinkled flame front is increased from the integral scale to the wrinkled flame brush thickness L_{max} defined in Section 4.4.1. The outer cut off for the fractal geometry of the islands will remain at the integral scale.

The turbulent burning velocity at the wrinkled flame front, S_W, is given by,

$$S_W = S_L \left(\frac{L_{max}}{L_{min}}\right)^{D_3-2} \tag{4.33}$$

A characteristic burning time of the wrinkled flame front is defined as,

$$\tau_W = {}^{L_{max}}/_{S_W} \tag{4.34}$$

The turbulent burning velocity of the combined wrinkled flame front and the reactant islands, S_C, is given by to the sum of the burning velocities of the wrinkled flame front and the islands.

$$S_C = L_{RIFF}\frac{f_W}{\tau_W} + L_{RIFF}\frac{f_D}{\tau_D} \tag{4.35}$$

The component of the turbulent burning velocity due to the wrinkled flame front is,

$$S_W = L_{RIFF}\frac{f_W}{\tau_W} \tag{4.36}$$

The characteristic time of the wrinkled flame front is τ_W given above, then the characteristic brush thickness may be calculated by,

$$S_W = L_{RIFF} \frac{f_W}{L_{max}} S_W \tag{4.37}$$

The dimension L_{RIFF} in Figure 4-13 represents the width of the flame brush, which includes the wrinkled flame brush and the further zone of reactant islands can be calculated from,

$$L_{RIFF} = {}^{L_{max}}/_{f_w} \tag{4.38}$$

4.6 Ignition Delay

The combustion process can be divided into specific phases, spark ignition, initial flame development, fully developed flame propagation and end of combustion. Often for whole engine simulation the spark ignition phase including the spark plasma formation and early flame kernel development is not considered. At the point of ignition, or after a short delay period, an instantaneous burned zone with a prescribed mass or volume is defined. The ignition delay period is used here to define the short time period between the onset of spark and a stable early flame kernel with a defined volume. The size of the burned zone at ignition has been defined by different methods including a percentage of the cylinder mass, an arbitrary diameter or the distance between the spark plug electrodes. Research into the ignition and early flame development was carried out by Herweg and Maly (1992) using an experimental spark ignition engine with a remote combustion chamber. The remote combustion chamber had quartz windows which allowed optical access through which Schlieren photographs were taken. Herweg and Maly note that for a small flame kernel radius, less than 1 mm diameter, the ignition system is the dominant factor in kernel growth. After approximately 200 μs a 2 mm radius flame kernel exists and the ignition system will no longer influence the flame kernel growth. The ignition spark and plasma phase are not included in the current combustion model, instead after the ignition delay period a burned zone of 2 mm radius is produced at the spark plug location.

A model to define the ignition delay period has been developed by Hires et al. (1978), it was based on the assumption that the ignition delay is proportional to the time period required to

burn a single integral scale eddy. The model shows the ignition delay is inversely proportional to the turbulence intensity and laminar burning velocity. Herweg and Maly (1992) have shown that the initial flame kernel development is also dependent upon the mean flow velocity at the spark plug electrodes. During the finite time period of spark discharge flame kernels are being continuously created and displaced by the mean flow to create a "horn of plenty" shaped flame. For the combustion model developed here the ignition delay is modelled simply as being inversely proportional to the mean flow velocity, turbulence intensity and laminar burning velocity,

$$T_{del} = c_{ign}\left(\frac{1}{U}\right)^{\alpha}\left(\frac{1}{u'_{rms}}\right)^{\beta}\left(\frac{1}{S_L}\right)^{\gamma} \tag{4.39}$$

Where the constant c_{ign} and the polynomial coefficients α, β and γ are adjustable model constants, which are set at values of 0.0015, 0.5 0.85 and 0.3 respectively.

4.7 Flame Kernal Development and Early Propagation

Schleiren images of the flame kernel development at the spark plug electrodes of an engine have been presented by Maly and Herweg (2009), which show a smooth spherically growing kernel up to about 270 μs, after which the kernel starts to become wrinkled. At its formation the flame kernel is smaller than the size of the integral scale of turbulence so that the most significant energy containing eddies are unable to wrinkle the flame kernel. Smaller scales of turbulence with less energy will however be able wrinkle the growing flame front. As the kernel grows in size the spectrum of turbulent scales able to wrinkle the flame front will increase. The fractal dimension discussed in Section 4.4.3 defines the degree of flame front wrinkling and a fractal dimension of two defines a smooth laminar flame. As the flame kernel develops from a smooth laminar to a fully developed wrinkled flame front the fractal dimension will increase from a value of two. Once the flame front is wrinkled by all the turbulent scales then it becomes a fully developed flame front. In the fractal combustion model described by Wu et al. (1993) the fractal dimension during early flame growth was calculated with a modified version of the Santavicca Equation (4.25), where the turbulence

intensity of the integral scale is replaced with an intensity of an eddy which has the scale the same size as the flame kernel,

$$D_3 = 2.35\frac{u'_{max}}{u'_{max} + S_L} + 2.05\frac{S_L}{u'_{max} + S_L} \tag{4.40}$$

Where u_{max} is the intensity of an eddy at the kernel scale which is determined from an energy cascade principle,

$$\varepsilon = \frac{u'^3}{l} = \frac{u_{max}^3}{r_f} \tag{4.41}$$

In this approach the fully developed fractal dimension is reached once the flame radius is equal to or larger than the integral scale.

A different approach to the initial flame kernel development and fractal dimension was taken by Bozza et al. (2005). A factor for the fractal dimension was based on the exponential of a ratio of the flame radius with a reference radius and a ratio of the engine speed with a reference speed. The reference radius was given as being the order of 10 mm.

A similar approach to Bozza will be used in the current model with an exponential term used to define the fractal dimension during the early flame development. An initially smooth unwrinkled flame kernel is represented with a fractal dimension of two, as the flame front grows the fractal dimension increases until the point when the flame radius is equal to or greater than half the maximum scale of wrinkling, which is the outer cut off. Once the flame radius exceeds half the outer cut off the flame propagation is considered to be fully developed and the fractal dimension given by Equation (4.25).

Here the ratio of the flame radius to the integral scale is used in the exponential equation but engine speed is not included.

$$D_{3,ker} = \left\{\left[1 - exp\left(-1.9\left({}^{r_f}/_{(L_{max}/1.9)}\right)^2\right)\right](D_3 - D_L)\right\} + D_L \tag{4.42}$$

Where D_3 is calculated from the Santavicca equation.

As the initially laminar flame kernel expands towards the fully developed flame front the maximum scale of wrinkling, L_{max} will increase until it reaches a maximum at the start of the fully developed flame propagation phase. It is assumed that the maximum scale of wrinkling is twice the flame front radius until the maximum scale reaches the outer cut off defined by Equation (4.20).

4.8 End Wall Effects on Fractal Model

As the wrinkled flame front approaches the combustion chamber walls the rate of heat release reduces. One explanation for this is that as the leading edges of the wrinkled flame reach the cylinder wall the surface area of the flame front reduces, this concept is shown schematically below in Figure 4-14, on the left is the wrinkled flame front before any part reaches the cylinder wall and on the right the leading edges of the wrinkled flame front have reached the cylinder wall.

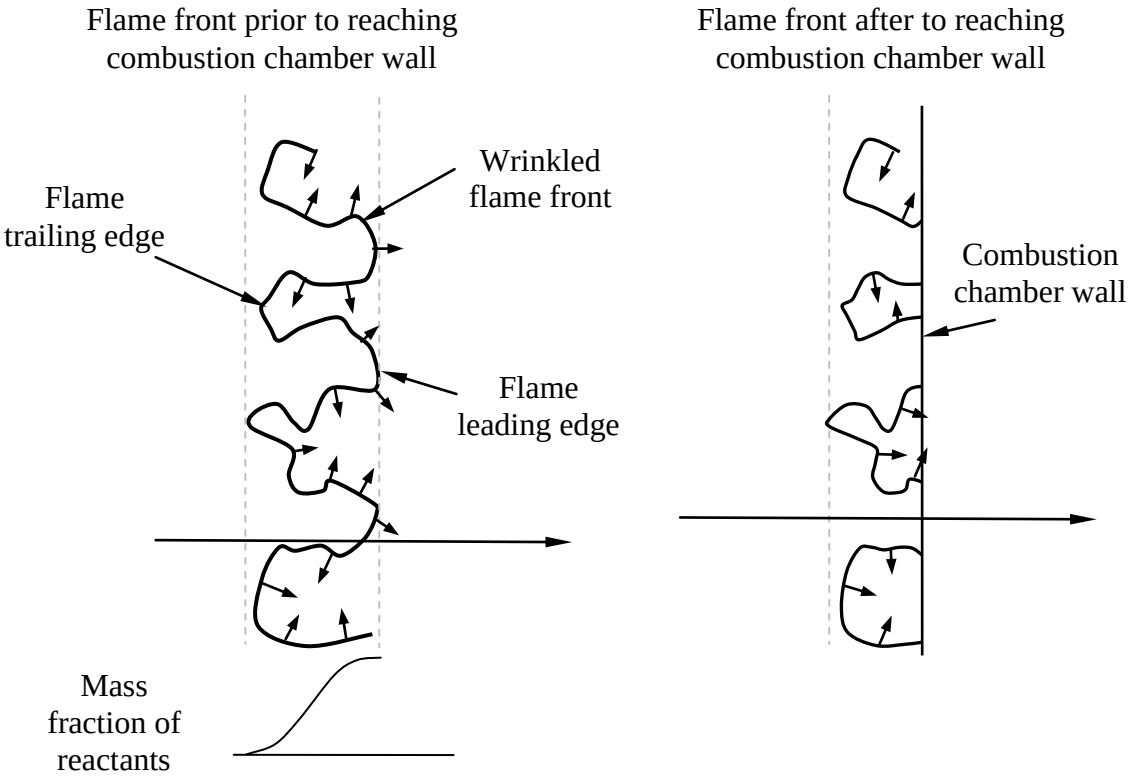

Figure 4-14, Flame front before and after reaching combustion chamber wall

Another mechanism for the reduction in heat release is that as the flame front approaches the wall heat is lost from the flame front to the wall which leads to quenching and flame extinction. In Figure 4-14, when the last of the trailing edges reaches the cylinder wall all the reactants will have been consumed.

The interaction between the propagating flame front and the cylinder wall was accounted for in a fractal combustion model by Bozza et al. (2005). The leading edge of the flame radius is defined by the radius of the spherical flame front plus half of the maximum scale of wrinkling. The maximum wrinkling scale in the fractal model is the integral length scale, then the leading edge of the wrinkled flame front will reach cylinder wall when,

$$r + \frac{l}{2} \geq B/2 \tag{4.43}$$

After the above condition is satisfied the mass burn rate is calculated based on a weighted fraction of the fractal model and an exponential decay. This approach maybe applicable to a cylindrical flame which expands radially from the cylinder axis, but not so in the case of a spherical flame which is likely to contact the piston crown before it reaches the cylinder wall.

The quasi-dimensional flame geometry model, discussed in the next section, accounts for the interaction between the spherical flame front and combustion chamber, including piston crown, cylinder bore and cylinder head. To account for the quench effects an exponential decay is defined after the mass fraction burned, x_b, exceeds 0.8,the exponential wall function is,

$$w = e^{-a(x_b-0.8)^b} \tag{4.44}$$

Where a and b are constants set at -0.25 and 3.

4.9 Flame Front Geometry

The quasi-dimensional model developed in this study assumes an infinitely thin semi-spherical flame front that is initiated at the spark plug location which is on the centre line axis of the cylinder. The centre location the spherical flame moves from the spark plug location due to the in-cylinder tumble motion, as described in Chapter 3. The flame front divides the combustion chamber into two zones burned and unburned. The volume of the two zones and also the spherical flame surface area are dependent on the bore dimension, cylinder head geometry, piston position, spherical flame radius and flame offset. During an engine simulation the combustion model will use look up tables to define the spherical flame front geometry including burned volume and flame surface area. The look up tables have been generated using a Computer Aided Design (CAD) parametric model which includes variables for the flame radius, piston position and flame offset. A similar method using CAD geometry was also used to define spherical flame front geometry by Bozza and Gimmeli (2004) and also by Catania et al. (2003). Tables for both surface area and burned

volume have been generated. The tables use piston position and flame radius as variables to define the surface area and burned volume, a number of similar tables have been generated but at different flame offset locations. The combustion model calculates a burned mass, temperature and pressure from which a burned volume can be defined. With a known volume a search and interpolation procedure is then used with the look up tables to determine the spherical flame radius from the burned volume, piston position and flame offset values.

The look up tables, described above, define volumes and areas based on a spherical flame front. The usual approach in quasi-dimensional models, Poulos and Heywood (1983), Reid (1993) and Bozza et al. (2005), is to use the infinitely thin spherical flame front area with a turbulent to laminar factor to calculate the heat release rate. In this study the heat release rate is calculated for an average engine cycle in which a wrinkled flame brush thickness has been determined. The interaction between a flame brush and the combustion chamber will be different from the interaction between an infinitely thin spherical flame and combustion chamber. This is particularly important when considering the squish combustion chamber. Figure 4-15 below shows the flame front arriving at the squish area of the combustion chamber when the piston is near TDC, the flame front is spherical and centred at the spark plug location. The flame front area reduces as the flame approaches the squish area which will result in a reduction in heat release rate at that point.

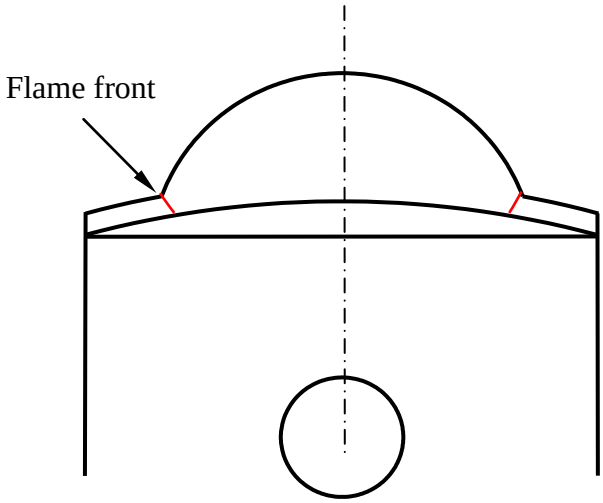

Figure 4-15, Flame front arrival at the squish radius

The turbulent combustion model developed in this work assumes the flame front is a highly convoluted wrinkled surface and the wrinkled surface area is evaluated from the infinitely thin spherical flame and the fractal model. The concept of the wrinkled flame brush thickness based on an averaged engine cycle was discussed in Section 4.4, where the brush thickness was defined as the fractal outer cut off. The infinitely thin spherical surface and the wrinkled brush thickness produce a volume which may be considered as the volume zone which bounds the convoluted flame front. The concept of a wrinkled brush zone is shown below in Figure 4-16, where the volume is calculated based on the spherical area and brush thickness. Figure 4-16 shows that the brush zone does not fill the available space in the combustion chamber and as a result the heat release from the zone will under predict the heat release for an averaged engine cycle.

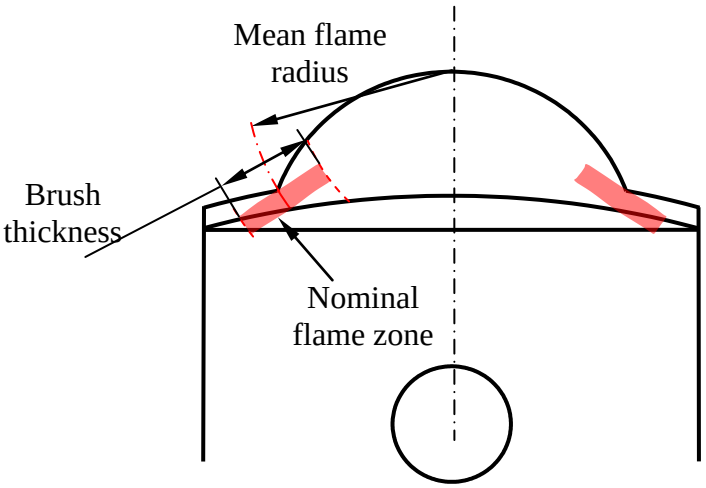

Figure 4-16, Wrinkled brush zone based on spherical area and brush thickness

The wrinkled brush zone may be calculated from the volume look up tables. Once the spherical flame radius has been calculated from the burned volume, maximum and minimum flame radii representing the outer and inner radii of the wrinkled brush zone may be calculated. The volume look up tables are used to establish volumes for the maximum and minimum radii and then a brush volume defined by the difference, Figure 4-17 below shows the brush volume calculated using the volume tables. The figure shows a flame centred at the spark plug but the same procedure is used for the offset flame.

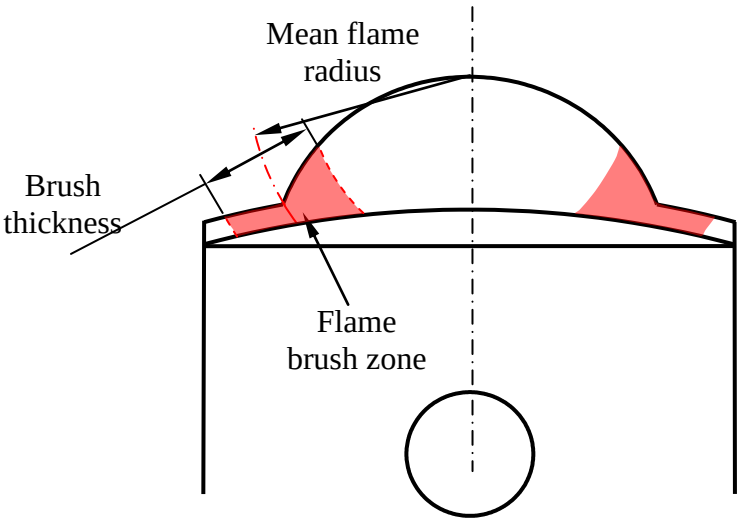

Figure 4-17, Wrinkled brush zone based on volumes

To account for the difference in the volumes shown in Figure 4-16 and Figure 4-17 a volume ratio is applied to the fractal model, Equation (4.19), when calculating the mass burn rate, hence

$$\dot{m}_b = \left[\frac{V_w}{A_f L_{max}}\right] \rho_u S_L A_f \left(\frac{L_{max}}{L_{min}}\right)^{D-2} w \tag{4.45}$$

Where V_w is the wrinkled brush zone volume shown in Figure 4-17 and w is the exponential wall function given by Equation (4.44).

5 Thermodynamic Model

In Chapter 2 the basic operation of a two stroke engine was described, one engine cycle is complete in 360° crankshaft rotation. At the start of the engine cycle, during the scavenge period, a mass of fresh charge enters the cylinder. During the compression stroke the fresh charge is compressed and then near TDC ignited by a spark discharge. The fresh charge is burned, energy released and expansion work done on the piston. During each part of the cycle the thermodynamic state of the cylinder must be calculated.

The thermodynamic properties of the cylinder contents are calculated as a single zone or two zones depending on which point in the engine cycle the calculation is being made. During the open cycle, or scavenge period, the cylinder is considered as a single control volume. During the compression process the cylinder is considered as a single closed system. After the ignition delay period, discussed in Section 4.6, a 2 mm radius semi-spherical flame kernel is formed and the cylinder volume is then divided into two zones, burned and unburned. During the combustion process the properties of the burned and unburned gas are calculated based on two separate zones of equal pressure. After the completion of the combustion process and prior to the exhaust port opening the cylinder is again treated as a single closed system.

5.1.1 Open Cycle

During the open cycle fresh charge enters the cylinder through the transfer ports and a mixture of burned gas and fresh charge will exit the cylinder through the exhaust port. The composition of the gas exiting through the exhaust port is determined by the scavenging model which is discussed in Section 6.6. During an engine simulation the 360° engine cycle is divided into a number of small steps of approximately 0.5°. During a small step in the open cycle the cylinder is considered as a control volume undergoing a non-steady flow process. The energy balance for the non-steady flow process may be written as,

$$\delta Q_{ht} + m_{in}\left(h_{in} + \frac{u_{in}^2}{2}\right) - \delta W - m_{out}\left(h_{out} + \frac{u_{out}^2}{2}\right) = \delta E \tag{5.1}$$

Where Q_{ht} is the heat transfer between the cylinder contents and the cylinder wall, W is the work done and δE is the change in internal energy of the cylinder contents which may be also defined as,

$$\delta E = m_{\theta+1} c_{v\theta+1} T_{\theta+1} - m_{\theta} c_{v\theta} T_{\theta} \tag{5.2}$$

The work done which may be defined assuming a mean pressure from the start and end of the step,

$$\delta W = \frac{(P_{\theta} + P_{\theta+1})}{2} dV \tag{5.3}$$

Combining the above equations and rearranging,

$$\begin{aligned} m_{\theta+1} c_{v\theta+1} T_{\theta+1} & \\ &= \delta Q_{ht} + m_{in}\left(h_{in} + \frac{u_{in}^2}{2}\right) - \frac{(P_{\theta} + P_{\theta+1})}{2} dV \\ &- m_{out}\left(h_{out} + \frac{u_{out}^2}{2}\right) + m_{\theta} c_{v\theta} T_{\theta} \end{aligned} \tag{5.4}$$

The state equation can be written assuming the gas constant R does not change during the small time step,

$$P_{\theta+1} = \frac{m_{\theta+1} R T_{\theta+1}}{V_{\theta+1}} \tag{5.5}$$

Incorporating the state equation into Equation (5.4) and rearranging,

$$\begin{aligned} m_{\theta+1} c_{v,\theta+1} T_{\theta+1} + \frac{m_{\theta+1} R_{\theta+1} T_{\theta+1}}{2V_{\theta+1}} dV & \\ = \delta Q_{ht} + dh_{in} - dh_{out} + m_{\theta} c_{v,\theta} T_{\theta} - \left(\frac{P_{\theta}}{2}\right) dV & \end{aligned} \tag{5.6}$$

Rearranging

$$T_{\theta+1}\left[m_{\theta+1}c_{v,\theta+1}+\frac{m_{\theta+1}R_{\theta+1}}{2V_{\theta+1}}dV\right] = \delta Q_{ht}+dh_{in}-dh_{out}+m_{\theta}c_{v,\theta}T_{\theta}-\left(\frac{P_{\theta}}{2}\right)dV \tag{5.7}$$

Then

$$T_{\theta+1}=\frac{\delta Q_{ht}+dh_{in}-dh_{out}+m_{\theta}c_{v,\theta}T_{\theta}-\left(\frac{P_{\theta}}{2}\right)dV}{\left[m_{\theta+1}c_{v,\theta+1}+\frac{m_{\theta+1}R_{\theta+1}}{2V_{\theta+1}}dV\right]} \tag{5.8}$$

The cylinder pressure at the end of the time step is then calculated from the state equation,

$$P_{\theta+1}=\frac{m_{\theta+1}R_{\theta+1}T_{\theta+1}}{V_{\theta+1}} \tag{5.9}$$

5.1.2 Closed Cycle Single Zone

After the exhaust port has closed the compression process begins, prior to the combustion process beginning, the cylinder is considered as a single zone of a closed thermodynamic system. During this period the first law of thermodynamics is used to define the change in pressure in the cylinder. The first law in this situation may be written as

$$\delta Q_{ht}=\delta E+\delta W \tag{5.10}$$

It is assumed that the mass of fuel in the cylinder is vaporized during the compression stroke prior to ignition and that the loss of heat from the cylinder contents due to the latent heat of vaporization is defined by,

$$\delta Q_{vap}=\frac{m_f}{\theta_{ign}-\theta_{exh}}h_{fg}.d\theta \tag{5.11}$$

Where m_f is the mass of fuel in the cylinder, θ_{exh} is the exhaust port closure time in degrees, θ_{ign} is the ignition time in degrees and h_{fg} is the latent heat of vaporization. The enthalpy of vaporization of gasoline is taken from Ferguson and Kirkpatrick (2001) with a value of 38.5 kJ/mole or 380.5 kJ/kg.

The first law for the compression process can defined as,

$$\delta Q_{ht} + \delta Q_{vap} = mc_v(T_{\theta+1} - T_\theta) + \frac{(P_{\theta+1} + P_\theta)}{2} dV \tag{5.12}$$

Using the state equation in the form

$$\frac{P_{\theta+1}V_{\theta+1}}{R} = m_{\theta+1}T_{\theta+1} \tag{5.13}$$

then

$$\delta Q_{ht} + \delta Q_{vap} = \frac{P_{\theta+1}V_{\theta+1}c_v}{R} - \frac{P_\theta V_\theta c_v}{R} + \frac{(P_{\theta+1} + P_\theta)}{2} dV \tag{5.14}$$

Using the relationship between the gas constant and specific heats,

$$\gamma = \frac{c_p}{c_v} \tag{5.15}$$

$$c_p - c_v = R \tag{5.16}$$

$$\frac{c_v}{R} = \frac{1}{\gamma - 1} \tag{5.17}$$

Using Equation (5.17) in Equation (5.14) and rearranging,

$$\delta Q_{ht} + \delta Q_{vap} + \frac{P_\theta V_\theta}{\gamma - 1} - \frac{P_\theta}{2} dV = \frac{P_{\theta+1} V_{\theta+1}}{\gamma - 1} - \frac{P_{\theta+1}}{2} dV \tag{5.18}$$

And finally

$$P_{\theta+1} = \left[\delta Q_{ht} + \delta Q_{vap} + P_\theta \left(\frac{V_\theta}{\gamma - 1} - \frac{dV}{2}\right)\right]\left[\frac{V_{\theta+1}}{\gamma - 1} - \frac{dV}{2}\right]^{-1} \tag{5.19}$$

The temperature of the cylinder contents is then determined from the state equation.

5.1.3 Flame Kernel Formation

After an ignition delay period a flame kernel is formed which is a half a sphere of 2 mm radius centred at the spark plug. At the time the kernel is formed it is assumed that the small burned volume has the adiabatic flame temperature for the air fuel mixture calculated at constant pressure. The adiabatic temperature is calculated based on the assumption that the enthalpy of the reactants is equal to the enthalpy of the products. The enthalpy of either the reactants or products is calculated from the sum of the enthalpies of the individual species that make up the reactants or products (Turns 2000), hence,

$$\sum\nolimits_R N_i \bar{h}_i = \sum\nolimits_P N_i \, \bar{h}_i \tag{5.20}$$

Where i indicates the species and the enthalpy of the individual species is given by,

$$\bar{h}_i = \bar{h}_{fi}^0 + \int_{298}^{T} \bar{c}_{pi} dt \tag{5.21}$$

The overbar in Equation (5.21) indicates molar based properties.

Where $\bar{h}_{fi}^{0}$ is the enthalpy of formation of species i at reference conditions of 298K and 101325 N/m^2, values for the enthalpy of formation are provided by Turns (2000). The specific heat for the individual species, $\bar{c}_{pi}$, are temperature dependent and taken from polynomial curve fits provided by Turns (2000) .

For a hydrocarbon fuel an atom balance may be used with the equivalence ratio to determine the amounts of CO_2, CO, H_2O, O_2 and N_2 in the exhaust gas. At high temperatures, however, dissociation produces a number of other species. To account for some of the species produced by dissociation a chemical equilibrium model is used, the model is taken from Ferguson and Kirkpatrick (2001) and is based on the work of Olikara and Borman (1975), details of the chemical equilibrium model are given in Appendix B. Ten species are considered in the chemical equilibrium calculation which are CO_2, H_2O, N_2, O_2, CO, H_2, H, O, OH and NO, these are considered to be the most important species for equivalence ratios less than three.

The enthalpy of products may be written,

$$H_{prod} = Ntot_P \sum\nolimits_P \chi_i \bar{h}_{fi}^{0} + Ntot_P \sum\nolimits_P \chi_i c_{pi}(T_{ad} - 298) \tag{5.22}$$

Where $Ntot_P$ is the total number of moles of exhaust gas per mole of fuel and χ_i is the molar fraction for product species i. T_{ad} is the adiabatic temperature and the value of the specific heat is taken at mean temperature between the reference temperature of 298K and product adiabatic temperature.

The enthalpy of the reactants which includes the enthalpy of the fuel, enthalpy of the air and also the enthalpy of the trapped exhaust gas residual, is given by

$$H_{reac} = H_{fuel} + H_{air} + H_{exh} \tag{5.23}$$

Assuming air is made up of just 21% oxygen and 79% nitrogen then for air,

$$H_{air} = N_{air}\left[0.21\bar{h}^0_{fO2} + 0.21c_{pO2}\left(T_{ign} - 298\right) + 0.79\bar{h}^0_{fN2} + 0.79c_{pN2}\left(T_{ign} - 298\right)\right] \quad (5.24)$$

Where T_{ign} is the temperature of the cylinder contents at the spark timing. For the trapped exhaust residual,

$$H_{exh} = N_{exh}\sum \chi_i \bar{h}^0_{fi} + N_{exh}\sum \chi_i c_{pi}(T_i - 298) \quad (5.25)$$

Where N_{exh} is the number of moles of trapped exhaust residual.

Once the enthalpy of reactants is known and equating the enthalpy of reactants with the enthalpy of products then Equation (5.22) can be rearranged for the adiabatic temperature,

$$T_{ad} = \frac{H_{reac}}{Ntot_P \sum_P \chi_i c_{pi}} - \frac{\sum_P \chi_i \bar{h}^0_{fi}}{Ntot_P \sum_P \chi_i c_{pi}} + 298 \quad (5.26)$$

The volume of the burned zone is then found from the state equation.

5.1.4 Closed Cycle Two Zone

After a burned zone has formed the cylinder is treated as having two thermodynamic zones burned and unburned. The following assumptions are used for the two zone model,

- Constant pressure throughout the cylinder
- No heat transfer between the zones
- Zones are separated by an infinitely thin flame front
- Ideal gas laws apply
- No account is made for piston ring blow by
- Both unburned and burned zones have uniform temperature

The thermodynamic model developed Verhelst and Sheppard (2009) is used in this study, the model has three differential equations which are used to solve for the unburned zone temperature, the burned zone temperature and the common pressure, the equations are shown below and a derivation of the equations can be found in Appendix A. The equations are solved iteratively for T_b, T_u and P using a Newton Raphson technique.

$$\frac{dT_u}{dt} = \frac{1}{m_u c_{pu}}\left[\frac{dQ_u}{dt} + V_u \frac{dP}{dt}\right] \tag{5.27}$$

$$\frac{dT_b}{dt} = \frac{P}{m_b R_b}\left\{\frac{dV}{dt} - \left[\frac{R_b T_b}{P} - \frac{R_u T_u}{P}\right]\frac{dm_x}{dt} - \frac{m_u R_u}{P}\frac{dT_u}{dt} + \frac{dP}{dt}\left[\frac{V_u}{P} - \frac{V_b}{P}\right]\right\} \tag{5.28}$$

$$\begin{aligned}\frac{dP}{dt} = \left[\frac{c_{vu}}{c_{pu}}V_u - \frac{c_{vb}P}{R_b}\frac{R_u}{Pc_{pu}}V_u + \frac{c_{vb}P}{R_b}\frac{V}{P}\right]^{-1} \\ \times\left\{\frac{dQ}{dt} - P\frac{dV}{dt}\left[1 + \frac{c_{vb}}{R_b}\right]\right. \\ + \frac{dm_x}{dt}\left[\frac{c_{vb}P}{R_b}\left(\frac{R_b T_b}{P} - \frac{R_u T_u}{P}\right) - (e_b - e_u)\right] \\ \left. - \frac{dQ_u}{dt}\left[\frac{c_{vu}}{c_{pu}} - \frac{c_{vb}}{R_b}\frac{R_u}{c_{pu}}\right]\right\}\end{aligned} \tag{5.29}$$

In Equation (5.29) $\frac{dQ}{dt}$ represents the sum of the rate of heat supplied by combustion, the rate of heat transfer by convection from the unburned zone and the rate of heat transfer by convection from the burned zone, hence,

$$\frac{dQ}{dt} = \frac{dQ_R}{dt} + \frac{dQ_u}{dt} + \frac{dQ_b}{dt} \tag{5.30}$$

The internal energy is represented by e for either the burned or unburned zones and m_x is the mass fraction burned. The specific heats and the gas constant c_v, c_p and R need to be determined for both the burned and unburned zones. The burned zone composition will

depend on the chemical composition of the fuel and the equivalence ratio. The specific heats for the burned gas is determined by the sum of the fractions of the ten species determined from chemical equilibrium. During the combustion process the chemical equilibrium is calculated at the burned gas temperature. Specific heats for each component of the exhaust gas,

$$c_{vb} = \chi_i c_{vi} \tag{5.31}$$

$$c_{pb} = \chi_i c_{pi} \tag{5.32}$$

The composition of the gas in the unburned zone should be mostly air however there is likely to be some amount of residual exhaust gas from the previous cycle. The composition of the trapped exhaust gas is taken from the end of the combustion process from the previous cycle where chemical equilibrium is considered to be frozen when the exhaust port opens. The specific heats are then calculated as a mixture of air and exhaust gas defined as,

$$c_{vu} = \Pi c_{vair} + (1 - \Pi) c_{vb} \tag{5.33}$$

$$c_{pu} = \Pi c_{pair} + (1 - \Pi) c_{pb} \tag{5.34}$$

Where Π is the unburned mixture purity.

5.1.5 Heat Release Rate

The heat release during the combustion period is calculated from the lower heating value of the fuel and the predicted mass of fuel burned in a time step.

$$Q_{R0} = m_{fuel} LHV \tag{5.35}$$

Where m_{fuel} is the mass of fuel burned in a time step, LHV is the lower heating value. The lower heating value for gasoline is taken from Ferguson and Kirkpatrick (2001) with a value

of 44.51 MJ/kg which is estimated for a typical fuel. The chemical composition of the fuel was given as C_7H_{17} and the molecular weight as 101.21 kg/kmol.

The reference heat release value Q_{R0} represents the chemical energy of the mass of fuel burned, this would be the energy released if all the carbon in the fuel were oxidised to form CO_2 and all the hydrogen oxidised to form H_2O. However due to the effects of dissociation at high temperature other species are formed, also in the case of rich mixtures there will be insufficient oxygen available to oxidise the fuel completely. As well as dissociation and the air fuel ratio affecting the heat release during combustion the trapped exhaust gas residuals will also tend to reduce the amount of heat release for a given amount of fuel. To account for the air/fuel ratio and the trapped exhaust residuals two combustion efficiencies have been taken from Blair (1996) to calculate the heat release in the cylinder. For the air/fuel ratio a combustion efficiency is given as,

$$\eta_{afr} = -1.6082 + 4.6509\left(1/\phi\right) - 2.0746\left(1/\phi\right)^2 \tag{5.36}$$

For the trapped exhaust gas residuals, or scavenging efficiency, a combustion efficiency is given as,

$$\eta_{SE} = -12.558 + 70.108SE - 135.67SE^2 + 114.77SE^3 - 35.542SE^4 \tag{5.37}$$

For scavenging efficiencies greater than 0.9 η_{SE} is taken as 1.0 and for scavenging efficiencies below 0.51 η_{SE} is taken as 0.73.

The heat release due to combustion taking into account both air/fuel ratio and trapped exhaust residuals, Q_R, which is required for the two zone thermodynamic model is the given by,

$$Q_R = Q_{R0}.\eta_{afr}.\eta_{SE} \tag{5.38}$$

5.2 Heat Transfer

Heat transfer from the cylinder contents to the cylinder wall will occur due to forced convection and radiation. For a gasoline engine the heat transfer due to convection is the predominant mechanism and that due to radiation is neglected for simplicity. The rate of heat transfer due to convection will depend on the temperature difference between the gas and cylinder wall, the area of the cylinder wall and a heat transfer coefficient on the cylinder walls. The heat transfer coefficient for forced convection will depend on the fluid motion in the cylinder, however as the details of the 3D flow field are not solved in the quasi-dimensional model an empirically derived method is used to define the heat transfer coefficient. A Nusselt number correlation, taken from Annand (1963), will be used in this study to determine the heat transfer from the cylinder contents to the cylinder wall, the Nusselt number correlation is defined as,

$$Nu = aRe^{0.7} \tag{5.39}$$

Blair recommends the same correlation be used for both closed and open cycles and that a value for a is taken to be 0.26 for a two stroke engine. The Reynolds number in the correlation is based on the mean piston speed, $\overline{u_p}$, and bore diameter, B,

$$Re = \frac{\rho \overline{u_p} B}{\mu} \tag{5.40}$$

The heat transfer coefficient is calculated by,

$$HTC = \frac{k_{th} Nu}{B} \tag{5.41}$$

Where k_{th} is the thermal conductivity of the gas in the cylinder, then the heat transfer during a small time step is the calculated from the following,

$$Q_{ht} = HTC(T - T_{wall})A_{wall}dt \tag{5.42}$$

Where T_{wall} is the temperature of the cylinder wall and is taken as the mean temperature of the cylinder head, bore and piston crown. A_{wall} is the total surface area of the combustion chamber wall including cylinder head, bore and piston crown.

During the open cycle and closed cycle up to the point that the flame kernel is formed the cylinder contents is considered to be at uniform temperature and pressure. During this period the heat transferred from the gas to the cylinder wall is then calculated based on a single gas temperature. After the flame kernel has formed there are two zones, burned and unburned, each with different gas temperatures and surface areas. In this period heat transfer is calculated for the two zones. A parametric CAD model was used to generate look up tables for the burned zone volume and spherical flame front area. Look up tables, however, were not generated for the combustion chamber wall surface areas, either burned or unburned zones. The total surface area of the combustion chamber is calculated based on cylinder head geometry, bore size and piston position. The fraction of the total surface area which is within the burned zone is then taken as a function of the mass fraction burned. Catania et al. (2003) developed a two zone combustion model which used CAD geometry to define the heat transfer wall areas and these were compared with areas calculated based on mass fraction burned and volume fraction burned. It was shown that the area calculated based on the mass fraction burned were closer to the areas based on the CAD geometry than the areas based on volume fraction burned. Areas used for the heat transfer calculation are then,

$$A_u = (1 - x_b)A_{wall} \tag{5.43}$$

$$A_b = (x_b)A_{wall} \tag{5.44}$$

6 Whole Engine Simulation

A whole engine simulation code has been written in visual basic to model a single cylinder two stroke engine. The whole engine model is made up of a number of sub routines which describe the various thermodynamic and fluid mechanic processes of the engine, these include the fractal combustion model described in Chapter 4 and the tumble and turbulence model described in Chapter 3. Other sub routines that are required for the whole engine model, which will be described only briefly in the following sections, include a zero dimensional scavenging model, a variable volume thermodynamic model for the crankcase and a fixed volume plenum. A one dimensional gas dynamic sub routine is used to calculate the pressure wave motion in the engine ducts and boundary conditions for the ends of each duct. Figure 6-1 below shows a schematic of the simulation model.

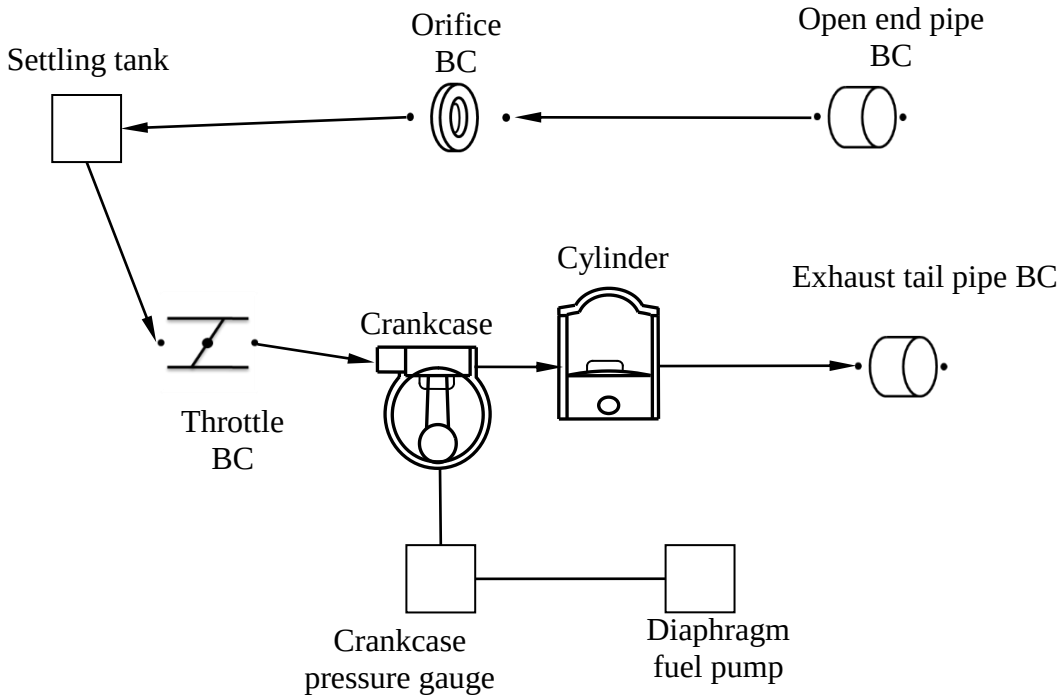

Figure 6-1, Schematic of the whole engine simulation model

The schematic of the whole engine model shown in Figure 6-1 represents the experimental set up for the engine used in this study. There are eight ducts in the model, the first duct is 250 mm long, 64 mm diameter and connects open atmosphere to an orifice flow meter. The second duct is 2500 mm long, 64 mm diameter and connects the orifice flow meter to large plenum. The orifice flow meter is modelled as a boundary condition to ducts 1 and 2. The settling tank shown is modelled as fixed volume plenum, the purpose of the settling tank is to remove the pressure wave oscillations generated by the engine inlet and produce a near steady flow through the orifice flow meter. Duct 3 is 660 mm long and 66 mm diameter and connects the settling tank to the engine carburettor. The throttle slide in the carburettor is modelled as a boundary condition. Duct 4 represents the engine inlet manifold, duct 5 the transfer ports and duct 6 is the exhaust. The exhaust system is designed with divergent and convergent sections to use pressure wave motion to improve the scavenging and trapping efficiency. Where duct 4 connects to the crankcase and where duct 5 and 6 connect to the cylinder there are cylinder port boundary conditions. Duct 7 represents a 170 mm long, 6 mm diameter pipe which connects the crankcase to a pressure sensor. The pressure sensor fits into a small manifold which is modelled as a small plenum. Duct 8 is a 100 mm long 6 mm diameter pipe that connects the pressure sensor to a diaphragm fuel pump.

6.1 Gas Dynamics

As already mentioned in the introduction two stroke engines often rely on pressure wave motion in the engines ducts to improve performance and for this reason it is important to include a gas dynamic routine for the ducts in the whole engine simulation. In this study a one dimensional gas dynamic routine is taken from Blair (1996), known as the GPB model. In the GPB model each of the engine ducts is divided into a number of finite length mesh spaces and the model predicts the pressure wave motion in both directions of the one dimensional duct. Changes in cross sectional area of the ducts produce partial reflections of compression or expansion waves, which depends on whether the duct is converging or diverging. The magnitude of the reflected pressure waves depends on the rate at which the duct converges or diverges and the magnitude of the incidence wave. The gas composition is accounted for in the ducts, this is particularly important for the exhaust duct which will

have a mixture of fresh charge and exhaust gas that varies significantly along the length of the duct. The gas composition in each of the ducts is considered to be air with mass fraction of exhaust gas, the mass fraction of exhaust is defines as purity, Π, where 0.3 purity defines mixture of 30% air and 70% exhaust gas. Heat transfer is also accounted for in the ducts using a Dittus Boelter correlation.

6.2 Simulation Time Step

The two stroke cycle is complete in one crankshaft revolution or 360° and the simulation engine cycle is sub divided into approximately 720 steps with each step being approximately 0.5° crankshaft angle. The actual time step size is defined by the velocity of the propagating pressure waves in each of the ducts and the length of mesh spaces. A criterion for the time step is set such that a pressure wave should not propagate the entire length of any mesh space, if a mesh space is length L and the propagating velocity of a pressure wave is α then the time for the pressure wave to propagate the mesh space is given by,

$$t_{cfl} = \frac{L}{\alpha} \tag{6.1}$$

During each step of the engine cycle the minimum t_{cfl} of all the mesh spaces is recorded and then at the beginning of next engine cycle the number steps is adjusted as,

$$Newsteps = steps.\frac{dt}{t_{cfl}} \tag{6.2}$$

6.3 Cycle Convergence

The simulation requires a number of cycles to converge to a steady state condition. Convergence is established by comparing cylinder mass flow for sequential cycles. A total of 40 cycles for each engine simulation has been used. The number of cycles required to reach convergence is largely dependent upon the gas dynamics of the exhaust system. The

volume of the exhaust duct is considerably larger than the engine cylinder and hence a number of cycles are required to fill the exhaust duct with hot gas.

6.4 Cylinder, Crankcase and Plenums

The cylinder and crankcase are modelled as plenums with volumes that vary with crankshaft angle. Mass of either fresh charge, exhaust or a mixture of both enter and leave the cylinder, crankcase or fixed volume plenums. The mass flows in and out are defined by the duct boundary conditions. The state conditions for the cylinder are calculated at each cycle step as discussed in Chapter 5, similarly the conditions in the crankcase and fixed volume plenums are calculated at each cycle step accounting for the mass flow in and out. At the start of each step the state conditions for the cylinder, crankcase and plenums are calculated based on changing volumes, mass flow in or out, heat transfer etc. At the end of a cycle the conditions in the cylinder, crankcase, plenums and ducts become the starting conditions for the next cycle.

6.5 Duct Boundary Conditions

For the gas dynamic sub routine boundary conditions are required at the ends of each duct. A number of different type boundary conditions are used which include open end pipes, orifice plates, throttles and cylinder ports. The boundary condition is required to define a flow area. Where the ducts connect to the cylinder or crankcase the cylinder port boundary condition is used. The ports that enter the cylinder are controlled by the piston crown whilst the port that enters the crankcase is controlled by the piston skirt. The cylinder port boundary condition determines the port height and area from defined engine geometry and crank angle position. The throttle boundary condition defines a geometric area based on throttle body size and throttle position, the throttle position remains fixed during the engine simulation. The orifice area is defined as a diameter and the pipe end boundary conditions have geometric area based on the duct diameter. Each of the boundary conditions defines a geometric area and also a discharge coefficient which accounts for a vena contracta formed

by a converging fluid flow. The discharge coefficient value is dependent on both the geometry and pressure ratio across the boundary condition and is stored in look up tables.

6.6 Scavenging

On the downward stroke of the piston, after the combustion process, the exhaust port will open and exhaust gas will exit the cylinder. Shortly after the exhaust port opens the transfer ports will open and fresh charge will enter the cylinder. During the open cycle period when both the exhaust and transfer ports are open a mixture of exhaust gas and fresh charge will exit through the exhaust port. The composition of the gas leaving through the exhaust port is defined by a scavenging model. In the whole engine simulation model used in this study the scavenging model described by Blair (1996) is used. There are a number of standard definitions used to describe engine performance parameters which includes Delivery Ratio, DR. The DR is defined by the mass of air supplied to the cylinder, m_{as}, divided by the mass of air at atmospheric conditions, $m_{cyl,air}$, that would fill the cylinder at BDC.

$$DR = \frac{m_{as}}{m_{cyl,air}} \tag{6.3}$$

The Scavenge Ratio, SR, is defined by the mass of air supplied to the cylinder divided by the mass of air that would fill the swept volume at atmospheric conditions, $m_{swept,air}$, the swept volume does not include the combustion chamber clearance volume.

$$SR = \frac{m_{as}}{m_{swept,air}} \tag{6.4}$$

The Scavenge Efficiency, SE, is the ratio of mass of fresh charge trapped in the cylinder, $m_{trapped,air}$, to the total cylinder trapped mass including exhaust gas residuals, $m_{trapped}$.

$$SE = \frac{m_{trapped,air}}{m_{trapped}} \tag{6.5}$$

The scavenge ratio and scavenge efficiency may also be defined on a volumetric basis then,

$$SR_V = \frac{V_{as}}{V_{swept}} \tag{6.6}$$

and

$$SE_V = \frac{V_{trapped,air}}{V_{cyl}} \tag{6.7}$$

The volumetric scavenging efficiency and scavenge ratio have been measured in tests and a second order polynomial curve fit has been defined to relate the two in the following form,

$$\ln(1 - SE_V) = \kappa_0 + \kappa_1 SR_V + \kappa_2 SR_V^2 \tag{6.8}$$

Or

$$SE_V = 1 - e^{\kappa_0 + \kappa_1 SR_V + \kappa_2 SR_V^2} \tag{6.9}$$

In Equations (6.8) and (6.9) κ_0 , κ_1 and κ_2 are polynomial curve fit coefficients which are determined experimentally. Values of the three constants have been determined for a Yamaha 250cc loop scavenge engine with values of κ_0 = 2.9204E-2, κ_1 = -1.0505 and κ_2= -0.34226, taken from Blair (1996).

The purity of the gas leaving the cylinder through the exhaust port is defined as

$$\Pi_{ex} = \Pi_{as} - \frac{dSE_V}{dSR_V} \tag{6.10}$$

Then using the differential of Equation (6.10)

$$\Pi_{ex} = \Pi_{as} - (\kappa_1 + 2\kappa_2 SR_V) e^{\kappa_0 + \kappa_1 SR_V + \kappa_2 SR_V^2} \tag{6.11}$$

Where Π defines the gas composition or purity.

6.7 Engine Geometry

The basic engine geometry is given in Table 7-1 and the engine described in Section 7.2.

An engine simulation is conducted for each of the experimental test points in Table 7-2, the table shows the engine speeds and throttle positions which are input parameters for the engine simulation. The whole engine simulation uses adjustable model constants for the tumble and turbulence models which include c_{sp} for the scavenging jet velocity, c_{sh} for the tumble vortex shear torque, c_{β} for turbulence production, c_{ε} for turbulence dissipation and c_h for the integral scale. The fractal combustion model uses coefficients for the wrinkled brush zone thickness, c_{Lmax}, coefficients for the fractal dimension D_L and D_T, and also a coefficient for the fraction of fractal islands, c_{RIFF}. A list of model constants and their values are given in Table 8-2.

7 Engine Experiments

Engine experiments have been conducted on a single cylinder two stroke engine to validate the tumble and turbulence model developed in Chapter 3 as well as the combustion model developed in Chapter 4. Ionization probes were used to monitor the progression of the flame front in the combustion chamber. Ionization probes were primarily chosen for cost reasons, the use of laser techniques with an optically accessible combustion chamber was beyond the budget of this project. Ionization probes have been proven to be effective at monitoring the flame progression in high speed engines by Pfeffer et al. (2002) and Kato et al. (2007). An existing engine was used in these experiments with cylinder heads modified to accommodate the ionization probes. The only other additional equipment required to monitor the flame front progress was a simple electronic circuit board and data logger.

7.1 Test Objectives

The main objects of the experiments of this study are

- To assess the spherical flame front assumption
- Measure the movement of the burned zone due to the in-cylinder tumble motion
- Measure the flame propagation speed
- To determine a wrinkled flame brush thickness, based on a mean cycle
- To measure the in-cylinder pressure in order to assess the two zone combustion model developed here

7.2 Test Set Up

7.2.1 Engine

The engine used in these tests is a single cylinder loop scavenged air cooled two stroke fitted to a motor scooter. Fuel and air mixture preparation is by a carburettor and the exhaust duct is designed to use pressure wave motion to improve scavenging and trapping efficiency. A capacitor discharge ignition system is used with fixed ignition timing. The normal operating speed range of the engine is between 7000 and 10,000 rpm and transmission is via a multi-

plate clutch and four speed gearbox. The basic dimensions of the engine and cylinder port timings are given in the Table 7-1 below.

The tests have been conducted with two different combustion chamber geometries, a squish chamber and a simple disc chamber. Each of the cylinder heads has been fitted with the same number of ionization probes to monitor the progress of the propagating flame front. The probes are positioned in the same locations for both cylinder heads for a comparative analysis of the combustion chambers. The compression ratio of each cylinder head is common and was checked by measuring the clearance volume of each cylinder head with a burette.

Table 7-1, Basic Engine Geometry Data

Bore	67
Stroke	58
Inlet timing	opens 101° BTDC, closes 101° ATDC
Exhaust timing	opens 85° ATDC, closes 85° BTDC
Transfer timing	opens 111° ATDC, closes 111° BTDC
Ignition timing	18.5° BTDC
Trapped compression ratio	7*

*Note: The compression is defined as the ratio of volume of the cylinder with the piston position at exhaust port closure to the volume of the cylinder at top dead centre. This is usually referred to as the trapped compression ratio.

An eddy current rolling road chassis dynamometer was used to control the engine at constant speed whilst at load. The back wheel of the scooter was positioned on the top of a single rotor of the dynamometer and tests conducted at a number of different engine speeds and throttle positions. The chassis dynamometer set up is shown below in Figure 7-1.

Figure 7-1, Chassis dynamometer set up

7.2.2 Cylinder Pressure Measurement

The cylinder pressure is measured with a Kistler 601A piezoelectric pressure transducer fitted to a water cooled adapter, type 6509, and fitted to the cylinder head with a 14 mm thread. Prior to the tests the pressure transducer was calibrated with a dead weight pressure tester. The cylinder pressure is referenced to the crankcase pressure which is measured with an Omega PX409 piezoresistive pressure transducer. To relate the cylinder pressure to crank angle position a 360 division Kubler miniature type 2400 rotary encoder is fitted to the ignition side of the crankshaft.

7.2.3 Air and Fuel Measurement

A large diameter flexible duct, 64 mm diameter, connects the carburettor to a large plenum with a volume of 0.24 m^3. A second flexible duct then connects the plenum to an orifice flow meter with a 42 mm diameter sharp edge orifice. The pressure drop across the orifice is measured with a Testo differential pressure digital manometer. The large plenum acts as a settling tank which removes the pressure oscillations present at the carburettor so that a steady flow can be measured at the orifice flow meter. Fuel flow is measured with a Pelton wheel flow meter fitted between the fuel tank and carburettor.

BP Ultimate gasoline is used which has a 98 RON octane rating. The fuel was mixed with lubricating oil a at ratio of 2.5% oil by volume.

7.2.4 Ionization Probe Design

In its basic operation when a DC voltage is applied to the electrodes of an ionization probe and if free ions or electrons are present in the gap between the electrodes a current will flow. The magnitude of the current will depend on the applied voltage, electrode surface area and density of the ions and electrons present in the vicinity of the electrodes. A brief discussion about ion concentrations in hydrocarbon flames was given by Tanaka et al. (2005) and Mehresh et al. (2005). Chemical ionization occurs in the reaction zone and C_3H_3, CHO and H_3O are thought to be the main positive ions. Thermal ionization may occur in the post flame zone which is thought to be due to NO ions although they have a lower ionization energy.

A brief discussion on the different approaches used to insert ionization probes into an engine combustion chamber was given in Chapter 2. The probes must be robust enough to operate in the combustion chamber of a two stroke engine operating at speeds up to 10,000 rpm. It is also a requirement that the size of the probes, inside the combustion chamber, is small enough that they do not influence either the tumble motion or turbulence in the cylinder. A further requirement is that the probes be easily replaced during tests without removing the cylinder head in the event that a probe should become fouled.

The size of the probe relative to the wrinkling scales of the flame front defines the spatial resolution of the probe. If the smallest scale of wrinkling is similar to the laminar flame thickness which is of the order of 0.9 mm, Clarke and Hargrave (2009), at atmospheric conditions and approximately 0.3 mm at 30 bar then the exposed electrode should be just smaller in order to capture all the wrinkling scales. There is, however, a limit on the size of the electrode for manufacturing reasons, as smaller size probes become more complicated to machine and assemble. Different researchers have used different size electrodes and materials for ionization probes, including 1.1 mm copper and 1.1 mm titanium wire used by Pfeffer et al. (2002), 1 mm diameter Inconel wire with a magnesia insulating layer used by

Kato et al. (2007), 0.81 mm (0.032 in) diameter nickel wire in ceramic tube were used by Blizard and Keck (1974) and 0.5 mm nickel wire by Tomita et al. (2000). The ionization probes used in the present study use a 0.7 mm diameter nickel wire for the electrode which is inserted in an alumina ceramic tube which in turn is fixed into a stainless steel body. The stainless steel probe body is threaded and the assembly is then screwed into the cylinder head, Figure 7-2 shows the probe assembly. OmegaBond 200 two part epoxy high temperature adhesive is used to fix the ceramic tube in the probe body and Silicoset 158 silicone sealant is used to seal the wire into the ceramic tube.

In these experiments it is not intended here to measure the small scale structure of the flame but rather the larger wrinkling scales of the order of the flame brush thickness. The width of the wrinkled flame brush is expected to be of the order of 10 mm and hence a probe diameter of 0.7 mm will be sufficient. Hu et al. (1992) estimated a flame brush thickness between 2 and 7 mm based on a single ion signal. One of the objectives of the engine experiments is to determine the wrinkled flame brush thickness based on an average cycle. The probes used here are required to measure the first flame arrival time at a number of locations in the combustion chamber and for a number of engine cycles and then determine the wrinkled flame brush thickness on statistical basis.

During early trials in this study with a cylinder head fitted with a number of different style ionization probes on an engine running at a fast idle and no load, signals were observed at some ionization probes whilst other probes did not produce a signal during the same cycle. It was found that increasing the immersion depth of the probe into the combustion chamber improved the reliability of the signal. The probes in this study have been designed such that the immersion depth may be adjusted from flush to 4 mm penetration. Meyer et al. (1993) also noted problems with signal strength using head gasket ionization probes with a supply voltage of 140 volts whilst running at idle condition. It was not possible to identify whether the flame had quenched, the engine misfired, if a flame had failed to propagate or if the ionization probe had just failed to produce a signal.

Nicholson and Witze (1993) experimented with different size ionization probes in a head gasket to improve the reliability of the signal and found that “bigger is always better”. However in this work it is considered that increasing the size of the probe would adversely

affect the spatial resolution of the probe and also increase the ability of the probe to influence the flow structure in the cylinder.

Figure 7-2 shows the ionization probe assembly, the anode of the probe is the 0.7 mm diameter nickel wire and the cathode in the ionization circuit is formed by the probe body and the cylinder head, which also acts as the earth in the circuit. SMA coaxial cables were used to connect the ionization probes to the circuit board and then BNC coaxial cables were used to connect the circuit board to the data logger.

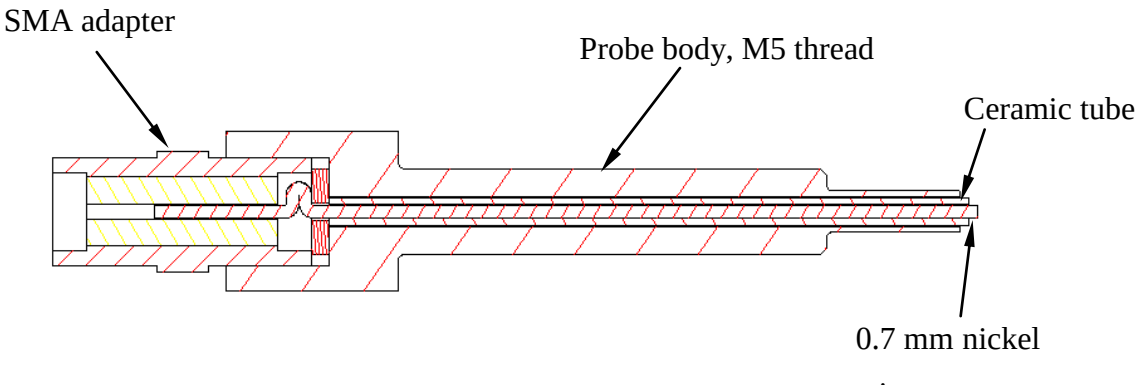

Figure 7-2, Ionization probe

7.2.5 Ionization Probe Location

The function of the ionization probe is to indicate the arrival of the flame front at a known location in the combustion chamber. By using a number probes spaced about the combustion chamber both the size and location of the flame front can be inferred.

The first objective of the engine experiments is to assess the spherical flame front assumption most commonly used in two zone combustion models. This is done by monitoring the flame front arrival at two circumferential rows of ionization probes in the combustion chamber. Figure 7-3 shows a schematic of the squish cylinder head, looking from the inside out, and the location of 14 ionization probes. The inner circumferential row of six probes are numbers 1, 7, 9, 4, 11 and 13, these are located at a radial distance of 10.4

mm from the axis of the cylinder and spaced every 60°. The outer circumferential row of probes 2, 8, 10, 5, 12 and 14 are at a radial distance of 21.5 mm.

To determine the movement of the burned zone and flame front due to the in-cylinder tumble motion, the second test objective, a row of six ionization probes have been located on the tumble plane. The tumble plane is equivalent to the symmetry plane of the transfer ports and passes through the centre of the exhaust port. The probes 1, 2 and 3 will monitor the flame front moving away from the exhaust port and 4, 5 and 6 will monitor the flame front moving towards the exhaust port.

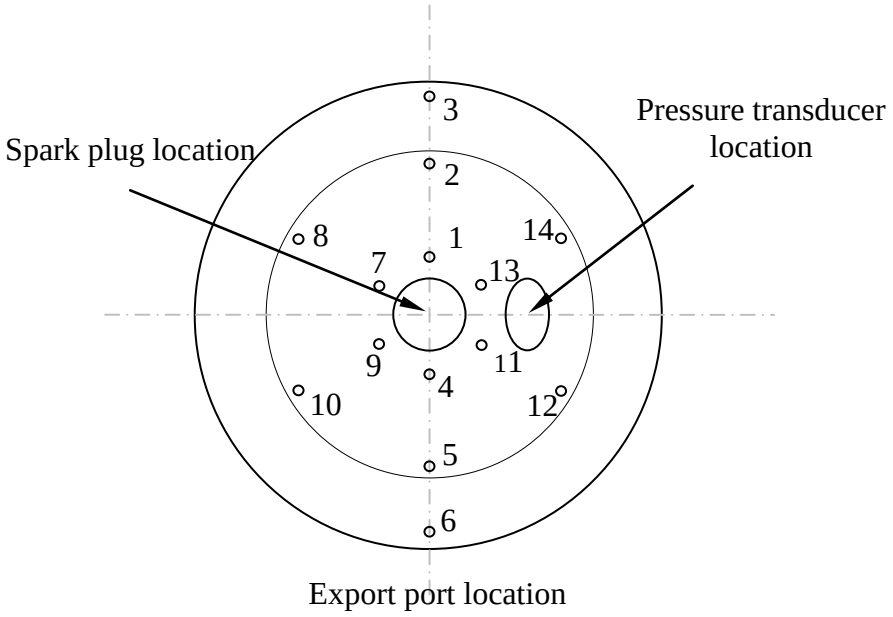

Figure 7-3, Ionization probe location and nomenclature

Figure 7-4 below shows a cross section through the tumble plane of the squish head and Figure 7-5 shows photographs of the inside and outside of the squish head with the 14 probes fitted. Figure 7-6 shows a cross section of the disc type head and Figure 7-7 shows photographs of the inside and outside the disc type head.

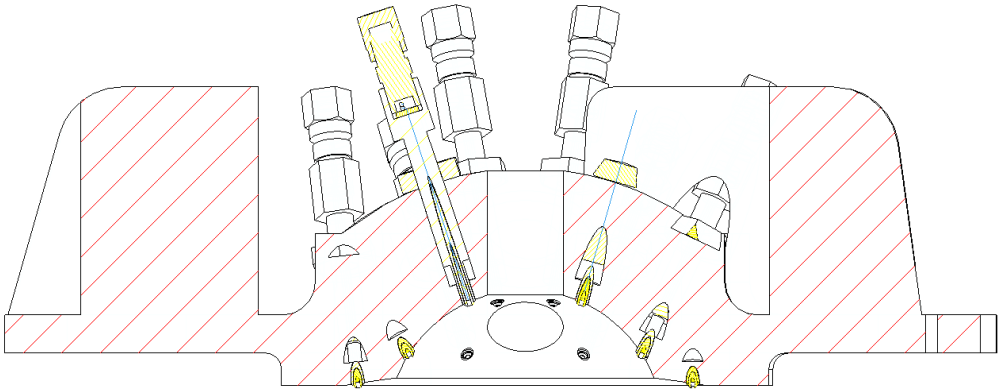

Figure 7-4, Cross section of instrumented squish head

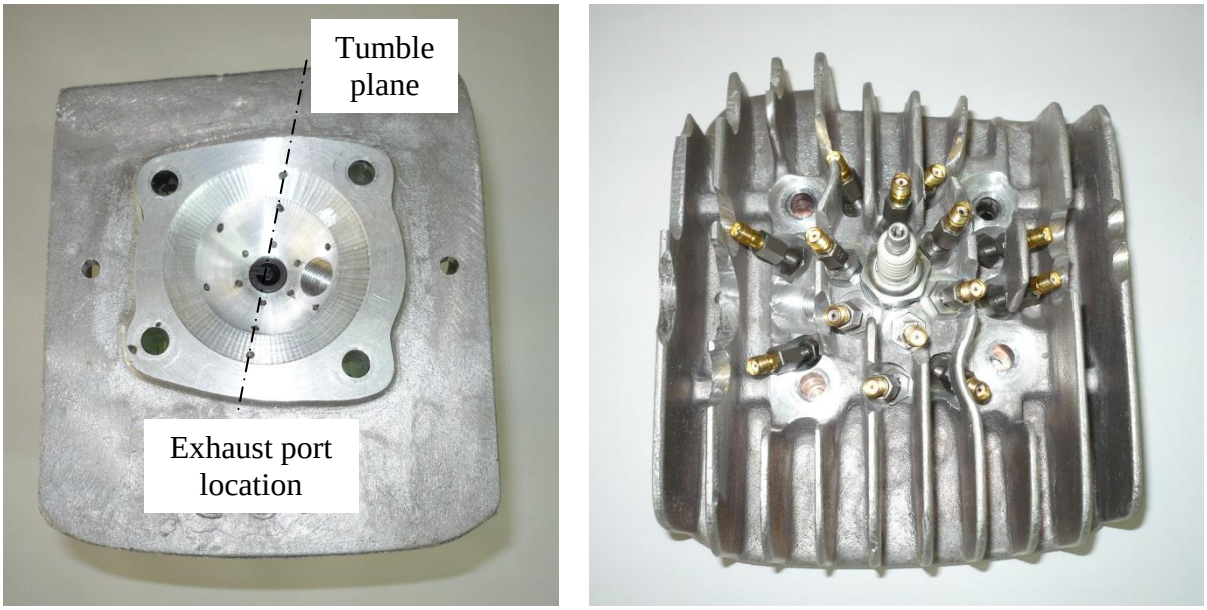

Figure 7-5, Instrumented squish head

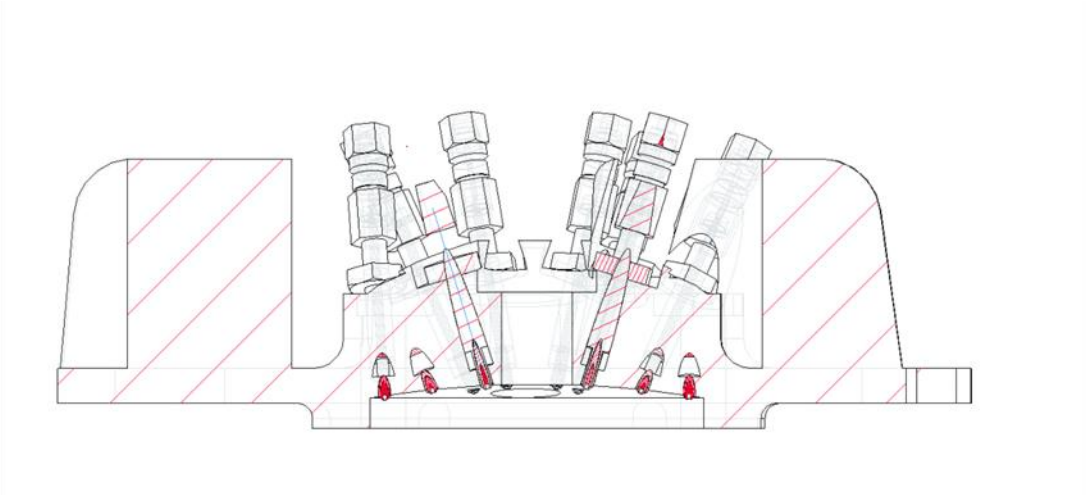

Figure 7-6, Cross section of instrumented disc head

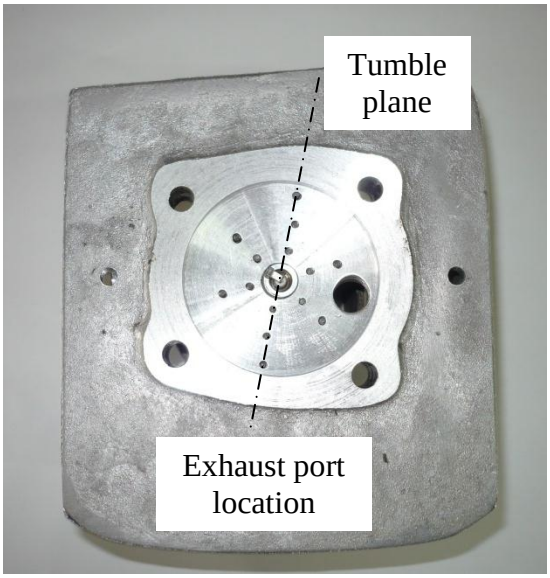

Figure 7-7, Instrumented disc head

7.2.6 Ionization Probe Circuit Board

An electronic circuit is required to supply a DC voltage to the ionization probes and condition the signal from the probes for data logging. The ionization circuit board used in this work is similar to that developed by Nicholson and Witze (1993) and also used by Pfeffer et al. (2002). The electronic circuit is shown below in Figure 7-8, it includes an operational amplifier with a potentiometer in the feedback loop which allows the output signal to be adjusted to suit the data logger. A positive voltage applied to the ionization probe will produce a negative voltage signal. The negative signal can be inverted by the use of an additional operational amplifier as the Nicholson and Witze circuit but was not deemed necessary here as the data logger can record +- 10 volts. Although not shown in Figure 7-8, the circuit board contains 14 identical circuits for each of the 14 probes. After initial trials the gain on the amplifier was set to three then during tests and the DC voltage supply to the probes was adjusted such that the maximum voltage of any of the probe signals remains below 10 volts.

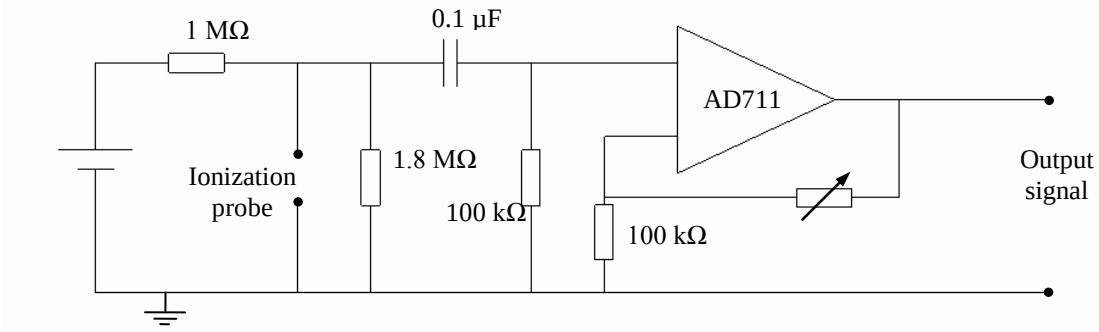

Figure 7-8, Ionization circuit board

7.2.7 Electrode Voltage

Different DC supply voltages for ionization probes have been used by different researchers, for example Nicholson and Witz (1993) used 150 volts, Witze (1989) 300 volts, Salvat et al. (1994) 200 volts, Tomita et al. (2000) 100 volts, Pfeffer et al. (2002) 150 – 170 volts and Vressner et al. (2004) 85 volts. A study of the ionization probe voltage supply and ion

current response was presented by Larsson et al. (2007) which showed that the signal response increases with a positive supply voltage up to around 250 volts after which the rate of increase reduces. They also mention that with increasing voltage there is an increase liability of fouling the probe with soot. The signal from the ionization probe will depend on the applied voltage as well as the ion and electron density in the vicinity of the electrode gap. Hu et al. (1993), noted that the ion sensor signal increases with engine load, using a 20 volt supply and a signal amplifier in the circuit board. Meyer et al. (1993) noted that at light load ion probes did not always pick up a signal. In the engine experiments of this study to ensure a measureable signal was recorded the supply voltage was increased at light loads. To ensure the signal did not exceed +-10 volts, the limit of the data logger, the DC supply voltage was reduced at higher loads. A number of pp3 batteries were connected in series to supply the DC voltage, this then gave an easy adjustment of the supply voltage by adding or removing batteries. Figure 7-9 below shows a graph of the supply voltages used during these tests.

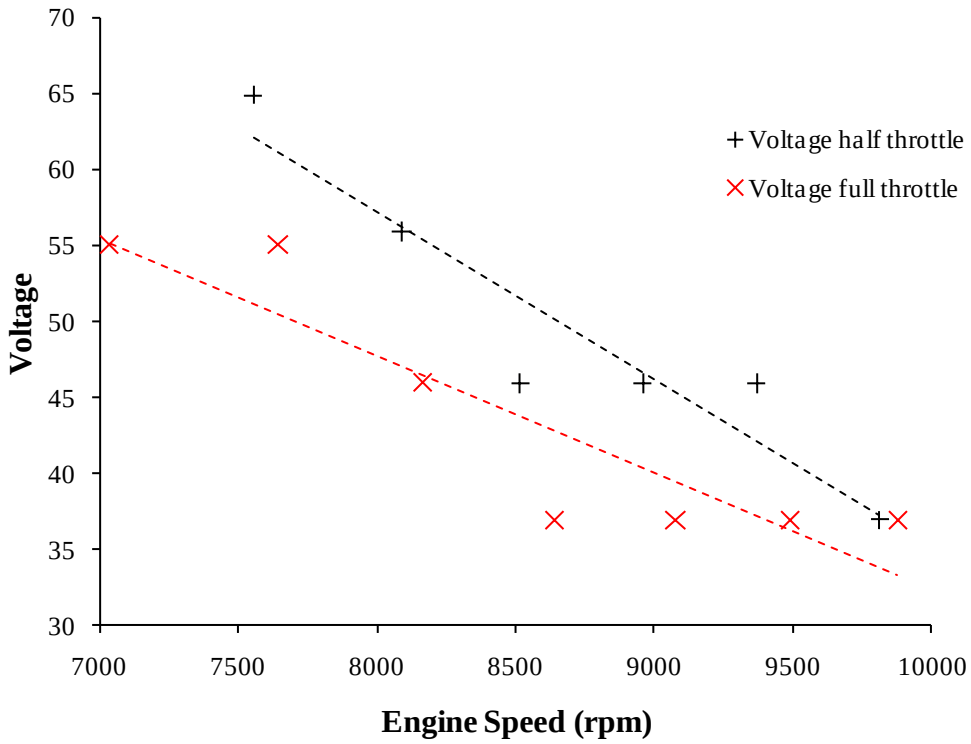

Figure 7-9, Ionization probe supply voltage

7.2.8 Data Acquisition

A PC based data logger, using an Omega DAQBoard 3000 series PCI board, has been used to record the signals from the 14 ionization probes, cylinder and crankcase pressure transducers. The DAQBoard has a total recording frequency of 1 MHz for 16 channels which gives a recording rate of 62.5 kHz for each probe. This equates to a recording rate of just less than every crank angle degree at 10,000rpm, for comparison Pfeffer et al. (2002) used a recording rate of 1° CA in their high speed engine tests. A second data logger was used to monitor fuel flow, throttle position, exhaust gas temperature and cylinder barrel temperature. The second data logger was a Race Technologies DL1 type, with a low frequency recording rate of 100 Hz.

7.3 Test Procedure

In all tests the eddy current dynamometer rotor was held at constant speed. An initial test was conducted in which the engine was motored at 4500 rpm and full throttle whilst cylinder pressure data was recorded. An engine simulation was carried out using a single zone thermodynamic model without combustion, from the simulation the crankshaft TDC position was established relative to the once per revolution signal on the rotary encoder. Engine tests for both squish and disc type cylinder heads were conducted at full and half throttle. During each test the engine was operated in third gear and the dynamometer roller held at constant speed between 80 and 110 kilometres an hour and incremented in steps of 5 kmh. The engine speed was increased between tests in a range between approximately 7000 and 10,000 rpm. Due to slip between the tyre and dynamometer roller, engine speeds varied by at most 3% between tests at the same fixed roller speed. However during any individual test the engine speed varied by no more than 0.6%. Table 7-2 gives a test matrix of wheel speed, engine speed and throttle position. The engine speeds used for data analysis have been calculated using the rotary encoder mounted on the crankshaft. During tests the engine was stopped after each speed increment and the signals from each of the ionization probes checked using Omega DaqView-XL software.

Although the ionization probes were assembled with high temperature adhesive and sealant their durability was poor. In early tests probes failed after approximately 15 minutes testing.

It was also noted that after short tests some of the probes became fouled and would then produce a noisy signal. For these reasons tests were kept short, each test taking approximately 20-30 seconds. By checking the probe signals between each test any probes producing noisy signals could be identified and replaced. The signals were also checked to ensure that they were below the 10 volt maximum limit of the data logger.

7.4 Results

During each test data from between 250 and 360 engine cycles were recorded. For consistent data processing only the first 200 cycles from each test have been analysed.

7.4.1 Air Fuel Ratio

Although an orifice flow meter was used in these tests the size of the orifice was not optimised. The size of the orifice, 42 mm diameter, was on the lower limit of the discharge coefficient table given in BS1042, Section 1.1. Also the pressure across the orifice plate was monitored with a digital manometer with a measuring range of 0 – 100 hPa and an accuracy of ± 0.1 hPa, whilst the pressure drop across the orifice was approximately 1-2 hPa. The combination of these two issues results in measured air mass flow rate into the engine that is believed to lower than the actual air flow rate. The low air mass flow measurements results in equivalence ratios greater than 1.6. For this reason air fuel ratios have been calculated using an air mass flow predicted by engine simulations and the measured fuel flow rate. The calculated air-fuel ratios are shown in Figure 8-4, Chapter 8.

7.4.2 In-Cylinder Pressure

The cylinder pressure is measured with a piezoelectric transducer and this is referenced to the crankcase pressure measured with a piezoresistive transducer. The pressures in the crankcase and cylinder are approximately equal towards the end of the scavenge period, around 30° after BDC. The mean pressure at the crankcase transducer, averaged over a cycle, varies between 0.92 to 1.12 bar for all tests. As the pressure transducer is connected

to the crankcase via a short length of pipe there will be a phase lag between the measured and actual crankcase pressure. As the difference between the mean pressure and the actual pressure in the crankcase towards the end of the scavenge period is small it is considered sufficiently accurate to reference the cylinder pressure to the mean crankcase pressure.

Table 7-2, Test matrix with calculated air-fuel ratio and engine speed

	Squish head		Disc head	
Wheel speed	Engine speed, full throttle	Engine speed, half throttle	Engine speed, full throttle	Engine speed, half throttle
85	7640	7555	7446	7433
90	8162	8069	7991	7938
95	8640	8517	8437	8359
100	9075	8981	8896	8808
105	9489	9369	9335	**
110	9878	9812	9718	9683

** Engine mis-firing during this test point

7.4.3 Signal Processing

Engine researchers have in the past attempted to use ionization probes to investigate flame structure, Ohigashi et al. (1971) conducted tests in a disc style combustion chamber in which turbulence was generated by an oscillating perforated disc. The flame front arrival at a particular point with the combustion chamber was monitored using an ionization probe, it was noticed that the current signal produced multiple peaks with increasing turbulence whilst in quiescent combustion chamber the ion current produced a single peak. The multiple peaks were assumed to be produced by a number of reaction zones in the flame brush. The width of the ion current signal was also related to the turbulence intensity.

An attempt to relate the signal from an ionization probe to curvature of a wrinkled flame front was made by Furukawa et al. (1993). In their work they presented the effects on the ionization signal produced by the wrinkled flame curvature radius, distance between the probe and the centre of curvature and the direction of motion of the wrinkled flame relative to the cylindrical probe. In all their signal predictions two distinct signal peaks were shown as the probe passes through just one flame convolution.

Turbulence intensities were measured in a pent roof four stroke engine using LDA methods and flame front location measured using ionization probes by Tomita et al. (2000). Some basic dimensions and nomenclature are given from which the flame front brush thickness and number of flamelets may be determined. They noted that as turbulence increased the number of peaks in ionization probe response increased, this might indicate a more convoluted flame front with increasing turbulence. They also defined a flame velocity based on the time between ignition and a signal arriving at a probe and by the distance between the spark plug and the probe. A characteristic flame thickness is then based on the calculated velocity and the time between the first flame ionization signal arriving at a probe and last signal peak.

In this study no attempt will be made to analyse ionization probe data to describe a flame structure during an individual engine cycle, rather the ion probe signals will be analysed by statistical means over a number of cycles.

7.4.4 Flame Arrival

Data from each test is stored as a text file and each file contains the signal data from all of the 14 ionization probes, two pressure transducers, rotary encoder signals and a time. A visual basic, data reduction, program has been developed to process the signals from the ionization probes and pressure transducers. The crank angle offset between the rotary encoder once per revolution signal and TDC position has been determined from the motored test. When the test data is imported into the data reduction program the stream of data is divided into engine cycles with the start of each cycle being BDC, the data may then be interrogated on an individual cycle basis. Figure 7-10 shows a typical ionization probe

signal, on the horizontal scale of the graph is crank angle degrees with 0° CA being BDC. A positive DC voltage applied to the probe centre electrode produces a negative voltage signal due to chemical ionization. The steep negative gradient at approximately 190° CA indicates the arrival of the chemical reaction zone at the probe. During tests, occasionally, a probe would produce a noisy signal and in most cases it was still possible to determine the arrival flame time, Figure 7-11 shows a typically noisy signal. In all cases the flame arrival time is defined by the intersection of two lines as shown in Figure 7-11. The first line drawn represents the flame arrival signal and is defined by two points. The data reduction program interrogates the ionization signal point by point from BDC identifying if the signal has a positive or negative gradient. If two successive points in the signal produce a negative gradient then the first point is identified as *point 1*, the interrogation continues until a positive gradient in the signal is identified at which point the previous signal point is identified as *point 2*. The difference in signal amplitude between *point 1* and *point 2* is identified as a *delta value*. The interrogation continues, as above, identifying negative and subsequent positive gradients, if two new points are identified and the *delta value* between them is greater than that previously identified the new points replace those previously identified. The process continues until the end of the engine cycle at which point the peak signal with a negative gradient would have been identified. The second line is generated by least mean squares of the signal data from BDC to *point 1* on the peak signal line. The point of flame arrival can then be calculated from the intersection of the two lines. The flame arrival times are calculated in terms of crank angle degrees and time in seconds. The flame arrival times for each engine cycle in the test are then stored in an array.

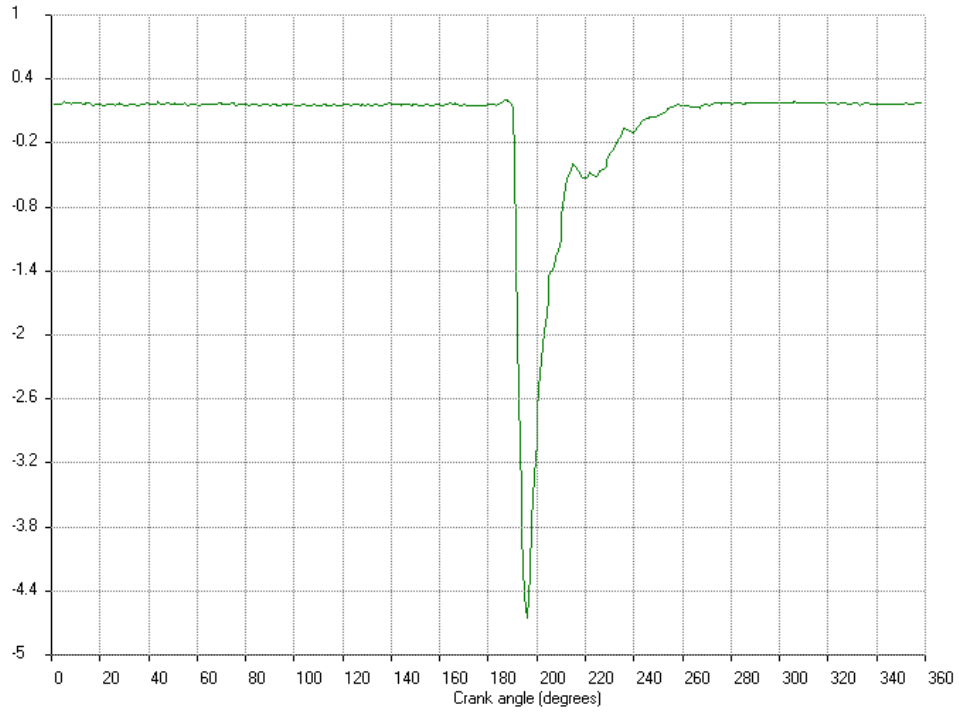

Figure 7-10, Ionization probe 4 signal at cycle one

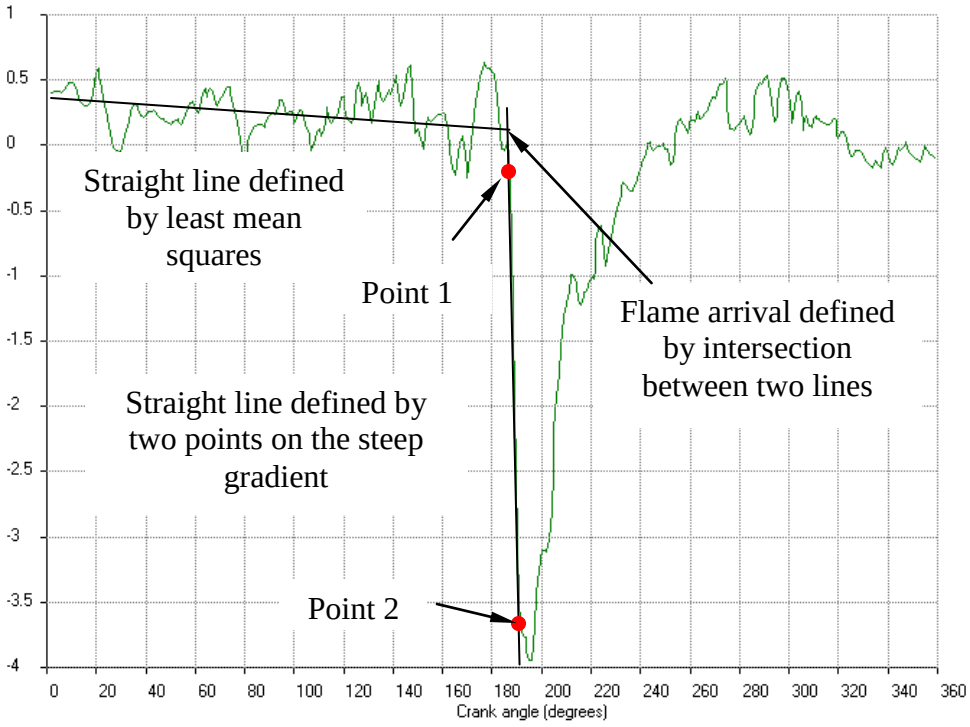

Figure 7-11, Noisy ionization probe signal

From a statistical analysis the flame mean arrival times and standard deviations are then calculated based on time in seconds and crank angle degrees. Figure 7-12 shows a typical histogram of flame arrival times at one particular probe for 200 engine cycles taken from one test.

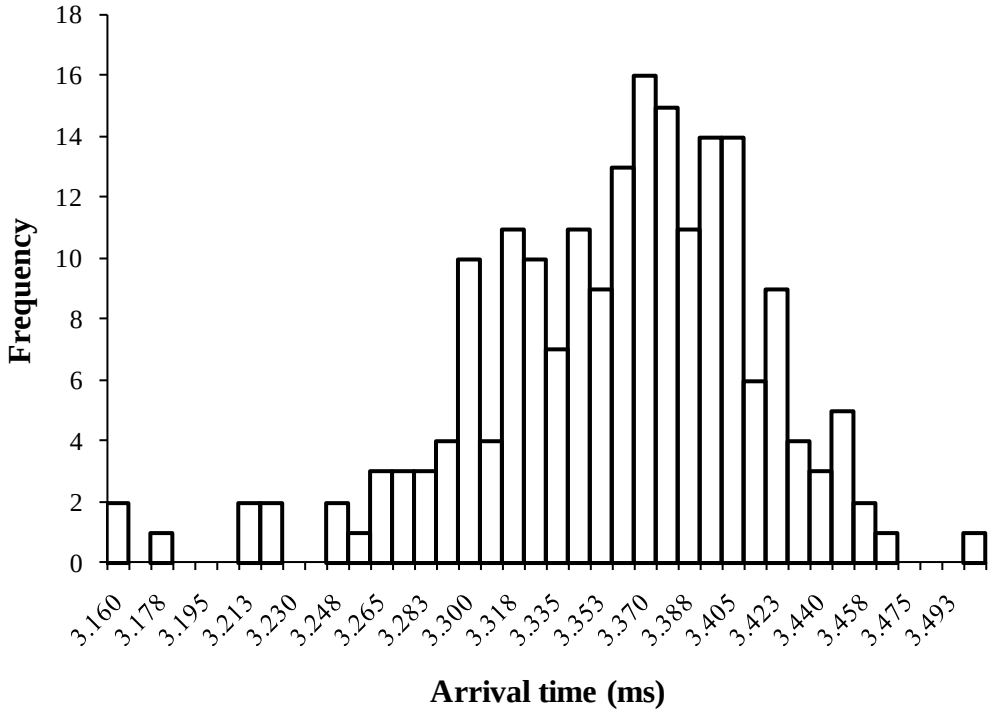

Figure 7-12, Typical histogram for flame arrival time, data taken from probe four of the squish head at full throttle and 9075 rpm.

As mentioned previously it is not intended to analyse the flame structure of a single cycle but to characterise the wrinkled flame front on a statistical basis over a number of cycles. From the histogram data a mean flame arrival time can be determined and also a standard deviation.

7.4.5 Flame Speed

Flame speeds can be calculated based on the distance between probes and the mean flame arrival times between the two probes. Flame speeds have been calculated between probes

1 - 2, 4 - 5, 7 - 8, 9 - 10, 11 - 12 and 13 - 14 for each test. The flame speeds have been plotted in Figure 7-13 to Figure 7-16.

As expected the squish combustion chamber produces faster flame speeds than the disc chamber. The graphs also show that the flame speeds are greater at full throttle than at half throttle. The greatest flame speeds are seen in the squish combustion chamber at full throttle and 9489 rpm where the maximum flame speed was approximately 190 m/s. This speed can be compared with the results of Pfeffer et al. (2002) who predicted speeds of just over 120 m/s at 17,000 rpm in a four stroke engine. Flame speeds were also measured in a four stroke engine by Kato et al. (2007) where a peak speed of approximately 180 m/s at 14,000 rpm were seen. A further discussion on the performance of the two cylinder heads will be given in Chapter 8.

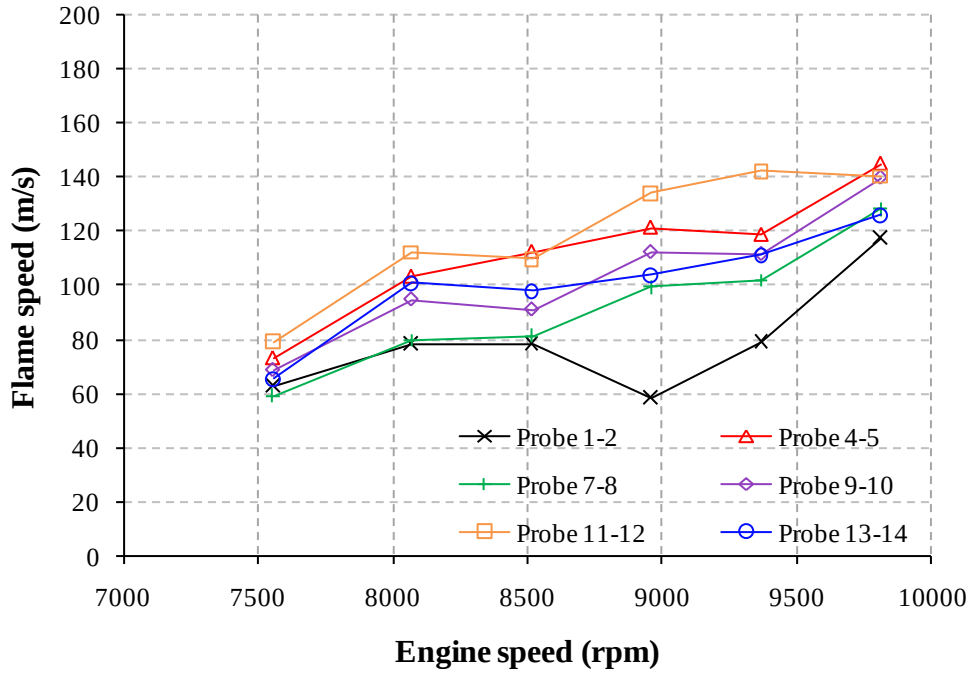

Figure 7-13, Flame speeds for the squish head at half throttle

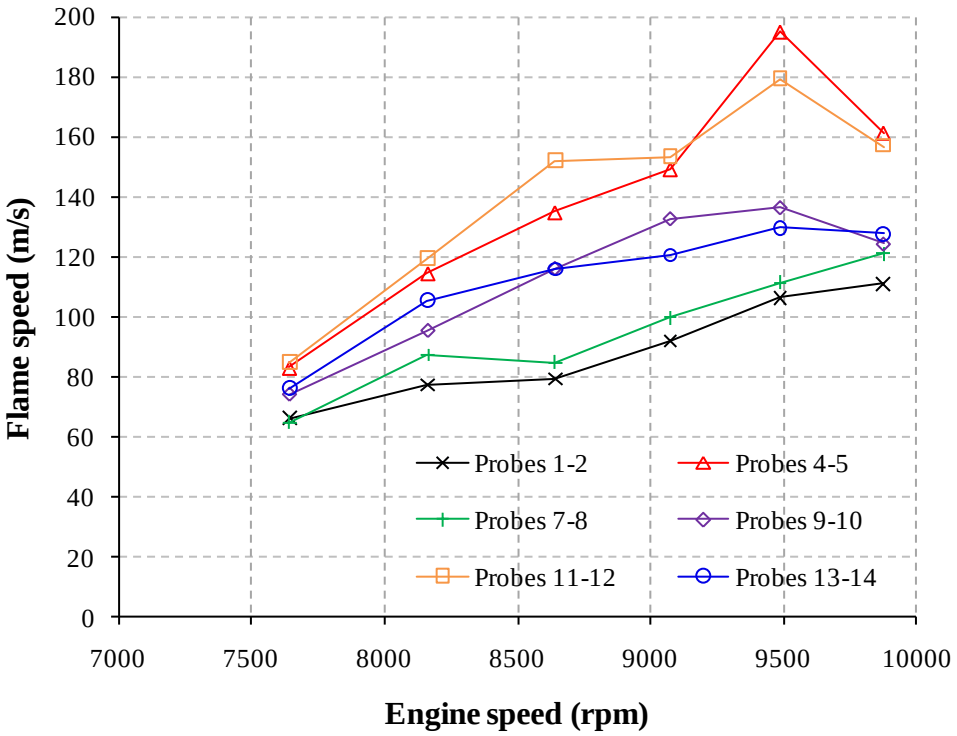

Figure 7-14, Flame speeds for the squish head at full throttle

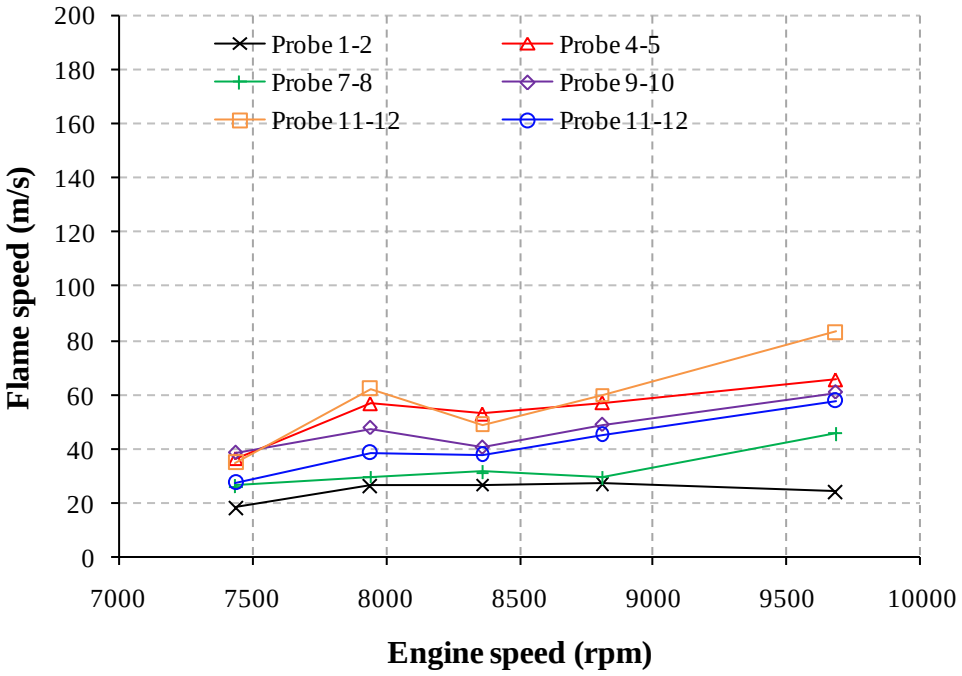

Figure 7-15, Flame speeds for the disc head at half throttle

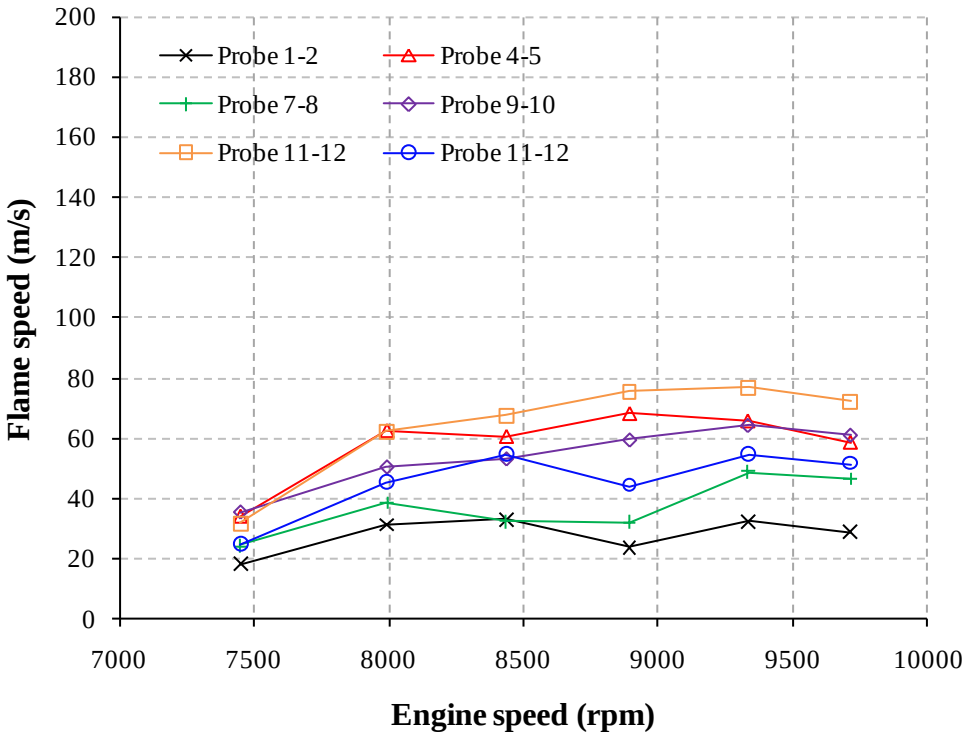

Figure 7-16, Flame speeds for the disc at full throttle

7.4.6 Wrinkled Flame Brush Thickness

The concept of the wrinkled flame brush thickness was introduced in Section 4.4, where the fractal model outer cut off was assumed to be equal to the wrinkled flame brush thickness. Figure 7-17 shows a schematic of a number of flame fronts from different cycles but at the same crank angle location plotted coincidently. The coincident flame fronts represent the flame brush. A line section is taken through the flame brush, A-A, and also shown is a normal distribution or a bell curve which represents the number of flame fronts which occur through the section A-A. This bell curve is equivalent to the flame arrival histogram shown in Figure 7-12. Using the flame arrival times with a statistical approach a wrinkled flame brush thickness can be defined. It is assumed here that the time between the leading and trailing edges of the statistical flame brush passing a fixed point in the combustion chamber is given as two standard deviations calculated from the flame arrival times. With the flame speeds previously calculated in Section 7.4.5 and the standard deviations calculated from the histogram the wrinkled flame brush thickness can be determined.

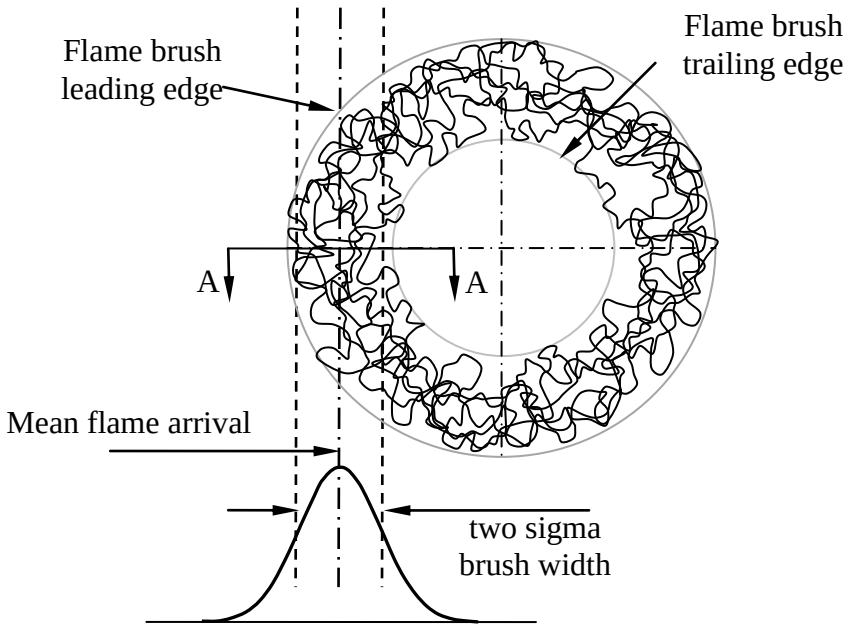

Figure 7-17, Flame brush width based on flame arrival statistics

Figure 7-18 to Figure 7-21 shows the results from the wrinkle brush thickness calculations. The marker points represent the brush thickness at the inner probes 1, 7, 9, 4, 11 and 13, and also the outer probes 2, 8, 10, 5, 12 and 14. The lines on the graphs represent the calculated average thickness from either the inner or outer probes. With the exception of the squish head results at full throttle there is a considerable scatter in the predicted brush thickness from each of the probes. There is however a coherent trend in the graphs which shows that the brush thickness is approximately 10 – 15 mm at the inner probes and that the flame thickness grows as the flame front radius gets larger.

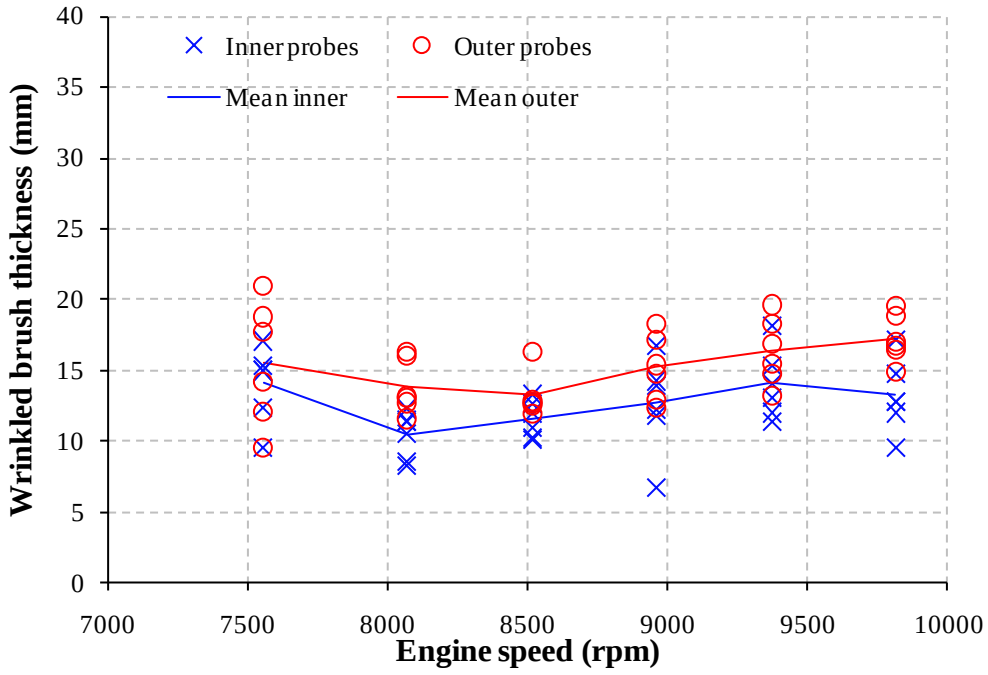

Figure 7-18, Wrinkled flame brush thickness squish head half throttle

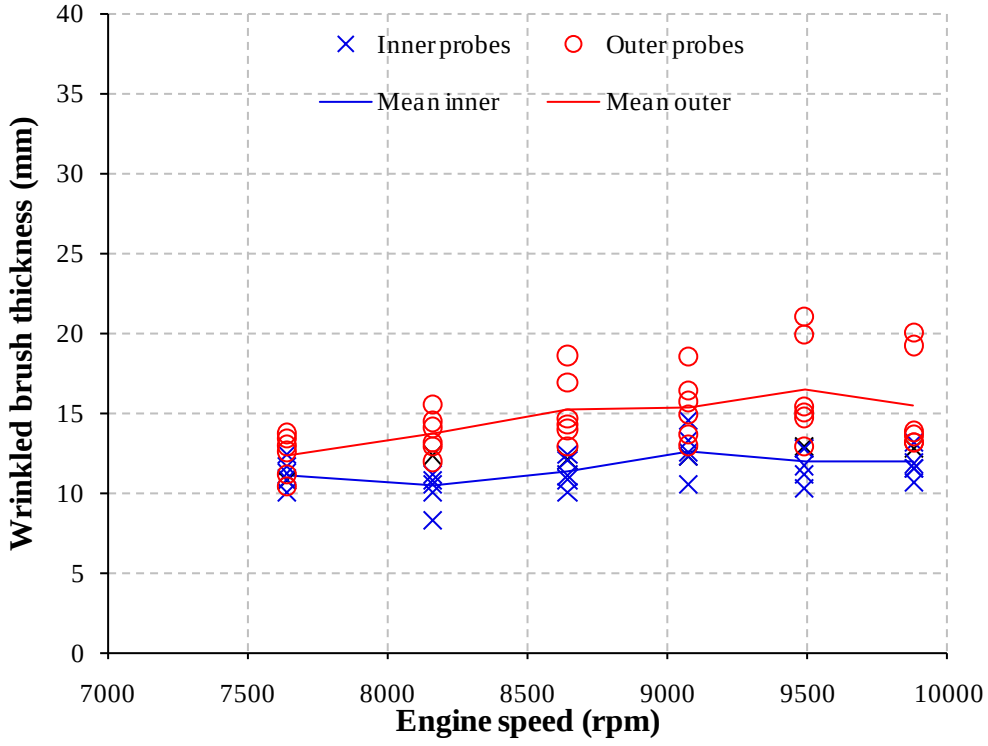

Figure 7-19, Wrinkled flame brush thickness squish head full throttle

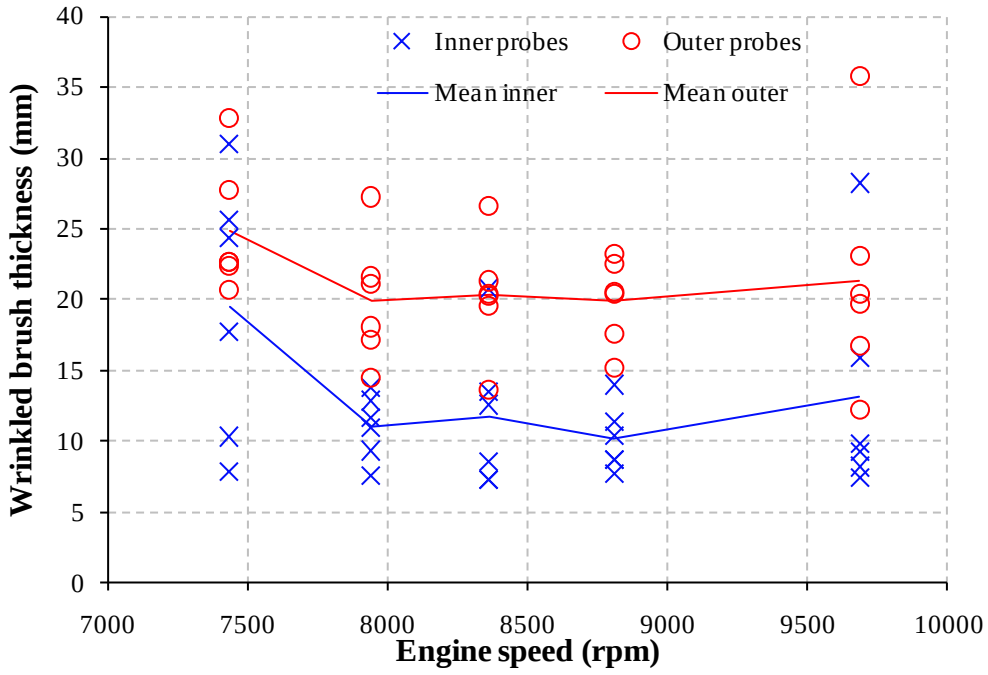

Figure 7-20, Wrinkled flame brush thickness disc head half throttle

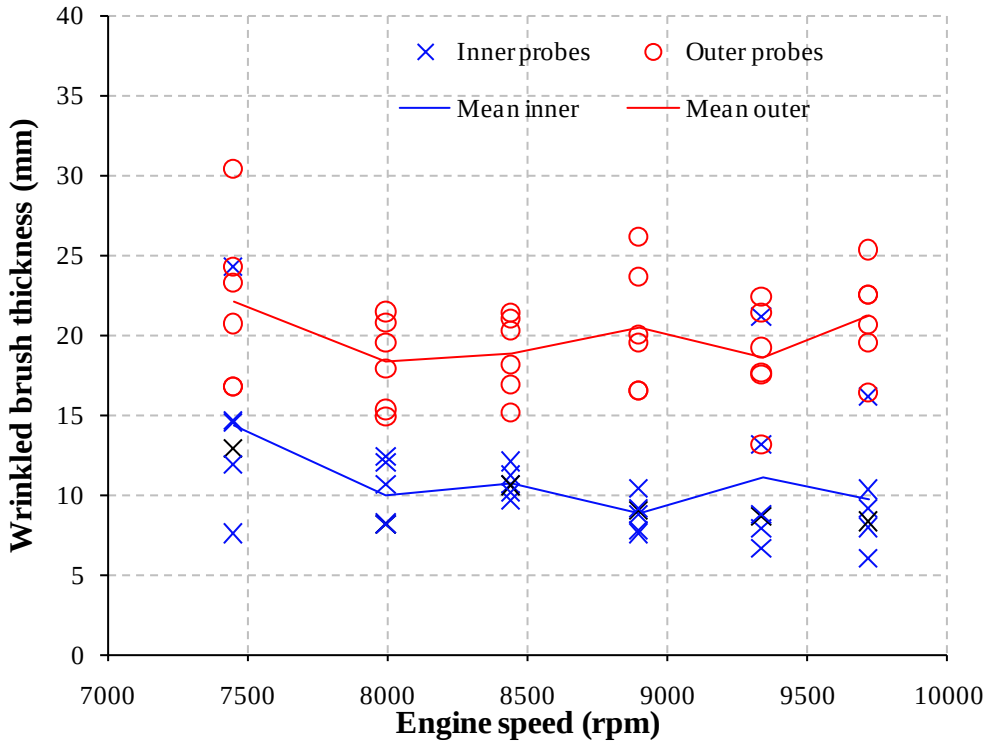

Figure 7-21, Wrinkled flame brush thickness disc head full throttle

7.4.7 Polar Plots of Flame Propagation

The mean flame arrival times calculated from the histogram data, of the type shown in Figure 7-12, for all the probes can be plotted on polar diagrams. Figure 7-22 to Figure 7-33 show the polar plots of the mean flame arrival time at the probes, the flame arrival times are in crank angle degrees. In each plot there are two lines, the blue line represents the inner probes 1, 4, 7, 9, 11 and 13 whilst the red line represents the outer probes 2, 5, 8, 10, 12 and 14. The plots should be viewed as looking into the combustion chamber from outside of the engine with the exhaust port at the bottom of the plot. In all of the plots the curves representing the flame arrival times approximate to a circle which supports the spherical flame front assumption. In all cases the approximate circle is offset upwards. As the plots represent flame front arrival times, the position of the burned zone and flame front is offset towards the exhaust port, downwards in the polar plots. Some plots do indicate the flame front movement is not directly towards the exhaust and that there is some asymmetry about the vertical plane which represents the tumble plane.

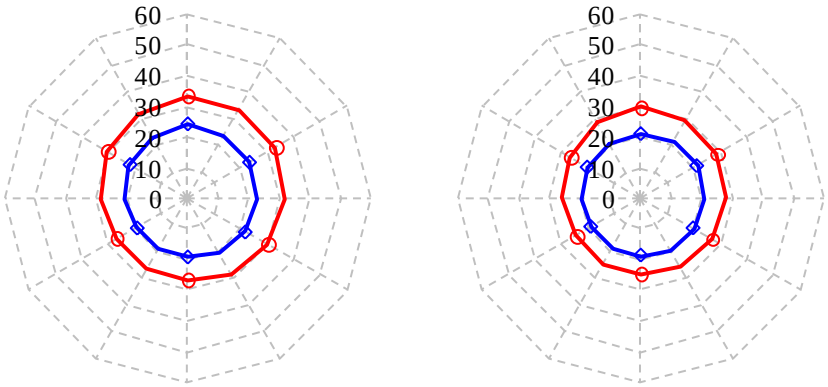

Figure 7-22, Flame arrival in crank angle degrees, squish head full throttle 7640 and 8162 rpm

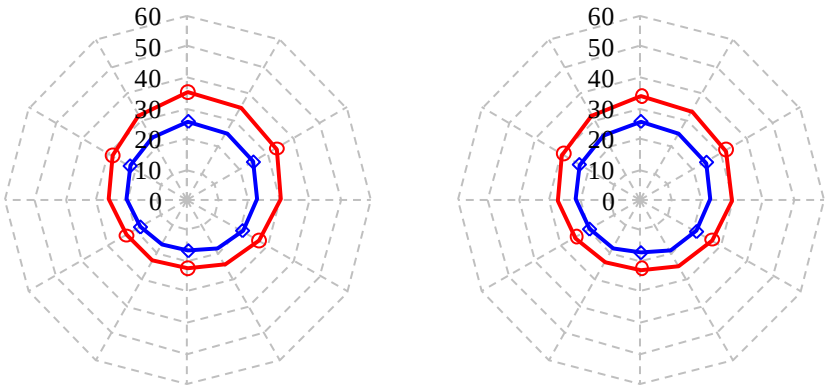

Figure 7-23, Flame arrival in crank angle degrees, squish head full throttle 8640 and 9075 rpm

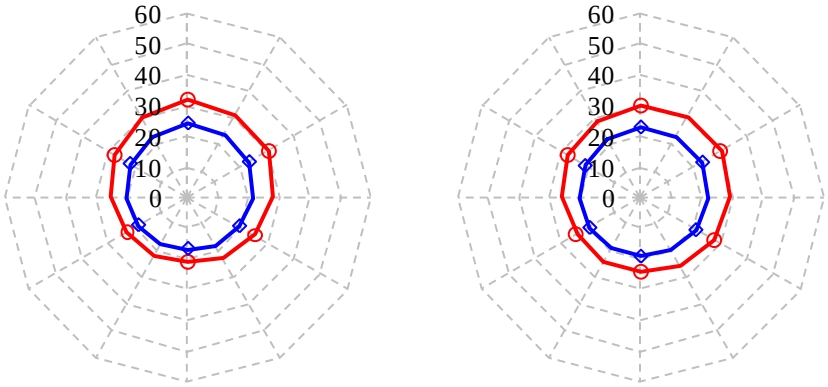

Figure 7-24, Flame arrival in crank angle degrees, squish head full throttle 9489 and 9878 rpm

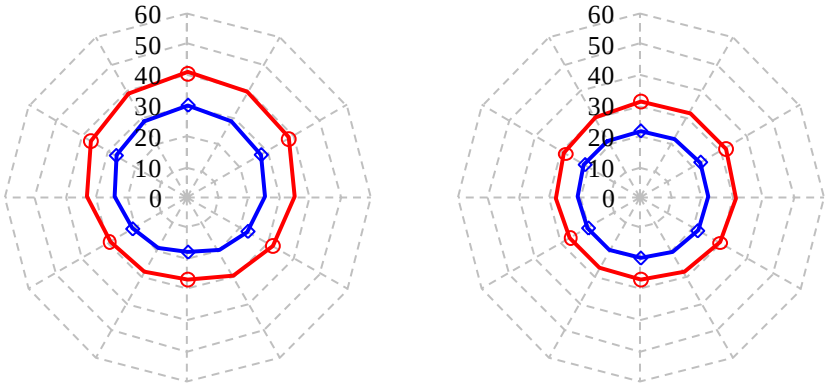

Figure 7-25, Flame arrival in crank angle degrees, squish head half throttle 7555 and 8069 rpm

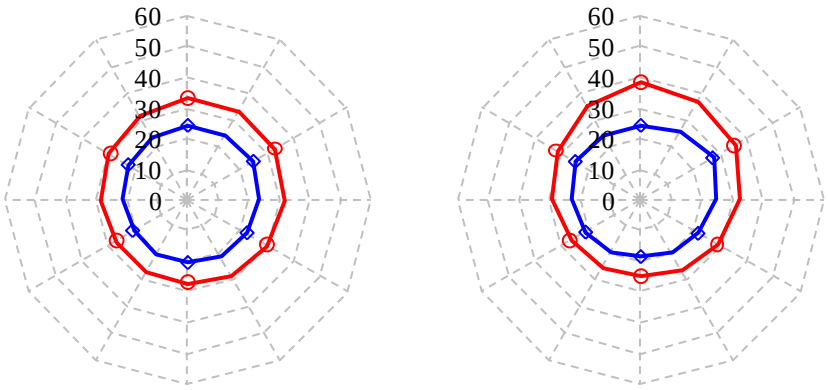

Figure 7-26, Flame arrival in crank angle degrees, squish head half throttle 8517 and 8981 rpm

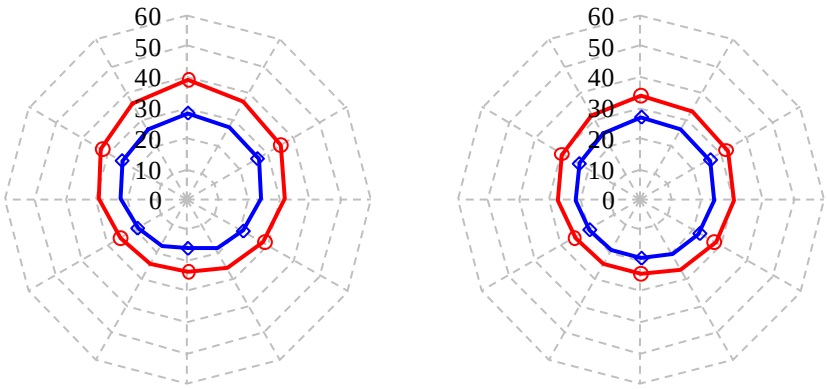

Figure 7-27, Flame arrival in crank angle degrees, squish head half throttle 9369 and 9812 rpm

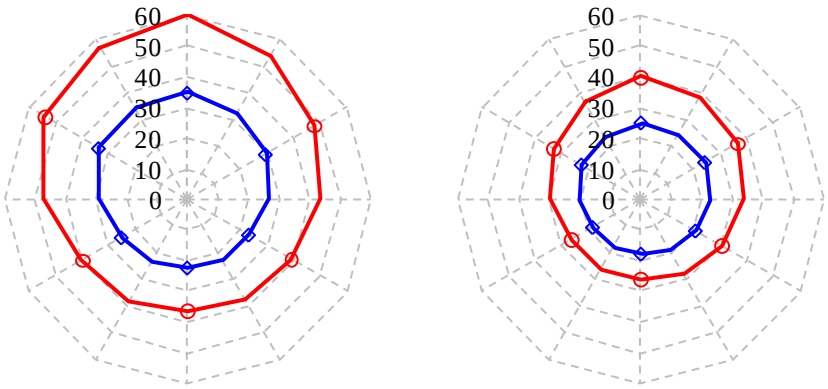

Figure 7-28, Flame arrival in crank angle degrees, disc head full throttle 7446 and 7991 rpm

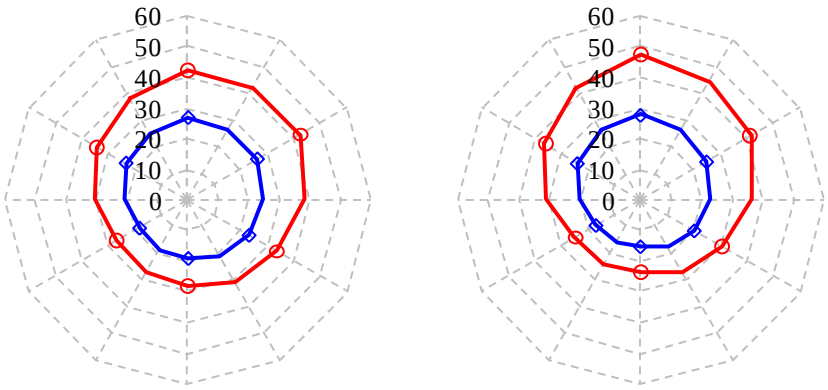

Figure 7-29, Flame arrival in crank angle degrees, disc head full throttle 8437 and 8896 rpm

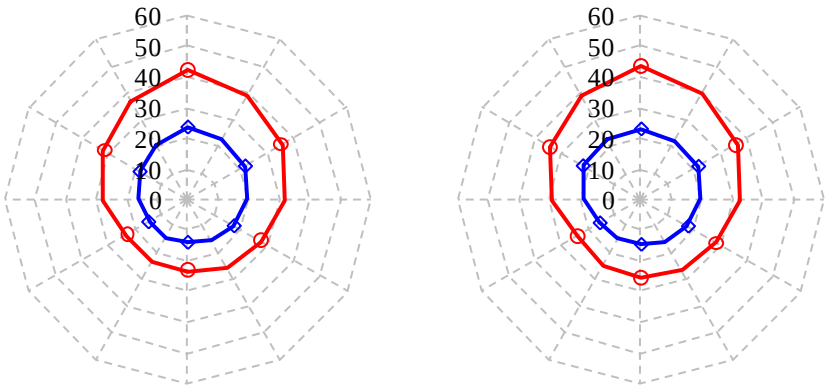

Figure 7-30, Flame arrival in crank angle degrees, disc head full throttle 9335 and 9718 rpm

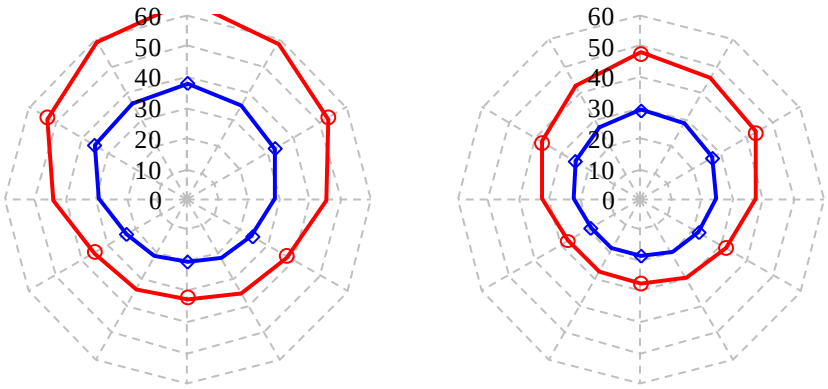

Figure 7-31, Flame arrival in crank angle degrees, disc head half throttle 7433 rpm and 7938 rpm

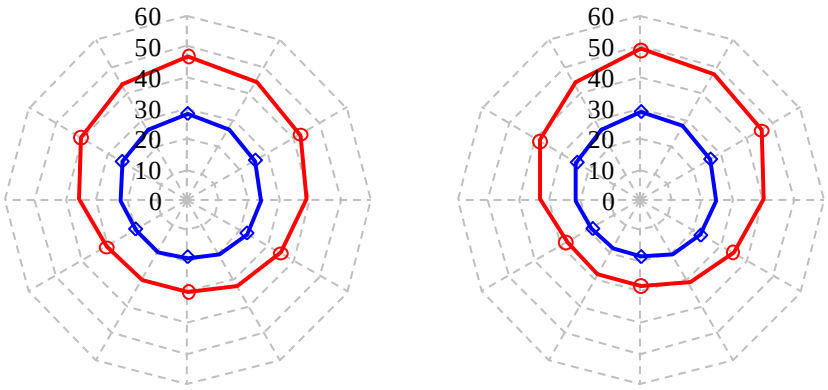

Figure 7-32, Flame arrival in crank angle degrees, disc head half throttle 8359 rpm and 8808 rpm

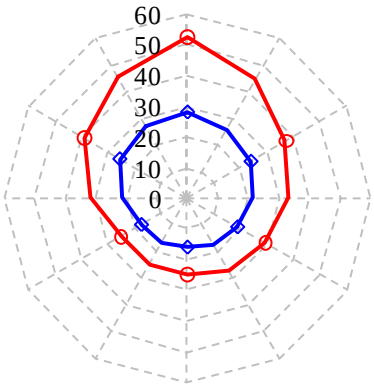

Figure 7-33, Flame arrival in crank angle degrees, disc head half throttle 9683 rpm

7.4.8 Concluding Remarks

The polar plots shown in Section 7.4.7 show flame front profiles which approximate to a circle, this supports the assumption of the spherical flame front. In all engine tests, at the different speeds and throttle positions, the flame front was shown to be offset towards the exhaust port which supports the theory of the tumble motion advecting the burned zone towards the exhaust port. The flame brush thickness has been determined using a statistical approach with the flame arrival times at the location of the ionization probes, the brush thickness is approximately 10 – 15 mm thick.

8 Engine Simulation Results and Discussion

The whole engine simulation model described in Chapter 6 has been used to analyse the engine and experimental set up described in Chapter 7. The engine has been analysed with both the squish and the disc type combustion chambers at each of the engine speeds and throttle positions shown in Table 7-2.

8.1 Tumble Model Validation

To assess the ability of the tumble and turbulence model, described in Chapter 3, to predict the flow motion in a cylinder a whole engine simulation has been conducted for a 50 cc two stroke engine. The 50 cc engine was the subject of an experimental study conducted by Reddy et al. (1986). In Section 3.2.1 the tumble model constant c_{sp} was introduced which is intended to account for the fact that not all the kinetic energy entering the cylinder is converted into tumble momentum. The c_{sp} constant here has been adjusted such that the measured and predicted tumble velocities of the Reddy engine show a reasonable correlation. The tumble and turbulence model constants used in the simulation are given in Table 8-1.

Table 8-1, Tumble and turbulence model constants for a 50 cc engine

Model Constant	Constant Value
c_h	0.5
c_ε	0.5
c_{sh}	2.5
c_β	2.0
c_{kin}	0.4
c_{sp}	0.45

In the tests conducted by Reddy et al. (1986) the 50 cc engine was motored at 3000 rpm, at full throttle whilst the in-cylinder bulk flow motion and turbulence were measured using a hot wire anemometer positioned at the spark plug location. The measured bulk flow tumble

velocity is shown in Figure 8-1, also shown in the graph is the predicted tumble velocity from the engine simulation for the 50 cc engine. There is a reasonable correlation between predicted velocity and experimental results.

Both the measured and predicted peak tumble velocities occur shortly after the transfer port opens which is caused by the scavenge jets entering the cylinder creating the large scale tumble motion. The mean flow velocity falls sharply around BDC, with the engine being motored the transfer of fresh charge from the crankcase to the cylinder would be complete shortly after BDC, approximately 10° CA. The velocity remains fairly constant between the transfer port closing and 60 BTDC then falls again during compression such that at TDC the mean flow velocity is approximately 5 m/s.

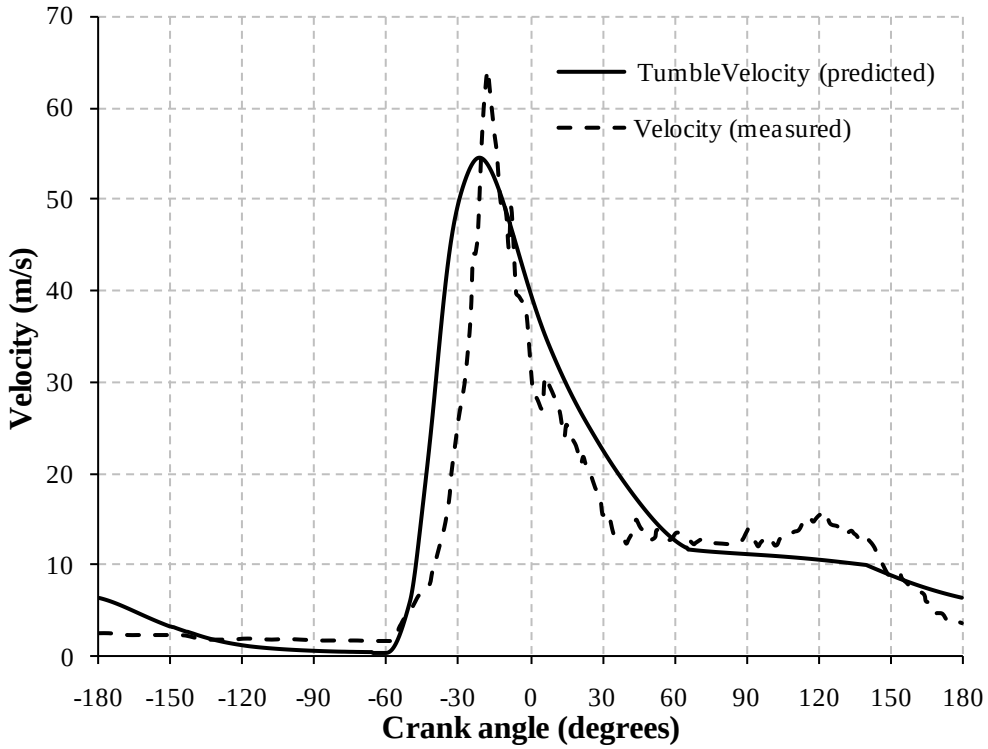

Figure 8-1, Measured and predicted tumble velocity for 50 cc engine motored at 3000 rpm and full throttle, data adapted from Reddy et al. (1985)

Shown in Figure 8-2 is the measured and predicted turbulence intensity for the 50 cc engine, the predicted results follow the trend of the evolution of the turbulence quite well.

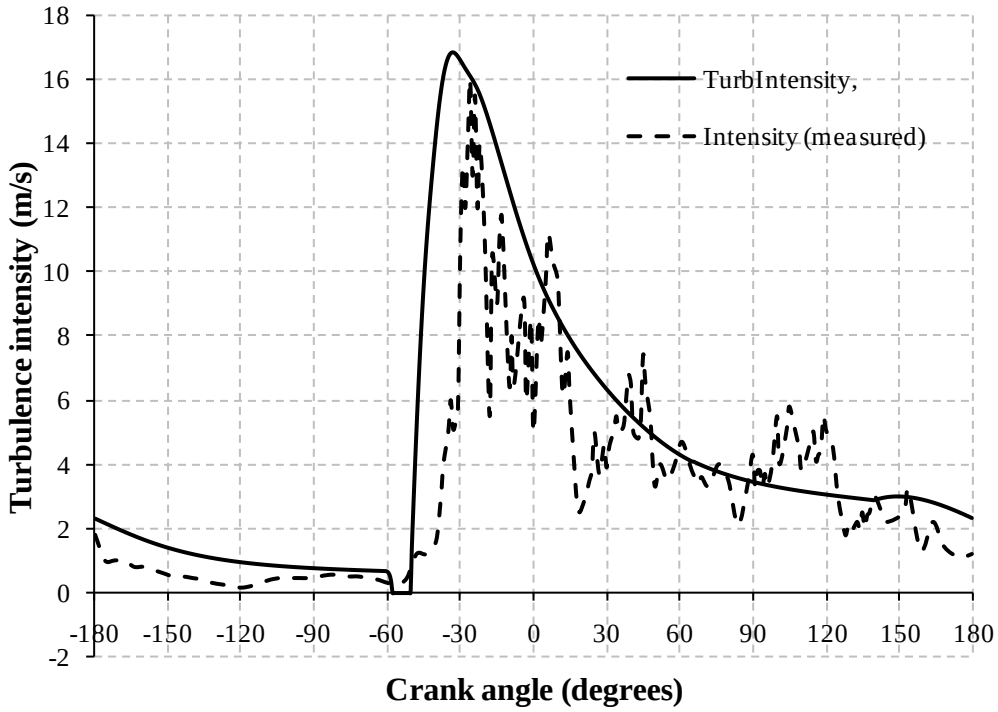

Figure 8-2, Measured and predicted turbulence for 50 cc engine motored at 3000 rpm and full throttle, data adapted from Reddy et al. (1986)

8.2 Modelling Squish and Disc Combustion Chambers

A schematic of the whole engine simulation model for the test set up used in the current study was shown in Figure 7-1. Engine simulations have been solved for both the squish and disc type combustion chambers. Other than the cylinder head geometry all the other components of the engine models, ducts, plenums, boundary conditions etc. are the same for both engine models.

8.2.1 Model Parameters and Constants

Wrinkled Brush Thickness

The wrinkled brush zone thickness was discussed in Section 4.4.1. The fractal combustion model requires an outer cut off which is taken as the wrinkled brush zone thickness. The brush zone is assumed to be a function of the integral scale and Equation (4.20) introduced

the model constant c_{Lmax}, this is used to calculate the wrinkled brush thickness which is equivalent to the fractal outer cut off L_{max}. The flame brush thickness was determined in engine tests using the signals from ionization probes as discussed in Section 7.4.6. Figure 8-3 shows the measured flame brush thickness for the disc head engine at 8896 rpm and full throttle, also shown is the calculated wrinkled brush thickness or outer cut off, L_{max}, the value of c_{Lmax} used was 5.0.

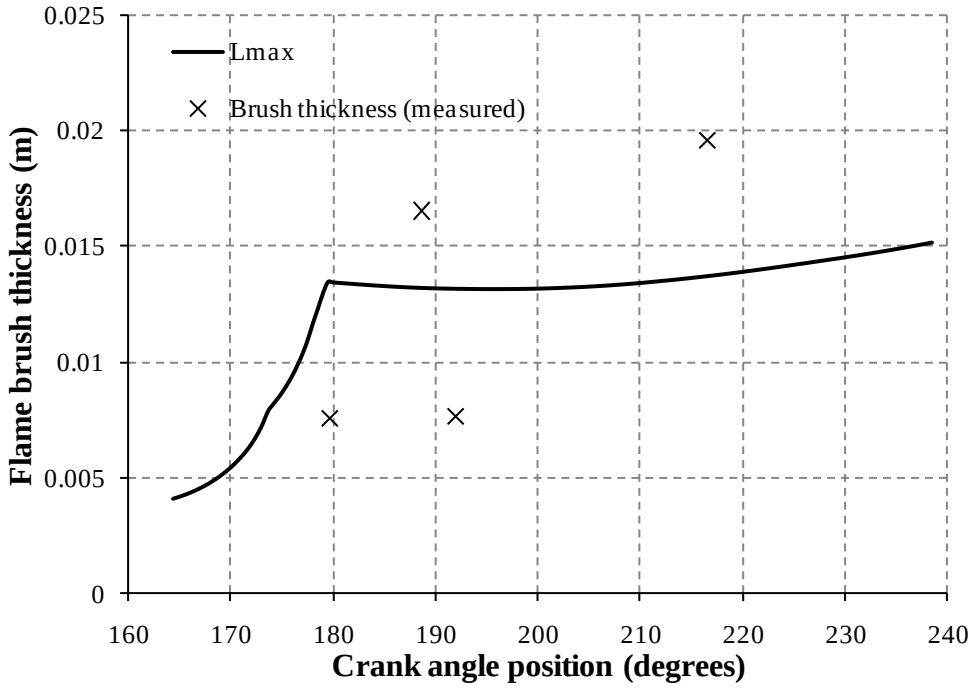

Figure 8-3, Measured wrinkled brush thickness and predicted fractal outer cut off for the disc head at full throttle and 8896 rpm

For the simulation of the engine used in this study the model constants for the tumble and turbulence model are shown in Table 8-2. All the other engine parameters, except air/fuel ratio remain constant for the engine using both the squish and disc combustion chambers.

Table 8-2, Tumble and turbulence model constants

Model Constant	Squish Head	Disc Head
c_h	0.5	0.5
c_ε	0.5	0.5
c_{sh}	3.1	2.5
c_β	3.5	2.0
c_{kin}	0.4	0.4
c_{sp}	0.3	0.3
D_T	2.39	2.39
c_{RIFF}	0.05	0.05
c_{Lmax}	5	5

8.2.2 Air Fuel Ratio

As mentioned in the experiments chapter the accuracy of the air flow meter used in the tests was questionable, therefore the air/fuel ratio used in the engine simulation is determined from a measured fuel flow rate and an air flow rate calculated by the engine simulation. An initial simulation was conducted with an estimated air/fuel ratio and then the predicted air flow from that simulation was compared with the measured fuel flow to determine a new air/fuel ratio. If the difference between the initial and new air/fuel ratios was more than 2% the procedure was repeated until the air/fuel ratio converges.

On the following page, Figure 8-4, is plotted the predicted air fuel ratio, delivery ratio and scavenge efficiency against engine speed for both the squish and disc combustion chambers at full and half throttle. For comparison Bell (1984) gives air/fuel ratios for two strokes as between 10:1 and 13:1 for low speed running and between 12:1 and 14:1 for heavy load running. Also Blair (1976) used air fuel ratios of between 10.65:1 and 11.56:1 at engine speeds of between 5000 and 7500 rpm on a similar air cooled two stroke 250 cc engine. The air/fuel ratios calculated here using predicted air mass flow and measured fuel mass flow seem reasonable compared with that data.

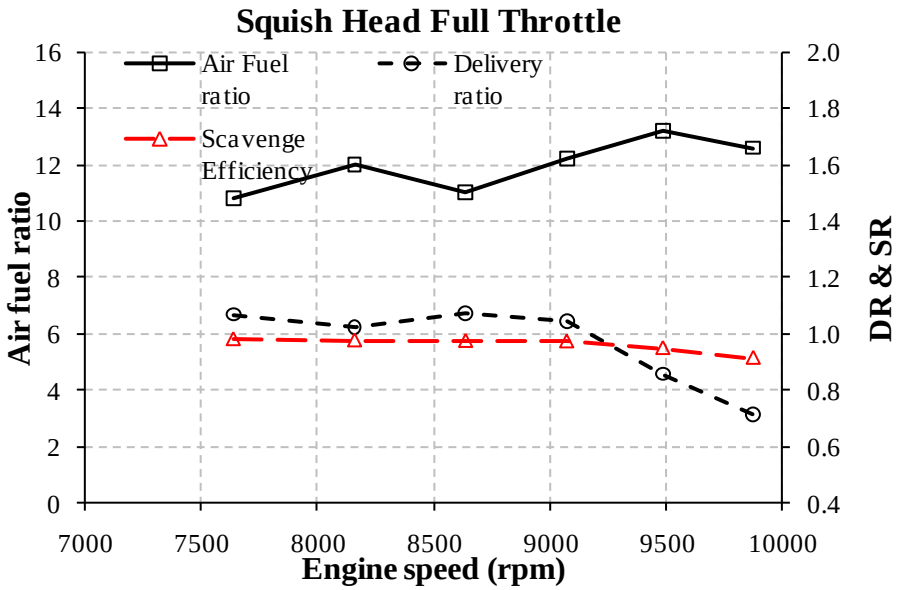

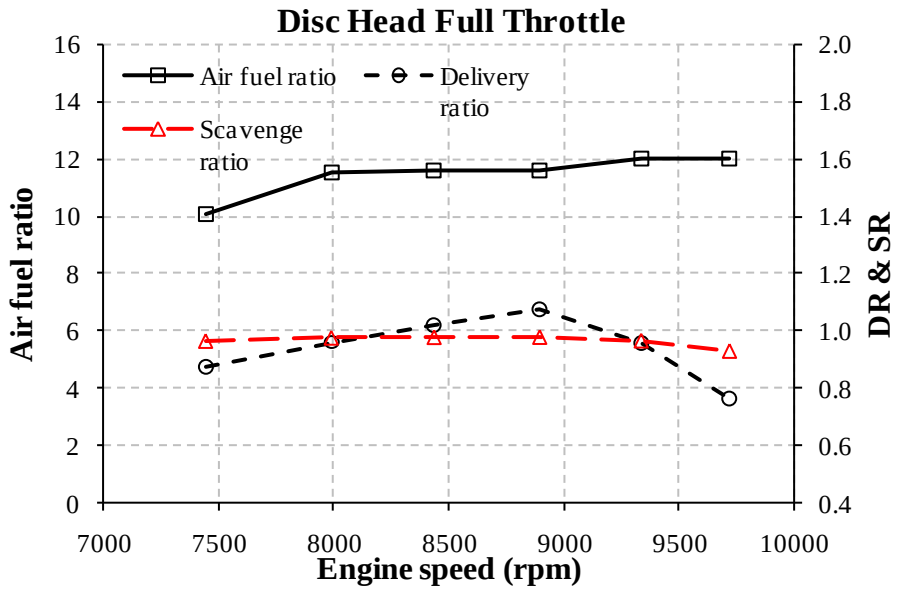

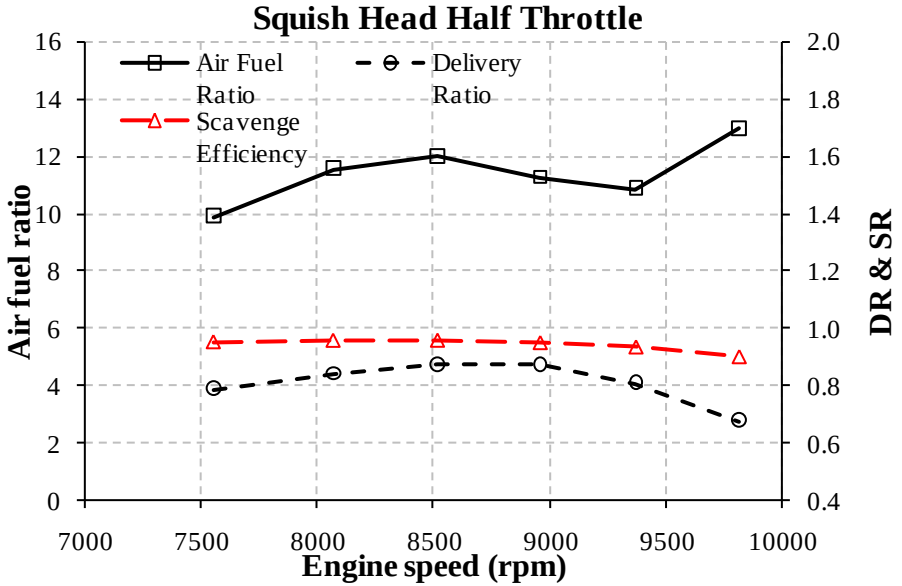

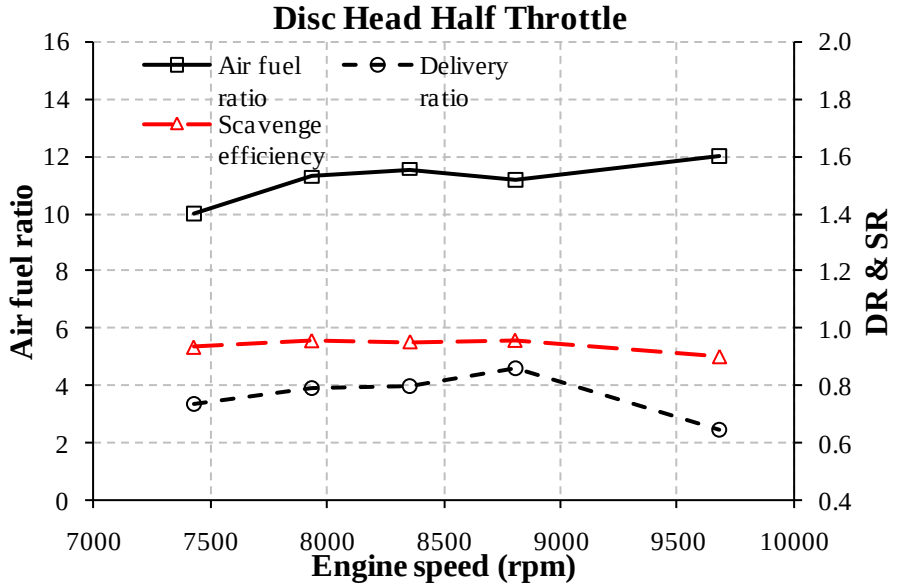

Figure 8-4, Air fuel ratio, delivery ratio and scavenge afficiency

8.2.3 Engine Performance Comparison

The mean effective pressure of an engine cylinder is used as a measure of the ability of an engine to do work. The Indicated Mean Effective Pressure (IMEP) is used here to compare the performance of the squish and disc cylinder heads. The IMEP is calculated from both the predicted and measured cylinder pressure through the 360° engine cycle. The IMEP is calculated for the cylinder only and does not include the pumping work of the crankcase. Figure 8-5 shows the predicted and measured IMEPs for both the squish and disc combustion chambers at full and half throttle. For both combustion chamber geometries there is a good correlation between the measured and predicted IMEP. Both the measured and predicted IMEP values are higher for the squish combustion chamber indicating that the squish combustion chamber performs better than the disc type head and will have a greater ability to do work.

The peak IMEP values in all cases occurs around 9000 rpm which is generally consistent with the engine speed that produces the best delivery ratio.

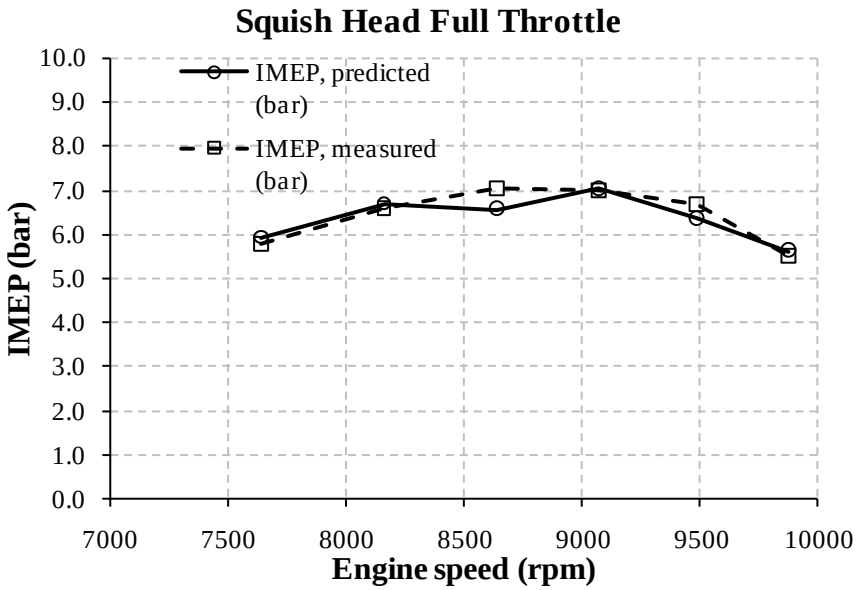

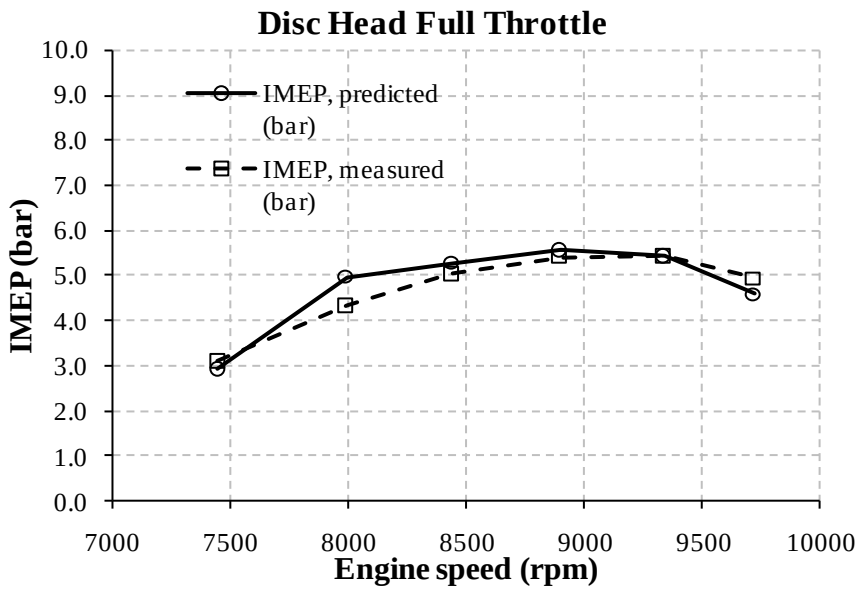

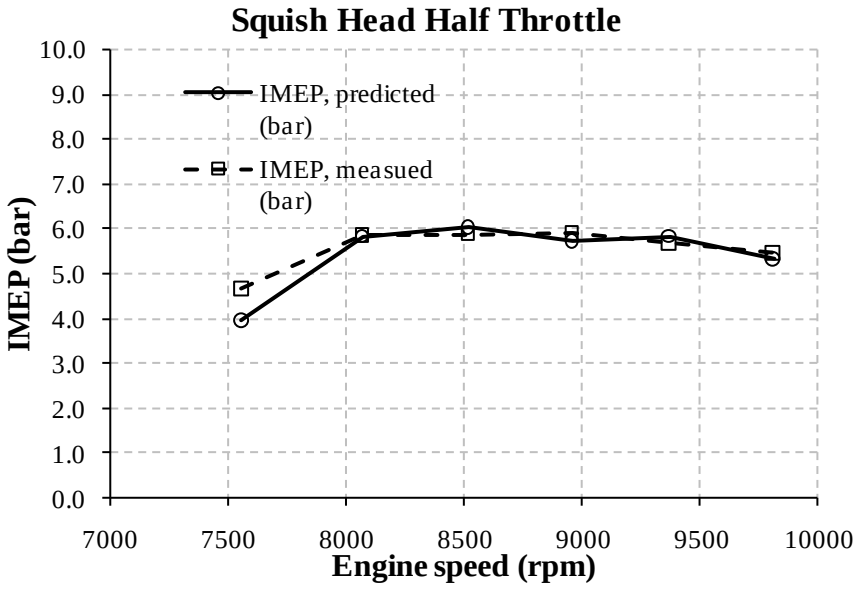

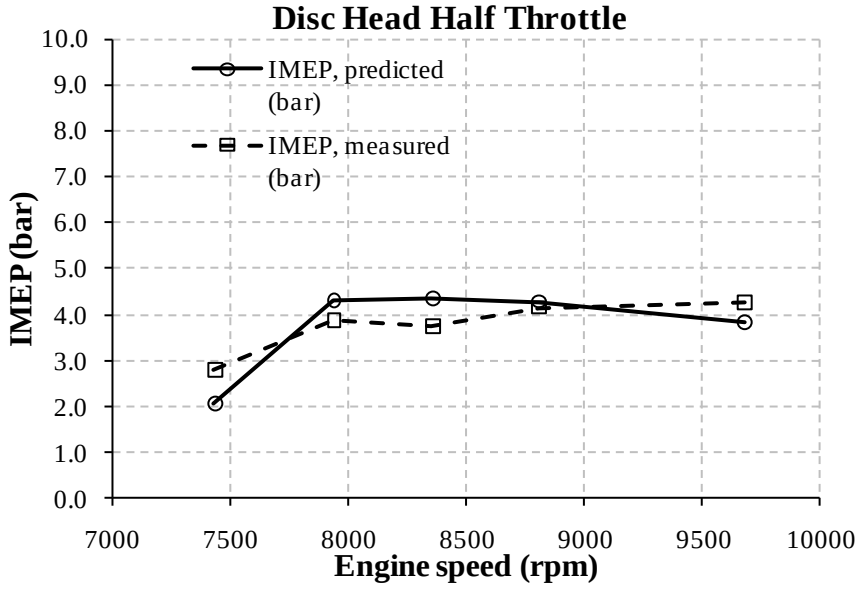

Figure 8-5, Indicated mean effective pressure

Further insight into the causes of the difference in performance between the squish and disc combustion chambers may be found by inspection of the cylinder pressure development diagrams. Figure 8-6 below shows the cylinder pressure and crankcase pressure for the squish combustion chamber at full throttle and 9075 rpm. Both the predicted and measured pressures are plotted in Figure 8-6. Note that for all the cylinder pressure graphs plotted against crank angle, 180° is TDC. The measured and predicted peak cylinder pressures are approximately 40 bar at 195°, there is a good correlation with both cylinder and crankcase pressures. Pressure diagrams for all of the engine test conditions can be found in Appendix C.

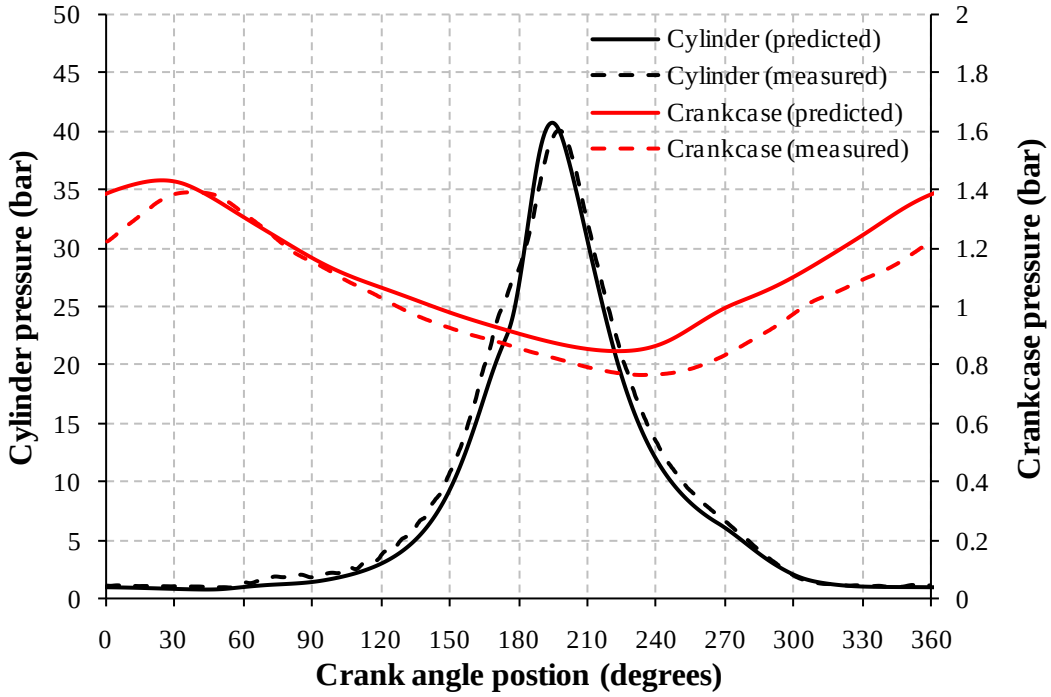

Figure 8-6, Cylinder pressure for the squish head at full throttle and 9075 rpm

The crankcase pressure was measured with a pressure transducer connected to the crankcase via a 170 mm long and 6 mm diameter flexible pipe, this produces a phase lag of approximately 75° between the actual and measured crankcase pressures. The crankcase pressure transducer and connecting pipe were modelled in the engine simulations. The pressures in the cylinder, crankcase and at the pressure transducer, as predicted by the whole engine simulation, are plotted in Figure 8-7, for the squish combustion chamber at full

throttle and 9075 rpm. The graph shows that the cylinder and crankcase pressures reach near equilibrium around 30° after BDC, which is towards the end of the scavenge period. The graph also shows how the pressure transducer lags the actual crankcase pressure and also has a reduced alternating pressure amplitude due to the losses between crankcase and transducer. Also shown in the pressure plot is the averaged pressure at the transducer. At 30° the difference between the mean crankcase pressure and the cylinder pressure is approximately 0.2 bar. Piezoelectric pressure transducers used to measure cylinder pressures have a tendency to vary their signal primarily due to thermal effects, for this reason the pressure transducer needs to be 'pegged' to a reference pressure near BDC. The cylinder pressure transducer used in this work is referenced against the mean pressure measured by the crankcase transducer at 30° ATDC. The error introduced by referencing the cylinder pressure to a mean crankcase pressure is approximately 0.2 bar which is considered acceptable.

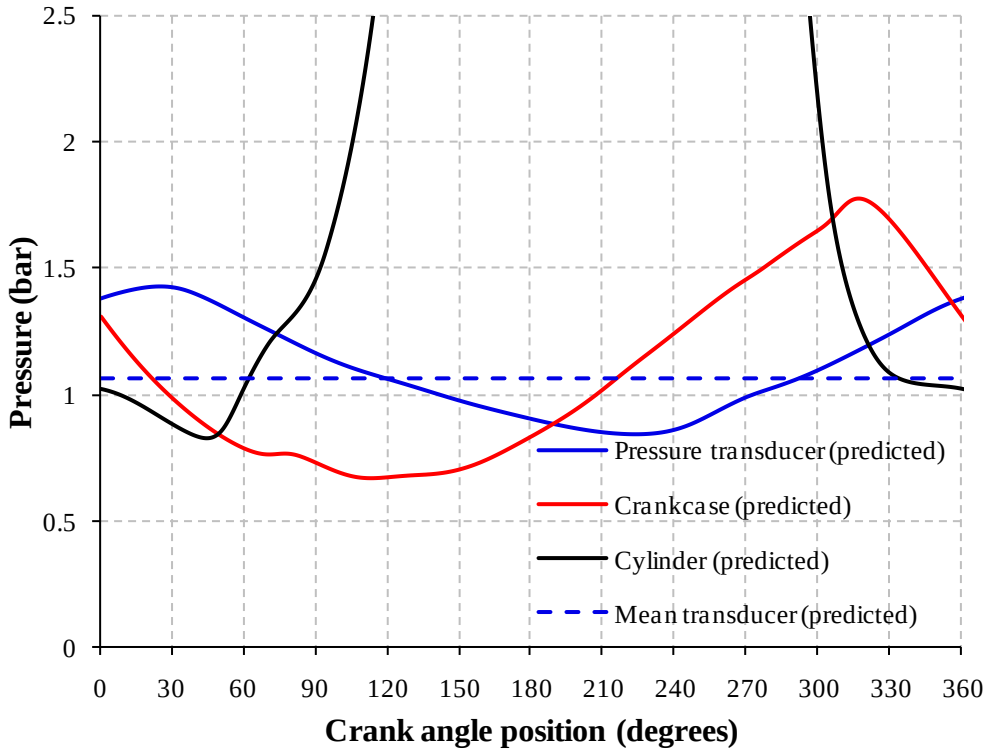

Figure 8-7, Predicted cylinder, crankcase and pressure transducer pressures for the squish head at full throttle and 9075 rpm

In the cylinder pressure graph, Figure 8-6, there is small increase in measured pressure at approximately 60° which does not appear to be predicted, this small increase in pressure occurs in most of the cylinder pressure plots. Below in Figure 8-8 is plotted the measured and predicted cylinder pressure as well as the predicted exhaust port pressure. The graph shows a positive pressure pulse at the exhaust port at 60° produced by the pressure wave motion in the exhaust duct, this pressure wave causes a reverse flow of gas from the exhaust into the cylinder. The predicted cylinder pressure does show a small increase consistent with the reverse flow from the exhaust, however the magnitude of the pressure rise in under predicted.

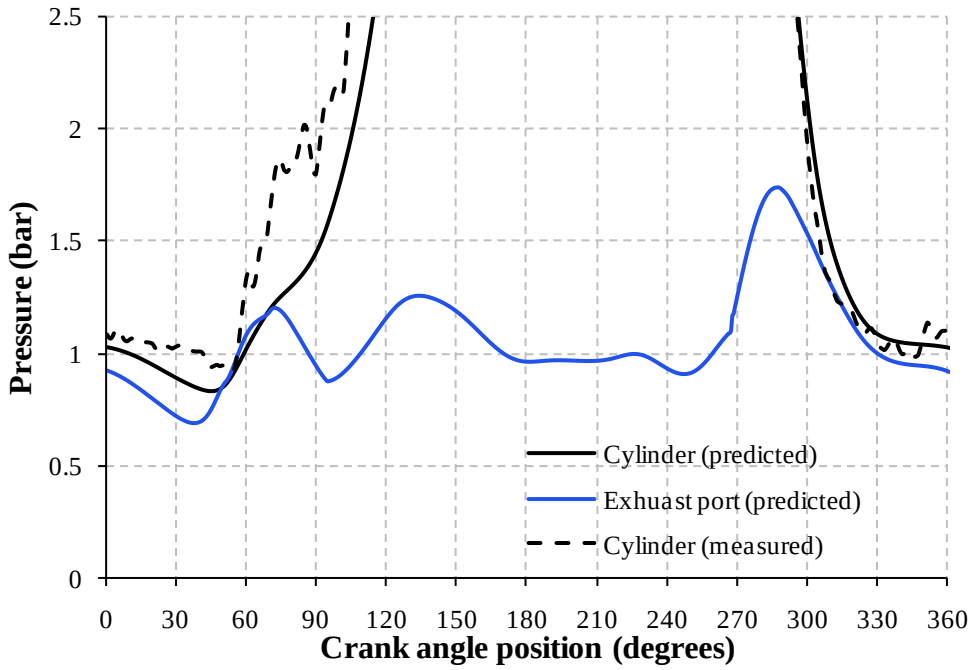

Figure 8-8, Cylinder and exhaust port pressure for the squish head at full throttle and 9075 rpm

The cylinder pressure plotted in Figure 8-9 is for the disc combustion chamber and this may be compared to the squish combustion chamber plotted in Figure 8-6, the engine test conditions are equivalent. Again both the measured and predicted pressures are plotted and the peak cylinder pressure in the disc combustion chamber is shown to be significantly less, approximately 25 bar at 190°.

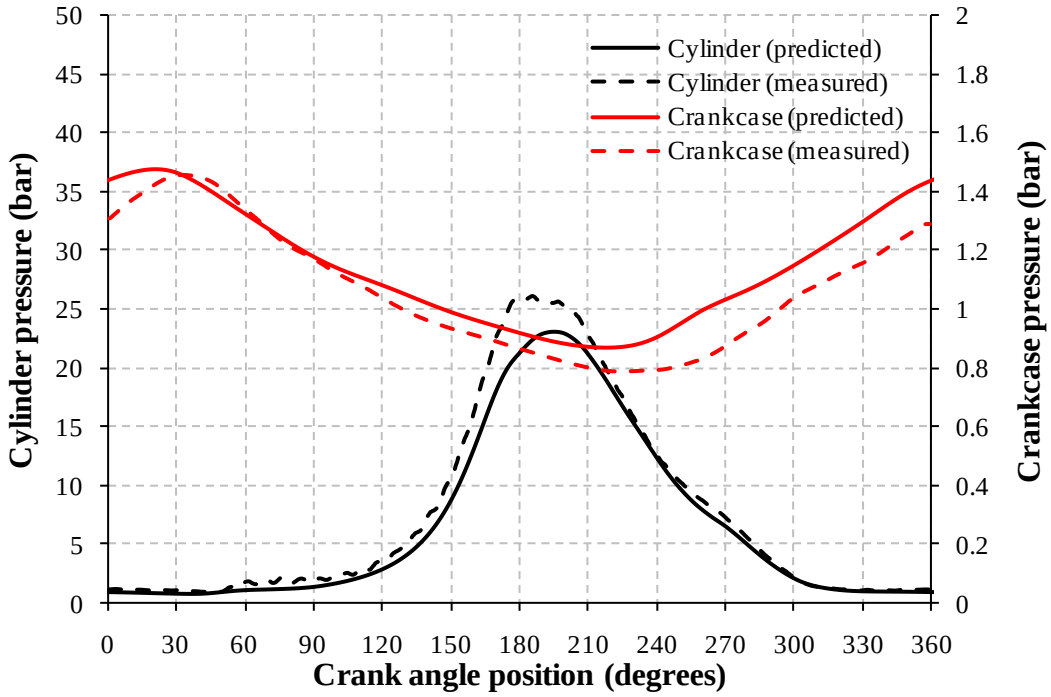

Figure 8-9, Cylinder pressure for the disc head at full throttle and 8896 rpm

A further comparison of the performance of the two combustion chambers can be made by interrogation of the mass fraction burned. The mass fraction burned is calculated using a method taken from Stone (1999), which was devised by Rassweiler and Withrow (1938). The method divides the change in pressure in the cylinder into two parts, that due to combustion and that due to the change in cylinder volume. It is assumed that the change in pressure due to the changing volume occurs as a polytropic process and Stone suggests using a polytropic exponent of between 1.2 and 1.3. The exact value of the exponent will depend upon the heat transfer in the cylinder, which will vary with operating conditions. In all the mass fraction burned calculations made in this work an exponent value of 1.29 has been used. A slightly low value of the exponent can produce a predicted mass fraction burn prior to ignition. Figure 8-10, again at full throttle and 9075 rpm, shows the mass fraction burned for the squish head. The ignition timing is set constant for all tests at 18.5° BTDC, which is 161.5° on the graphs plotted. The mass fraction burned curve has a number of characteristics which include a delay period where, after spark timing, there appears to be no combustion. After the delay period there is an early flame development period with an

increasing rate of combustion upto approximately 20% mass fraction burned. During the early development period the spherical flame radius grows, in the simulation, from its initial 2 mm upto half the maximum scale of wrinkling or the fractal outer cut off. The early flame development was introduced in Section 4.7. After approximately 20% mass fraction there appears to be a near constant mass burn rate which represents the fully developed flame propagation. The fractal model is used to model the wrinkled flame front geometry during the fully developed period. After approximately 80% mass fraction burned there is reduction in rate of burn as the flame front approaches the combustion chamber walls, modelling the end of combustion was discussed in Section 4.8.

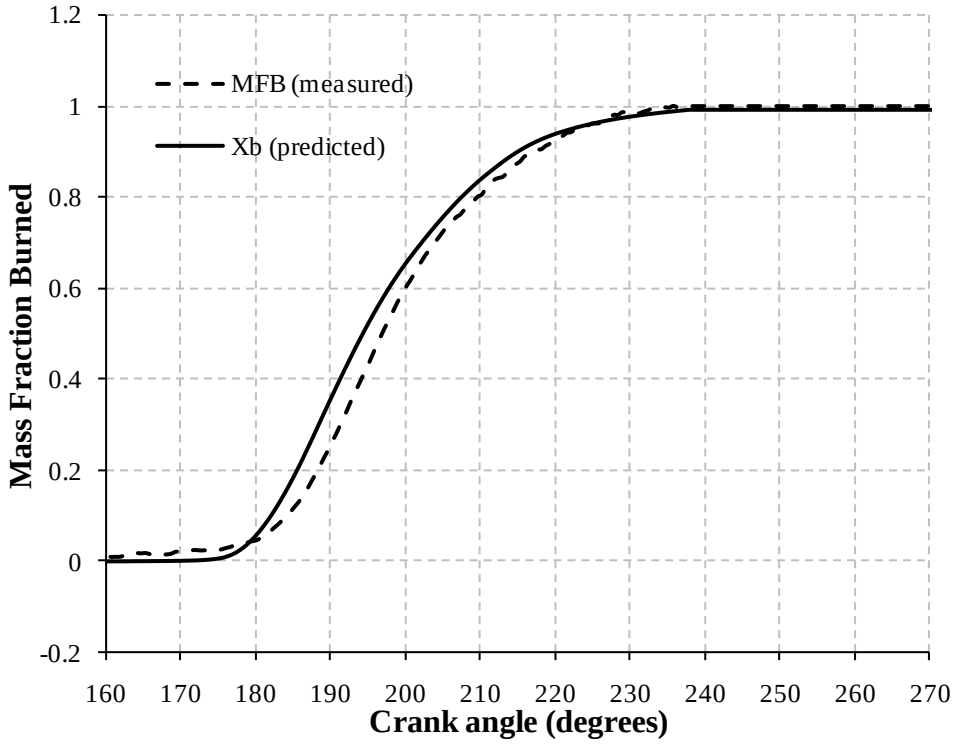

Figure 8-10, Mass fraction burned for the squish head full throttle 9075 rpm

For the squish combustion chamber the predicted and measured 20% burn fraction occurs at approximately 187° and the 80% burn fraction occurs at approximately 210°, hence the fully developed flame propagation period occurs over 23°. By comparison the mass fraction burn curve for the disc combustion chamber is shown below, Figure 8-11. For the disc chamber

the measured 20% burn fraction occurs at 196° and the 80% burn fraction at 230° which gives the fully developed flame propagation period as approximately 34°. The difference between the fully developed flame propagation periods shows that the disc combustion chamber is a slower burning than the squish combustion chamber. Also time to 20% burn is longer which includes the delay period and early development.

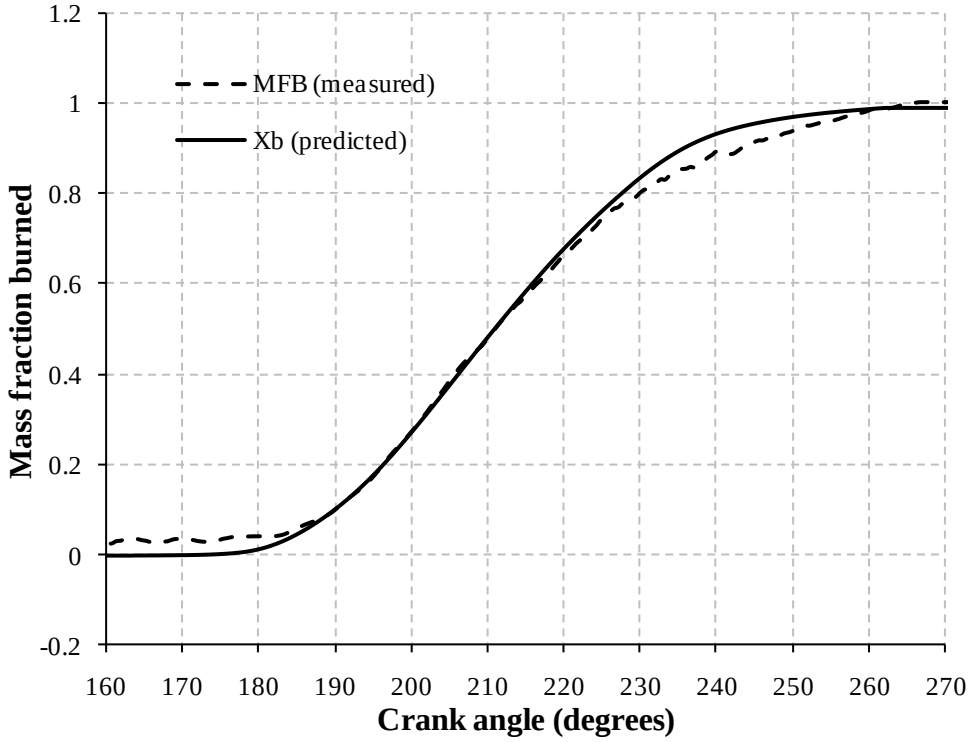

Figure 8-11, Mass fraction burned for the disc head at full throttle at 8896 rpm

A similar analysis to the above can be conducted at the half throttle condition, Figure 8-12 shows the cylinder pressure for the squish combustion chamber and Figure 8-14 shows the cylinder pressure for the disc combustion chamber. As with the full throttle condition the peak pressure in the squish combustion chamber is significantly greater than the disc combustion chamber. The mass fraction burned for the squish combustion chamber is shown in Figure 8-13 and for the disc head combustion chamber Figure 8-15. Once again the fully developed flame propagation period is shorter for the squish combustion chamber than the disc combustion chamber.

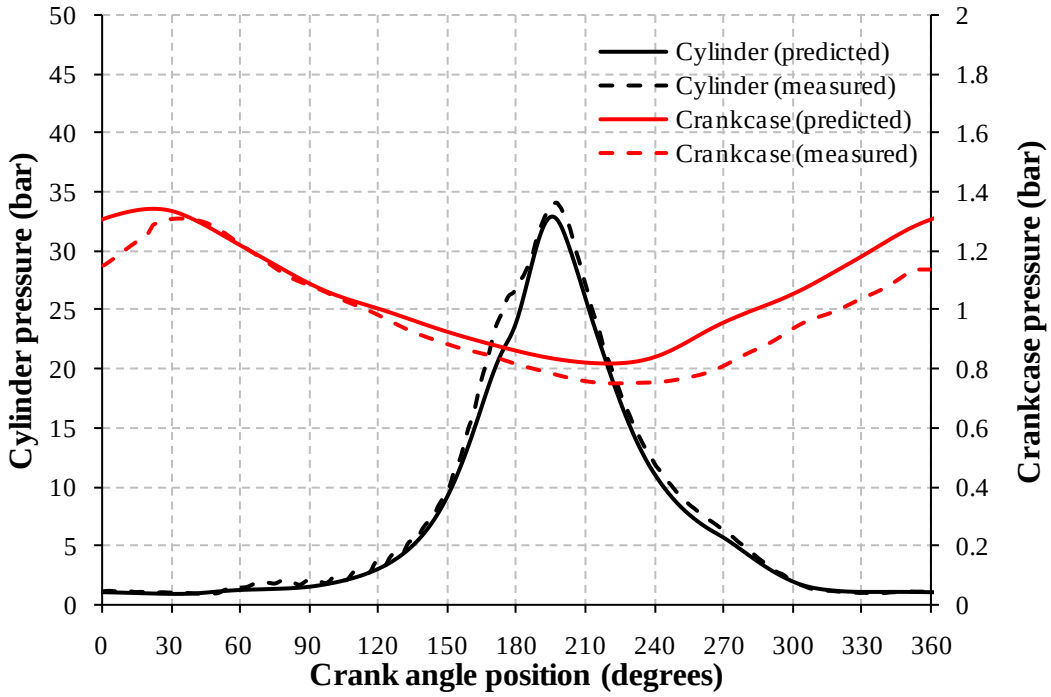

Figure 8-12, Cylinder pressure for the squish head half throttle at 8981 rpm

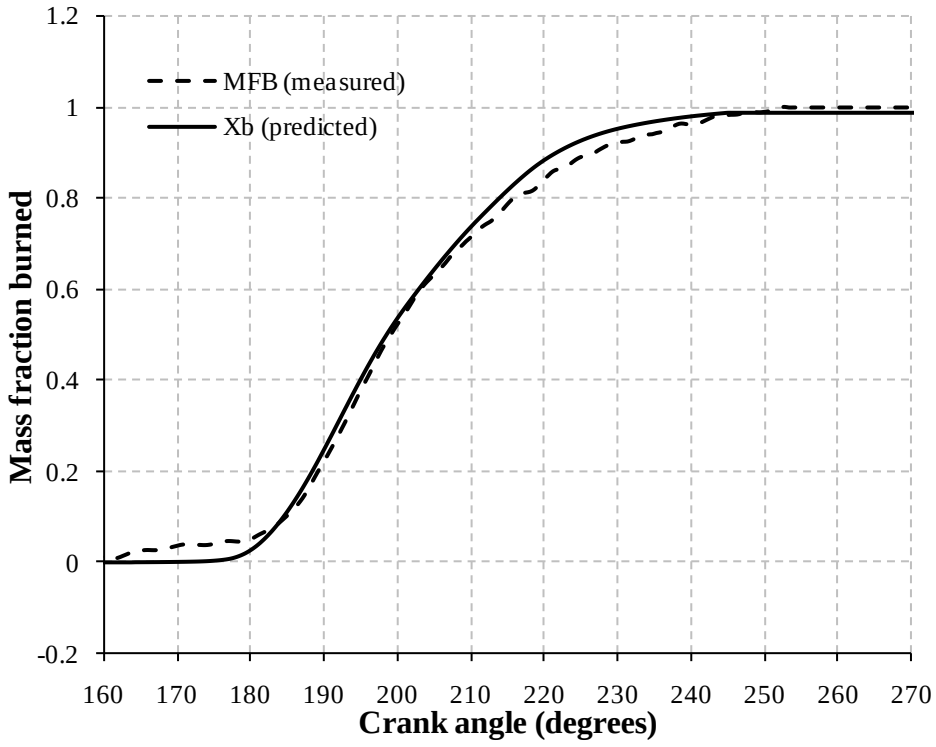

Figure 8-13, Mass fraction burned for the squish head half throttle and 8981 rpm

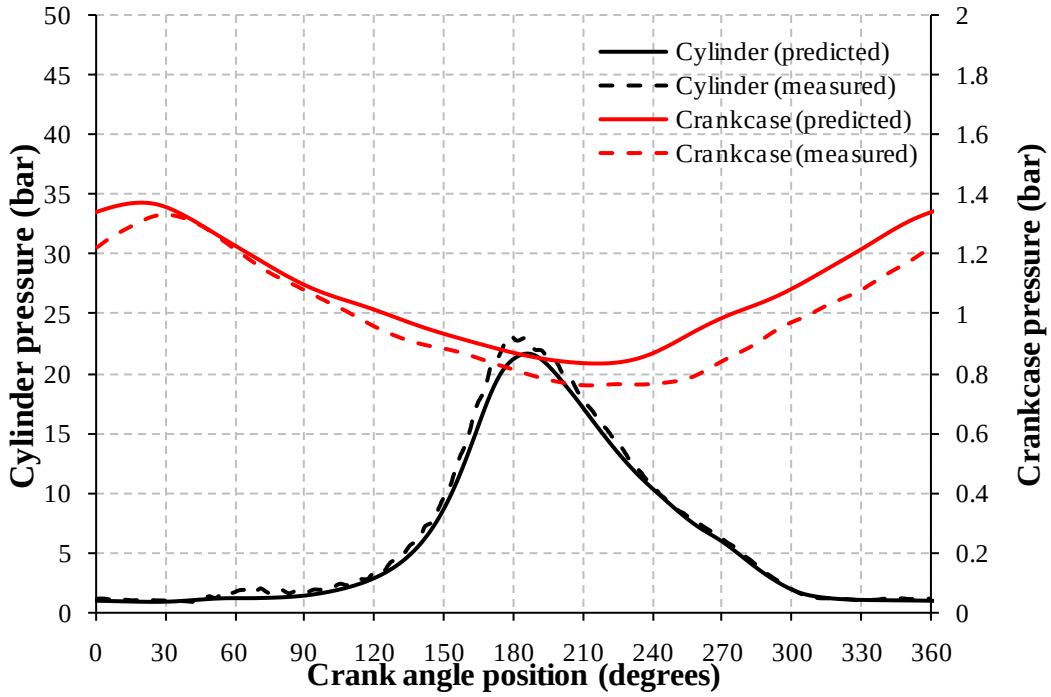

Figure 8-14, Cylinder pressure for the disc head half throttle and 8808 rpm

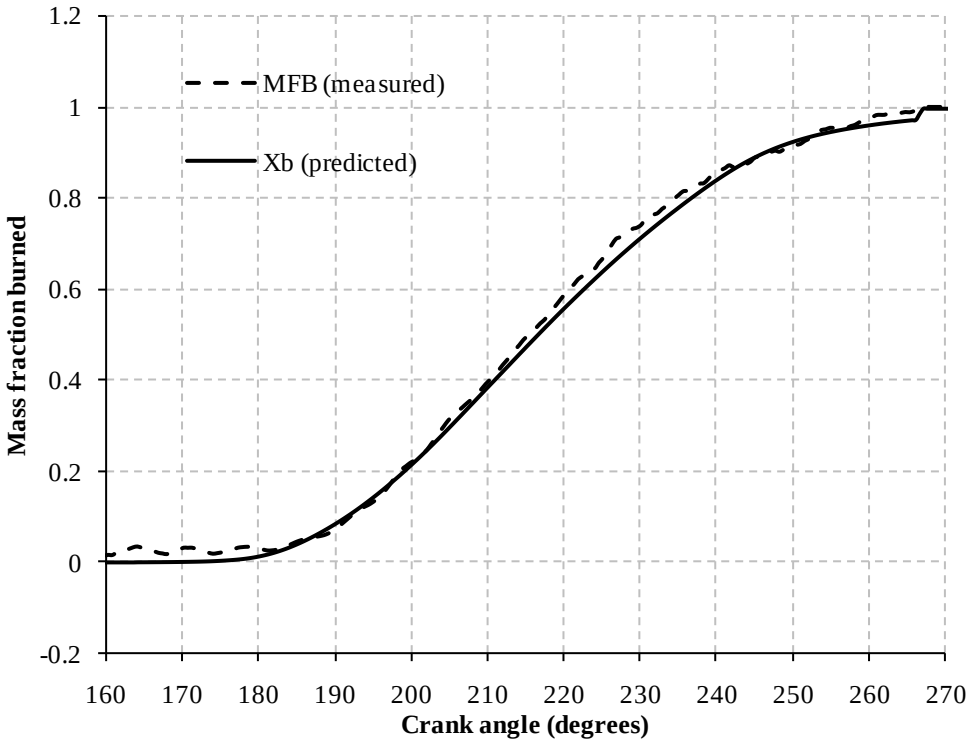

Figure 8-15, Mass fraction burned for the disc head half throttle and 8808 rpm

The causes for the difference in the fully developed burn rate between the two combustion chambers will include the spherical flame front area, which is defined by the flame front geometry model and the turbulent burning velocity, which is defined by the laminar burning velocity and the fractal model.

8.3 Flame Front Spherical Area

The spherical flame front area is defined by the geometry model and depends on both the combustion chamber geometry and piston position. With the piston at TDC the height of the disc combustion chamber is much less than the height of the squish combustion chamber. As the flame front expands with the piston near TDC it will, at some point, make contact with the piston crown. Once the flame front has reached the piston crown the flame front area becomes restricted.

Figure 8-16 shows the flame front areas predicted by the engine simulation for both the squish and disc combustion chambers. For the squish combustion chamber the engine conditions are 9075 rpm and full throttle whilst the disc combustion chamber conditions are 8896 rpm and full throttle. The graph shows that initially the flame front areas are similar as the flame kernel is small and unaffected by the piston position. At approximately 175° or 13.5° after spark time the area of the flame front in the squish combustion chamber increases rapidly whilst the flame area in the disc combustion chamber continues to grow at a slower rate. Figure 8-17 shows the flame front radius for both combustion chambers and also shows the instantaneous disc combustion chamber height. The graph shows that the point at which the flame front areas, for the two combustion chambers, begin to diverge is close to the point where the spherical flame front reaches the piston crown in the disc head.

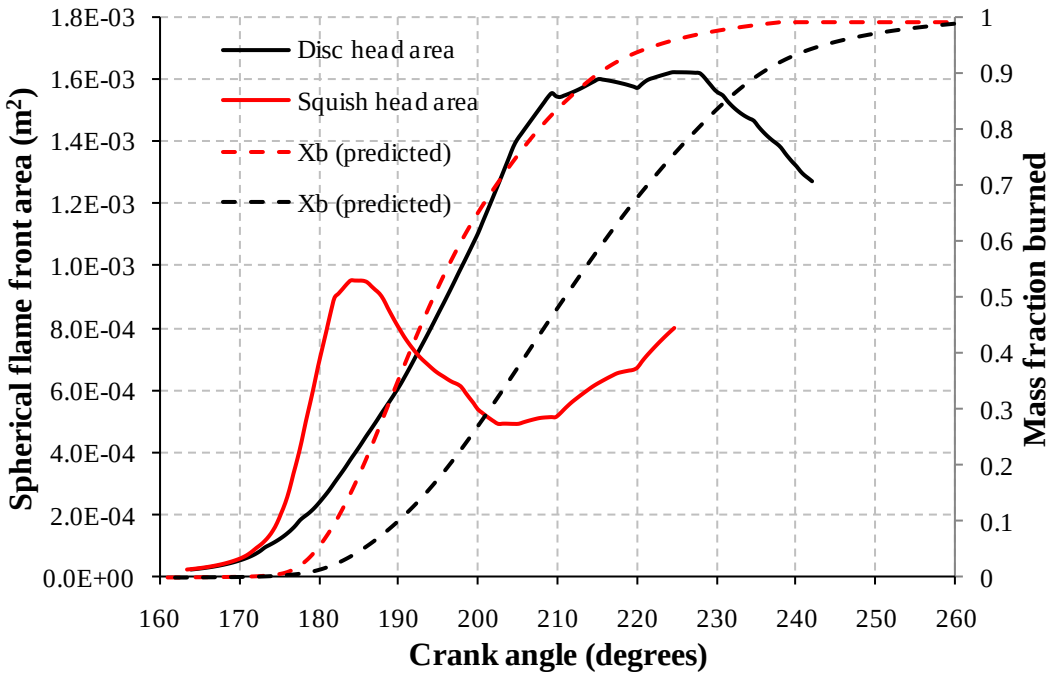

Figure 8-16, Flame front area for both disc and squish combustion chambers at full throttle and 8896 and 9075 rpm respectively

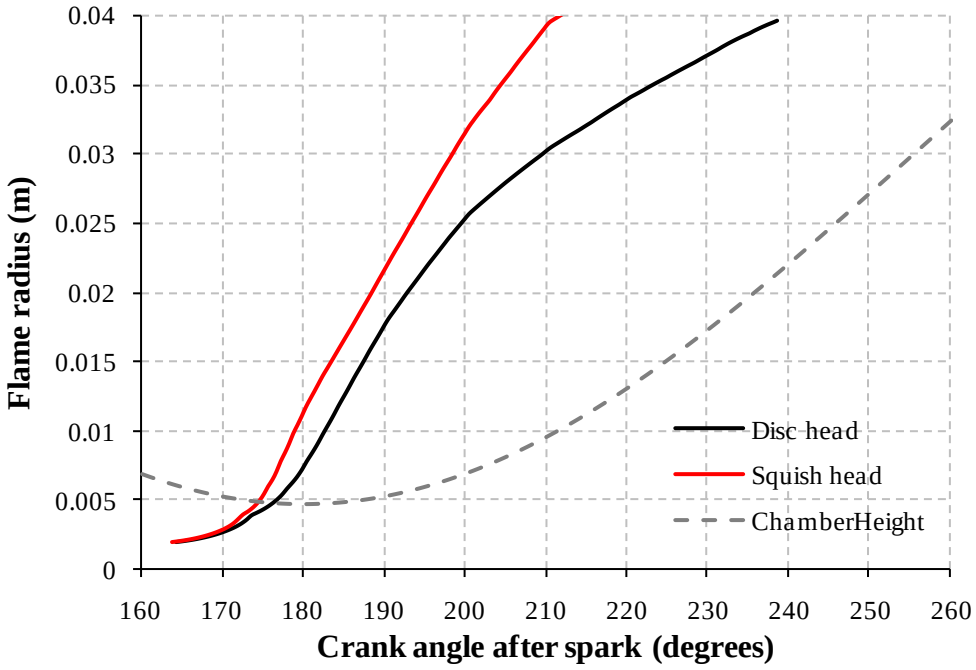

Figure 8-17, Flame radius for both disc and squish combustion chambers at full throttle and 8896 and 9075 rpm respectively

8.4 Tumble Velocity and Flame Offset

With the squish combustion chamber the tumble motion will advect the centre of the burned zone along the surface of the combustion bowl which in turn moves the flame front towards the piston crown. The tumble motion will cause the flame front to contact the piston earlier than if the flame front stayed centred at the spark plug location.

8.4.1 Predicted Tumble Velocities

The tumble velocities from the engine simulations for both squish and disc combustion chambers are shown in Figure 8-18. In each graph is plotted the tumble velocities from all the engine test speeds at the same throttle position. In these graphs 0° is at BDC. The peak tumble velocity occurs shortly before BDC during the scavenge period, this is approximately the same point as the maximum mass flow through the transfer ports. The mass flow rate through the transfer port is shown in Figure 8-19 for the squish head at full throttle and 9489 rpm. After BDC the tumble velocity quickly reduces due to the viscous shear effects, tumble momentum will also be lost through the exhaust port prior to closing shortly after 90° BTCD. The peak velocity location is consistent with the measured data from Reddy et al. (1986). The predicted tumble velocities are much greater than that measured by Reddy due to the engine speed and also due to the fact that the engine is firing under load and the exhaust gas dynamics cause an increase the delivery ratio. The predicted delivery ratio of the engine used by Reddy at full throttle and 3000 rpm was 0.61, motored, whilst the delivery ratio for the engine used in this study may exceed unity at full throttle, Figure 8-4. The peak tumble velocity does not occur at the maximum engine speed. It would appear that the peak velocity varies as a function of the delivery ratio rather than the engine speed.

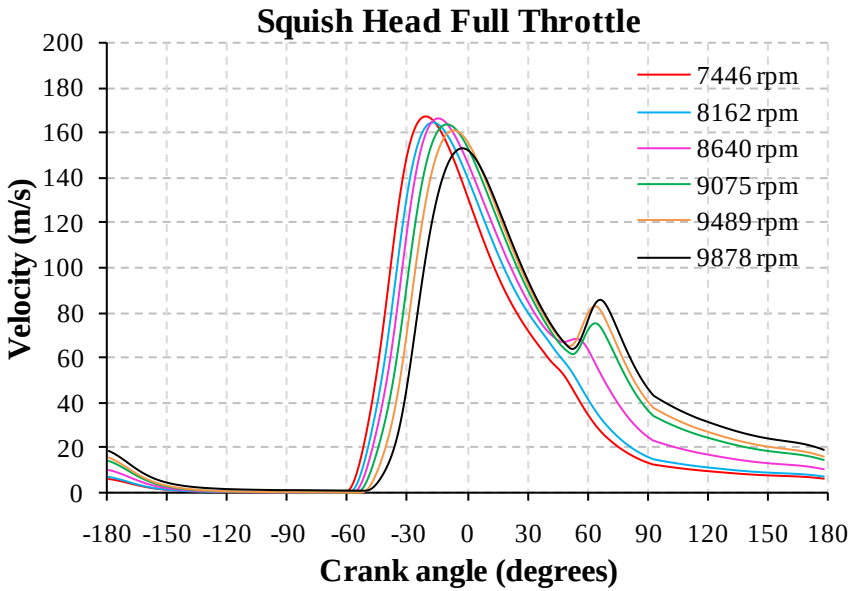

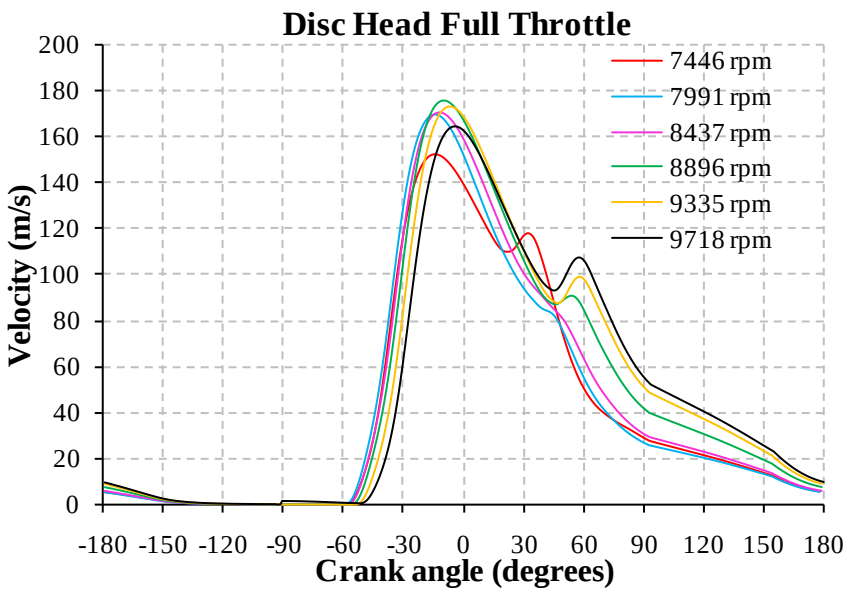

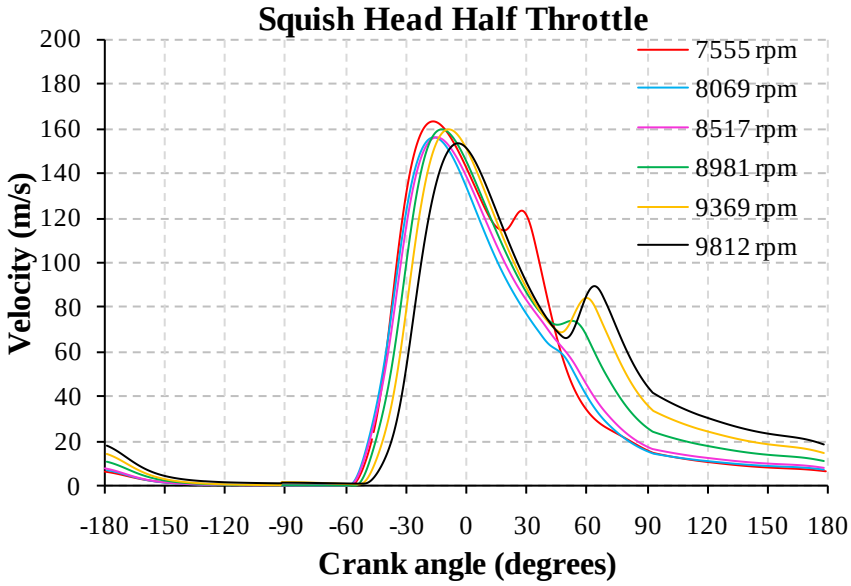

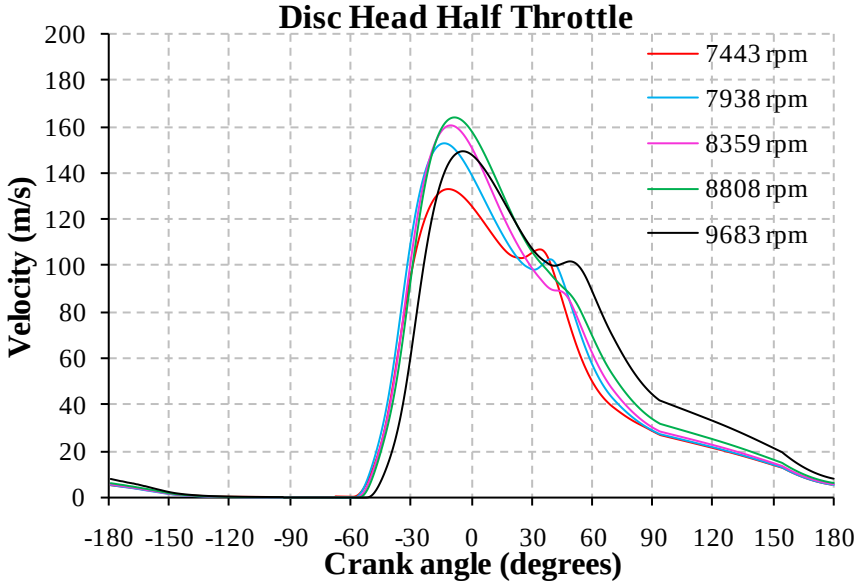

Figure 8-18, Tumble velocity

In the tumble velocity graphs just prior to the exhaust port closing and at approximately 60° there is a small increase in tumble velocity at engine speeds at and above 8640 rpm for the squish head and at and above 8896 rpm for the disc head. This small increase in tumble velocity can be explained by a reverse flow of gas from the exhaust system. Figure 8-19 shows the mass flow rate through the transfer and exhaust ports at full throttle and 9489 rpm and Figure 8-20 shows the mass flows at full throttle and 8162 rpm. At both engine speeds there is a reverse flow of gas through the exhaust port. The peak reverse mass flow rate occurs at approximately 45° and for the engine speed 9489 rpm is approximately three times greater than at 8162 rpm, the duration of the reverse flow is also slightly longer. The reverse flow will cause an increase in the tumble momentum, defined by Equation (3.6).

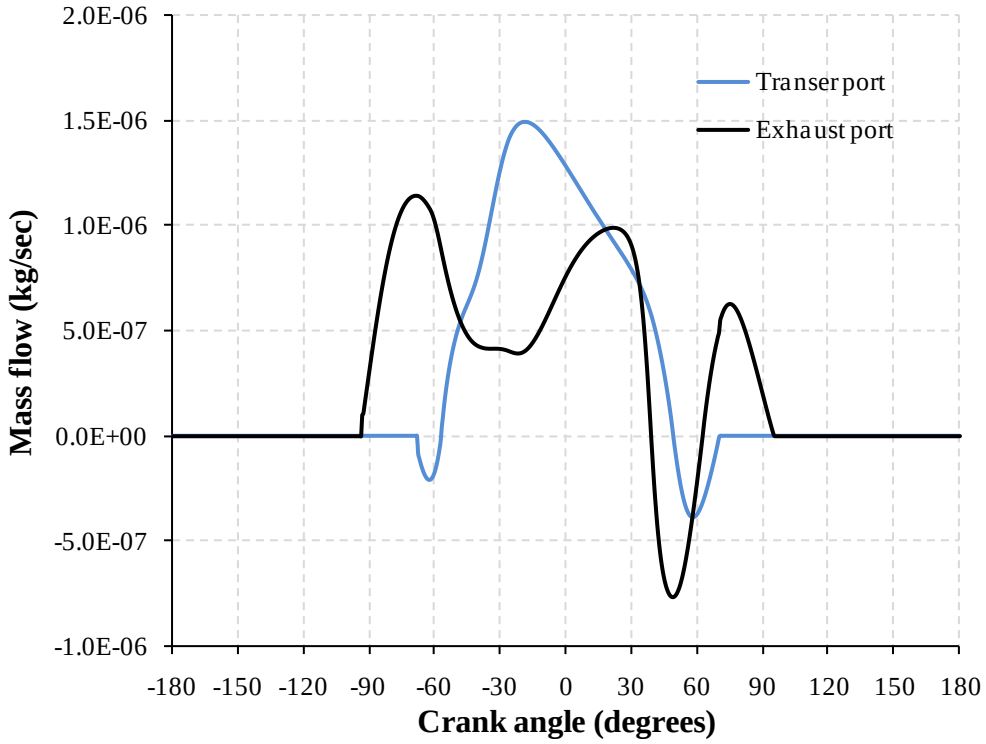

Figure 8-19, Port flow velocities squish head full throttle at 9489 rpm.

The engine speed which produces the peak tumble velocity, during the scavenge period, is not consistent with the engine speed that has the largest tumble velocity at TDC. The effects of the reverse flow is more significant at higher engine speeds as the exhaust system is

designed to produce best performance at just over 9000 rpm. The maximum tumble velocity at TDC occurs at the fastest engine speed, for both squish and disc combustion chambers and at both throttle positions.

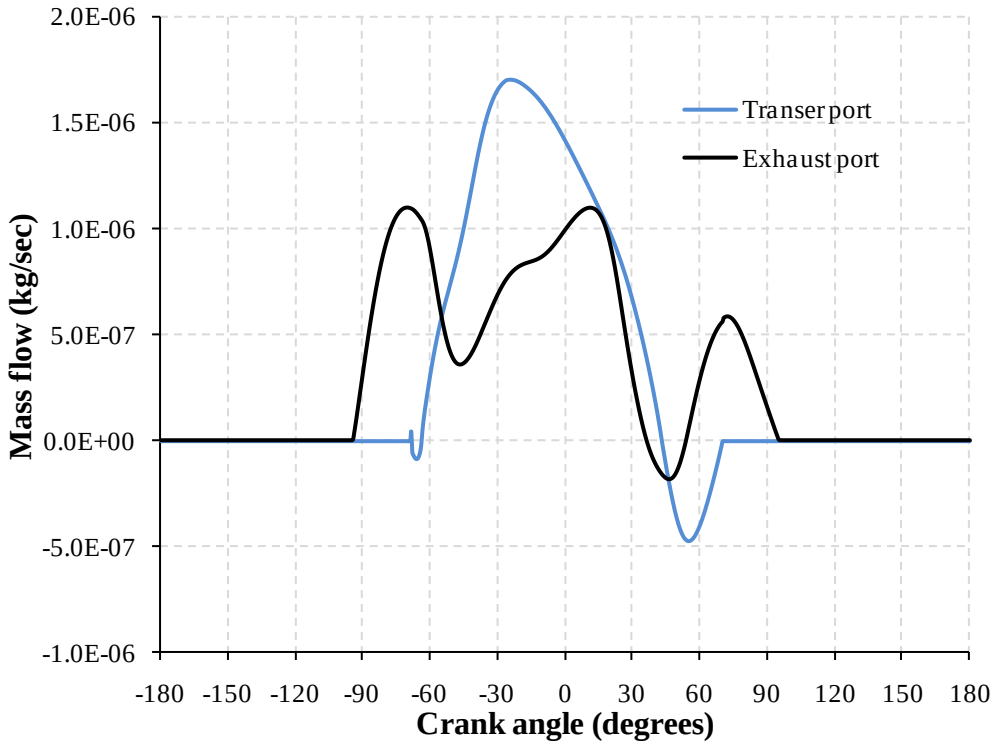

Figure 8-20, Port flow velocities squish head full throttle at 8162 rpm

At full throttle the increase in tumble velocity due to the reverse flow is greater with the squish combustion chamber than the disc combustion chamber. This difference will be due to the larger amplitude pressure waves in the exhaust duct of the engine using the squish combustion chamber. The larger pressure waves are produced by the greater cylinder pressures produced by the squish combustion chamber.

With the squish combustion chamber, after the exhaust port closes, the rate at which the tumble velocity reduces levels off. With the disc combustion chamber after the exhaust port closes the tumble velocity continues to reduce and there is increase in the rate at which velocity reduces at 150°. The increase in the rate at which velocity reduces is attributed to the instantaneous height of the combustion chamber and the limiting aspect ratio of the

ellipsoid vortex which causes a loss in mass of the tumbling vortex and consequently its inertia.

8.4.2 Flame Offset

The effect of the tumble velocity is to advect the flame front and burned zone from the spark plug location. In the engine tests six ionization probes were positioned on the tumble plane to monitor the flame front movement due to the tumble motion. Figure 8-21 below shows a spherical flame front offset from the spark plug location in the squish combustion chamber. The flame front in this case represents the mean spherical flame front rather than the wrinkled flame front. In the engine tests the mean flame arrival time at each of the probes was determined based on a statistical approach, as described in Chapter 7. In the simulation, with the flame radius and offset determined, the point at which the spherical flame front contacts the cylinder head surface can be defined.

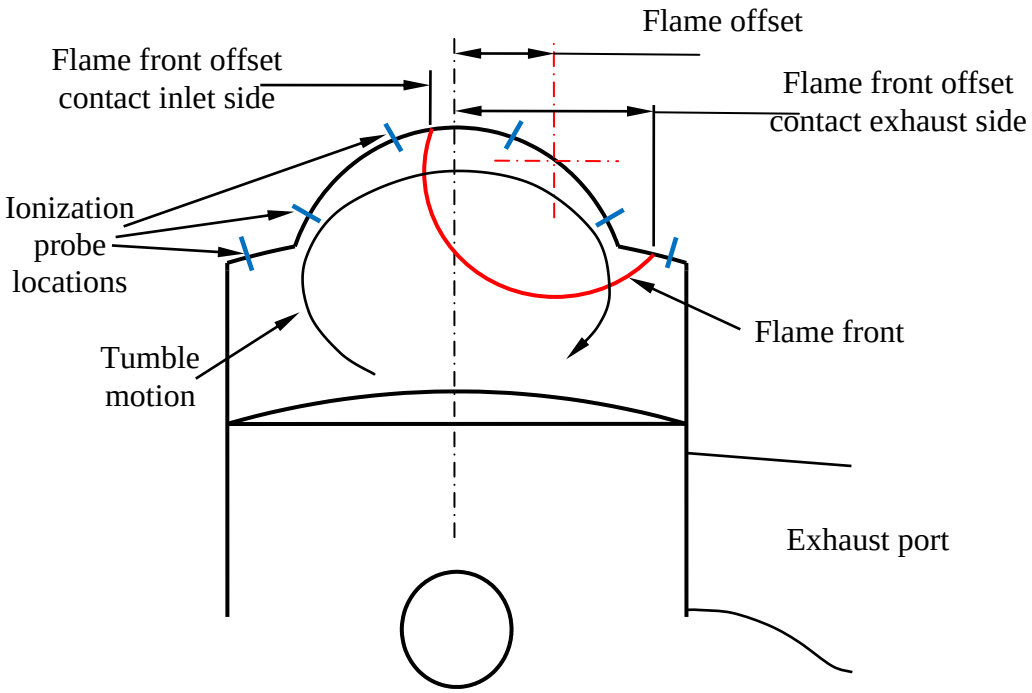

Figure 8-21, Flame front contact with cylinder head

In Figure 8-21 the flame front offset contact is defined as the dimension from the cylinder axis to the flame front point of contact with the cylinder head. The flame front offset contact is calculated in the x direction both towards and away from the exhaust port. In Figure 8-22 the flame front offset contact, calculated by the engine simulation, has been plotted against crank angle. The flame offset is plotted as positive in both directions, towards and away from the exhaust port. Also plotted in Figure 8-22 are the mean flame front arrival times measured by the ionization probes. There is a reasonable correlation between the predicted flame front offset contact and measured flame arrival times. Figure 8-23 is a similar graph to Figure 8-22 but at 8162 rpm for the squish head. At 8162 rpm the predicted and measured offsets, both towards and away from exhaust port are closer together which indicates that the burned zone has been advected by the tumble vortex by a lesser amount than at 9075 rpm, this will be due to a lower tumble velocity.

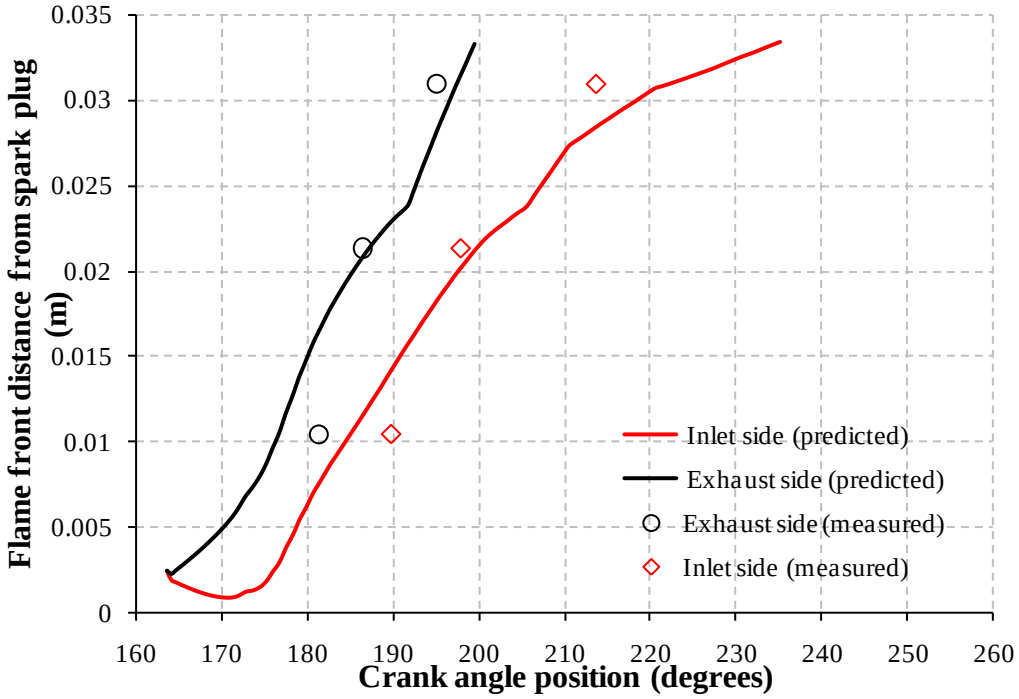

Figure 8-22, Flame front offset squish head at full throttle and 9075 rpm

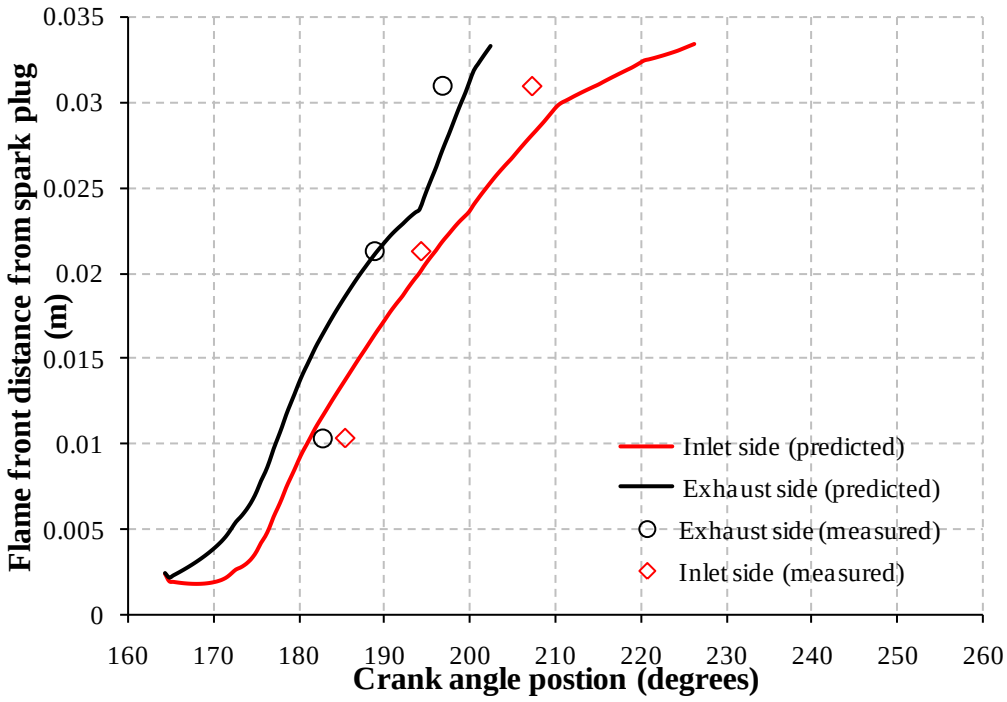

Figure 8-23, Flame front offset squish head at full throttle and 8162 rpm

Similar graphs have been plotted for the disc combustion chamber at 8896 rpm and 7991 rpm at full throttle in Figure 8-24 and Figure 8-25. Again there is a reasonable correlation between the predicted flame offset contact and the measured arrival times. With the disc combustion chamber there appears to be less difference between the flame offset at the two engine speeds as seen on the squish head. Again the offset measurements indicate a larger tumble velocity at the higher speed. Flame offset graphs for all the engine test conditions are given in Appendix D.

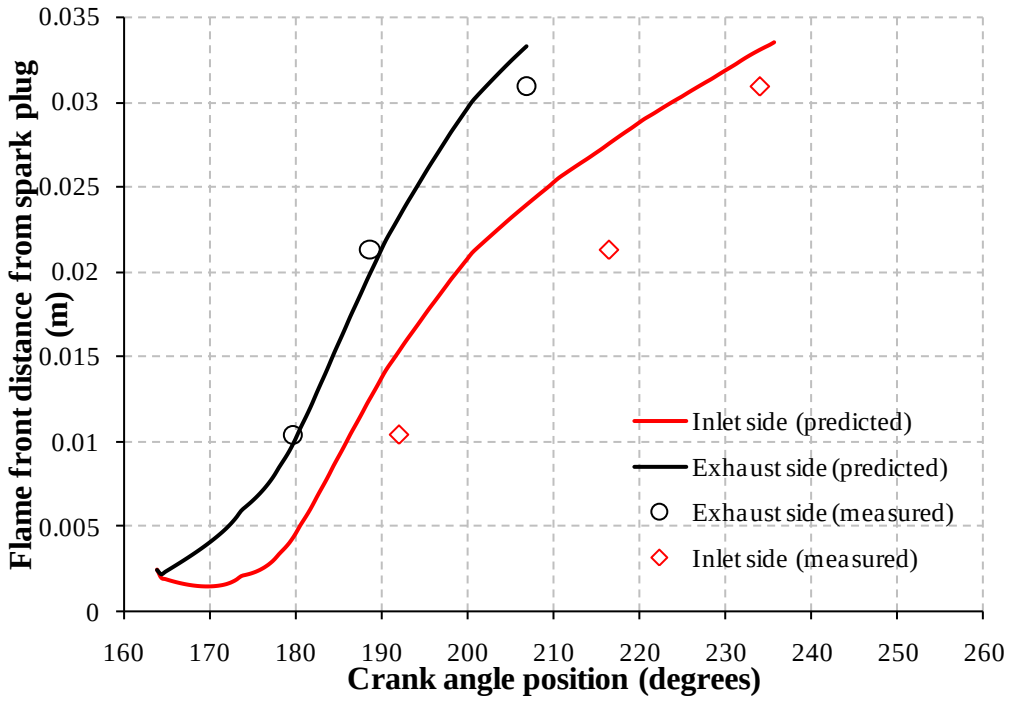

Figure 8-24, Flame front offset disc head at full throttle and 8896 rpm

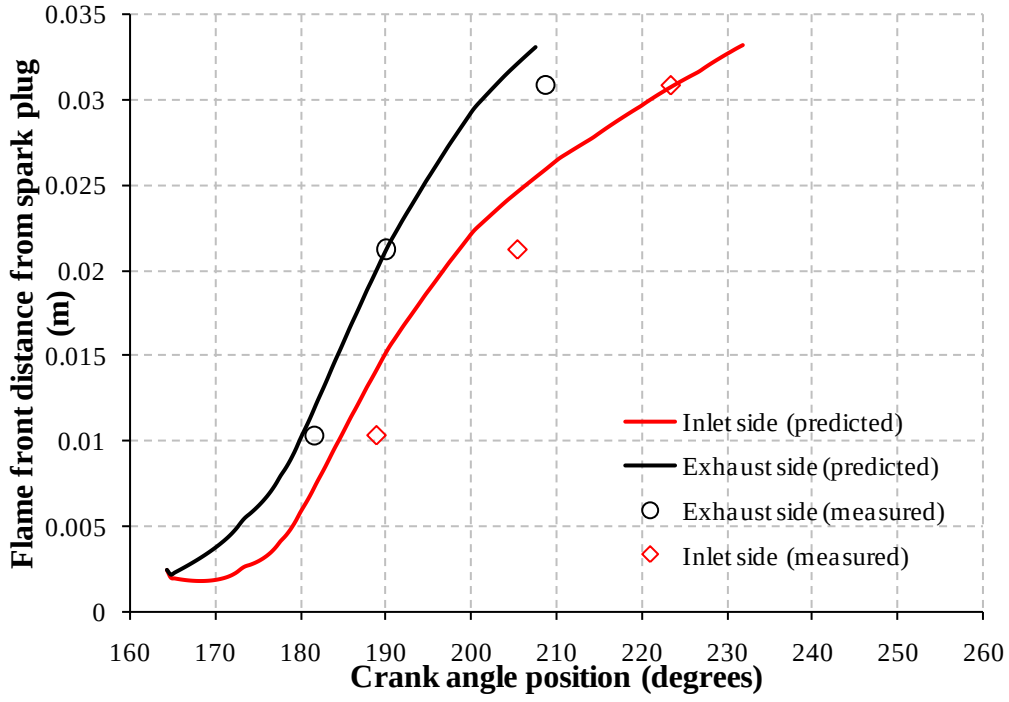

Figure 8-25, Flame front offset disc head at full throttle and 7991 rpm

Below, plotted in Figure 8-26, are the predicted spherical flame front centre offset for the squish head at full throttle and each of the engine speeds. The flame centre offset is measured in the x direction from the cylinder axis. Plotted in Figure 8-27 are the predicted flame centre offsets for the disc head at full throttle and each of the engine speed test points. The flame centre offset in the squish combustion chamber is greater than that in the disc combustion chamber, this is due to the size of the tumble vortex. For the squish combustion chamber the major diameter of the ellipsoid vortex shown in Figure 3-11, is greater than the major diameter in the disc head due to the chamber height and the limiting aspect ratio of the vortex. The offset in the disc chamber will reach a maximum when the offset reaches half the major diameter of the vortex.

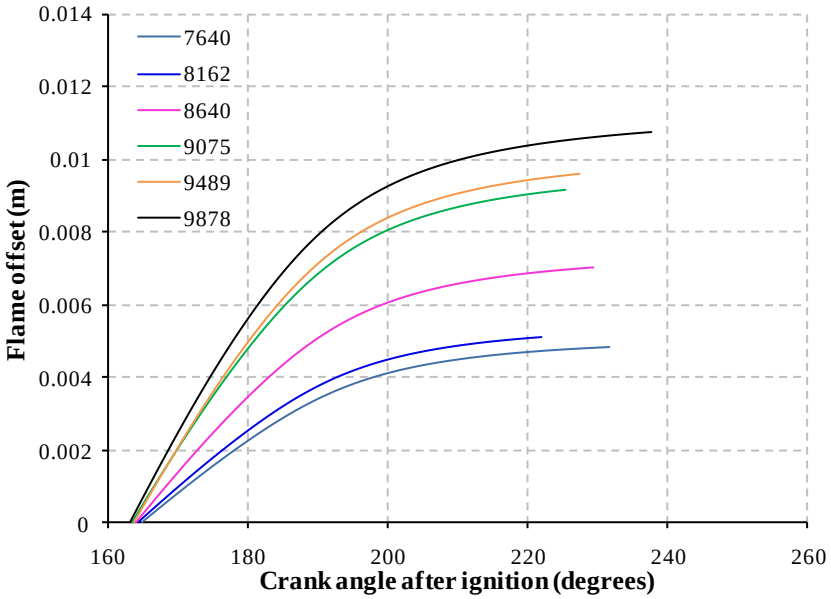

Figure 8-26, Flame offset squish head full throttle

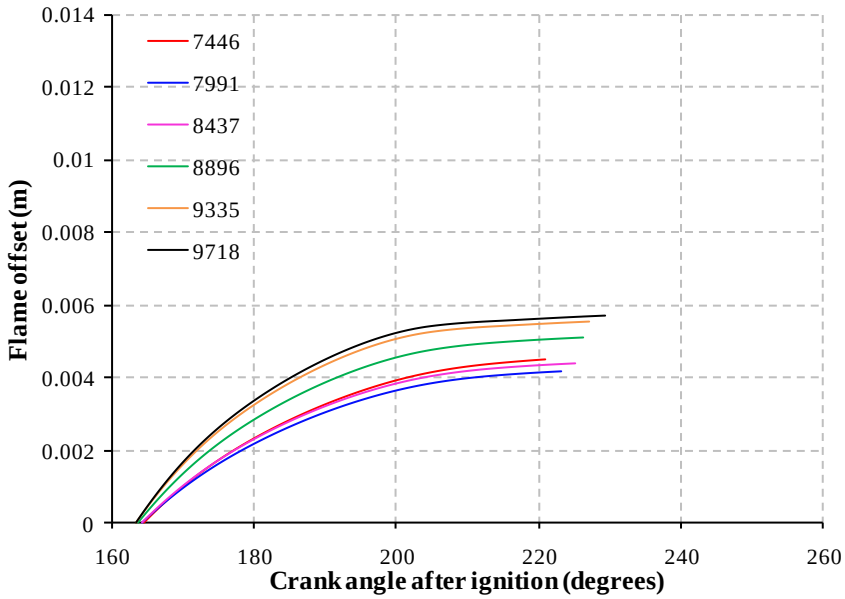

Figure 8-27, Flame offset disc head full throttle

8.5 Turbulence Flame Propagation and Structure

The turbulent flame regime in a combustion system may be defined using the modified Borghi diagram. The flame regime is dependent upon the turbulent intensity, laminar burning velocity, integral scale and laminar flame thickness. The fully developed turbulent flame structure will not however be present immediately following spark timing. As shown on the mass fraction burned graphs there is a delay between spark timing and any indication of combustion. After the ignition delay the combustion rate increases until it reaches the near constant fully developed turbulent burning velocity.

8.5.1 Turbulence Intensity

As well as the fully developed turbulent flame, the ignition delay and early flame development are also dependent on the turbulence intensity. The turbulence intensities are shown in Figure 8-28 for both the cylinder heads and at both throttle positions. The peak intensities occur near BDC during the scavenge period which is consistent with the time of peak tumble velocities, the intensity then reduces with the tumble velocity. After approximately 135° the turbulence for the disc head reduces quicker than the turbulence in

the squish head, this is due to the smaller tumble vortex with less momentum in the disc combustion chamber which produces less turbulent kinetic energy. The tumble vortex in the squish combustion chamber retains its mass longer during the compression stroke due to the combustion chamber height and the limiting ellipse ratio. The tumble vortex is then able to generate more turbulence due to the viscous shear stresses at the surface of the vortex towards the end of compression stroke. An increase in turbulence intensity later in the compression stroke was predicted using CFD analysis for domed cylinder heads rather than disc cylinder heads by Tsui and Cheng (1995). The domed cylinder heads will have a larger combustion chamber height at TDC than a disc head which results in a larger tumble vortex later in the compression stroke.

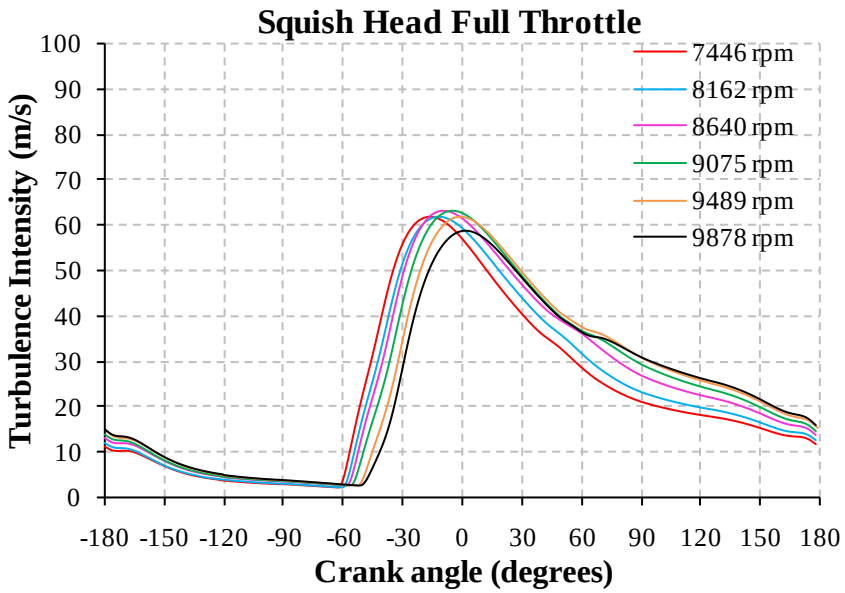

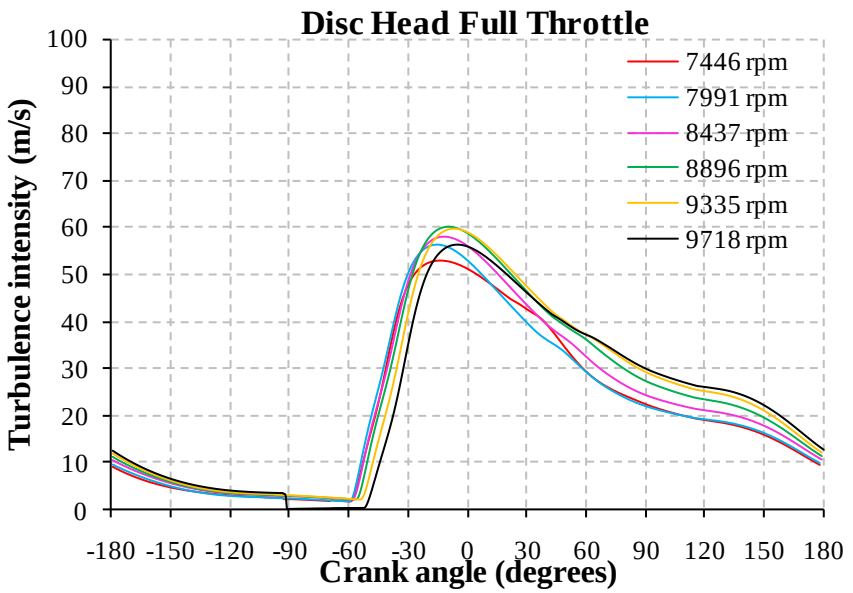

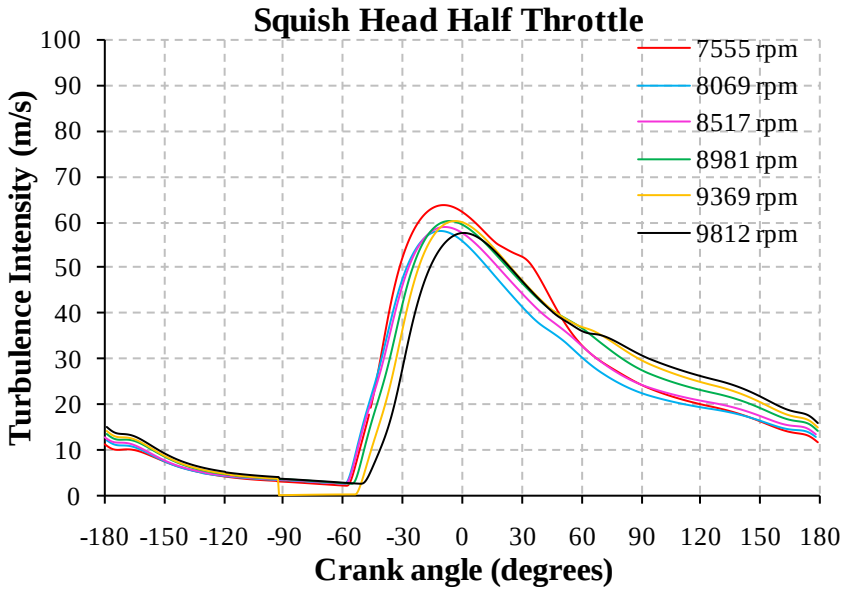

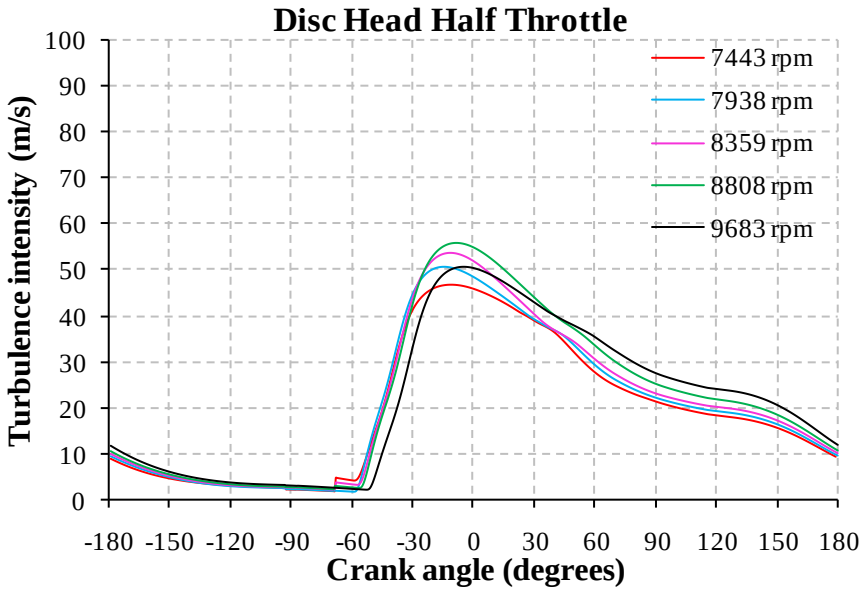

Figure 8-28, Turbulence intensity

8.5.2 Ignition Delay

The ignition delay period was discussed in Section 4.6 and was defined as a function of the tumble velocity, turbulence intensity and laminar burning velocity. For both the squish head and the disc head at both full and half throttle the same coefficients were used in the ignition delay model, the constant was set at 0.0015 and the polynomial coefficients were $\alpha = 0.5$, $\beta = 0.85$ and $\gamma = 0.3$

8.5.3 Early Flame Development

After the ignition delay period a flame kernel of 2 mm radius is formed, initially the flame kernel is considered as having a smooth laminar flame front. As the flame radius grows the flame front becomes increasingly wrinkled, the degree of wrinkling is defined by the fractal dimension, D_3. Figure 8-29 below shows how the fractal dimension and the maximum scale of wrinkling, L_{max}, change during the early flame propagation. The maximum scale of wrinkling is defined as a function of the spherical flame radius up until the radius exceeds half the integral scale multiplied by the model constant c_{Lmax}.

8.5.4 Fully Developed Flame

Once the spherical flame radius exceeds half the integral scale multiplied by the model constant c_{Lmax}, the flame front is considered to be fully developed. The most significant mechanism that enhances the turbulent burning velocity is considered to the increase in flame front surface area due to flame wrinkling. The wrinkled flame front area is defined by the fractal model with fractal dimension given by the Santavicca equation. Figure 8-29 also shows that after reaching a peak value the fractal dimension reduces as the turbulence intensity decays.

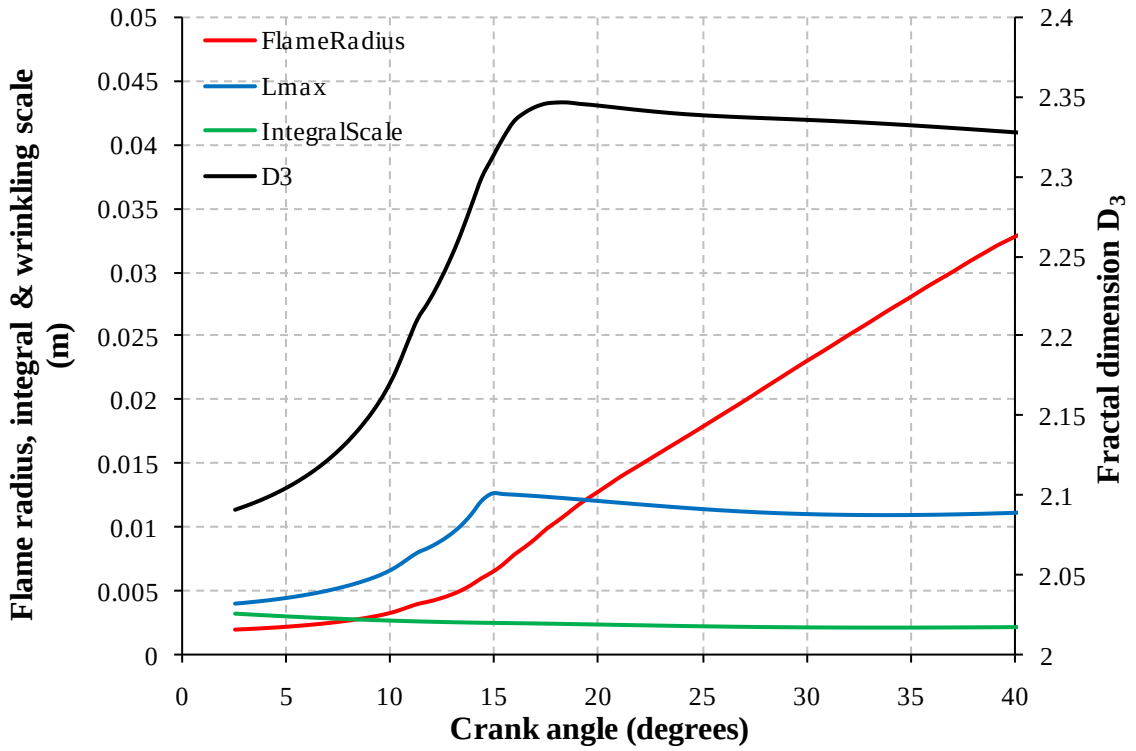

Figure 8-29, Fractal dimension during flame growth in the squish head at full throttle and 9075 rpm

The turbulent flame structure has been characterised by the modified Borghi diagram shown in Figure 8-30. Four separate diagrams are shown for the squish and disc combustion chambers at full and half throttle. In each of the diagrams the predicted flame regime is above the corrugated flamelet line which indicates that the flame front may become wrinkled and folded to a point where adjacent flamelets interact to cut off pockets or islands of fresh charge. As well as the wrinkled flame front a second mechanism which enhances flame propagation, reactant islands, is used in the combustion model. The RIFF model was described in Section 4.5.2.

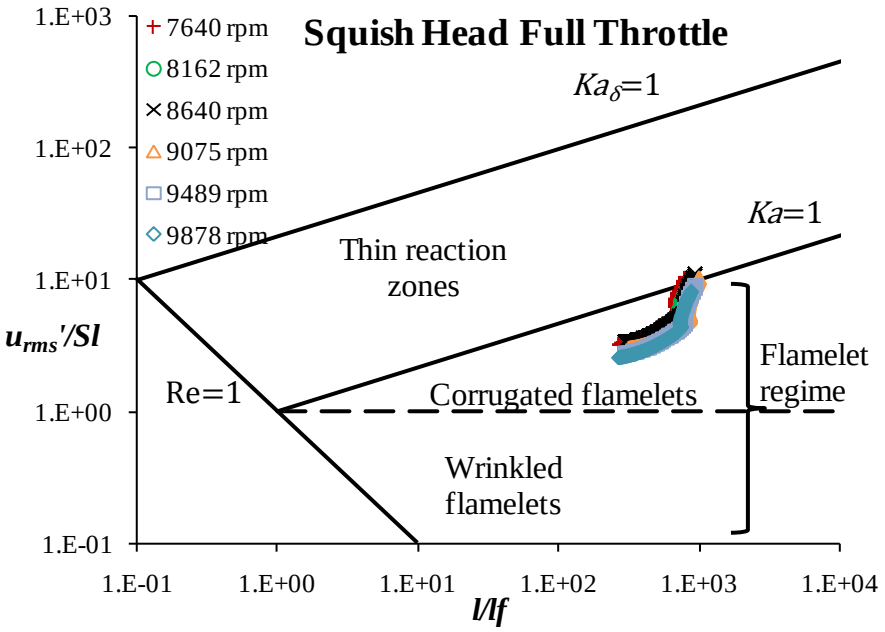

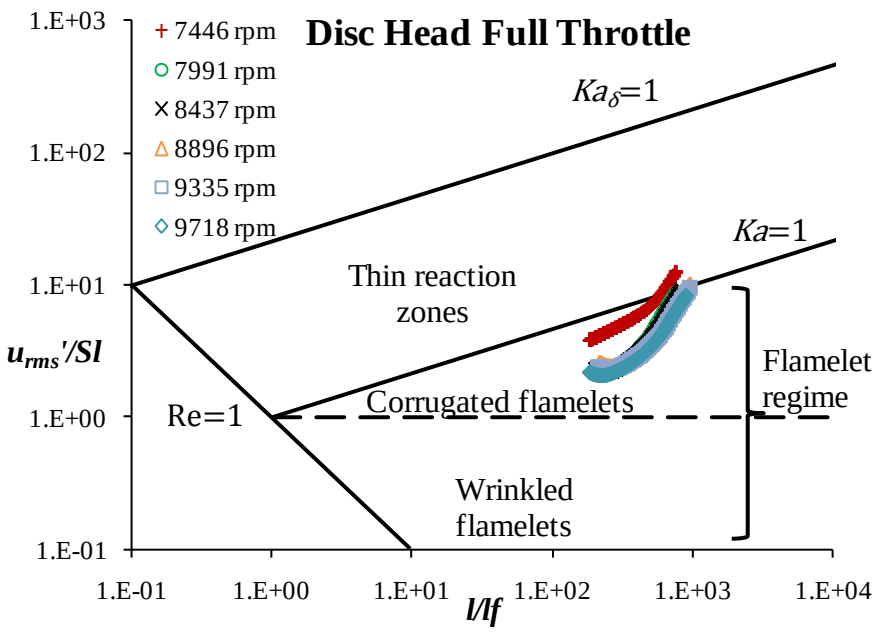

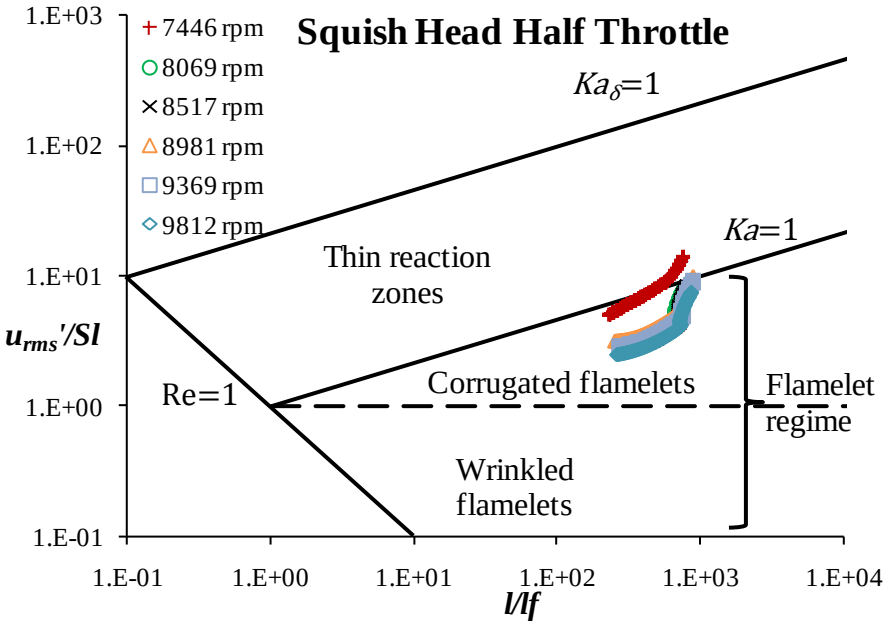

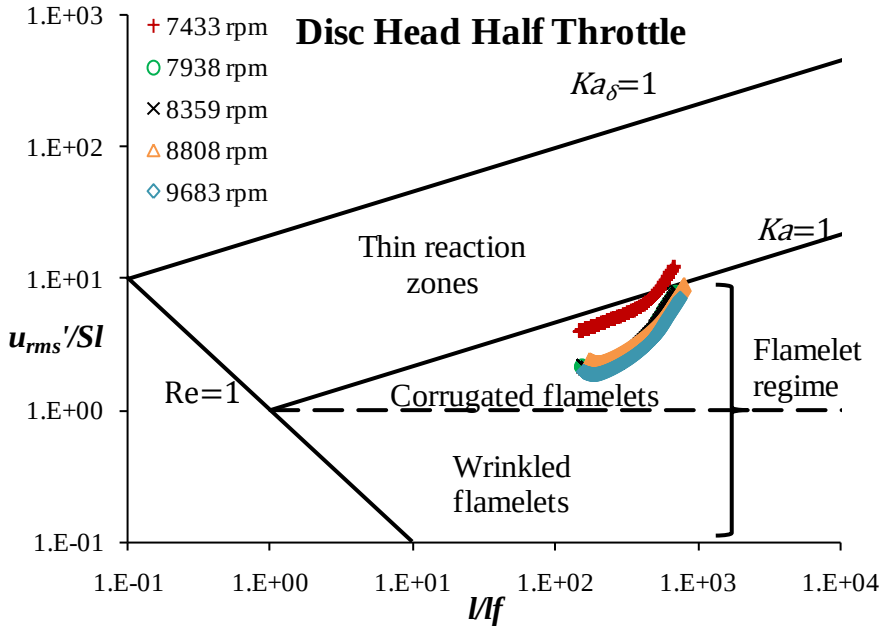

Figure 8-30, Modified Borghi flame regime diagrams

8.5.5 Fractal Dimension and Islands Fraction

The combustion model developed here is based on flame front wrinkling but also includes pockets or islands of reactants which are entrained and subsequently consumed. The mass fraction burned at the wrinkled flame front and the fraction burned as islands is defined by the RIFF model, discussed in Section 4.5. The mass burn rate at the wrinkled flame front is defined by the spherical flame front geometry, the minimum and maximum scales of wrinkling and the fractal dimension, D_3, which is given by Santavicca Equation (4.25). The variable D_T in Equation (4.25) represents the maximum possible fractal dimension and has been given a value of between 2.35 and 2.38 in other fractal combustion models, Bozza et al. (2005), Matthews and Chin (1991), Wu et al. (1993) and Verhelst and Sierens (2007). In this study the value of D_T is used as an adjustable model constant which has been adjusted to match predicted cylinder pressure with measured data. The RIFF model has a model constant c_{RIFF} is used to define the mass fraction of the combustion zone burned as islands. To evaluate the RIFF model a number of simulations have been carried out with the squish combustion chamber at 9075 rpm and full throttle, in these simulations different values of D_T and c_{RIFF} have been used. The values for D_T were set whilst the value of c_{RIFF} was adjusted to produce a reasonable correlation between measured and predicted cylinder pressure. Figure 8-31 below shows the measured and predicted cylinder pressures from the simulations with differing values of D_T and c_{RIFF} constants the values of which are given in Table 8-3.

Table 8-3, Fractal dimension and RIFF constants

D_T	c_{RIFF}
2.32	0.2
2.34	0.16
2.36	0.115
2.38	0.07
2.4	0.03
2.41	0.001

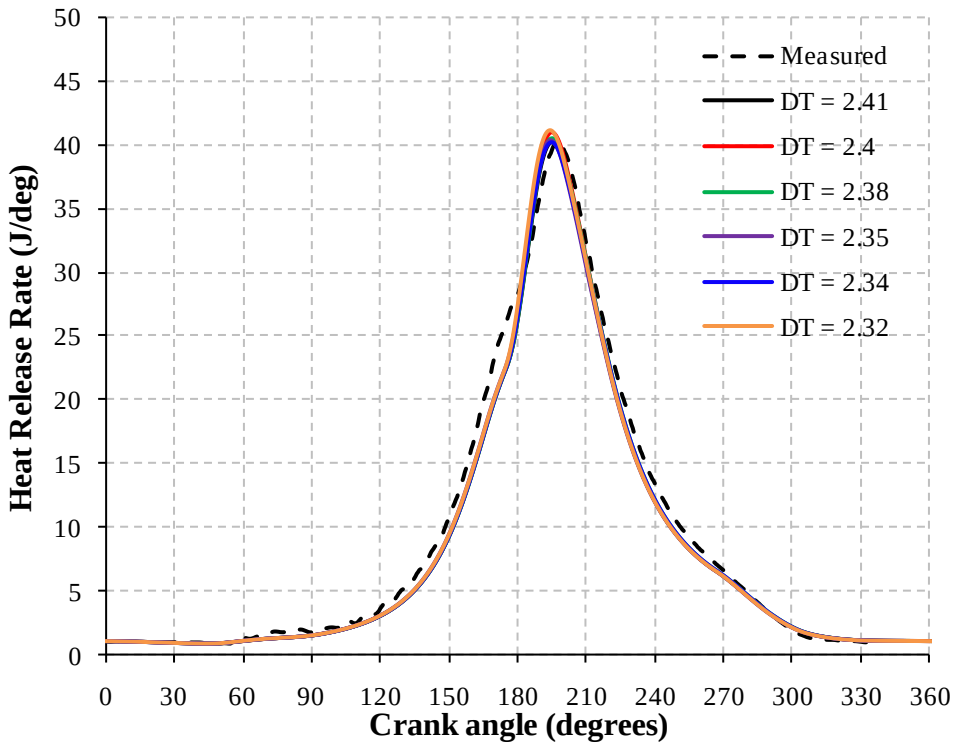

Figure 8-31, Cylinder pressure development with various values for D_T for the squish head at full throttle and 9075 rpm

The predicted cylinder pressures for the different fractal and RIFF model constants are all very similar. The heat release rate for each of the cases is shown below in Figure 8-32, again the different model coefficients produce similar results. The mass fraction burned for each case is shown in Figure 8-33 and once again the results are very similar.

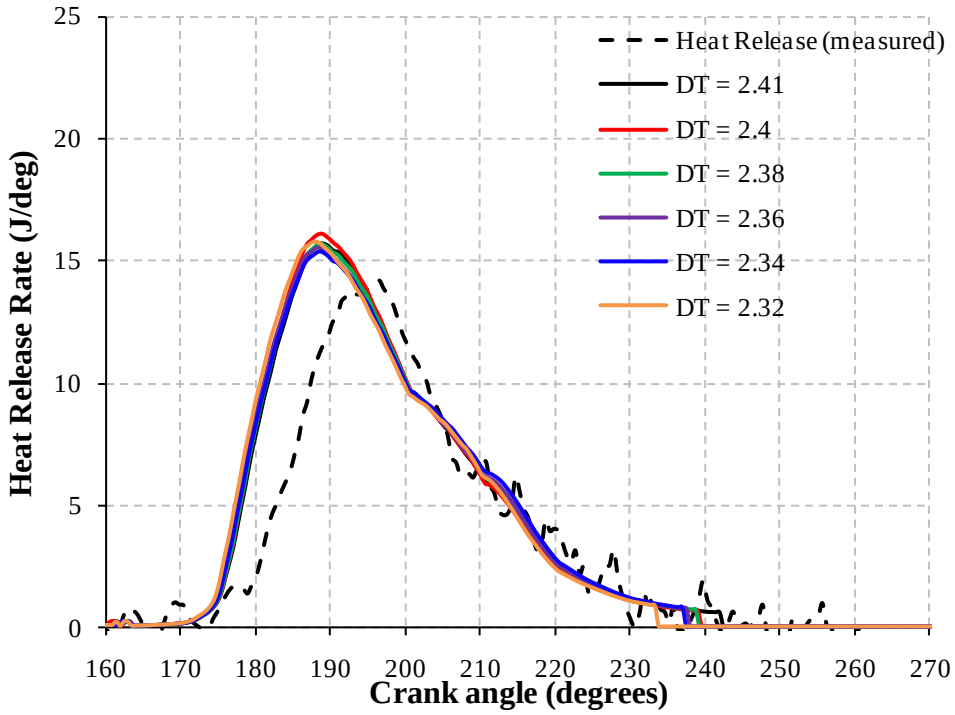

Figure 8-32, Heat release rate with various values for D_T for the squish head at full throttle and 9075 rpm

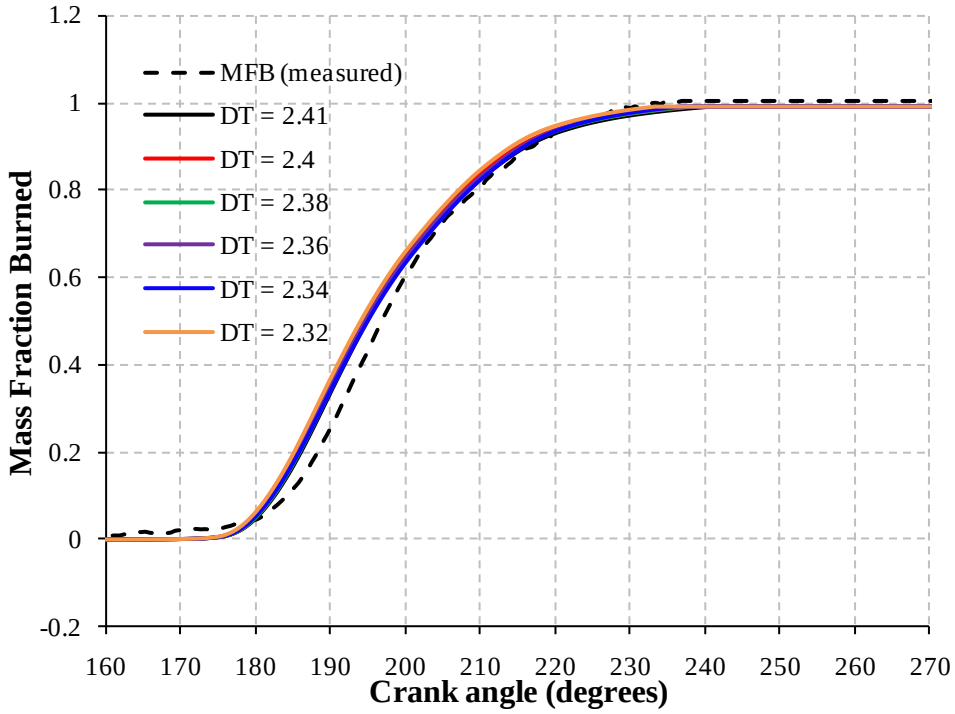

Figure 8-33, Mass fraction burned with various values for D_T for the squish head at full throttle and 9075 rpm

Both the fractal dimension and the fraction burned as islands are determined by equations that include the turbulent intensity as a variable. The fractal dimension has been plotted below in Figure 8-34 for each of the simulations. The early development of the flame is characterised by the fractal dimension which increases rapidly upto the point that the flame radius reaches half the maximum scale of wrinkling at which point the fractal dimension reaches a peak. The peak fractal dimension is always less than the D_T value used in the Santavicca equation.

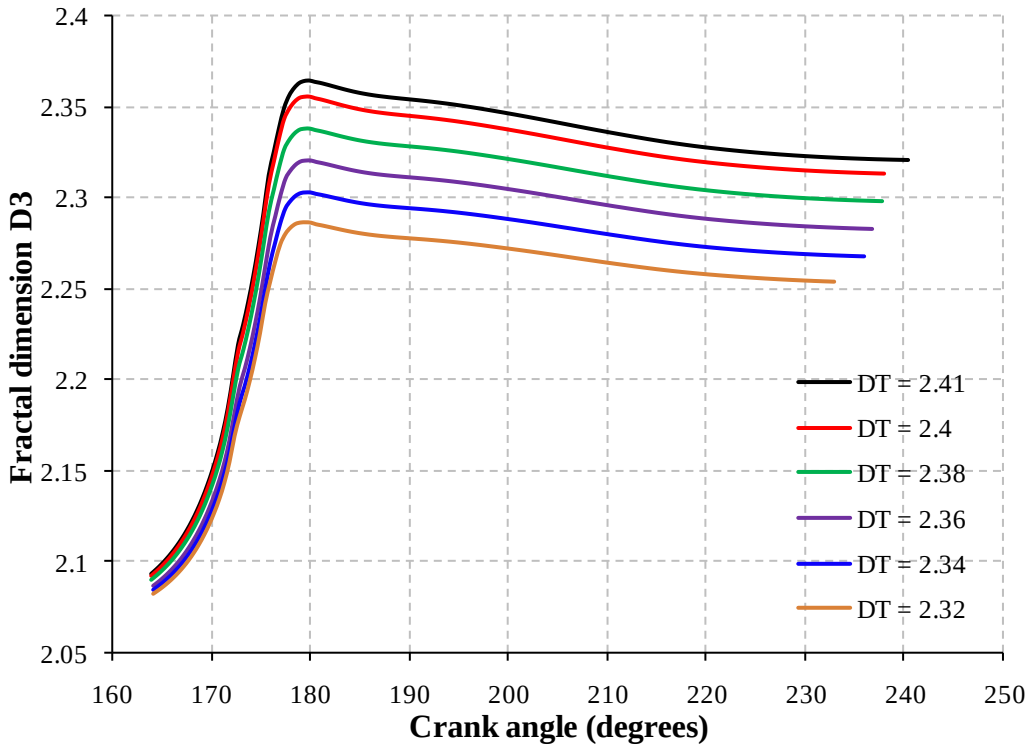

Figure 8-34, Fractal dimensions calculated during the simulation with different values of D_T for the squish head at full throttle and 9075 rpm

Below in Figure 8-35 is plotted the mass fraction burned as islands for the different simulation cases. As with the fractal dimension the fraction burned by islands increases rapidly as the spherical flame front radius increases. The maximum fraction burned by islands is approximately 13.5% when D_T is set at 2.32 and c_{RIFF} set at 0.2. After reaching its peak value islands fraction reduces as the turbulence intensity continues to dissipate, then

after 195° the fraction burned by islands increases again and this is due to the reduction in laminar burning velocity relative to the turbulence intensity.

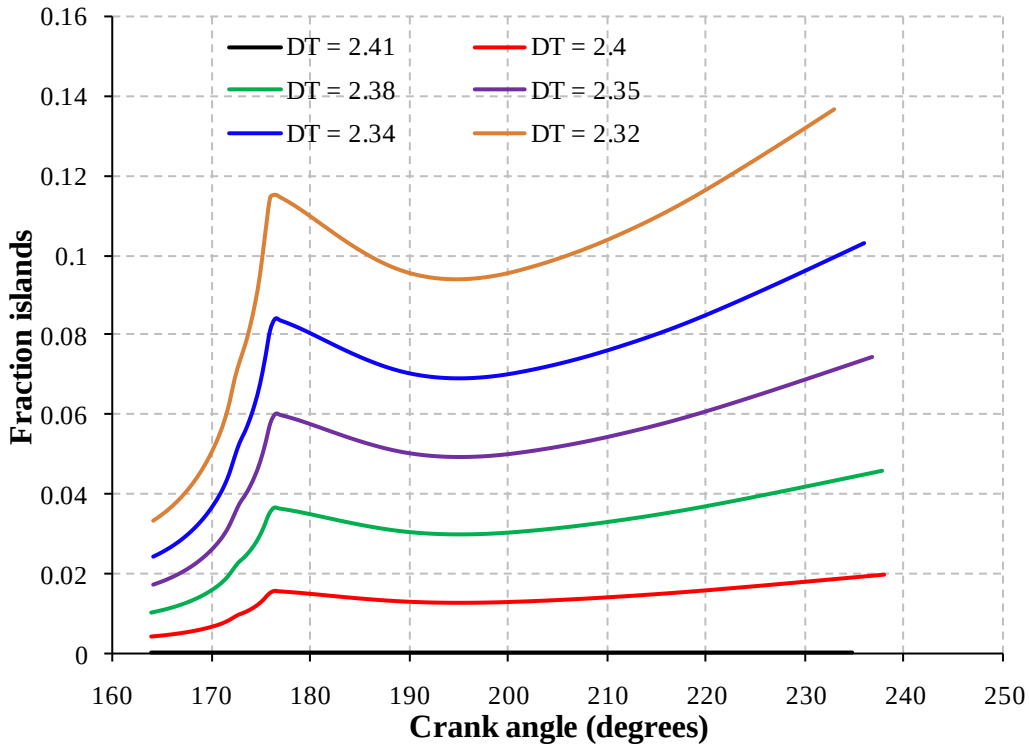

Figure 8-35, Fraction burned as islands calculated during the simulation with different values for C_{RIFF} for the squish head at full throttle and 9075 rpm

8.6 Heat Release With and Without Flame Offset and Brush Volume

Quasi-dimensional models usually define the heat release rate as a function of the infinitely thin spherical flame front area. It is also often assumed that the flame remains centred at the spark plug. The combustion model developed in this study accounts for both wrinkled flame brush thickness and an off centre flame. To assess the effects of the wrinkled flame brush thickness the whole engine simulation code developed here has been used to model the combustion process assuming an infinitely thin spherical flame front. The operating condition considered was for the squish head at full throttle and 9075 rpm. Further simulations have also been conducted with the flame front centred at the spark plug to assess the effects of the offset flame front. Plotted in Figure 8-36 are measured heat release rate and predicted heat release rate. The solid black line in the graph represents the heat release

when the wrinkled flame brush thickness and offset due to the tumble motion are accounted for. The red line represents the heat release rate calculated without accounting for the offset flame or the wrinkled brush zone. The heat release rate predicted by the infinitely thin, central flame front (red line) can be compared with the predicted heat release rate produced by Reid (1993), shown in Figure 2-3. The two predicted heat release curves both show the same characteristic inflection after the peak heat release rate. The inflection in the heat release curve at approximately 200° is due to the flame front interaction with the combustion chamber squish area. At the inflection point the flame front area is a minimum, this is shown schematically in Figure 4-15. After approximately 200° there is an increase in heat release rate which is due to an increase in the spherical flame front area produced by the downward motion of the piston. By accounting for the flame offset and the wrinkled flame brush thickness the inflection in the latter part of the combustion process is removed. This is purely due to the geometrical effect of the flame front area discussed in Section 4.9.

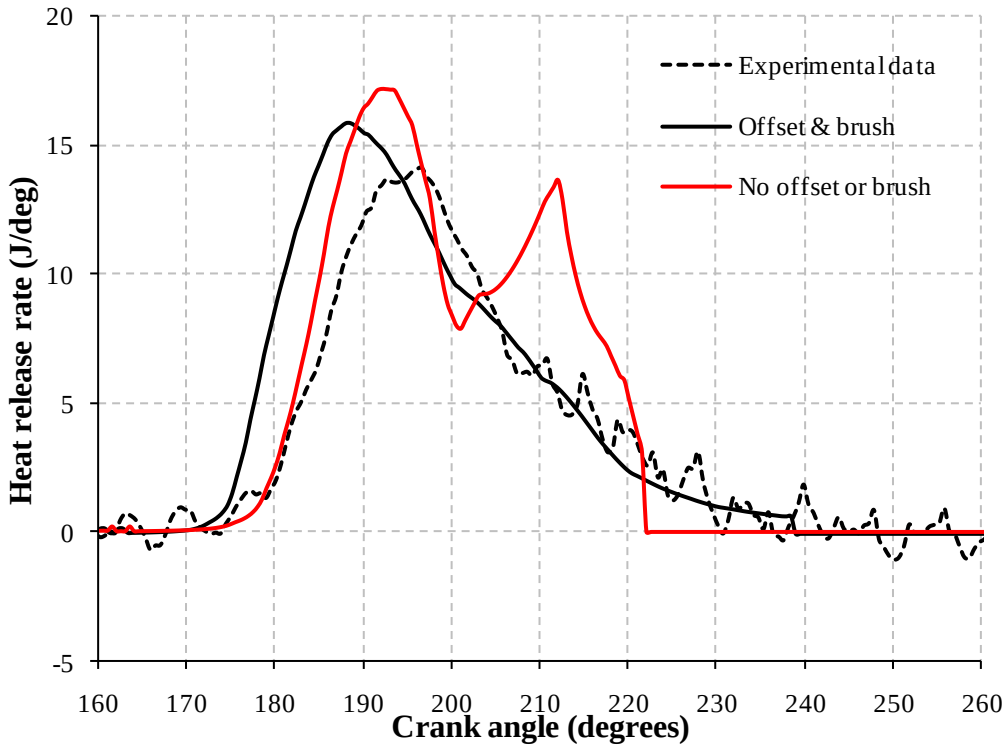

Figure 8-36, Heat release rate calculated with and without flame offset and brush zone effects for the squish head at full throttle and 9075 rpm

Two further simulations have been solved to assess whether it is the flame offset or the wrinkled flame brush zone that is the predominant mechanism which produces the inflection in the latter part of the heat release curve. The first simulation is with the brush zone included but without a flame offset and the second simulation accounts for the flame offset but assumes an infinitely thin flame front. The heat release for these two further simulations are shown in Figure 8-37, the blue curve represents the heat release calculated accounting for the wrinkled brush zone only and the red curve is the heat release accounting for the offset flame only. When the wrinkled flame brush is accounted for, but with a central flame, there is still a small inflection in the latter part of the heat release curve. However when the flame front offset is accounted for, but with and infinitely thin spherical flame, the inflection is removed. This might suggest that the flame offset is a more significant effect on flame front area than the wrinkled flame brush thickness.

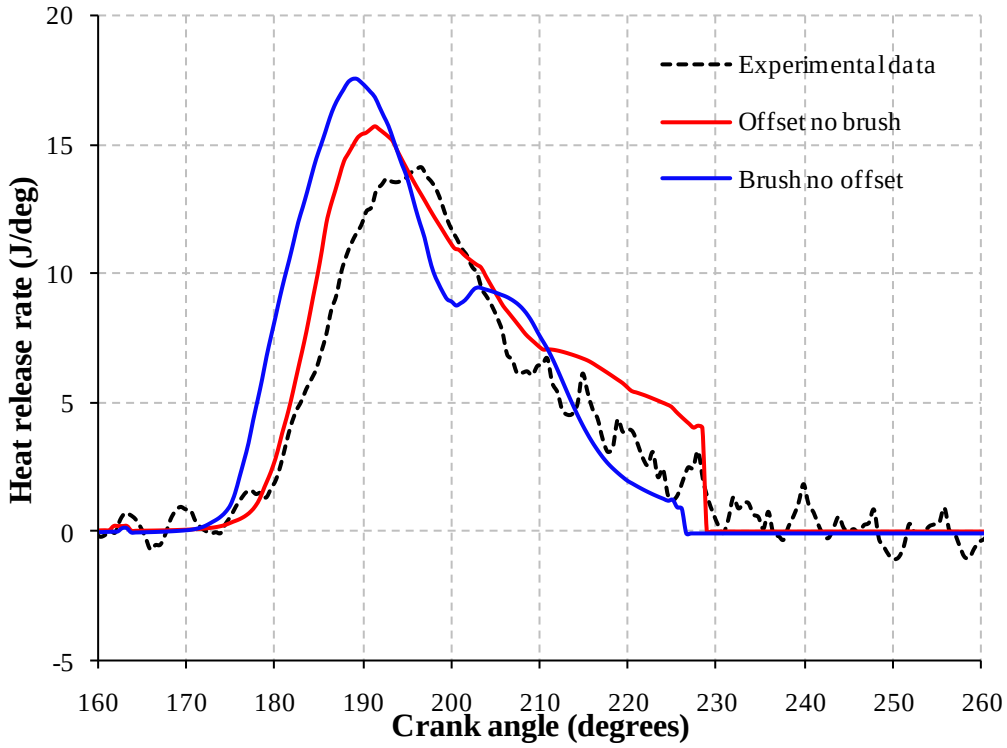

Figure 8-37, Heat release rate for the squish head at full throttle and 9075 rpm with just the flame offset accounted for and just a brush zone accounted for

8.7 Concluding Summary

A comparison of the performance of the squish and disc type combustion chambers has been made by analysis and experiment, the results of both show that the squish combustion chamber is the faster burning combustion chamber.

Simulations of both combustion chambers have been conducted using the tumble and turbulence model developed in this study. The engine simulation is able to predict the tumble velocity and the offset flame progression along the surface of the cylinder head. The predicted flame front progress for both combustion chambers has been compared with experimental data which shows a reasonable correlation.

Tumble velocity predictions show that exhaust duct gas dynamics will influence the tumble motion in the cylinder during the open cycle. A reverse flow of gas from the exhaust duct into the cylinder will act to increase the tumble momentum. The reverse flow is only significant at the higher engine speeds where the exhaust dynamics are designed to operate.

The combustion model developed in this work uses the fractal geometry approach to account for flame wrinkling. In the past other researchers have used the fractal approach with a fractal dimension of between 2.35 and 2.4. In this work it was found that a fractal dimension of upto 2.41 was required to match the measured burn rate. A second turbulent combustion mechanism is included in the combustion model which accounts for entrained islands of reactants consumed behind the wrinkled flame front. With the entrained islands included in the combustion model a fractal dimension as low as 2.32 could be used to match the measured cylinder pressure development with 9-14% mass fraction burned by islands.

The current quasi-dimensional combustion model accounts for a flame front offset as well as a wrinkled flame brush thickness and comparisons of simulations with and without flame offset and brush thickness have been made. Significant errors in the predicted heat release rate will occur during the latter part of the combustion process if the flame offset and wrinkled flame brush thickness is not accounted for.

9 Conclusions and Future Work

In this study a quasi-dimensional combustion model for a two stroke engine has been developed which accounts for the bulk flow movement of the flame front due to the in-cylinder tumble motion. A wrinkled flame brush zone thickness has also been accounted for using a simple geometry model. The new model uses the conservation of angular momentum to predict the development and evolution of the tumble motion in the engine cylinder. The tumble motion is represented by an ellipsoid vortex which is assumed to rotate as a solid body. The mass of the tumble vortex will always be less than the total cylinder mass and the size of the vortex is defined by the combustion chamber geometry and a limiting elliptical aspect ratio. The wrinkled flame brush thickness is based on the maximum scale of wrinkling which in turn is calculated as a function of the integral scale. It is assumed that the primary mechanism for the enhanced turbulent burning velocity is due to flame front wrinkling, which increases the flame front area. A fractal model has been used to predict the wrinkled flame front area and the fractal dimension is based on the turbulence intensity and the laminar burning velocity. A second mechanism for the enhanced burning velocity has also been included which accounts for islands of reactants entrained behind the wrinkled flame front. The combustion model was incorporated into a whole engine simulation program. The model was applied to a simple disc type combustion chamber and a squish type combustion chamber and engine simulations conducted over a number of different engine speeds and throttle positions. A test program was completed in which the flame front progression across the cylinder head was monitored using ionization probes and the flame front offset and wrinkled flame brush thickness determined, these measurements were compared with the simulation model predictions. The cylinder pressure was also measured and compared with the predicted pressure development, mass fraction burned and heat release rate.

9.1 Research Objectives and Achievements

- A phenomenological model for the in-cylinder tumble flow motion, generated during the scavenge period, has been developed for a two stroke engine.
- The tumble flow motion is modelled as an ellipsoid vortex, the dimensions of the vortex are defined by the combustion chamber geometry. The height of the vortex, about its rotational axis, is defined by the height of the chamber. The width of the vortex maybe as large as the cylinder bore dimension but is restricted to an elliptical aspect ratio of 2.5. The limiting aspect ratio has been observed in experimental work and 3D CFD analysis, published in the literature.
- During compression the conservation of angular momentum of the vortex is taken into account. As the size of the vortex is limited by the combustion chamber height and the elliptical aspect ratio and mass of the tumble vortex will reduce during compression, momentum loss due to a reducing vortex mass is also accounted for. The turbulent shear at the surface of the ellipsoid will act to reduce the tumble velocity and is included in the model.
- The tumble vortex will influence the combustion process not only by generating turbulent kinetic energy at the surface of the vortex but also by advecting the flame front and burned zone away from the central spark plug and towards the chamber walls. Both of these effects are included in the current study.
- The tumble model has been included in a whole engine simulation mode and it was shown that it is not just the fresh charge entering the cylinder that generates tumble momentum, but that a reverse flow through the exhaust port can increase the tumble momentum just prior to the exhaust port closing.
- The flame front and burned zone movement due to the tumble motion has been measured using ionization probes in an engine operating at speeds near 10,000 rpm. The predicted and measured flame front offset due to tumble motion show a reasonable correlation.
- A quasi-dimensional two zone combustion model has been developed which includes a flame front surface area geometry model which accounts for the burned zone and flame front being advected from the spark plug due to the tumble motion.

- The geometry model also accounts for a wrinkled flame brush thickness. Both the flame brush zone and the offset were shown to have a significant effect on the heat release rate in the later part of the combustion process.
- The wrinkled flame brush thickness has been measured in engine tests using the ionization probes. The brush thickness was determined on a statistical basis from 200 engine cycles.
- A fractal combustion model has been adapted from the literature, in which the outer cut off is defined as the wrinkled flame brush thickness. The combustion model also includes and entrainment model, again adapted from the literature.
- An ignition delay model has been incorporated where the delay period is defined a function of the tumble velocity, intensity and laminar burning velocity.
- Flame front propagation has been measured at a number of locations in the combustion chamber of a two stroke engine operating upto 10,000 rpm. Results indicate that a spherical flame front is appropriate.
- As well as using ionization probes to monitor the progression of the flame front through the combustion chamber a cylinder pressure transducer was used in engine tests to validate the combustion model in terms of pressure development and heat release.

9.2 Key Findings

- The squish combustion chamber was the faster burning cylinder head and this leads to an increase in peak pressure and mean effective pressure.
- The bulk motion of the burned zone and flame front is always towards the exhaust port.
- The nominal shape of the flame front based on a statistical mean of 200 engine cycles, as measured at the cylinder head, is circular. This supports the spherical flame front assumption.
- The flame offset due to tumble motion is greater in the squish combustion chamber than the disc combustion chamber. This is due to the size of the vortex which is

limited by the height of the combustion chamber and an elliptical aspect ratio of approximately 2.5.

- The flame offset and wrinkled flame brush thickness have a significant effect on the heat release rate during the latter part of the combustion process.
- The exhaust dynamics influence the tumble motion due to both delivery ratio and a reverse flow prior to exhaust port closure.

9.3 Future work

The predicted cylinder pressure results show a small increase in cylinder pressure due to reverse flow of gas from the exhaust duct into the cylinder. The measured increase in cylinder pressure is larger than that predicted and this may indicate that the gas dynamic predictions are inaccurate. The exhaust gas dynamics were also shown to cause an increase in tumble momentum, if the magnitude of the reverse flow is under predicted this suggests that the increase in tumble moment due to the reverse flow is under predicted. A comparison of the gas dynamic predictions of the present model with a different code, or comparison with tests may help elucidate these phenomena.

With reactant islands included in the combustion model the predicted pressure development could be matched to measured data with a wide range of fractal dimension and mass fraction burned as islands. Although there appears to be data in the literature to quantify wrinkling effects there appears to be little data to quantify the mass fraction burned as islands in an engine, particularly running at high speeds. Experimental data quantifying the mass fraction burned by islands is desirable.

The two zone combustion model uses a heat transfer mode based on Annand and this calculates the heat transfer coefficient based on a Reynolds number calculated using the mean piston speed as the characteristic velocity, this could be improved by using the tumble velocity and turbulence predictions.

ABDI AGHDAM , E., BURLUKA , A.A., HATTRELL , T., LIU , K., SHEPPARD , C. G. W., NEUMEISTER , J. and CRUNDWELL , N., 2007. *Study of Cyclic Variation in an SI Engine Using Quasi-Dimensional Combustion Model.* SAE Technical Paper 2007-01-0939.

ABRAHAM, J. and WILLIAMS, F.A., 1985. *A Discussion of Turbulent Flame Structure in Premixed Charges.* SAE Technical Paper 850345.

ACHUTH, M. and MEHTA, P.S., 2001. *Predictions of Tumble and Turbulence in Four-Valve Pentroof Spark Ignition Engines*, Int. J. Engine Research, Vol 2. No. 3, June 2001.

AGARWAL, A., FILIPI, Z.S., ASSANIS, D.N. and BAKER, D.M., 1998. *Assessment of Single- and Two-Zone Turbulence Formulations for Quasi-Dimensional Modeling of Spark-Ignition Engine Combustion.* Combustion Science and Technology, 07/01; 2013/08, vol. 136, no. 1-6, pp. 13-39.

AHMADI-BEFRUI, B., BRANDSTATTER,W. and KRATOCHWILL, H., 1989, Multidimensional *Calculation of the Flow Processes in a Loop-Scavenged Two-Stroke Cycle Engine*, SAE Technical Paper 890841.

AMSDEN, A.A., OROURKE, P.J., BUTLER, T.D., MEINTJES, K. and FANSLER, T.D., 1991. *Comparisons of computed and measured three-dimensional velocity fields in a motored two-stroke engine.* SAE Technical Paper 920418.

ANNAND, W.J.D. and Thermodynamics and Fluid Mechanics Group, 1963. *Heat Transfer in the Cylinders of Reciprocating Internal Combustion Engines*. Proceedings of the Institution of Mechanical Engineers, June 01, vol. 177, no. 1, pp. 973-996 DOI 10.1243/PIME_PROC_1963_177_069_02.

ARRIGONI , V., CALVI , F., CORNETTI , G.M. and POZZI , U., 1973. *Turbulent Flame Structure as Determined by Pressure Development and Ionization Intensity.* SAE Technical Paper 730088.

BARITAUD, T.A. and GREEN, R. M., 1986. *A 2-D Flame Visualisation Technique Applied to the I.C. Engine.* SAE Technical Paper 860025.

BARUAH , P.C., 1990. *A Simulation Model for Transient Operation of Spark-Ignition Engines.* SAE Technical Paper 900682.

BECK , K.W., BERNHARDT , S., SPICHER , U., GEGG , T., KOLMEL , A., PAA , A., WEISSGERBER , T. and WESTECKER , M., 2008. *Ion-Current Measurement in Small Two-Stroke SI Engines.* SAE Technical Paper 2008-32-0037.

BECK , K., SCHREER , K., BERNHARDT , S., SPICHER , U., ROSSKAMP , H. and GEGG , T., 2006. *Application of Multifiber Optics in Handheld Power Tools with High Speed Two-Stroke Gasoline Engines.* SAE Technical Paper 2006-32-0060.

BELL, A.G., 1984, *Performance Tuning in Theory and Practice, Two-Strokes*, Haynes Publishing Group.

BENJAMIN, S.F., 1992. *A Phenomenological Model for 'Barrel' Swirl in Reciprocating Engines.* Proceedings of the Institution of Mechanical Engineers, Part D: Journal of Automobile Engineering, January 01, vol. 206, no. 1, pp. 63-71.

BENJAMIN, S.F., 1993, *Prediction of Barrel Swirl and Turbulence in Reciprocating Engines Using a Phenomenological Model*, IMECHE C465/013/93

BERTSCH, M., SCHREER, K., DISCH, C., BECK, K. W. and SPICHER, U., 2011, *Investigation of the Flow Velocity in the Spark Plug Gap of a Two-Stroke Gasoline Engine using Laser-Doppler-Anemometry*, SAE Technical Paper 2011-32-0529.

BLAIR, G.P and ASHE, M.C., 1976, *The Unsteady Gas Exchange Characteristics of a Two-Cycle Engine*, SAE Technical Paper 760644.

BLAIR , G.P., 1996. *Design and Simulation of Two Stroke Engines*. first ed.

BLAIR , G.P., 1991. *An Alternative Method for the Prediction of Unsteady Gas Flow Through the Internal Combustion Engine*. SAE Technical Paper 911850.

BLIZARD , N.C. and KECK , J.C., 1974. *Experimental and Theoretical Investigation of Turbulent Burning Model for Internal Combustion Engines*. SAE Technical Paper 740191.

BOREE, J., MARC, D., BAZILE, R. and LECORDIER, B., 1999. *On the behavior of a large scale tumbling vortex flow submitted to compression.* ESAIM: Proc., vol. 7, pp. 56-65.

BORGNAKKE , C., DAVIS , G.C. and TABACZYNSKI , R.J., 1981. *Predictions of In-Cylinder Swirl Velocity and Turbulence Intensity for an Open Chamber Cup in Piston Engine*. SAE Technical Paper 810224.

BOZZA , F. and GIMELLI , A., 2004. *A Comprehensive 1D Model for the Simulation of a Small-Size Two-Stroke SI Engine*. SAE Technical Paper 2004-01-0999.

BOZZA , F., GIMELLI , A., ANDREASSI , L., ROCCO , V. and SCARCELLI , R., 2008. *1D-3D Analysis of the Scavenging and Combustion Process in a Gasoline and Natural-Gas Fuelled Two-Stroke Engine.* SAE Technical Paper 2008-01-1087.

BOZZA , F., GIMELLI , A., FONTANESI, S. and SEVERI, E., 2011, *1D and 3D CFD Investigation of Burning Process and Knock Occurrence in a Gasoline or CNG Fuelled Two-Stroke SI Engine*, SAE Technical Paper 2011-32-0526.

BOZZA , F., GIMELLI , A., MEROLA , S.S. and VAGLIECO , B.M., 2005. *Validation of a Fractal Combustion Model through Flame Imaging.* SAE Technical Paper 2005-01-1120.

BOZZA , F., TUCCILLO , R. and DE FALCO , D., 1995. *A Two-Stroke Engine Model Based on Advanced Simulation of Fundamental Processes.* SAE Technical Paper 952139.

BS1042, Section 1.1, 1981, *Specification for Square-Edged Orifice Plates, Nozzles and Venturi Tubes Inserted in Circular Cross-Section Conduits Running Full*

CANT, R.S., and MASTORAKOS E., 2008. *An Introduction to Turbulent Reacting Flows*, Imperial College Press.

CATANIA, A.E., MISUL, D., MITTICA, A. and SPESSA, E., 2003. *A Refined Two-Zone Heat Release Model for Combustion Analysis in SI Engines*. JSME International Journal Series B Fluids and Thermal Engineering, vol. 46, no. 1, pp. 75-85.

CHEN , C. and VESHAGH , A., 1992. *A Refinement of Flame Propagation Combustion Model for Spark-Ignition Engines*. SAE Technical Paper 920679.

CLARKE, A. and HARGRAVE, G.K., 2009, *Measurements of Laminar Premixed Methane-Air Flame Thickness at Ambient Conditions*, Proc. IMechE, vol. 223 Part C.

DAI , W., NEWMAN , C.E. and DAVIS , G.C., 1996. *Predictions of In-Cylinder Tumble Flow and Combustion in SI Engines with a Quasi-Dimensional Model*. SAE Technical Paper 961962.

DAVIDSON, P. A., 2007, *Turbulence, an Introduction for Scientists and Engineers*, Oxford University Press.

DIMOPOULOS , P. and BOULOUCHOS , K., 1997. *Turbulent Flow Field Characteristics in a Motored Reciprocating Engine*. SAE Technical Paper 972833.

ENIKEEV, R., CHERNOUSOV, A. and MIKHAILOV, V., 2011, *Identification Technique for Quasi-1D Model of Gas Exchange Processes in a Two-Stroke Engine*, SAE Technical Paper 2011-01-1145.

ERSOY, O., 2010, *Surface Area and Volume Measurements of Volcanic Ash Particles by SEM Stereoscopic Imaging*, Journal of Volcanology and Geothermal Research, 190 (2010) 290-296.

FANSLER, T.D. and DRAKE, M.C., 2009, *Flow, Mixture Preparation and Combustion in Direct-Injection Two-Stroke Engines, Flow and Combustion in Reciprocating Engines* (Eds C. Arcoumanis and T. Kamimoto, Springer 2009

FANSLER , T.D. and FRENCH , D.T., 1992. *The Scavenging Flow Field in a Crankcase-Compression Two-Stroke Engine - A Three-Dimensional Laser-Velocimetry Survey*. SAE Technical Paper 920417

FERGUSON, C.A. AND KIRKPATRICK, A.T., 2001, *Internal Combustion Engines, Applied Thermal Sciences*, John Wiley and Sons.

FILIPI , Z. and ASSANIS , D.N., 1991. *Quasi-Dimensional Computer Simulation of the Turbocharged Spark-Ignition Engine and its Use for 2- and 4-Valve Engine Matching Studies*. SAE Technical Paper 910075.

FLECK , B.J., FLECK , R., KEE , R.J., CHATFIELD , G.F. and MACKEY , D.,O., 2004. *Validation of a Computer Simulation of a High Performance Two-Stroke Motorcycle Racing Engine.* SAE Technical Paper 2004-01-3561.

FRASER , R.A., FELTON , P.G., BRACCO , F.V. and SANTAVICCA , D.A., 1986. *Preliminary Turbulence Length Scale Measurements in a Motored IC Engine.* SAE Technical Paper 860021.

FRASER , R.A. and BRACCO , F.V., 1989. *Cycle-Resolved LDV Integral Length Scale Measurements Investigating Clearance Height Scaling, Isotropy, and Homogeneity in an I.C. Engine*. SAE Technical Paper 890615.

FURUKAWA, J., NAKAMURA, T., GOMI, T. and HIRANO, T., 1991. *A fundamental study of electrostatic probe measurements to explore the structure of turbulent premixed flames (2nd report, dependence of the characteristics of ion current on the path of curved flames).* Trans. Japan Soc. Mech. Eng.(Ser.B), vol. 57, no. 544, pp. 4272-4277 Mechanical Engineering Abstracts. ISSN 0387-5016.

GALINDO, J., CLIMENT, H., PLÁ, B. and JIMÉNEZ, V.D., 2011. *Correlations for Wiebe function parameters for combustion simulation in two-stroke small engines.* Applied Thermal Engineering, 5, vol. 31, no. 6–7, pp. 1190-1199.

GEGG , T., KÖLMEL , A. and BECK , K.W., 2010. *Combustion Analysis on Small Two-Stroke SI-Engines for Handheld Power Tools.* SAE Technical Paper 2010-32-0062.

GILLESPIE , L., LAWES , M., Sheppard , C. G. W. and WOOLLEY , R., 2000. *Aspects of Laminar and Turbulent Burning Velocity Relevant to SI Engines.* SAE Technical Paper 2000-01-0192.

GOULDIN, F.C., 1987. *An application of fractals to modeling premixed turbulent flames.* Combustion and Flame, /6, vol. 68, no. 3, pp. 249-266.

GULDER, O.L., 2007. *Contribution of small scale turbulence to burning velocity of flamelets in the thin reaction zone regime.* Proceedings of the Combustion Institute, /1, vol. 31, no. 1, pp. 1369-1375 ISSN 1540-7489.

HADJICONSTANTINOU, N. G. and HEYWOOD, J. B., 1995, *A Model for Converting SI Engine Flame Arrival Signals into Flame Contours*, SAE Technical Paper 950109.

HAMAMOTO, Y., TOMITA, E. AND YOSHIYAMA, W., 1996, *Turbulent Premixed Flames in Closed Combustion Chambers*, JSME International Journal Series B, Vol. 39, No. 1.

HENG , T.Y., GITANO-BRIGGS , H. and HERN , T.Y., 2009. *Development of the Gaseous Fuel Direct Injection System for Small Two-Stroke Transports.* SAE Technical Paper 2009-32-0032.

HERWEG , R. and MALY , R.R., 1992. *A Fundamental Model for Flame Kernel Formation in S. I. Engines*. SAE Technical Paper 922243.

HEYWOOD , J.B., 2000. *Internal Combustion Engine Fundamentals*. McGraw-Hill.

HICKS , R.A., LAWES , M., SHEPPARD , C. G. W. and WHITAKER , B.J., 1994. *Multiple Laser Sheet Imaging Investigation of Turbulent Flame Structure in a Spark Ignition Engine*. SAE Technical Paper 941992.

HIRES , S.D., TABACZYNSKI , R.J. and NOVAK , J.M., 1978. *The Prediction of Ignition Delay and Combustion Intervals for a Homogeneous Charge, Spark Ignition Engine*. SAE Technical Paper 780232.

HIRZ , M., KORMAN , M., EICHLSEDER , H. and KIRCHBERGER , R., 2004. *Potential of the 50cc Two Wheeler Motor Vehicle Class in Respect of Future Exhaust Emission Targets*. SAE Technical Paper 2004-32-0050.

HONG, C.W. and TARNG, S.D., 1998. *Direct measurement and computational analysis of turbulence length scales of a motored engine.* Experimental Thermal and Fluid Science, /4, vol. 16, no. 4, pp. 277-285.

HORLOCK, J. H. and WINTERBONE, D. E., 1986, *The Thermodynamics and Gas Dynamics of Internal-Combustion Engines*, Clarendon Press, Oxford.

HOSSEIN MANSOURI , S., HEYWOOD , J.B. and RADHAKRISHNAN , K., 1982. *Divided-Chamber Diesel Engine, Part I: A Cycle-Simulation Which Predicts Performance and Emissions*. SAE Technical Paper 820273.

HU , Z., WHITELAW , J.H. and VAFIDIS , C., 1992. *Flame Propagation Studies in a Four-Valve Pentroof-Chamber Spark Ignition Engine.* SAE Technical Paper 922321.

HUNZINGER , N., ROTHE , M., SPICHER , U., GEGG , T., RIEBER , M., KLIMMEK , A. and JÃGER , A., 2006. *Quasi-Dimensional Combustion Simulation of a Two- Stroke Engine.* SAE Technical Paper 2006-32-0062.

INCROPERA, F. P., DEWITT, D. P., BERGMAN, T. L. and LAVINE, A. S., 2007, *Fundamentals of Heat and Mass Transfer*, Sixth Edition, Wiley

ISHIMA , T., OBOKATA , T., NOMURA , T. and TAKAHASHI , Y., 2008. *Analysis on In-Cylinder Flow by Means of LDA, PIV and Numerical Simulation under Steady State Flow Condition*. SAE Technical Paper 2008-01-1063.

JAJCEVIC , D., ALMBAUER , R.A., SCHMIDT , S.P. and GLINSNER , K., 2008. *CFD Simulation of a Real World High-Performance Two Stroke Engine with Use of a Multidimensional Coupling Methodology.* SAE Technical Paper 2008-32-0042.

JAJCEVIC , D., ALMBAUER , R.A., SCHMIDT , S.P., GLINSNER , K. and FITL, M., 2010, *Exhaust System Simulation of a 2-Cylinder 2-Stroke Engine Including Heat Transfer Effects*, SAE Technical Paper 2010-32-0035.

JAMES, K., CHEN, R. and TURNER, J., 2010, *Ionisation and Ionisation Rate of a Two-Stroke HCCI Engine Fuelled with E85 for Control Feedback*, SAE Technical Paper 2010-01-1247.

JOHNSON, J. and DEN BRAVEN, K. R., 2008,*Comparison of Homogeneous, Stratified and High-Squish Stratified Combustion in a Direct-Injected Two-Stroke Engine*, SAE Technical Paper 2008-32-0030.

KATO , T., AKIYAMA , K., NAKASHIMA , T. and SHIMIZU , R., 2007. *Development of Combustion Behavior Analysis Techniques in the Ultra High Engine Speed Range.* SAE Technical Paper 2007-01-0643

KHALIGHI , B., El TAHRY , S. H., HAWORTH , D.C. and HUEBLER , M.S., 1995. *Computation and Measurement of Flow and Combustion in a Four-Valve Engine with Intake Variations.* SAE Technical Paper 950287.

KIDO , H., HUANG , S. and NAKASHIMA, K.,1991, *A Premixed Turbulent Flame Structure Model Having Reactant Islands and Fractal Flame Surfaces*, JSME International Journal, Vol. 34, No. 4, 1991

KIDO , H. and HUANG , S., 1993. *Comparison of Premixed Turbulent Burning Velocity Models Taking Account of Turbulence and Flame Spatial Scales*. SAE Technical Paper 930218.

KIRCHBERGER, R., HIRZ, M., WINKLER, F., KORMAN, M. and EICHLSEDER, H., 2007. *Potential of high technology 50cm^3 two stroke and four stroke engines.* SAE Technical Paper 2007-32-0013.

KLINGMANN , J. and JOHANSSON , B., 1999. *Interaction Between Turbulence and Flame in an S.I. Engine and in a Stationary Burner*. SAE Technical Paper 1999-01-0569.

KORTSCHIK, C., PLESSING, T. and PETERS, N., 2004. *Laser optical investigation of turbulent transport of temperature ahead of the preheat zone in a premixed flame.* Combustion and Flame, /1, vol. 136, no. 1, pp. 43-50.

LA, C., MURPHY, P. and CAKEBREAD, S., 2012, *Benchmarking a 2-Stroke Spark Ignition Heavy Fuel Engine*, SAE Technical Paper 2012-01-0397.

LAFOSSAS , F.-., COLIN , O., LE BERR , F. and MENEGAZZI , P., 2005. *Application of a New 1D Combustion Model to Gasoline Transient Engine Operation.* SAE Technical Paper 2005-01-2107

LARSSON , M., DENBRATT , I. and KOOPMANS , L., 2007. *Ion Current Sensing in an Optical HCCI Engine with Negative Valve Overlap.* SAE Technical Paper 2007-01-0009.

LEE , J.H., DUDDY , B., THURSTON , M., BEARDSLEE , D. and ENYEART , R., 2011. *Increasing the Lubricity of JP-8 to Fuel Two-stroke Spark Ignition Engines for Midsized Unmanned Aerial Vehicles*. SAE Technical Paper 2011-01-0332.

LEE, T.-. and FILIPI, Z.S., 2011. *Improving the predictiveness of the quasi-d combustion model for spark ignition engines with flexible intake systems.* International Journal of Automotive Technology, 02/01, vol. 12, no. 1, pp. 1-9.

LI, Y., ZHAO, H., LEACH, B., MA, T. and LADOMMATOS, N., 2004. *Characterization of an in-cylinder flow structure in a high-tumble spark ignition engine.* International Journal of Engine Research, October 01, vol. 5, no. 5, pp. 375-400.

LI, Y., ZHAO, H., PENG, Z. and LADOMMATOS, N., 2002. *Particle image velocimetry measurement of in-cylinder flow in internal combustion engines-experiment and flow structure analysis*. Proceedings of the Institution of Mechanical Engineers, Part D: Journal of Automobile Engineering, January 01, vol. 216, no. 1, pp. 65-81.

MA , F., LIU , H., WANG , Y., WANG , J., DING , S. and ZHAO , S., 2008. *A Quasi-Dimensional Combustion Model for SI Engines Fuelled by Hydrogen Enriched Compressed Natural Gas.* SAE Technical Paper 2008-01-1633.

MALY, R.R. and HERWEG, R., 2009, *Spark Ignition and Combustion in Four-Stroke Gasoline Engines,* Flow and Combustion in Reciprocating Engines (Eds C. Arcoumanis and T. Kamimoto), Springer Berlin 2009.

MANDELBROT, B.B., 1982. *The fractal geometry of nature.* Updated and augmented ed. New York: Freeman.

MANTZARAS, J., FELTON, P. G. and BRACCO, F. V., 1988, *Three-Dimensional Visualization of Premixed-Charge Engine Flames: Islands of Reactants and Products; Fractal Dimension; and Homogeneity*, SAE Technical Paper 881635.

MARC , D., BOREE , J., BAZILE , R. and CHARNAY , G., 1997. *Tumbling Vortex Flow in a Model Square Piston Compression Machine: PIV and LDV Measurements*. SAE Technical Paper 972834.

MATTHEWS , R.D., HALL , M.J., DAI , W. and DAVIS , G.C., 1996. *Combustion Modeling in SI Engines with a Peninsula-Fractal Combustion Model.* SAE Technical Paper 960072.

MATTHEWS , R.D. and CHIN , Y., 1991. *A Fractal-Based SI Engine Model: Comparisons of Predictions with Experimental Data*. SAE Technical Paper910079.

MEHRESH, P., FLOWERS, D. and DIBBLE, R.W., 2005. *Experimental and numerical investigation of effect of fuel on ion sensor signal to determine combustion timing in homogeneous charge compression ignition engines*. International Journal of Engine Research, October 01, vol. 6, no. 5, pp. 465-474.

METGHALCHI, M. and KECK, J.C., 1982. *Burning velocities of mixtures of air with methanol, isooctane, and indolene at high pressure and temperature*. Combustion and Flame, vol. 48, no. 0, pp. 191-210.

MEYER , R., KUBESH , J.T., SHAHED , S.M. and DAVIS , J.K., 1993. *Simultaneous Application of Optical Spark Plug Probe and Head Gasket Ionization Probe to a Production Engine.* SAE Technical Paper 930464.

MORIYOSHI, Y., MORI, K. and MORIKAWA, K., 1999, *Numerical Analysis of Gas Exchange Process in a Small Two-Stroke Gasoline Engine*, SAE Technical Paper 1999-01-3330.

NICHOLSON , D.E. and WITZE , P.O., 1993. *Flame Location Measurements in a Production Engine Using Ionization Probes Embodied in a Printed-Circuit-Board Head Gasket.* SAE Technical Paper 930390.

NISHIDA , K., SAKUYAMA , H. and KIMIJIMA , T., 2009. *Improvement of Fuel Economy Using a New Concept of Two-Stroke Gasoline Engine Applying Stratified-Charge Auto-Ignition*. The Automotive Research Association of India.

NTZIACHRISTOS, L., PISTIKOPOULOS, P. and SAMARAS, Z., 2005. *Particle characterization from two-stroke powered two-wheelers.* International Journal of Engine Research, June 01, vol. 6, no. 3, pp. 263-275.

OBOKATA , T., HANADA , N. and KURABAYASHI , T., 1987. *Velocity and Turbulence Measurements in a Combustion Chamber of S. I. Engine under Motored and Firing Operations by L. D. A. with Fiber-Optic Pick-Up*. SAE Technical Paper 870166.

OHIGASHI, S., HAMAMOTO, Y. and KIZIMA, A., 1971. *Effects of Turbulence on Flame Propagation in Closed Vessel.* Bulletin of JSME, 08/00, vol. 14, no. 74, pp. 849-858.

OLIKARA, C and BORMAN, G.L., 1975, *A Computer Program for Calculating Properties of Equilibrium Combustion Products with Some Applications to I.C. Engines*, SAE Technical Paper 750468.

ONORATI , A. and FERRARI , G., 1998. *Modeling of 1-D Unsteady Flows in I.C. Engine Pipe Systems: Numerical Methods and Transport of Chemical Species*. SAE Technical Paper 980782.

ONORATI , A., FERRARI , G., MONTENEGRO , G., CARACENI , A. and PALLOTTI , P., 2004. *Prediction of S.I. Engine Emissions During an ECE Driving Cycle via Integrated Thermo-Fluid Dynamic Simulation.* SAE Technical Paper 2004-01-1001.

OSWALD, R., EBNER, A. and KIRCHBERGER, R., 2010, *High Efficient 125-250 cm^3 LPDI Two-Stroke Engines, a Cheap and Robust Alternative to Four-Stroke Solutions?,* SAE Technical Paper 2010-32-0019.

PAO, R.H.F., 1961, *Fluid Mechanics,* John Wiley and sons, New York and London.

PAYRI , F., GALINDO , J., CLIMENT , H., PASTOR , J.M. and GAIA , C., 2001. *Optimisation of The Scavenging and Injection Processes of An Air-Assisted Direct Fuel Injection 50 Cc. 2-Stroke S.I. Engine By Means of Modelling*. SAE Technical Paper 2001-01-1814.

PERINI, F., PALTRINIERI, F. and MATTARELLI, E., 2010, *A Quasi-Dimensional Combustion Model for Performance and Emissions of SI Engines Running on Hydrogen-Methane Blends,* International Journal of Hydrogen Energy 35 (2010), 4687-4701.

PETERS, N., 1999. *The turbulent burning velocity for large-scale and small-scale turbulence*. Journal of Fluid Mechanics, vol. 384, pp. 107-132.

PETERS, N., 1986. *Laminar flamelet concepts in turbulent combustion.* Symposium (International) on Combustion, vol. 21, no. 1, pp. 1231-1250.

PETERS, N., 2006. *Turbulent Combustion.* Cambridge: Cambridge University Press.

PETERSEN , B.R. and GHANDHI , J., 2010. *High Resolution Scalar Dissipation and Turbulence Length Scale Measurements in an Internal Combustion Engine*. SAE Technical Paper 2010-01-0185.

PFEFFER, T., BUHLER, P., MEIER, D.E. and HAMDANI, Z., 2002. *Influence of Intake Tumble Ratio on General Combustion Performance, Flame Speed and Propagation at a Formula One Type, High-Speed Research Engine.* SAE Technical Paper 2002-01-0244.

POINSOT, T., CANDEL, S. and TROUVE, A., 1995. *Applications of direct numerical simulation to premixed turbulent combustion.* Progress in Energy and Combustion Science, vol. 21, no. 6, pp. 531-576.

POINSOT, T. and VEYNANTE, D., 2001. *Theoretical and numerical combustion.* Philadelphia: PA: R.T. Edwards,.

POULOS , S.G. and HEYWOOD , J.B., 1983. *The Effect of Chamber Geometry on Spark-Ignition Engine Combustion.* SAE Technical Paper 830334.

RAMAJO, D., ZANOTTI, A. and NIGRO, N., 2007, *Assessment of a Zero-Dimensional Model of Tumble in Four-Valve High Performance Engine*, International Journal of Numerical Methods for Heat and Fluid Flow, Vol. 17, No. 8, pp 770-787, 2007.

RAMOS, J. I., 1989, *Internal Combustion Engine Modelling*, Hemisphere Publishing Corporation.

REDDY , K.V., GANESAN , V. and GOPALAKRISHNAN , K.V., 1986. *Under the Roof of the Cylinder Head-An Experimental Study of the in-Cylinder Air Movement in a Two-Stroke Spark Ignition Engine.* SAE Technical Paper 860166.

REID , M.G., 1993, *Combustion Modelling for Two-Stroke Cycle Engines*, PhD Thesis Queens University Belfast, UK.

REID , M.G. and DOUGLAS , R., 1994. *Quasi-Dimensional Modelling of Combustion in a Two-Stroke Cycle Spark Ignition Engine.* SAE Technical Paper 941680.

REUSS , D.L., ADRIAN , R.J., LANDRETH , C.C., FRENCH , D.T. and FANSLER , T.D., 1989. *Instantaneous Planar Measurements of Velocity and Large-Scale Vorticity and Strain Rate in an Engine Using Particle-Image Velocimetry.* SAE Technical Paper 890616.

REYNOLDS, W.C., 1980, *Modeling of Fluid Motions in Engines-An Introduction Overview,* Combustion Modelling in Reciprocating Engines, 1980.

RHODES , D.B. and KECK , J.C., 1985. *Laminar Burning Speed Measurements of Indolene-Air-Diluent Mixtures at High Pressures and Temperatures*. SAE Technical Paper 850047.

RIMMER , J. E. T., LONG , E.J., GARNER , C.P., HARGRAVE , G.K., RICHARDSON , D. and WALLACE , S., 2009. *The Influence of Single and Multiple Injection Strategies on In-Cylinder Flow and Combustion within a DISI Engine.* SAE Technical Paper 2009-01-0660.

ROTHBART, H.A. and BROWN, T.H., 2006. *Mechanical design handbook : measurement, analysis, and control of dynamic systems.* Second ed. New York: McGraw-Hill.

ROULAND , E., TRINITE , M., DIONNET , F., FLOCH , A. and AHMED , A., 1997. *Particle Image Velocimetry Measurements in a High Tumble Engine for In-Cylinder Flow Structure Analysis.* SAE Technical Paper 972831.

ROY, O.L. and PENVEN, L.L., 1998. *Compression of a turbulent vortex flow*. International Journal of Heat and Fluid Flow, 10, vol. 19, no. 5, pp. 533-540.

RUSS , S., PEET , G. and STOCKHAUSEN , W., 1997. *Measurements of the Effect of In-Cylinder Motion on Flame Development and Cycle-to-Cycle Variations Using an Ionization Probe Head Gasket.* SAE Technical Paper 970507.

SALVAT, O. P., CHENG, A. S., CHENG, W. K. and HEYWOOD, J. B., 1994, *Flame Shape Determination Using an Optical-Fiber Spark Plug and a Head-Gasket Ionization Probe,* SAE Technical Paper 941987.

SANTAVICCA , D.A., LIOU , D. and NORTH , G.L., 1990. *A Fractal Model of Turbulent Flame Kernel Growth.* SAE Technical Paper 900024.

SCHMIDT , S., WINKLER , F., SCHOEGL , O. and PONTOPPIDAN , M., 2004. *Development of a Combustion Process for a High Performance 2-Stroke Engine with High Pressure Direct Injection*. SAE Technical Paper 2004-01-2942.

SCHMIDT, S., SCHOEGL, O., ROTHBAUER, R. J., EICHLSEDER, H and KIRCHBERGER, R., 2007, *An Integrated 3D CFD Simulation Methodology for the Optimization of the Mixture Preparation of 2-Stroke DI Engines,* SAE Technical Paper 2007-32-0029.

SCHOEGL , O., SCHMIDT , S., ABART , M., ZINNER , C., KIRCHBERGER , R., FITL , M., GLINSNER , K. and LEIBER , S., 2010. *Possibilities and Limits of 1D CFD Simulation Methodology for the Layout of 2-Stroke GDI Combustion System.* SAE Technical Paper 2010-32-0017.

SCHREER, K., BECK, K. W., BERNHARDT, S., SPICHER, U. GEYER, W. and MEYER, S., 2009, *Knocking Investigations in a Small Two-Stroke SI Engine,* SAE Technical Paper 2009-32-0013.

SHAWCROSS , D., PUMPHREY , C. and ARNALL , D., 2000. *A Five-Million Kilometre, 100-Vehicle Fleet Trial, of an Air-Assist Direct Fuel Injected, Automotive 2-Stroke Engine.* SAE Technical Paper 2000-01-0898.

STONE, R., 1999, *Introduction to Internal Combustion Engines*, MacMillan Press Ltd.

TABACZYNSKI , R.J., FERGUSON , C.R. and RADHAKRISHNAN , K., 1977. *A Turbulent Entrainment Model for Spark-Ignition Engine Combustion.* SAE Technical Paper 770647.

TABACZYNSKI, R.J., TRINKER, F.H. and SHANNON, B.A.S., 1980. *Further refinement and validation of a turbulent flame propagation model for spark-ignition engines.* Combustion and Flame, 10, vol. 39, no. 2, pp. 111-121.

TANAKA , D., OKI , H., YAMAZAKI , T., MIURA , A. and TSUKAHARA , E., 2009. *Analysis of Cyclic Variations of Combustion in High Compression Ratio Boosted D.I.S.I. Engine by Ion-Current Probes and CFD.* SAE Technical Paper 2009-01-1484.

TANAKA, T., NARAHARA, K., TABATA, M., YOSHIYAMA, S. and TOMITA, E., 2005. *Ion current measurement in a homogeneous charge compression ignition engine.* International Journal of Engine Research, October 01, vol. 6, no. 5, pp. 453-463.

TEOH, Y.H., GITANO-BRIGGS, H. and TAN, Y.H., 2009, *Development of the Gaseous Fuel Direct Injection System for Small Two-Stroke Transports.* SAE Technical Paper 2009-32-0032.

TENNEKES, H., 1968. *Simple Model for the Small-Scale Structure of Turbulence.* Physics of Fluids, March 1968, vol. 11, no. 3, pp. 669-671.

TENNEKES, H. and LUMLEY, J. L., *A First Course in Turbulence*, 1974, The MIT Press, Cambridge, Massachusetts.

TOMITA , E., YOSHIYAMA , S., OHKURA , Y., TABUCHI , H. and HAMAMOTO , Y., 2000. *Turbulent Premixed Flames Under Lean Conditions Studied with Ion Current Measurement in a Homogeneous Charge Spark-Ignition Engine.* SAE Technical Paper 2000-01-1940.

TSAI, S. F., 1994, *An Improved Simulation of Small Two-Stroke Engines*, PhD Thesis, UMIST, Manchester, UK.

TSUI, Y. and CHENG, H., 1994, *Flow Calculation in a Loop-Scavenged Two-Stroke Motored Engine*, Int. J. Num. Meth. Heat Fluid Flow, Vol. 4, pp. 249-267.

TSUI, Y. and CHENG, H., 1995. *Tumbling Flow in Loop-Scavenged Two-Stroke Engines.* Journal of Fluids Engineering, 12/01, vol. 117, no. 4, pp. 628-632.

TURNER , J.W.G., BLUNDELL , D.W., PEARSON , R.J., PATEL , R., LARKMAN , D.B., BURKE , P., RICHARDSON , S., GREEN , N.M., BREWSTER , S., KENNY , R.G. and KEE , R.J., 2010. *Project Omnivore: A Variable Compression Ratio ATAC 2-Stroke Engine for Ultra-Wide-Range HCCI Operation on a Variety of Fuels.* SAE Technical Paper 2010-01-1249.

TURNS, S. R., 2000, *An Introduction to Combustion*, 2nd ed. McGraw-Hill Higher Education.

VERHELST, S. and SHEPPARD, C.G.W., 2009. *Multi-zone thermodynamic modelling of spark-ignition engine combustion - An overview.* Energy Conversion and Management, /5, vol. 50, no. 5, pp. 1326-1335.

VERHELST, S. and SIERENS, R., 2007. *A quasi-dimensional model for the power cycle of a hydrogen-fuelled ICE.* International Journal of Hydrogen Energy, 10, vol. 32, no. 15, pp. 3545-3554.

VRESSNER , A., STRANDH , P., HULTQVIST , A., TUNESTAL , P. and JOHANSSON , B., 2004. *Multiple Point Ion Current Diagnostics in an HCCI Engine.* SAE Technical Paper 2004-01-0934.

WATANABE , K., ITO , S. and TSURUSHIMA , T., 2010. *A New Quasi-Dimensional Combustion Model Applicable to Direct Injection Gasoline Engine*. SAE Technical Paper 2010-01-0544.

WIJESINGHE, J.S. and HONG, G., 2007. *Using Auto-Ignition to Improve the Cycle-to-Cycle Variations of a Small Two-Stroke Engine.* SAE Technical Paper 2007-32-0040.

WIJESINGHE, J.S. and HONG, G., 2011. *Effect of Spark Assistance on Autoignition Combustion in a Small Two-Stroke Engine*. Proceedings of the Institution of Mechanical Engineers, Part D: Journal of Automobile Engineering, January 01, vol. 225, no. 1, pp. 115-126.

WILCOX, D. C., 2006, *Turbulence Modelling for CFD,* DCW Industries.

WINKLER , F., SCHÖGL , O., OSWALD , R. and KIRCHBERGER , R., 2006. *Development of a Low Emission Two-Stroke Engine with Low Pressure Fuel Injection.* SAE Technical Paper 2006-32-0065.

WINERBONE, D. E. and PEARSON, R. J., 1999, *Design Techniques for Engine Manifolds, Wave Action Methods for IC Engines,* Professional Engineering Publishing.

WITZE, P. O., 1989, *Cycle Resolved Multipoint Ionization Probe Measurements in a Spark Ignition Engine,* SAE Technical Paper 892099.

WITZE, P. O., 1994, *Interpretation of Head-Gasket Ionization-Probe Measurements Using a Two-Zone Spherical Flame Model,* International Symposium COMODIA 94.

WU , C., ROBERTS , C.E., MATTHEWS , R.D. and HALL , M.J., 1993. *Effects of Engine Speed on Combustion in SI Engines: Comparisons of Predictions of a Fractal Burning Model with Experimental Data*. SAE Technical Paper 932714.

YOSHIYAMA , S., TOMITA , E., ZHANG , Z. and HAMAMOTO , Y., 2001. *Measurement and Simulation of Turbulent Flame Propagation in a Spark Ignition Engine by Using Fractal Burning Model.* SAE Technical Paper 2001-01-3603.

YU , L., CAMPBELL , T.and POLLOCK , W., 1997. *A Simulation Model for Direct-Fuel-Injection of Two-Stroke Gasoline Engines*. SAE Technical Paper 970366.

Two Zone Thermodynamic Model

The thermodynamic model for the two zone combustion model is taken from Verhelst and Sheppard (2009) with the following assumptions

- The original charge is homogeneous
- The pressure is uniform throughout the cylinder at any time
- The volume occupied by the flame reaction zone is negligible
- The burned gas is at full thermodynamic equilibrium except
- The unburned gas is frozen at its original composition
- Both burned and unburned gases have uniform but separate specific heats
- There is no heat transfer between burned and unburned zones

The first law of thermodynamics applied to the unburned zone is,

$$\frac{dQ_u}{dt} = \frac{dE_u}{dt} + \frac{dW}{dt} \tag{A.1}$$

$$\frac{dQ_u}{dt} = \frac{d(m_u e_u)}{dt} + P\frac{dV_u}{dt} + h_u\frac{dm_x}{dt} \tag{A.2}$$

Where dm_x is the mass transfer from unburned to burned zones.

Rearranging

$$m_u\frac{de_u}{dt} + e_u\frac{dm_u}{dt} = \frac{dQ_u}{dt} - P\frac{dV_u}{dt} - h_u\frac{dm_x}{dt} \tag{A.3}$$

Where $\frac{dm_u}{dt}$ is rate of mass leaving the unburned zone which is equal to $-\frac{dm_x}{dt}$

Then

$$m_u \frac{de_u}{dt} - e_u \frac{dm_x}{dt} = \frac{dQ_u}{dt} - P\frac{dV_u}{dt} - h_u \frac{dm_x}{dt} \tag{A.4}$$

Similarly for the burned zone,

$$m_b \frac{de_b}{dt} + e_b \frac{dm_b}{dt} = \frac{dQ_b}{dt} - P\frac{dV_b}{dt} + h_b \frac{dm_x}{dt} \tag{A.5}$$

Specific internal energy $e_u = c_{vu}T_u$

Then

$$m_u c_{vu} \frac{dT_u}{dt} - e_u \frac{dm_x}{dt} = \frac{dQ_u}{dt} - P\frac{dV_u}{dt} - h_u \frac{dm_x}{dt} \tag{A.6}$$

And

$$m_b c_{vb} \frac{dT_b}{dt} + e_b \frac{dm_b}{dt} = \frac{dQ_b}{dt} - P\frac{dV_b}{dt} + h_u \frac{dm_x}{dt} \tag{A.7}$$

Summing for the total internal energy,

$$\begin{aligned} m_u c_{vu} \frac{dT_u}{dt} - e_u \frac{dm_x}{dt} + m_b c_{vb} \frac{dT_b}{dt} + e_b \frac{dm_x}{dt} \\ = \frac{dQ_u}{dt} + \frac{dQ_b}{dt} - P\frac{dV_u}{dt} - P\frac{dV_b}{dt} - h_u \frac{dm_x}{dt} + h_u \frac{dm_x}{dt} \end{aligned} \tag{A.8}$$

Rearranging

$$m_u c_{vu} \frac{dT_u}{dt} + m_b c_{vb} \frac{dT_b}{dt} + \frac{dm_x}{dt}(e_b - e_u) = \frac{dQ}{dt} - P\frac{dV}{dt} \tag{A.9}$$

Where

$$\frac{dQ}{dt} = \frac{dQ_u}{dt} + \frac{dQ_b}{dt} \tag{A.10}$$

And

$$\frac{dV}{dt} = \frac{dV_u}{dt} + \frac{dV_b}{dt} \tag{A.11}$$

The state equation for the unburned zone can be written

$$PV_u = m_u R_u T_u \tag{A.12}$$

Differentiating state equation then

$$P\frac{dV_u}{dt} + V_u\frac{dP}{dt} = m_u R_u \frac{dT_u}{dt} + R_u T_u \frac{dm_u}{dt} \tag{A.13}$$

Substituting equation (A.13) into (A.6) then

$$m_u c_{vu}\frac{dT_u}{dt} - e_u\frac{dm_x}{dt} = \frac{dQ_u}{dt} - m_u R_u\frac{dT_u}{dt} - R_u T_u\frac{dm_u}{dt} + V_u\frac{dP}{dt} - h_u\frac{dm_x}{dt} \tag{A.14}$$

Rearranging and including the relationship $c_v + R = c_p$ then

$$m_u c_{pu}\frac{dT_u}{dt} = \frac{dQ_u}{dt} + V_u\frac{dP}{dt} + \frac{dm_x}{dt}[R_u T_u - h_u + e_u] \tag{A.15}$$

Specific enthalpy $h = e_u + PV$ and gas characteristic $PV = RT$ then Equation (A.15) becomes,

$$m_u c_{pu} \frac{dT_u}{dt} = \frac{dQ_u}{dt} + V_u \frac{dP}{dt} \tag{A.16}$$

Then for the unburned temperature

$$\frac{dT_u}{dt} = \frac{1}{m_u c_{pu}} \left[\frac{dQ_u}{dt} + V_u \frac{dP}{dt} \right] \tag{A.17}$$

Differentiating state equation for the burned zone

$$P \frac{dV_b}{dt} + V_b \frac{dP}{dt} = m_b R_b \frac{dT_b}{dt} + R_b T_b \frac{dm_b}{dt} \tag{A.18}$$

Or

$$\frac{dV_b}{dt} = \frac{m_b R_b}{P} \frac{dT_b}{dt} + \frac{R_b T_b}{P} \frac{dm_b}{dt} - \frac{V_b}{P} \frac{dP}{dt} \tag{A.19}$$

Similarly for the unburned zone

$$\frac{dV_u}{dt} = \frac{m_u R_u}{P} \frac{dT_u}{dt} + \frac{R_u T_u}{P} \frac{dm_u}{dt} - \frac{V_u}{P} \frac{dP}{dt} \tag{A.20}$$

Substituting equations (A.19) and (A.20) into (A.11) then

$$\frac{dV}{dt} = \frac{m_u R_u}{P} \frac{dT_u}{dt} + \frac{R_u T_u}{P} \frac{dm_u}{dt} - \frac{V_u}{P} \frac{dP}{dt} + \frac{m_b R_b}{P} \frac{dT_b}{dt} + \frac{R_b T_b}{P} \frac{dm_b}{dt} - \frac{V_b}{P} \frac{dP}{dt} \tag{A.21}$$

$\frac{dm_u}{dt} = -\frac{dm_x}{dt}$ and $\frac{dm_b}{dt} = \frac{dm_x}{dt}$

Then

$$\frac{dV}{dt} = \frac{R_b T_b}{P}\frac{dm_x}{dt} - \frac{R_u T_u}{P}\frac{dm_x}{dt} + \frac{m_u R_u}{P}\frac{dT_u}{dt} + \frac{m_b R_b}{P}\frac{dT_b}{dt} - \frac{V_u}{P}\frac{dP}{dt} - \frac{V_b}{P}\frac{dP}{dt} \tag{A.22}$$

Rearranging

$$\frac{dV}{dt} = \left[\frac{R_b T_b}{P} - \frac{R_u T_u}{P}\right]\frac{dm_x}{dt} + \frac{m_u R_u}{P}\frac{dT_u}{dt} + \frac{m_b R_b}{P}\frac{dT_b}{dt} - \frac{dP}{dt}\left[\frac{V_u}{P} + \frac{V_b}{P}\right] \tag{A.23}$$

Further rearrangement

$$\frac{dT_b}{dt} = \frac{P}{m_b R_b}\left\{\frac{dV}{dt} - \left[\frac{R_b T_b}{P} - \frac{R_u T_u}{P}\right]\frac{dm_x}{dt} - \frac{m_u R_u}{P}\frac{dT_u}{dt} + \frac{dP}{dt}\left[\frac{V_u}{P} + \frac{V_b}{P}\right]\right\} \tag{A.24}$$

Substituting (A.17) and (A.24) into equation (A.9)

$$\begin{aligned} m_u c_{vu}\frac{1}{m_u c_{pu}}\left[\frac{dQ_u}{dt} + V_u\frac{dP}{dt}\right] & \\ + m_b c_{vb}\frac{P}{m_b R_b}\left\{\frac{dV}{dt} - \left[\frac{R_b T_b}{P} - \frac{R_u T_u}{P}\right]\frac{dm_x}{dt}\right. & \\ \left. - \frac{m_u R_u}{P}\frac{1}{m_u c_{pu}}\left[\frac{dQ_u}{dt} + V_u\frac{dP}{dt}\right] + \frac{dP}{dt}\left[\frac{V_u}{P} + \frac{V_b}{P}\right]\right\} + \frac{dm_x}{dt}(e_b - e_u) & \\ = \frac{dQ}{dt} - P\frac{dV}{dt} & \end{aligned} \tag{A.25}$$

Which after rearrangement may be written

$$\begin{aligned} \frac{dP}{dt} = \left[\frac{c_{vu}}{c_{pu}}V_u - \frac{c_{vb}}{R_b}\frac{R_u}{c_{pu}}V_u + \frac{c_{vb}}{R_b}\mathrm{V}\right]^{-1} & \\ \times\left\{\frac{dQ}{dt} - P\frac{dV}{dt}\left[1 + \frac{c_{vb}}{R_b}\right] + \frac{dm_x}{dt}\left[\frac{c_{vb}}{R_b}\left(T_b - \frac{R_u T_u}{R_b}\right) - (e_b - e_u)\right]\right. & \\ \left. - \frac{dQ_u}{dt}\left[\frac{c_{vu}}{c_{pu}} - \frac{c_{vb}}{R_b}\frac{R_u}{c_{pu}}\right]\right\} & \end{aligned} \tag{A.26}$$

During the combustion cycle at each time step the new cylinder pressure is determined from equation (A.26), then the new unburned temperature may be determined from equation (A.17) and finally the burned temperature is determined from equation (A.24).

Chemical Equilibrium

The required amount of oxidiser to completely burn a hydrocarbon fuel is given by the stoichiometry relation

$$C_xH_y + a(O_2 + 3.76N_2) \rightarrow xCO_2 + \frac{y}{2}H_2O + 3.76aN_2 \quad \text{(B.1)}$$

For stoichiometric combustion $a = x + {}^{y}/_{4}$

The stoichiometric air/fuel ratio is given by

$$AFR_{stoic} = x + {}^{y}/_{4} . \frac{mwO_2 + (3.76mwN_2)}{mwFuel} \quad \text{(B.2)}$$

And then the equivalence ratio

$$\phi = \frac{AFR_{stoic}}{AFR} \quad \text{(B.3)}$$

Species concentration in the burned products is determined from chemical equilibrium of the products based on a calculation of ten species, taken from Ferguson and Kirkpatrick (2001), based on the work of Olikara and Borman (1975).

For a simple hydrocarbon fuel the reaction equation can be written

$$\begin{aligned} &C_xH_y + a(O_2 + 3.76N_2) \\ &\quad \rightarrow n_{CO2}CO_2 + n_{H2O}H_2O + n_{N2}N_2 + n_{O2}O_2 + n_{CO}CO + n_{H2}H_2 \\ &\quad + n_HH + n_OO + n_{OH}OH + n_{NO}NO \end{aligned} \quad \text{(B.4)}$$

Where x and y are number of carbon and hydrogen molecules, respectively, in the fuel. The number of air molecules is given by a and n_i is the number of moles of species i.

For atom balance the following four equations apply

$$\text{C: } x = (\chi_{CO2} + \chi_{CO})N_{tot} \tag{B.5}$$

$$\text{H: } y = (2\chi_{H2O} + 2\chi_{H2} + \chi_{H} + \chi_{OH})N_{tot} \tag{B.6}$$

$$\text{O: } 2a = (2\chi_{CO2} + \chi_{H2O} + 2\chi_{O2} + \chi_{CO} + \chi_{O} + \chi_{OH} + \chi_{NO})N_{tot} \tag{B.7}$$

$$\text{N: } 3.76a = (2\chi_{N2} + \chi_{NO})N_{tot} \tag{B.8}$$

Where χ_i represents the mole fraction and N_{tot} is the total number of moles,

The sum of the species fractions is equal to unity

$$\chi_{CO2} + \chi_{H2O} + \chi_{N2} + \chi_{O2} + \chi_{CO} + \chi_{H2} + \chi_{H} + \chi_{O} + \chi_{OH} + \chi_{NO} = 1 \tag{B.9}$$

Six gas phase equilibrium reactions, where K_i is an equilibrium constant which is defined by curve fit data provided by Ferguson and Kirkpatrick (2001)

$$\log_{10} K_i(T_{ad}) = A_i \ln(T_{ad}/1000) + \frac{B_i}{T_{ad}} + C_i + D_i T_{ad} + E_i T_{ad}^2 \tag{B.10}$$

Where Tad is the adiabatic temperature

$$\frac{1}{2}H_2 \leftrightarrow H, K_1 = \frac{\chi_H P^{1/2}}{\chi_{H_2}^{1/2}} \tag{B.11}$$

$$\frac{1}{2}O_2 \leftrightarrow O, K_2 = \frac{\chi_O P^{1/2}}{\chi_{O2}^{1/2}} \tag{B.12}$$

$$\frac{1}{2}H_2 + \frac{1}{2}O_2 \leftrightarrow OH, K_3 = \frac{\chi_{OH}}{\chi_{O2}^{1/2}\chi_{H2}^{1/2}} \tag{B.13}$$

$$\frac{1}{2}O_2 + \frac{1}{2}N_2 \leftrightarrow NO,\ K_4 = \frac{\chi_{NO}}{\chi_{O2}^{1/2}\chi_{N2}^{1/2}} \tag{B.14}$$

$$H_2 + \frac{1}{2}O_2 \leftrightarrow H_2O,\ K_5 = \frac{\chi_{H2O}}{\chi_{O2}^{1/2}\chi_{H2}P^{1/2}} \tag{B.15}$$

$$CO + \frac{1}{2}O_2 \leftrightarrow CO_2,\ K_6 = \frac{\chi_{CO2}}{\chi_{CO}\chi_{O2}^{1/2}P^{1/2}} \tag{B.16}$$

To determine the species fraction in the products an initial estimate is made for the adiabatic flame temperature. With the estimated adiabatic temperature the six equilibrium constants may be calculated and then the atomic balance Equation (B.2) to (B.5), the gas phase equilibrium reaction Equations (B.11) to (B.16) and species fraction Equation (B.9) may be solved iteratively using a Newton Rhaphson procedure to determine the product species fraction. From the species fraction the enthalpy of products can be determined and a new adiabatic temperature defined, the process is repeated until the adiabatic temperature converges to within 5%.

The fresh charge of reactants is made up of fuel, air and residual exhaust gas. For each mole of fuel the number of moles of air is given by,

$$N_{air} = \frac{x + {}^{y}/_{4}}{\phi} \times 4.76 \tag{B.17}$$

The exhaust residual is given as a fraction of the mass of air,

$$N_{exh} = \Pi N_{air} \tag{B.18}$$

$$H_R = H_{fuel} + H_{air} + H_{exh} \tag{B.19}$$

The specific enthalpy of the fuel is taken as -208450 kJ/kmol for octane and -267120 kJ/kmol for gasoline (Ferguson and Kirkpatrick, 2001). The molar specific enthalpy for air is calculated by,

$$h_{air} = 0.21\bar{h}_{O_2} + 0.79\bar{h}_{N_2} \tag{B.20}$$

Where the enthalpies are taken from tabulated data taken from Turns (2000) at the cylinder mixture temperature.

$$\sum_R N_i\bar{h}_i - \sum_P N_i\,\bar{h}_i - R_u(N_R T_i - N_P T_{ad}) = 0 \tag{B.21}$$

Where$\sum_R N_i\bar{h}_i$ is the sum of the enthalpies of the reactants and $\sum_P N_i\bar{h}_i$ the products.

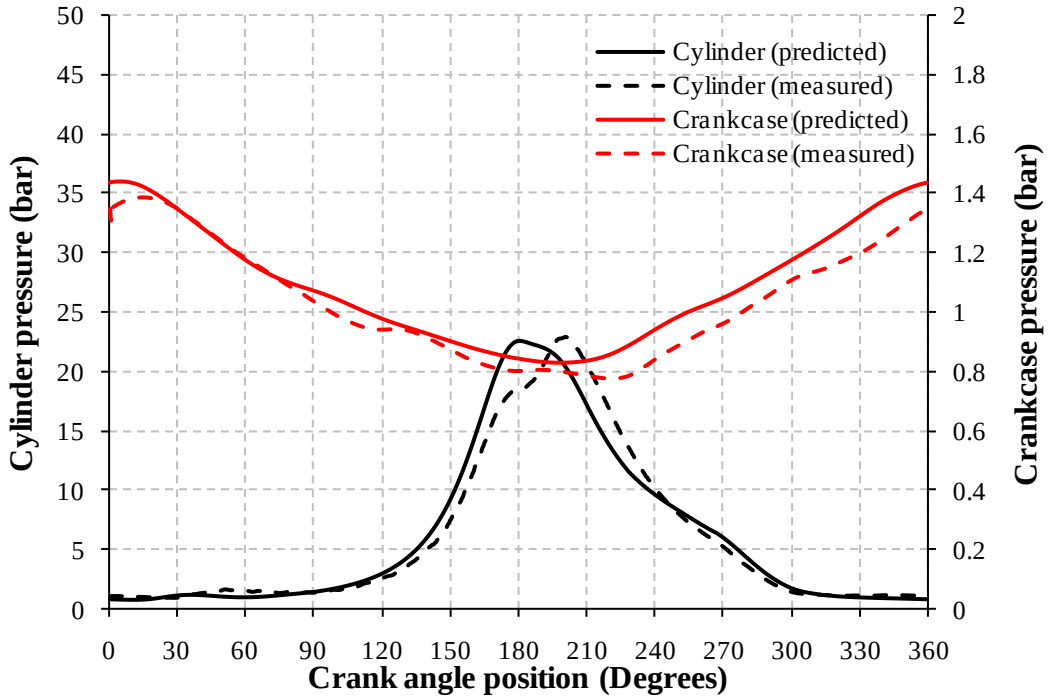

Squish head half throttle 7555 rpm.

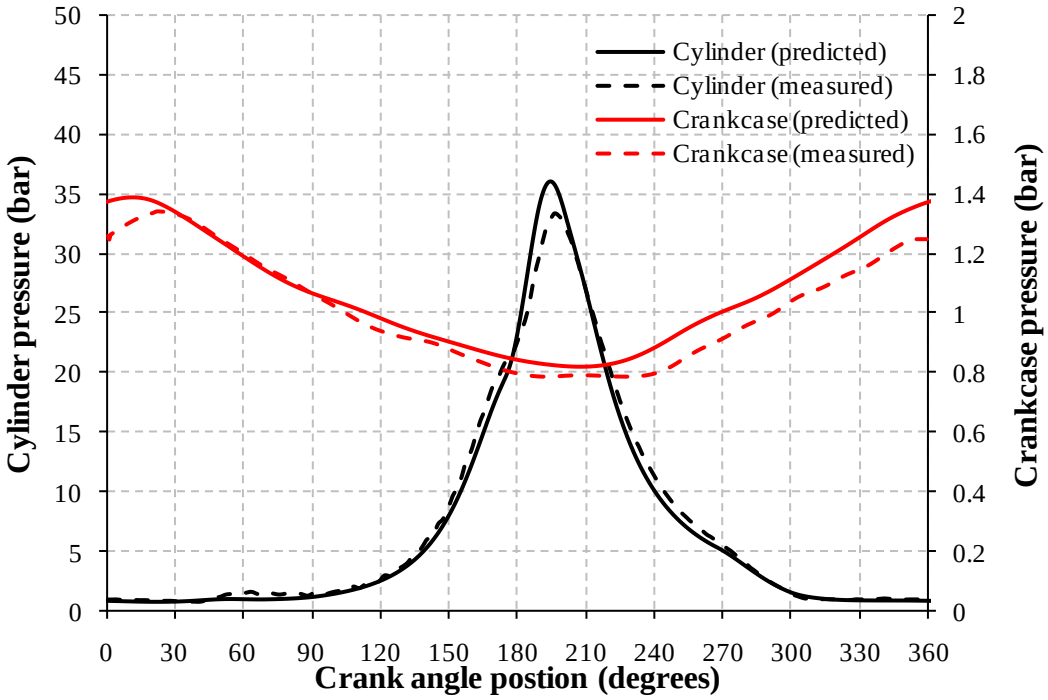

Squish head half throttle 8069 rpm.

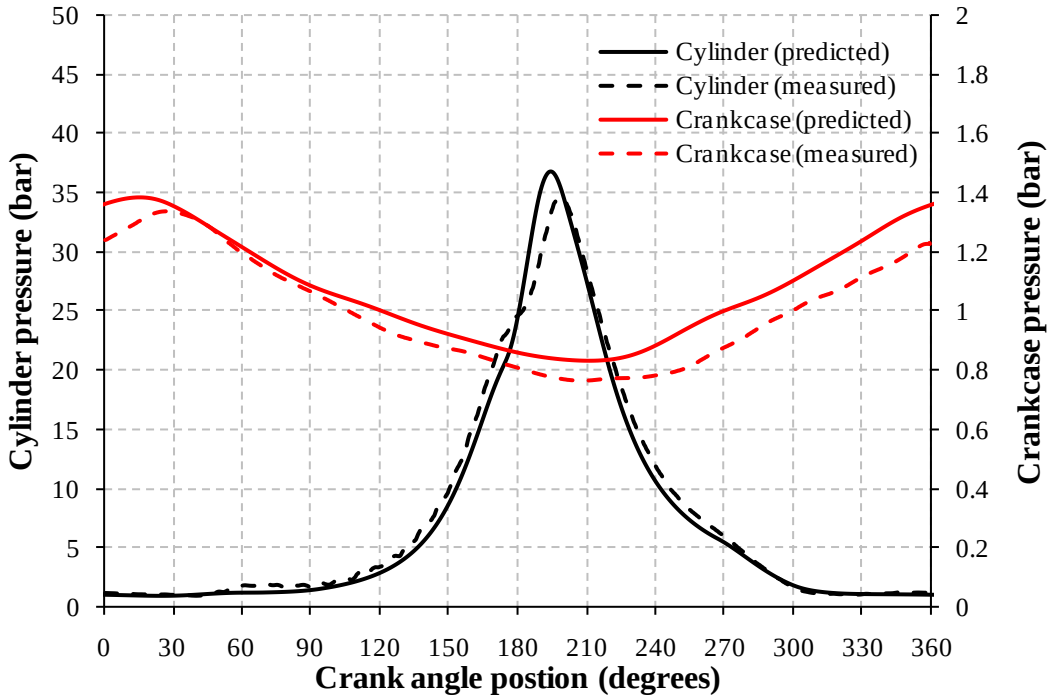

Squish head half throttle 8517 rpm.

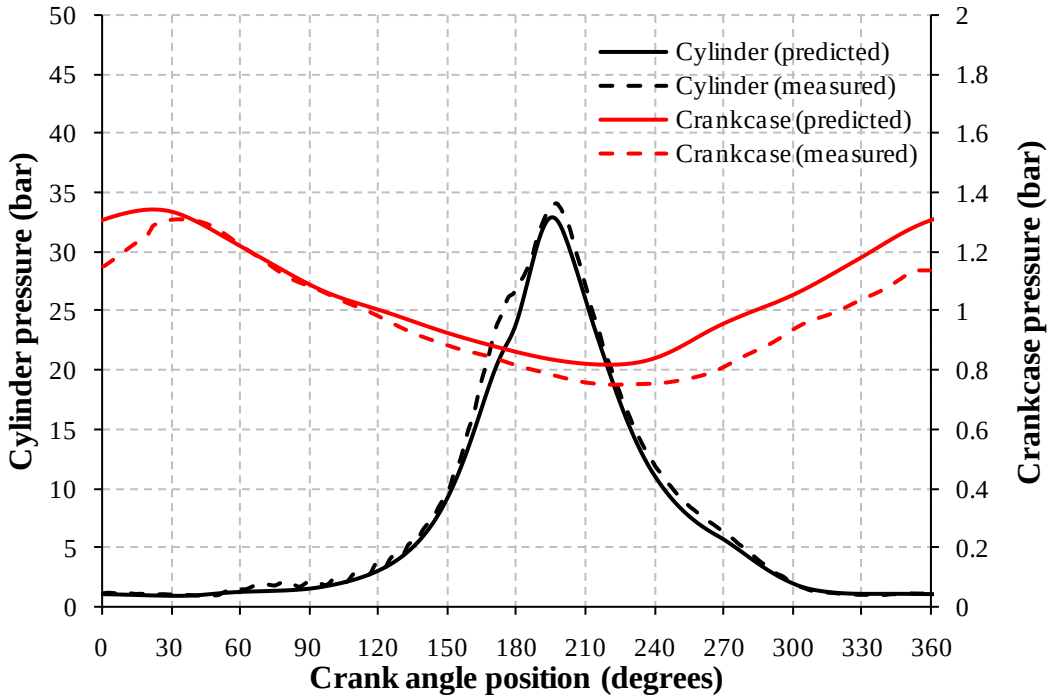

Squish head half throttle 8981 rpm.

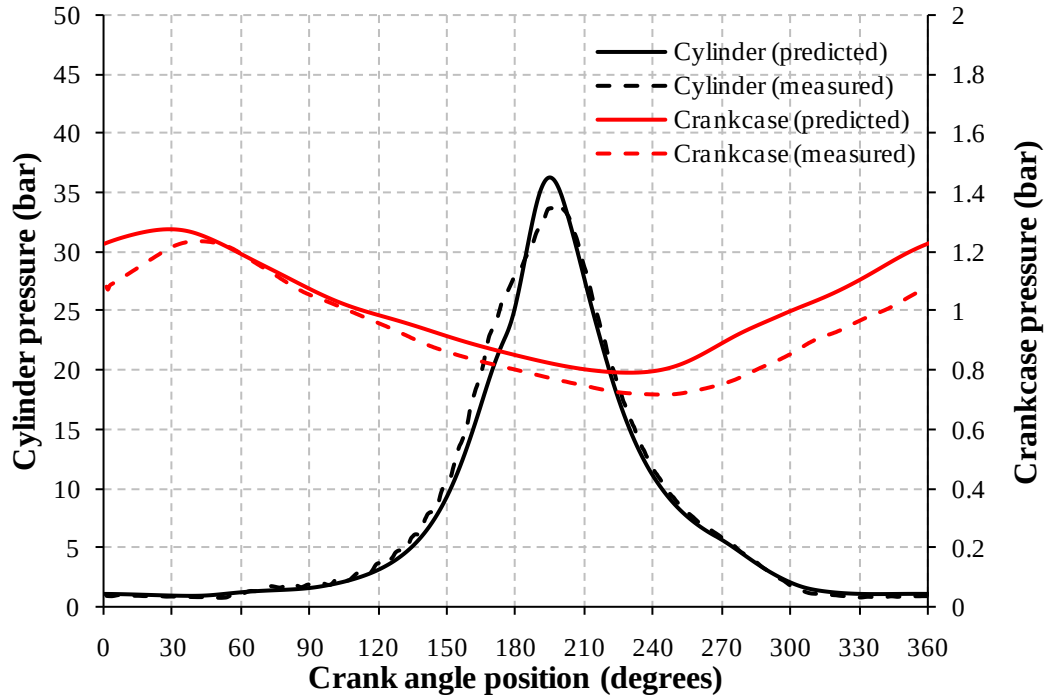

Squish head half throttle 9369 rpm.

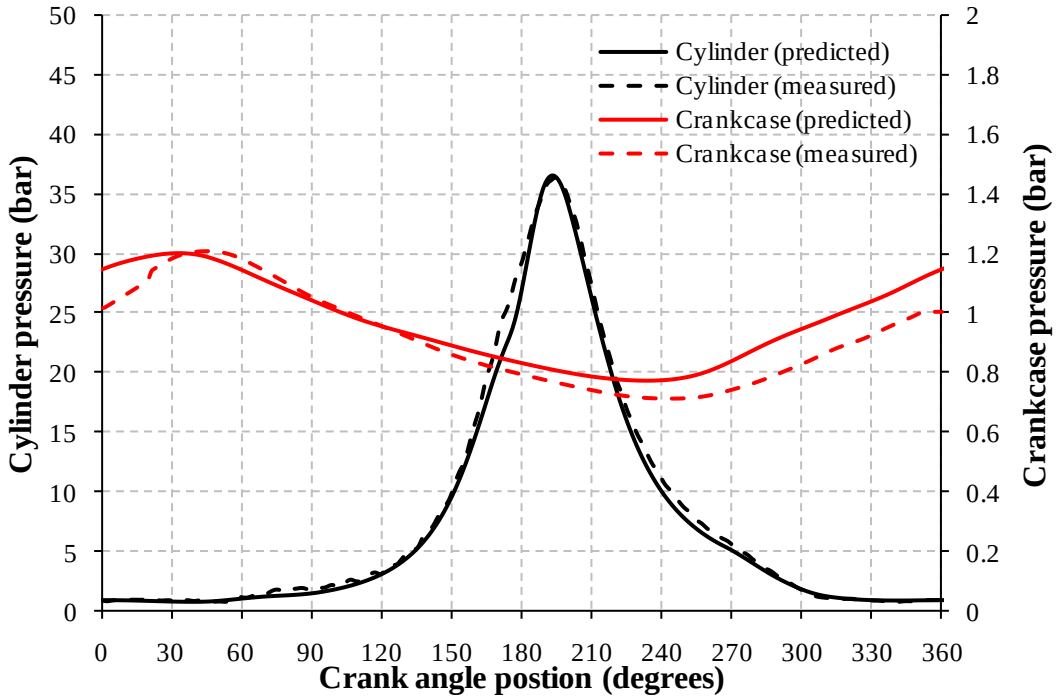

Squish head half throttle 9812 rpm.

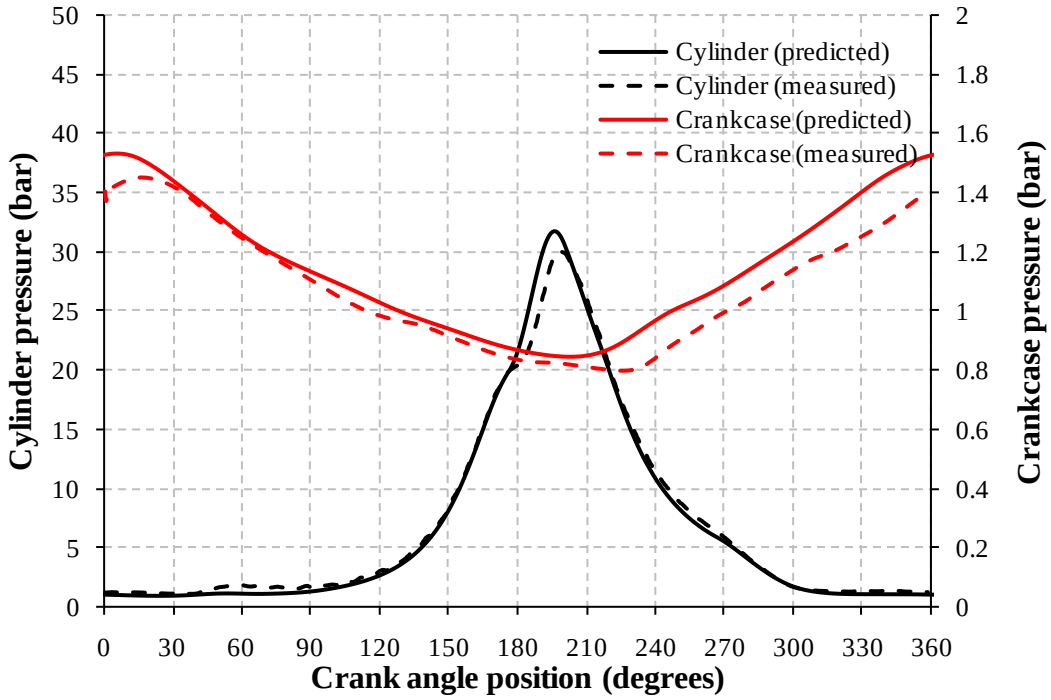

Squish head full throttle 7640 rpm.

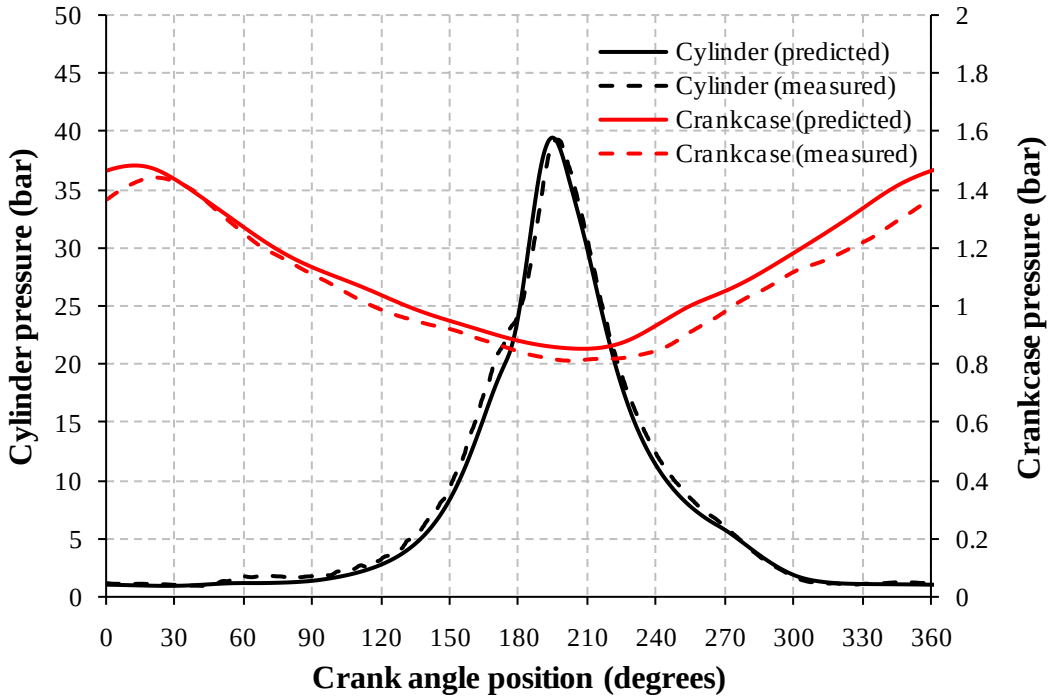

Squish head full throttle 8162 rpm.

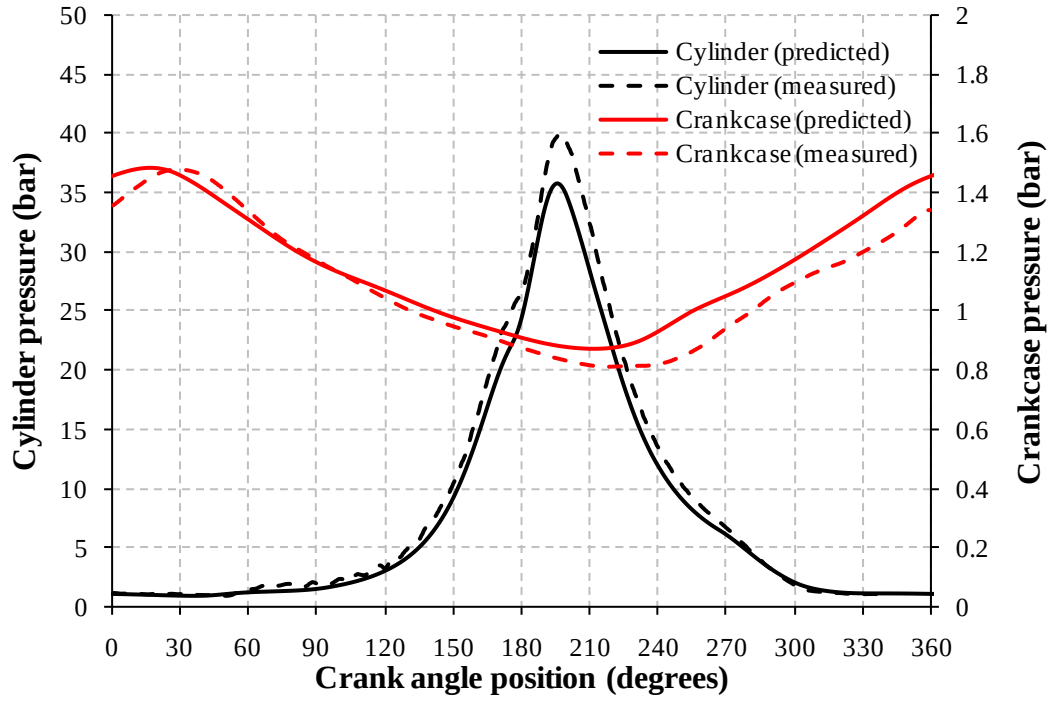

Squish head full throttle 8640 rpm.

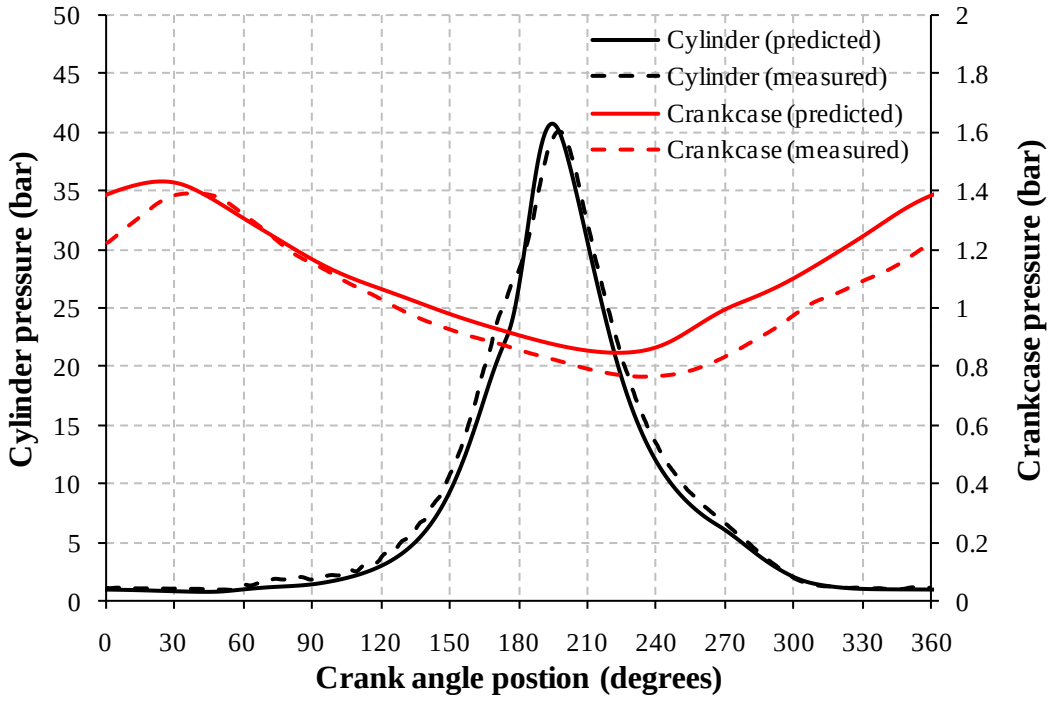

Squish head full throttle 9075 rpm.

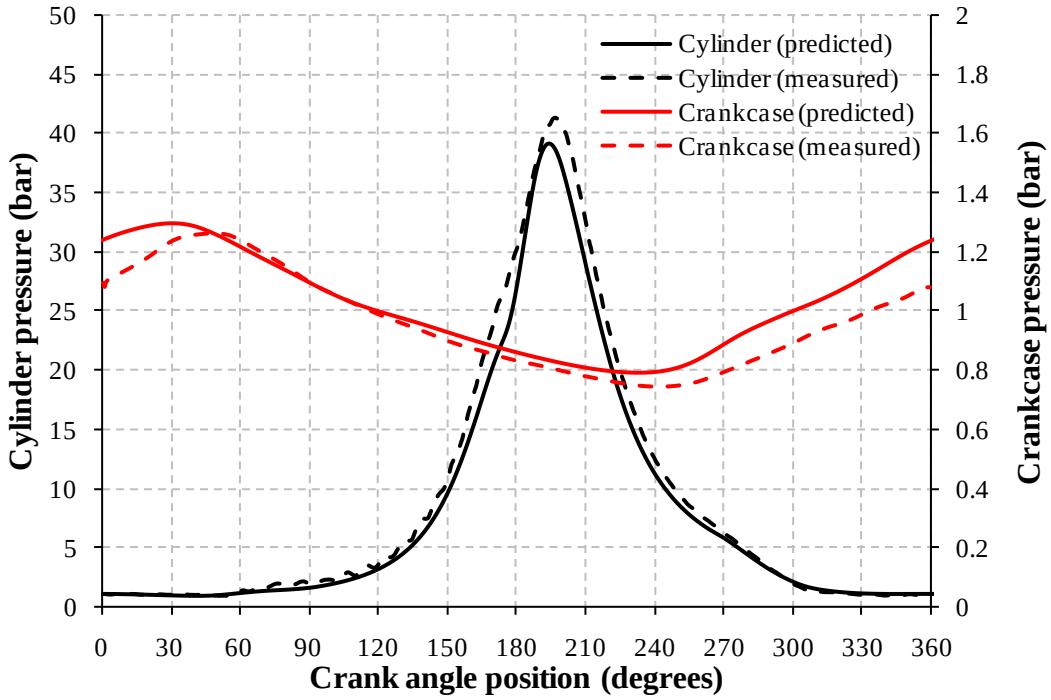

Squish head full throttle 9489 rpm.

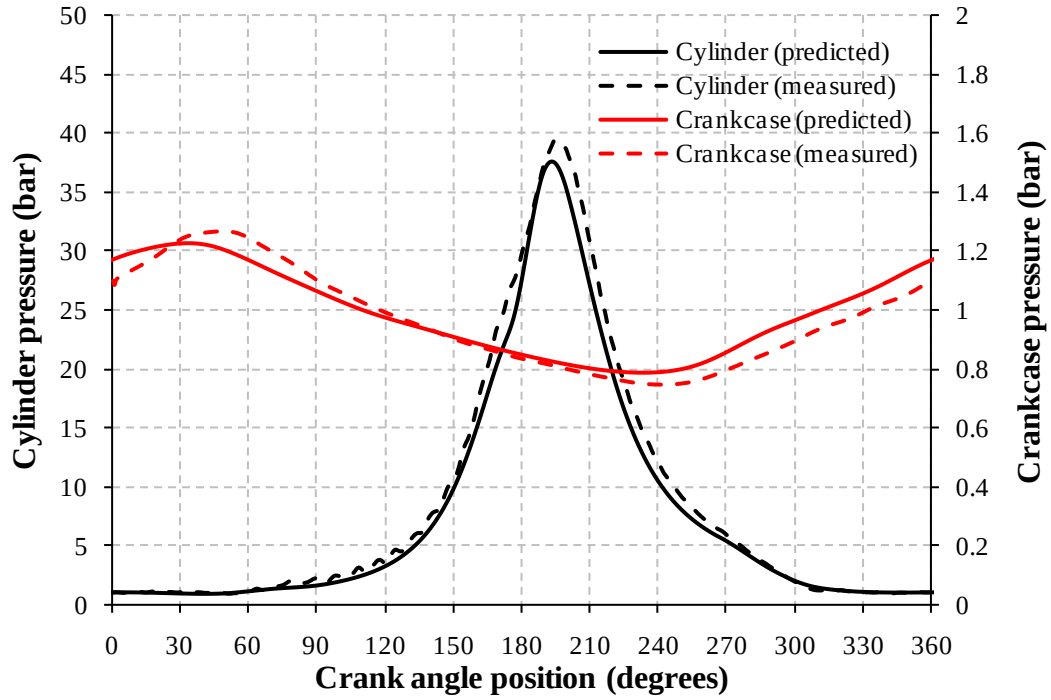

Squish head full throttle 9878 rpm.

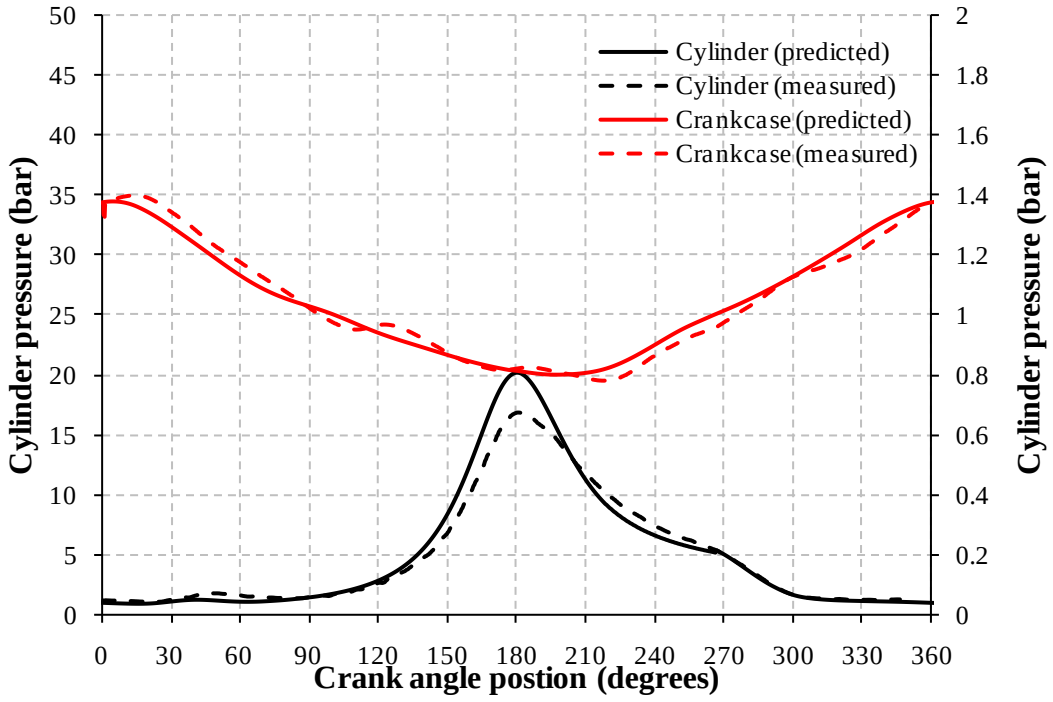

Disc head half throttle 7433 rpm.

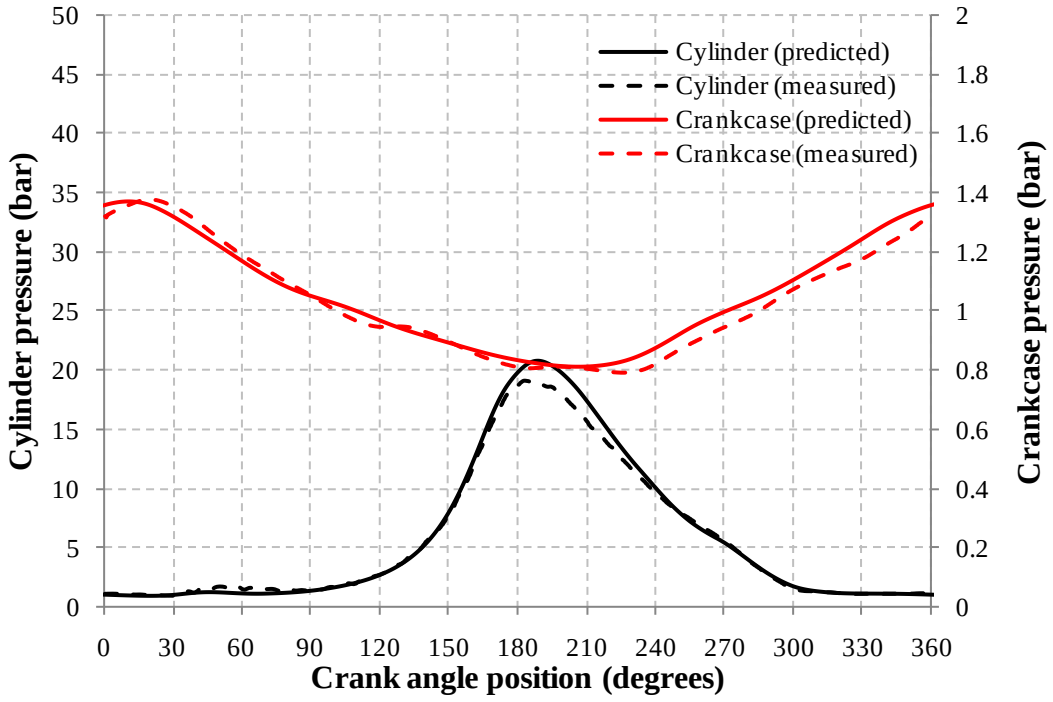

Disc head half throttle 7938 rpm.

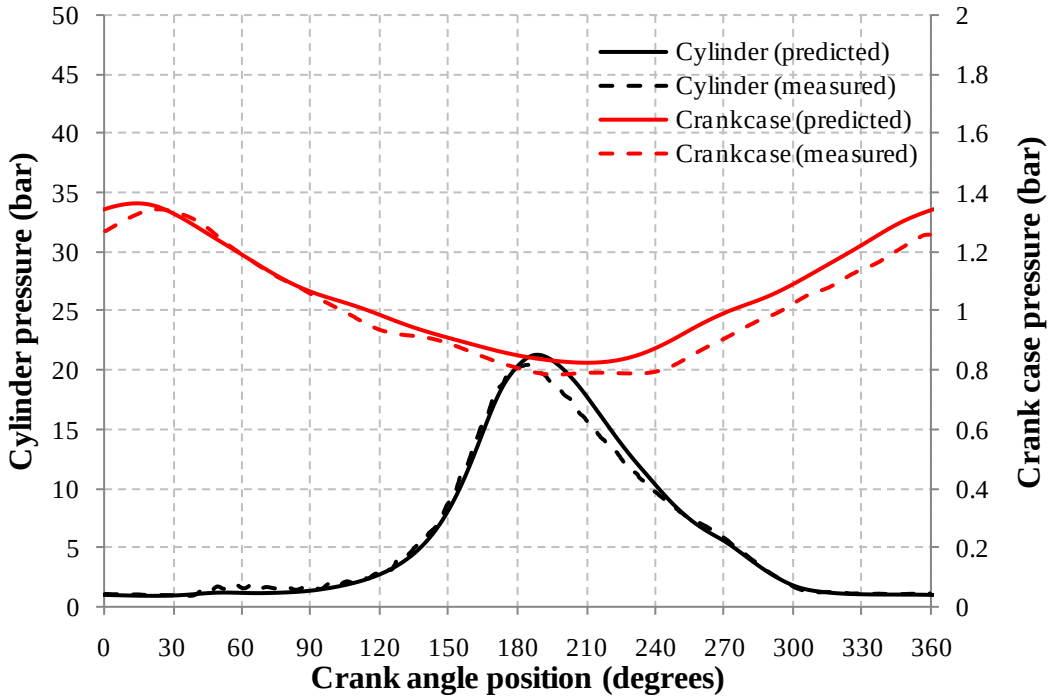

Disc head half throttle 8359 rpm.

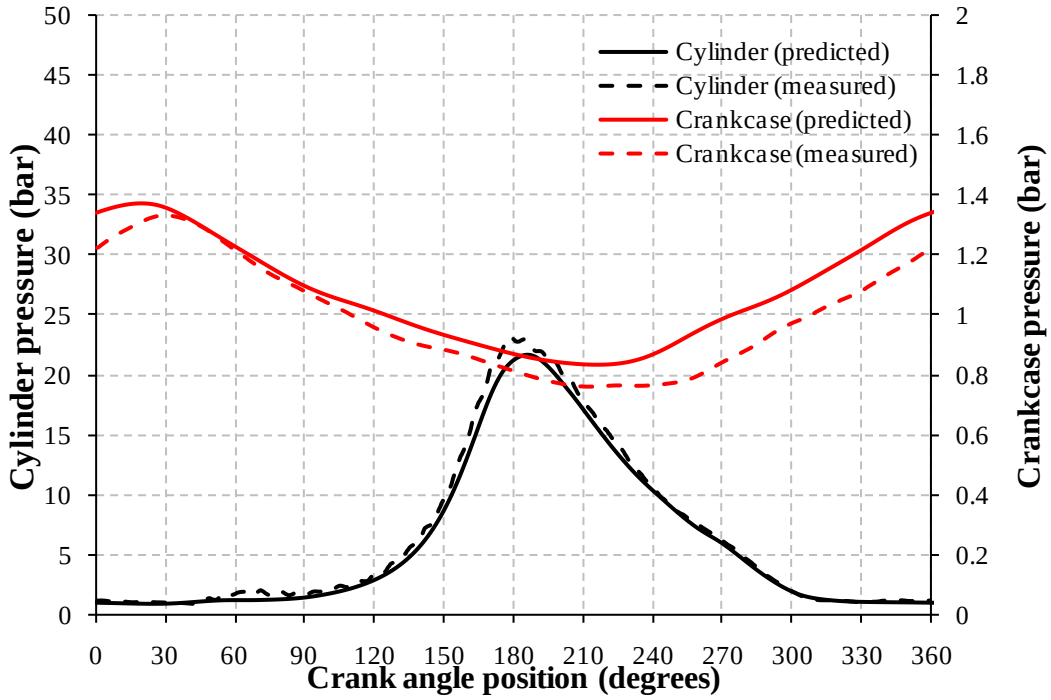

Disc head half throttle 8808 rpm.

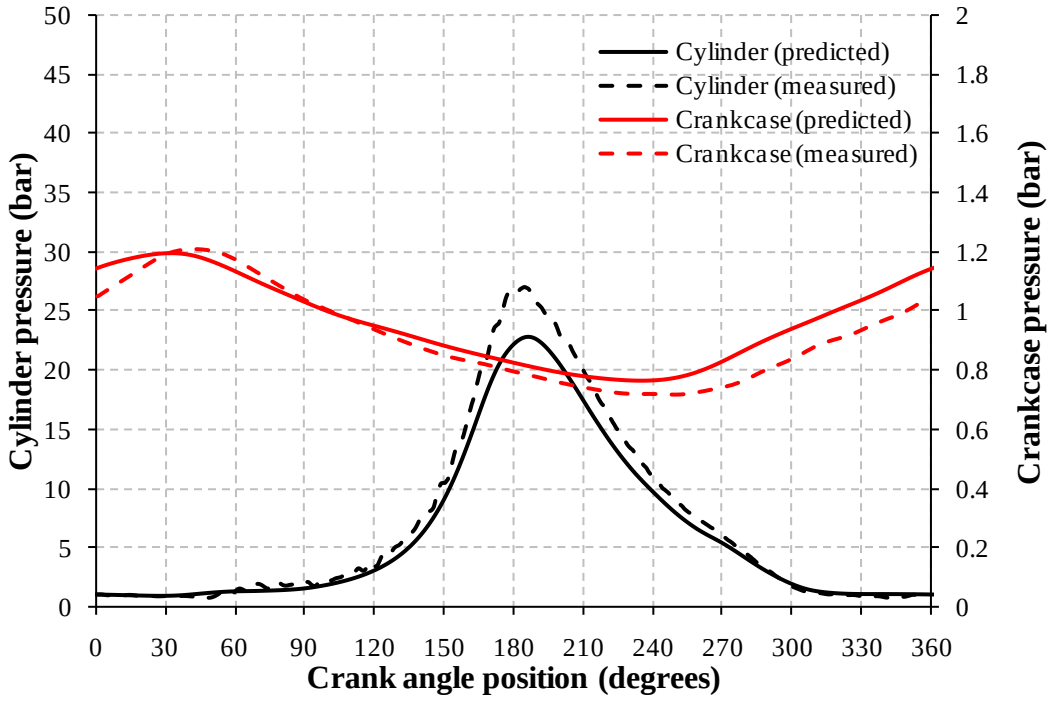

Disc head half throttle 9683 rpm.

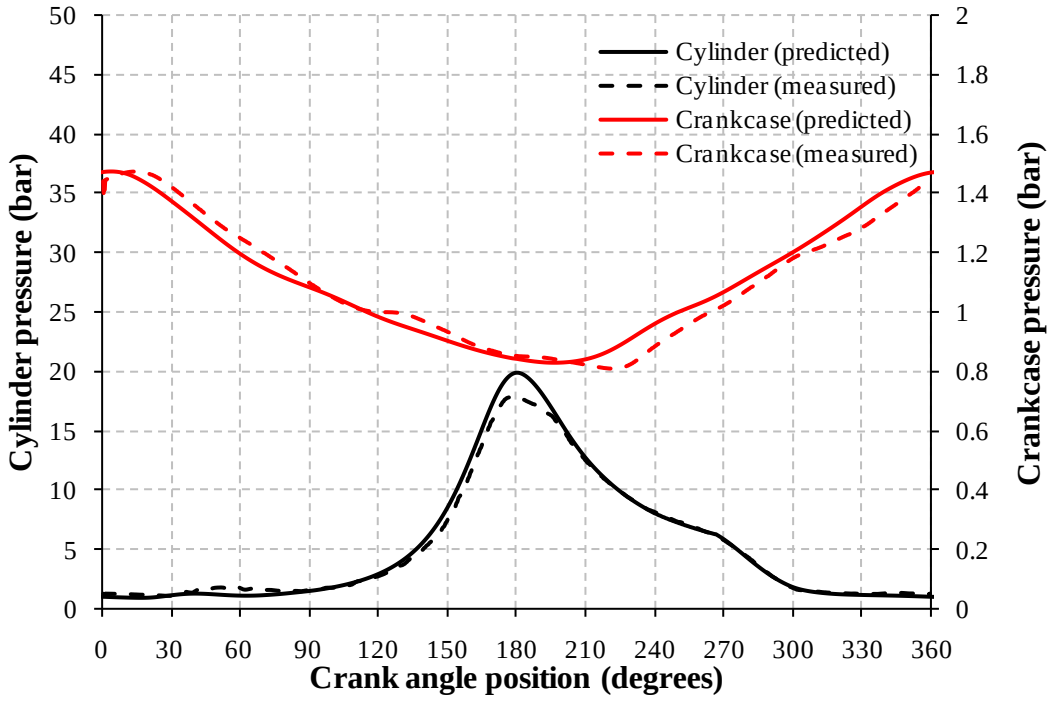

Disc head full throttle 7446 rpm.

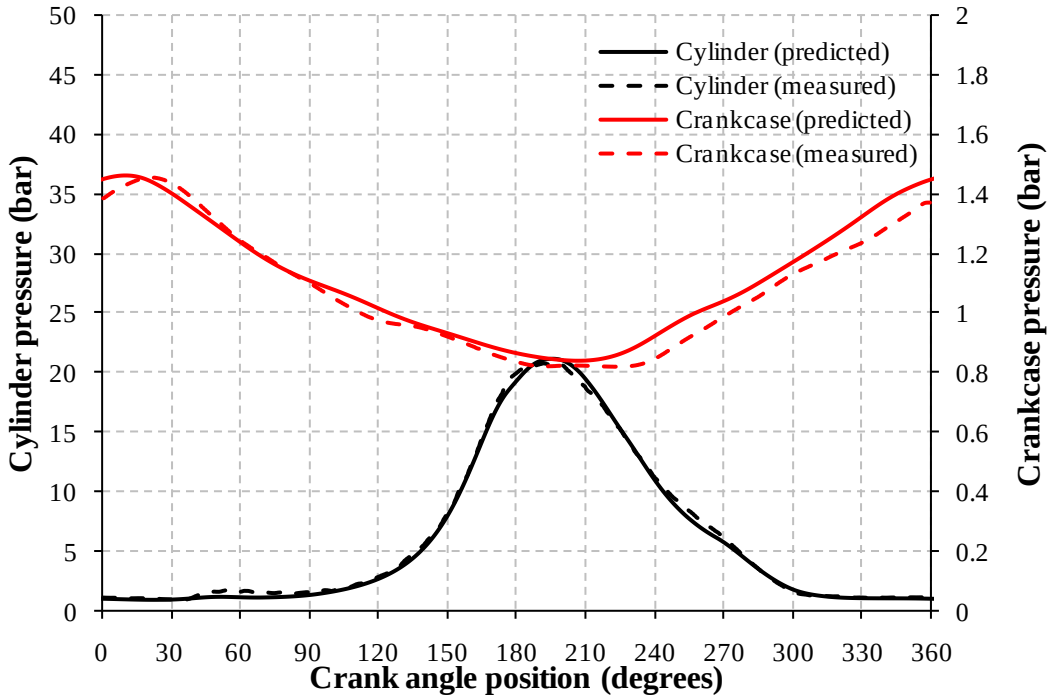

Disc head full throttle 7991 rpm.

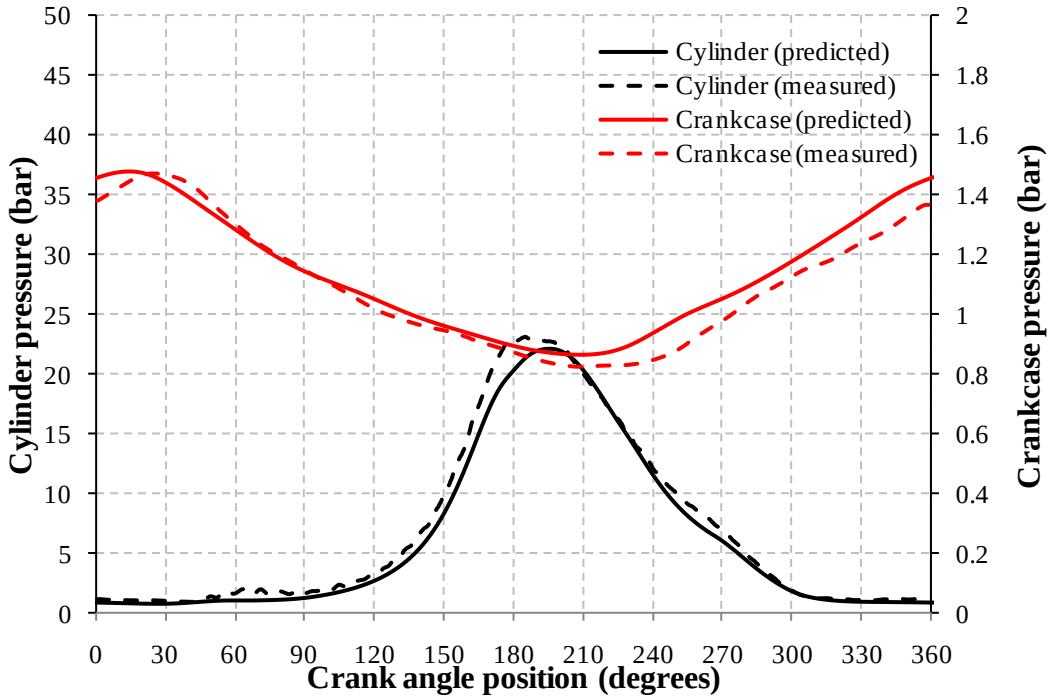

Disc head full throttle 8437 rpm.

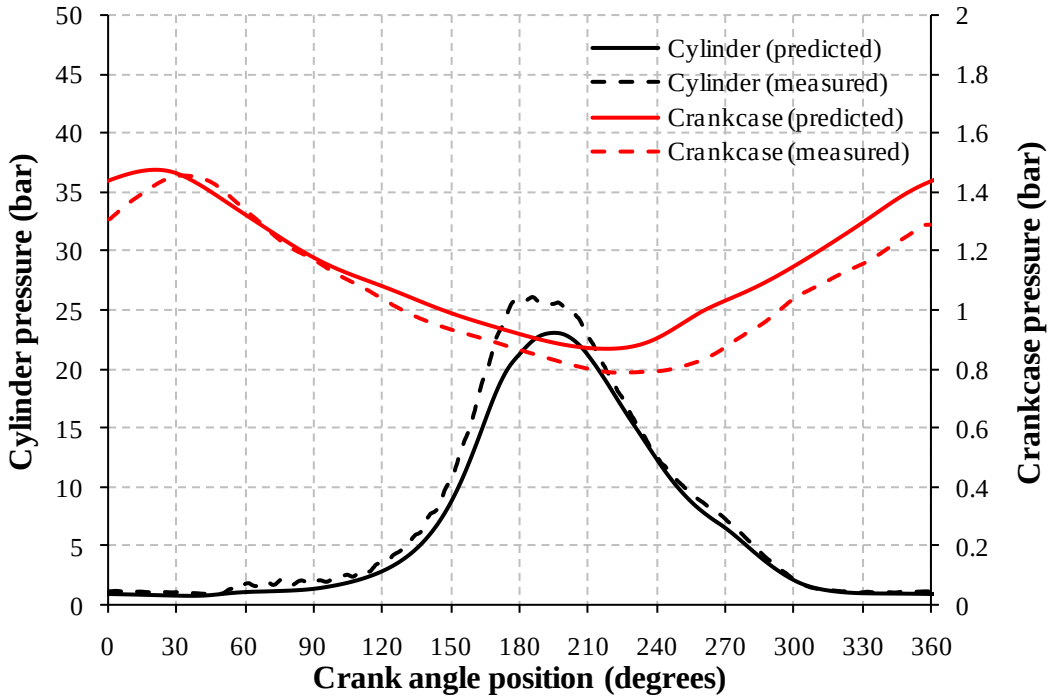

Disc head full throttle 8896 rpm.

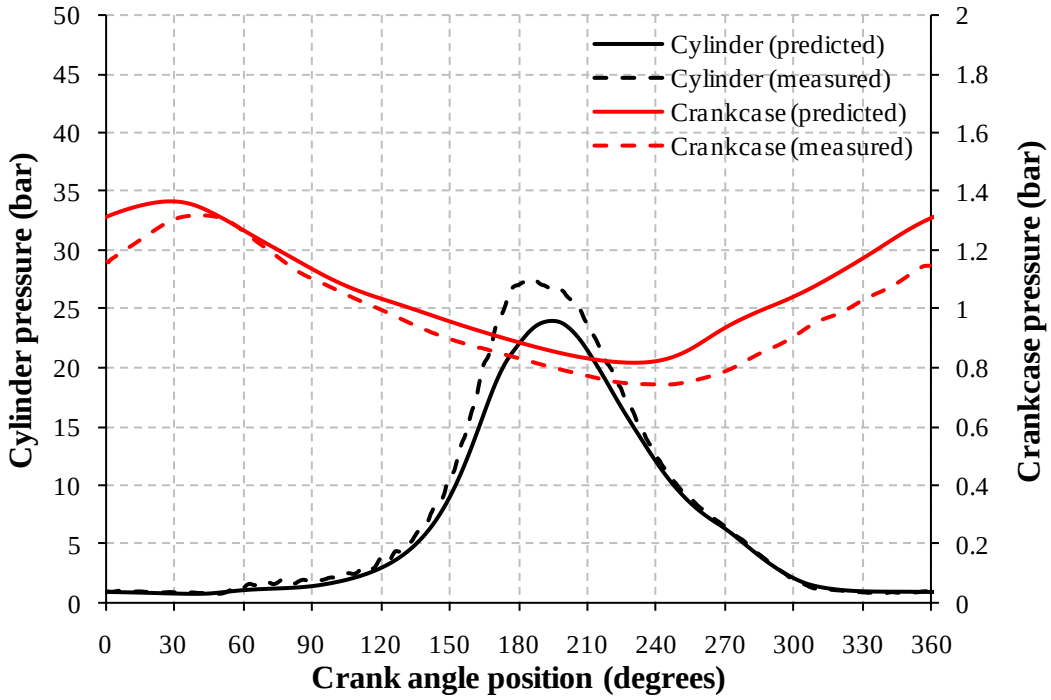

Disc head full throttle 9335 rpm.

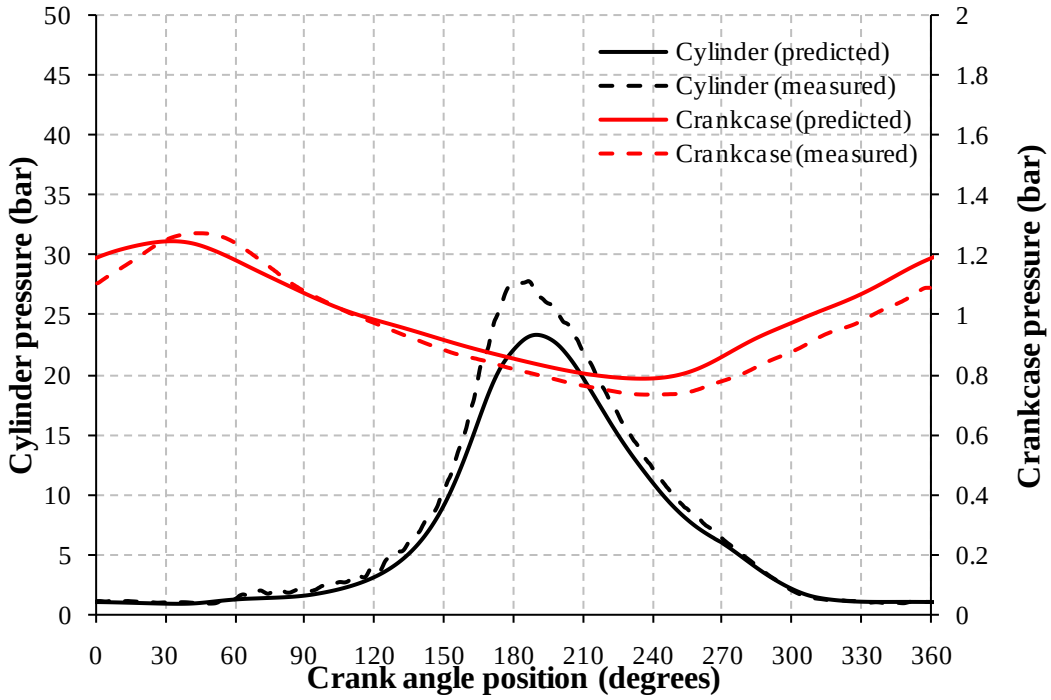

Disc head full throttle 9718 rpm.

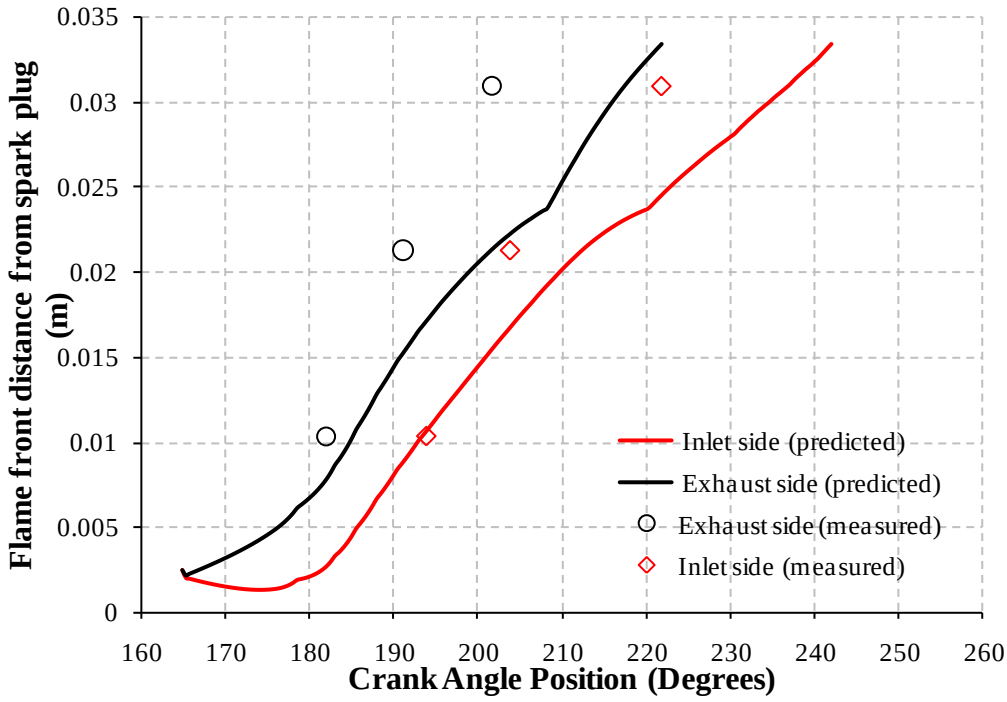

Squish head half throttle 7555 rpm.

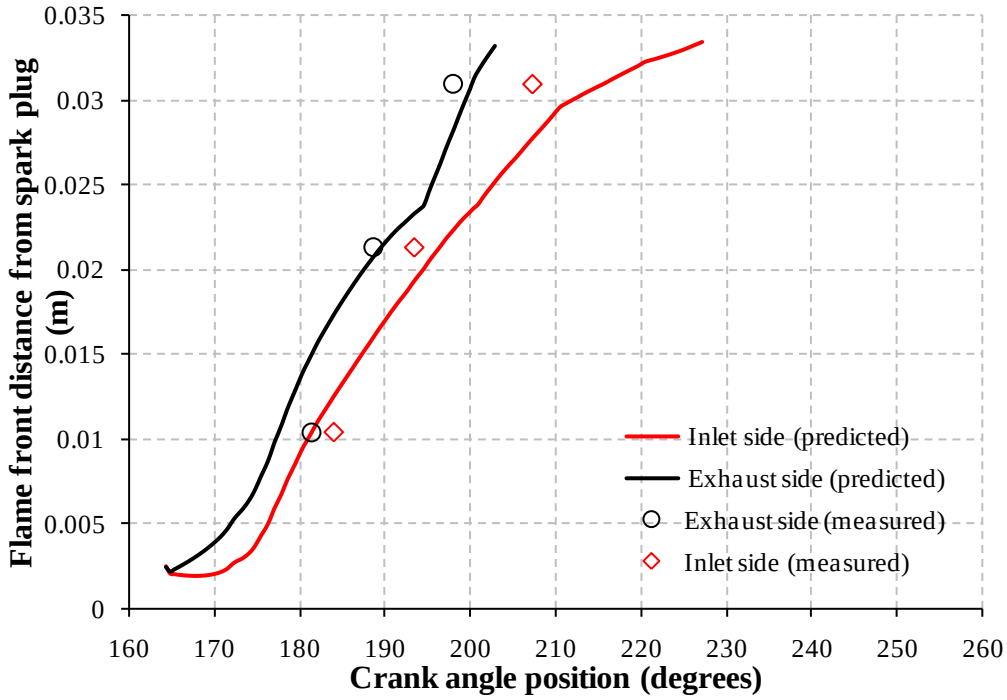

Squish head half throttle 8069 rpm.

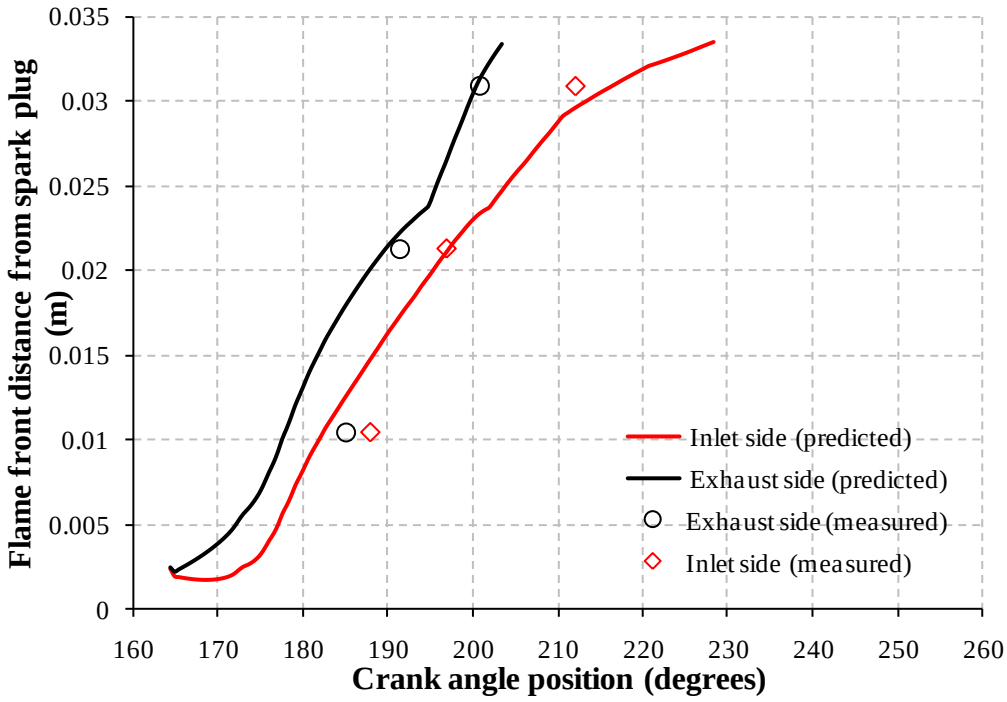

Squish head half throttle 8517 rpm.

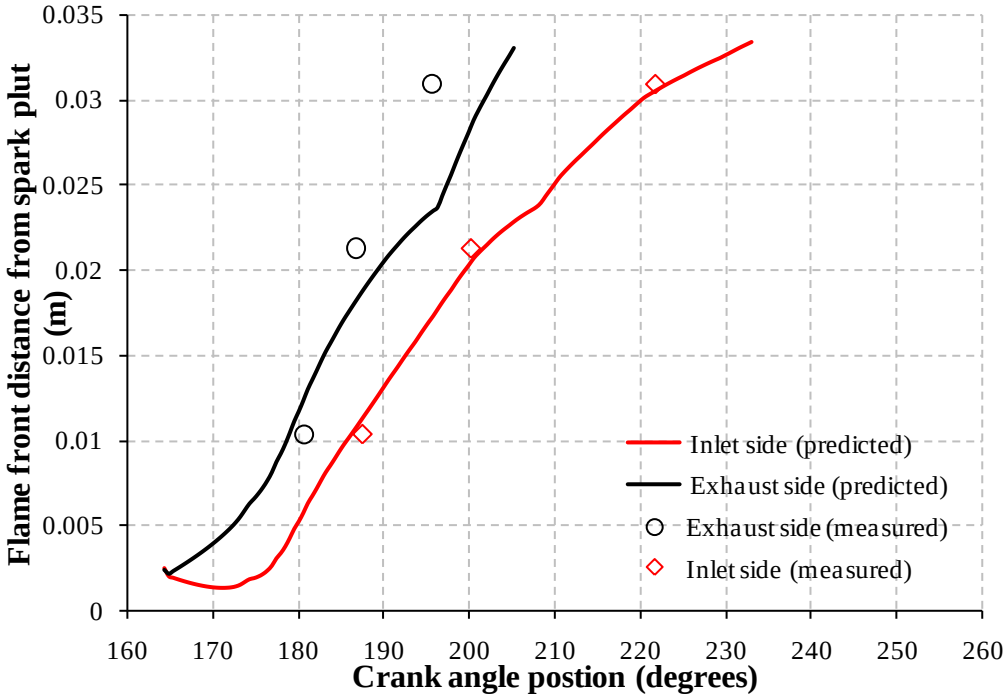

Squish head half throttle 8981 rpm.

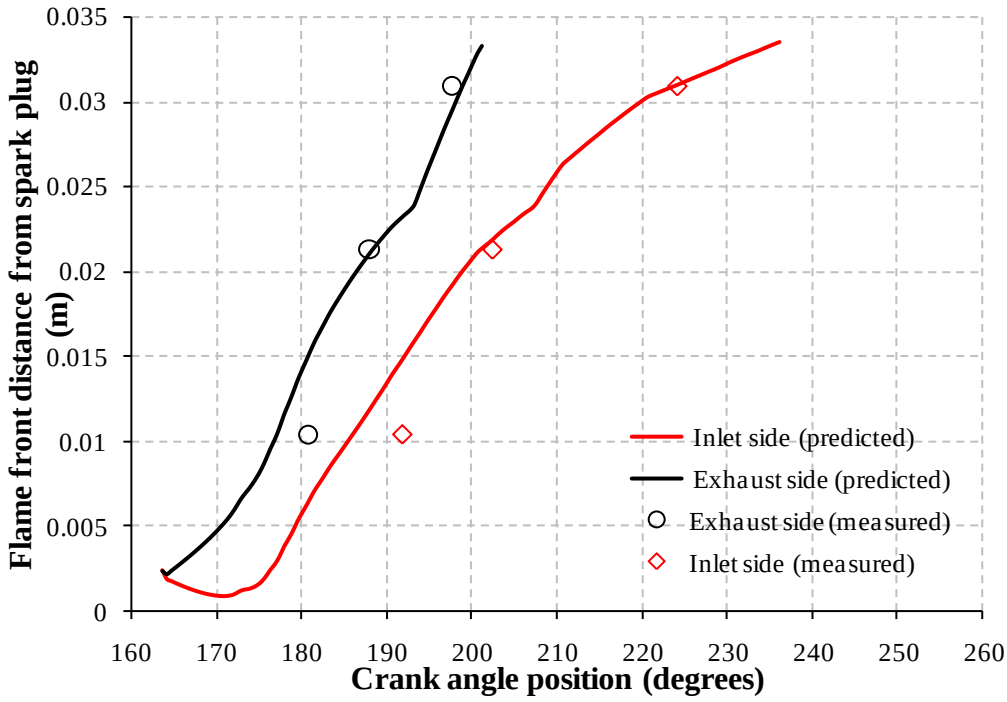

Squish head half throttle 9369 rpm.

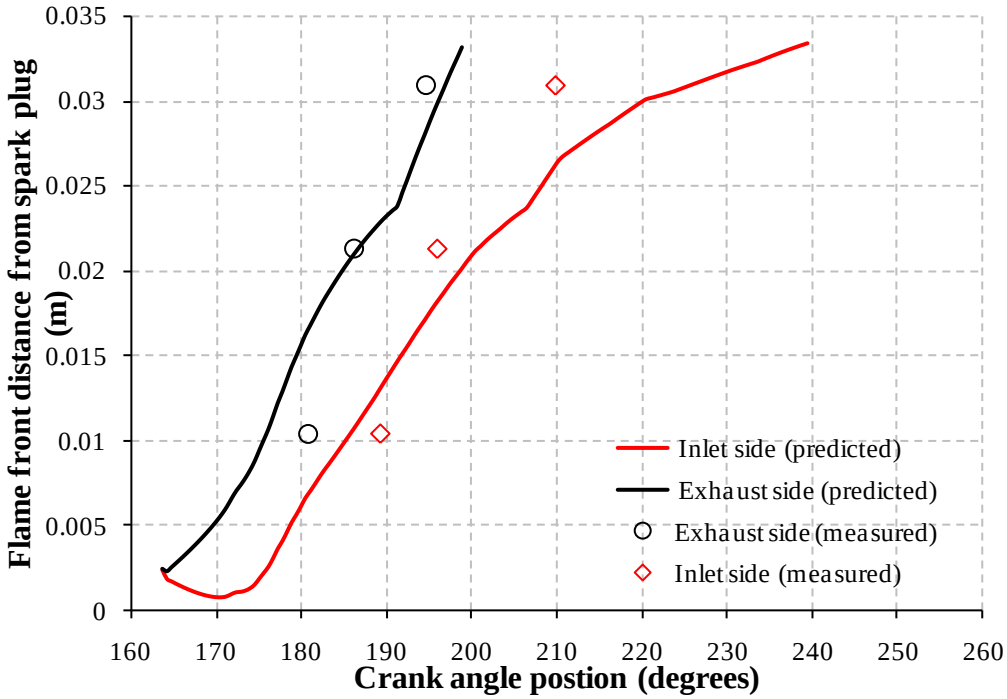

Squish head half throttle 9812 rpm.

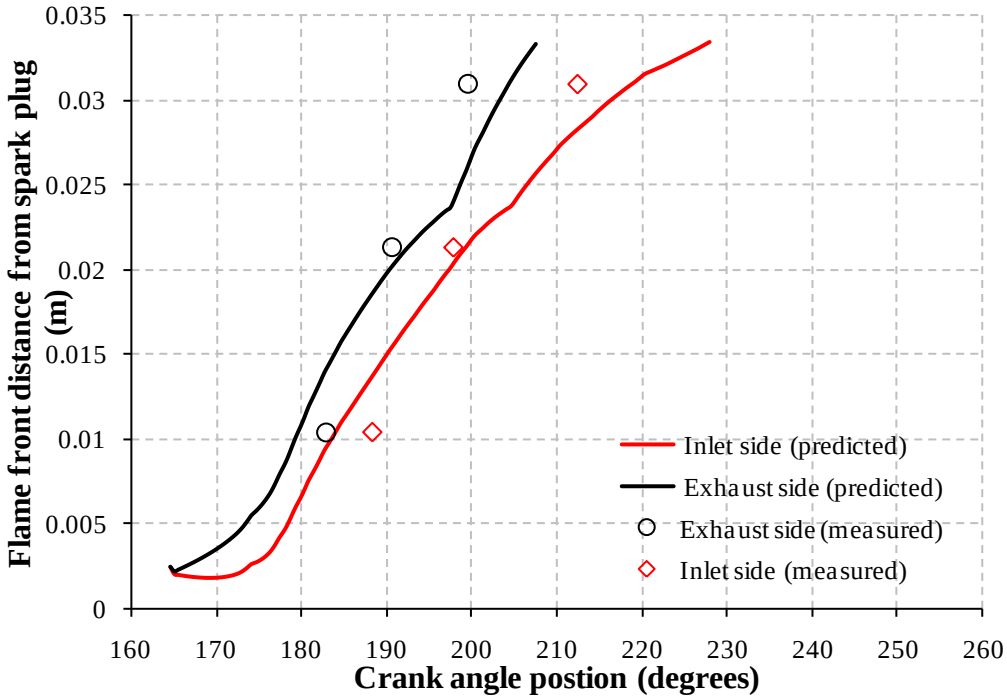

Squish head full throttle 7640 rpm.

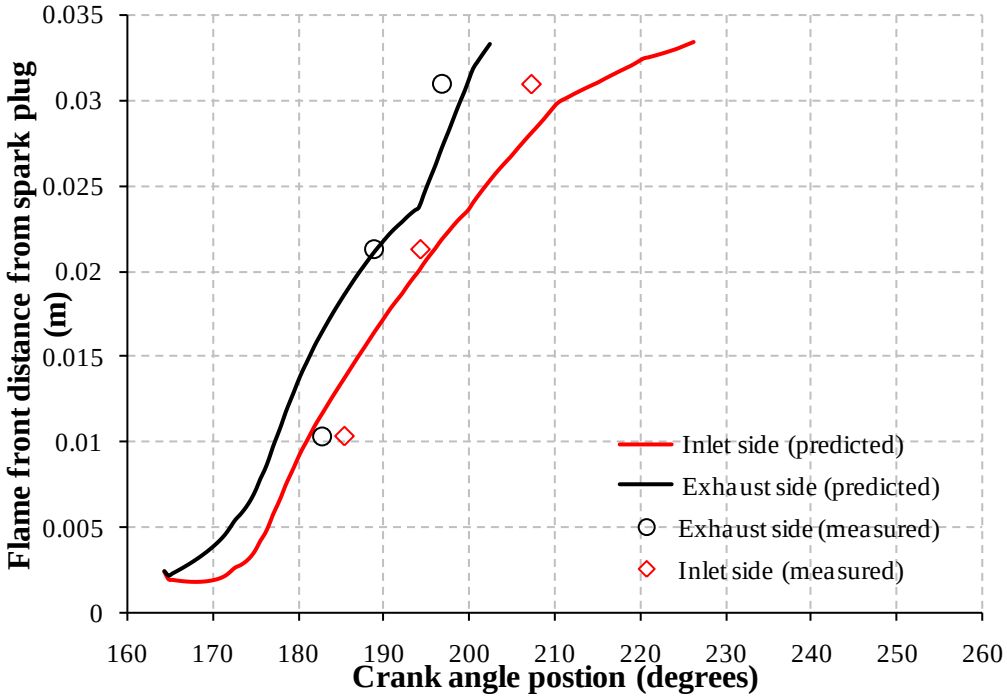

Squish head full throttle 8162 rpm.

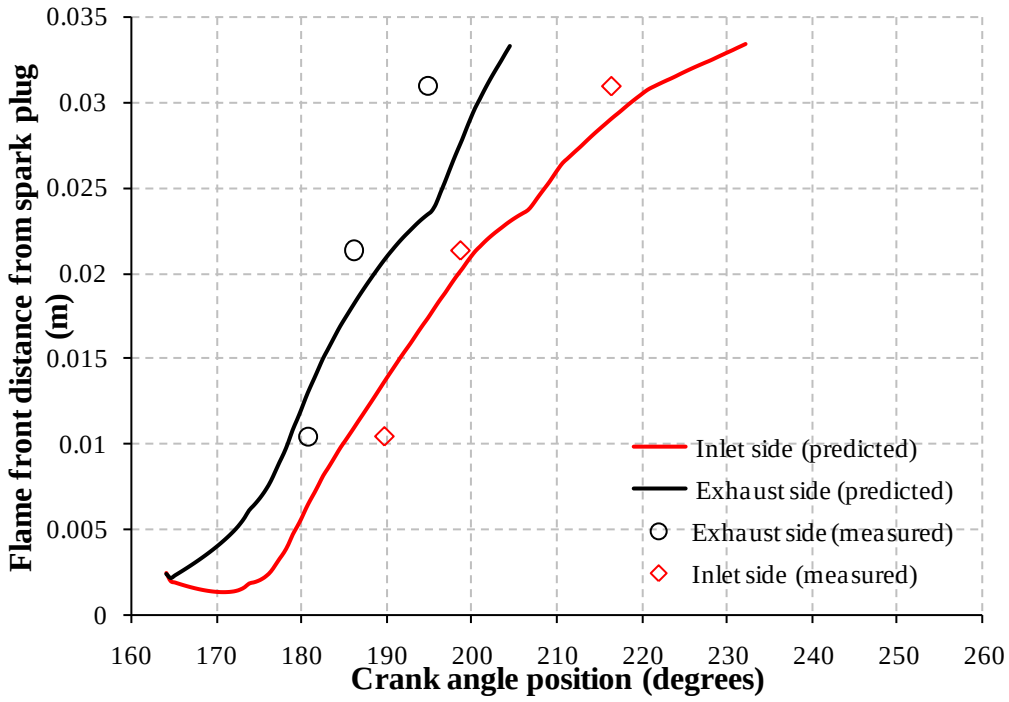

Squish head full throttle 8640 rpm.

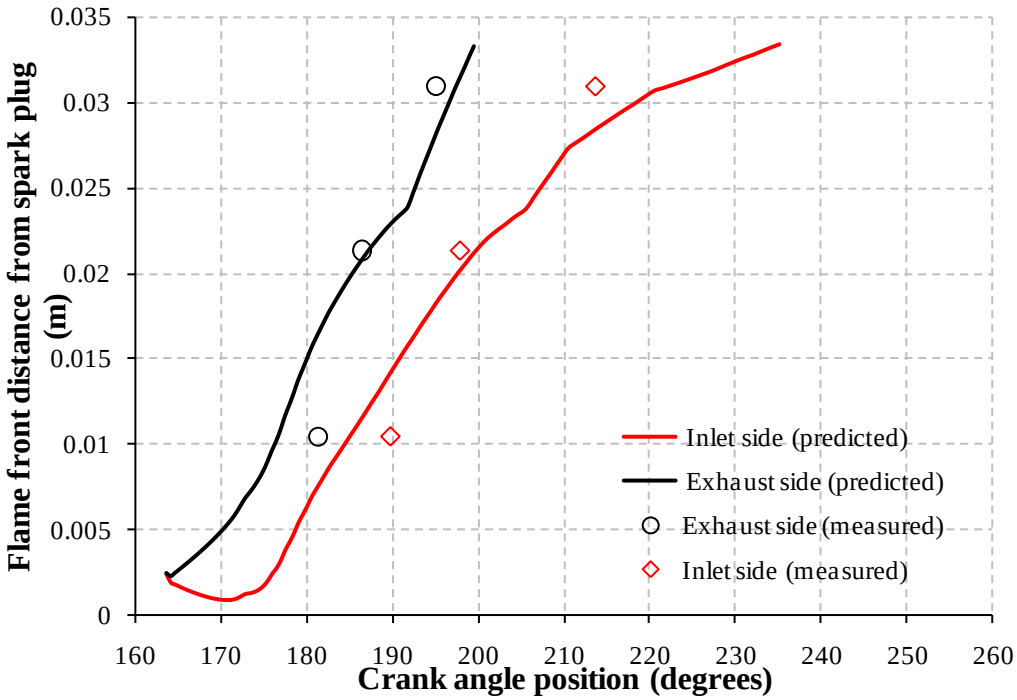

Squish head full throttle 9075 rpm.

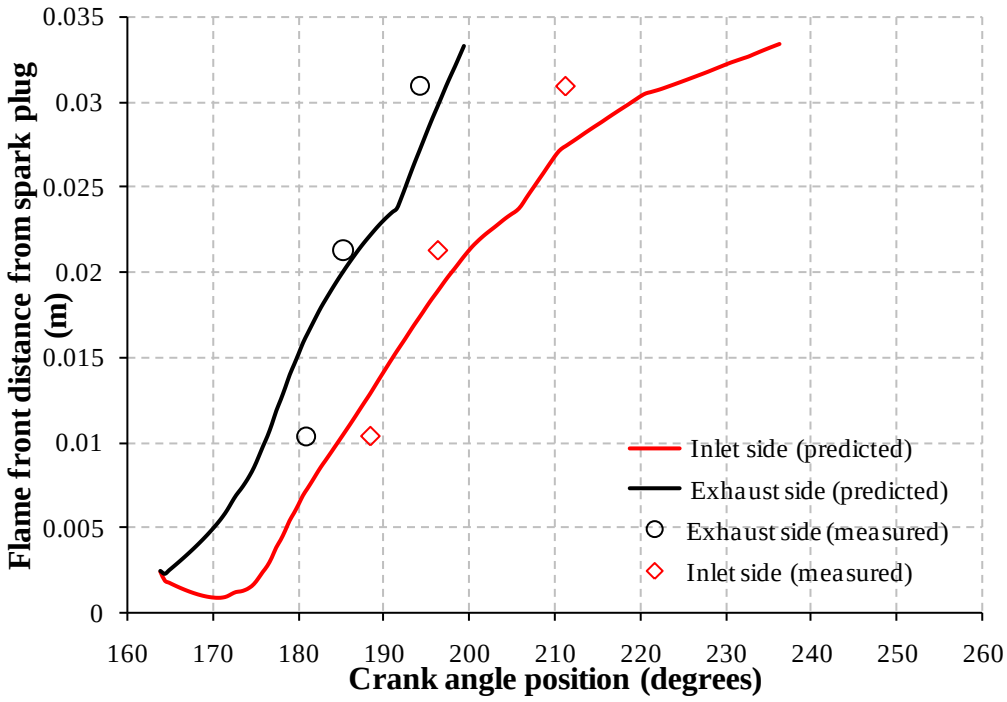

Squish head full throttle 9489 rpm.

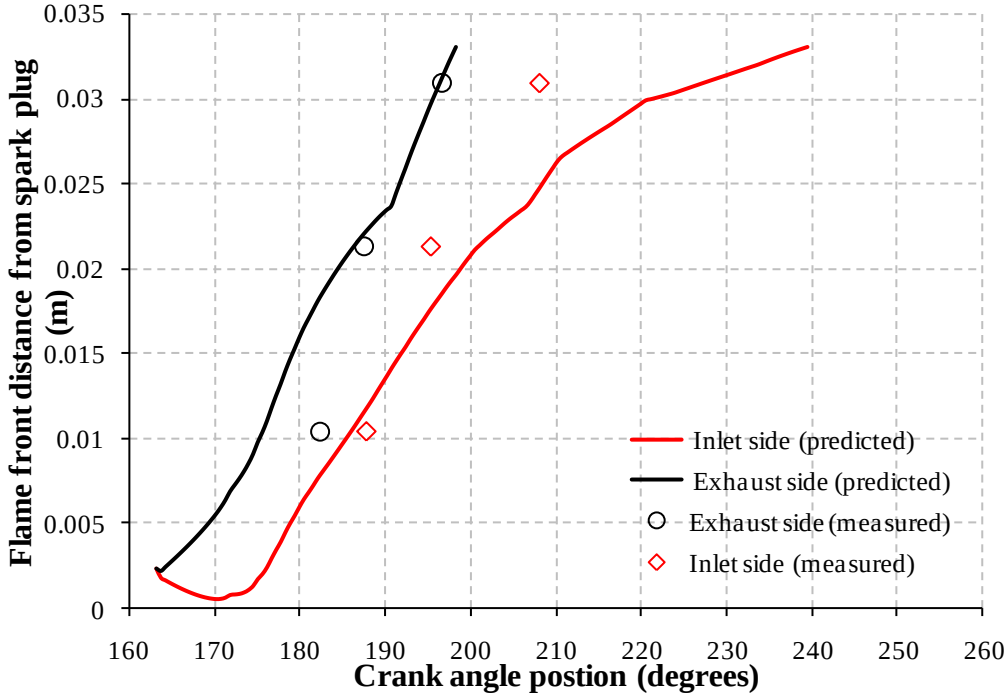

Squish head full throttle 9878 rpm.

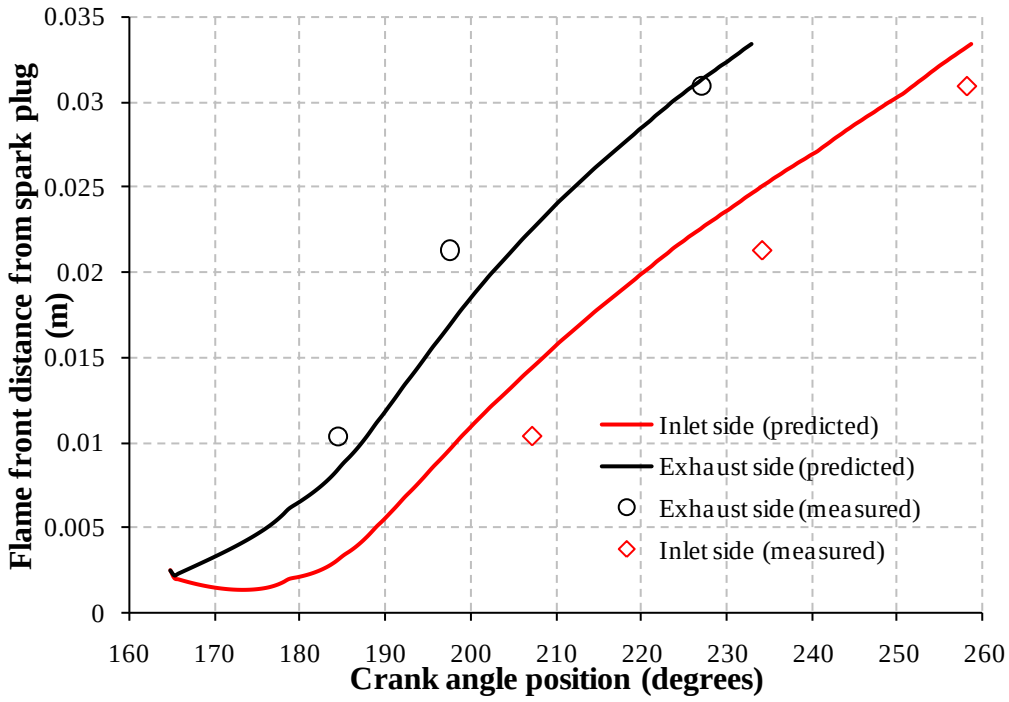

Disc head half throttle 7443 rpm.

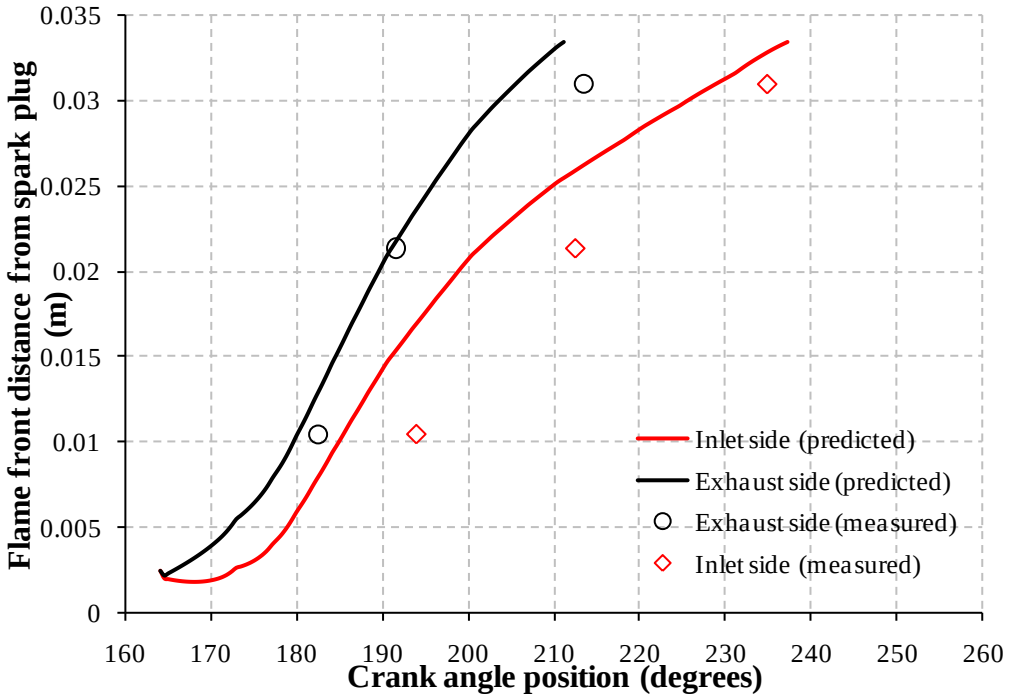

Disc head half throttle 7938 rpm.

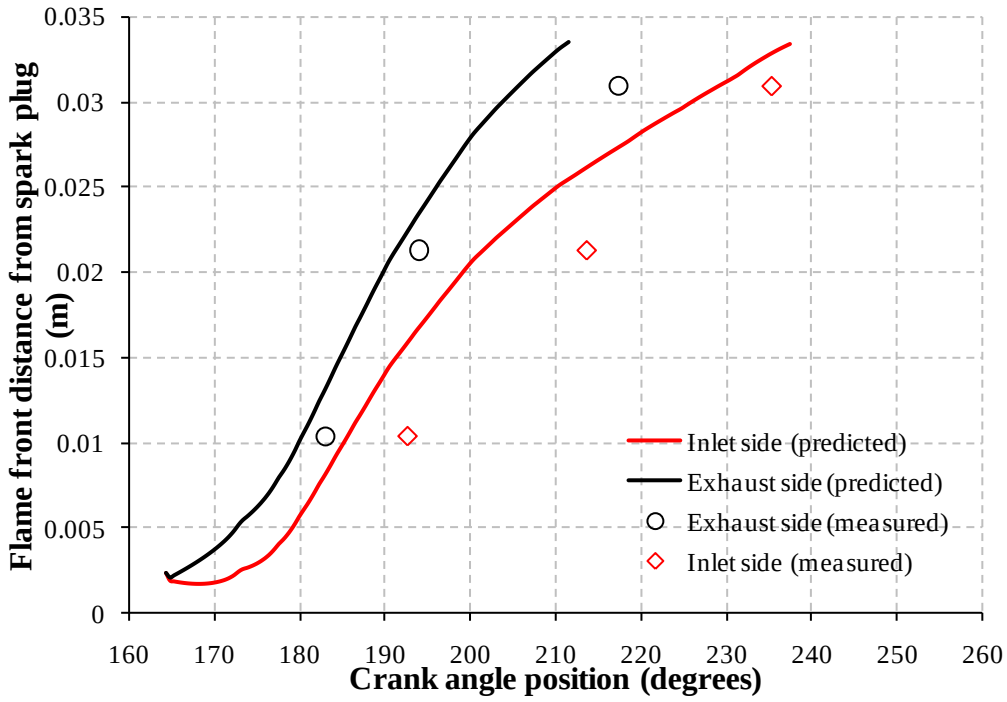

Disc head half throttle 8359 rpm.

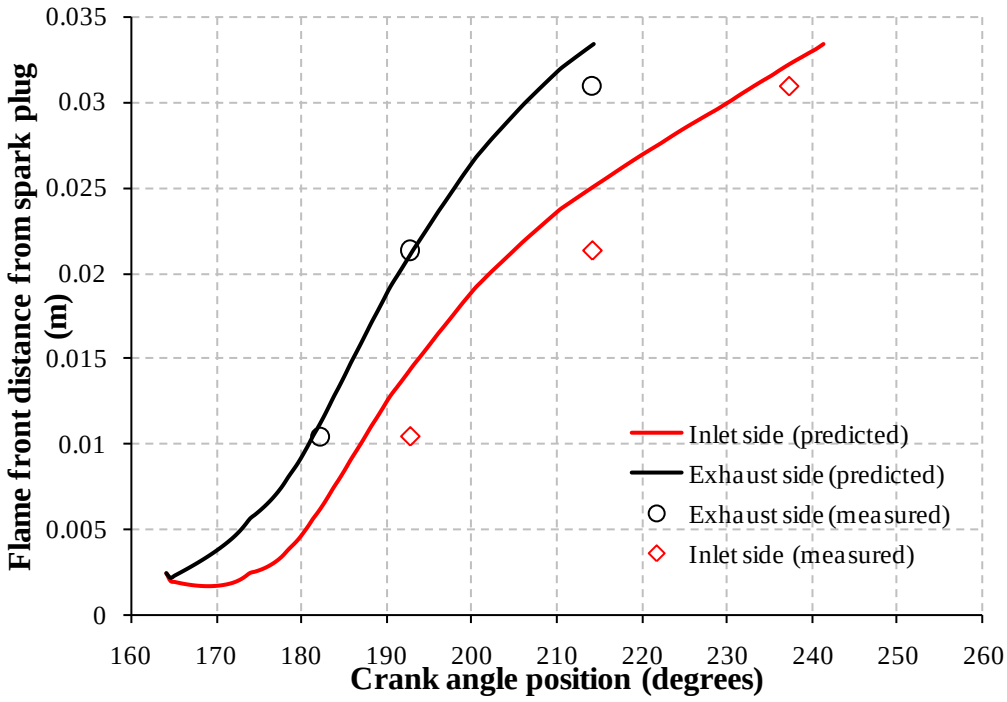

Disc head half throttle 8808 rpm.

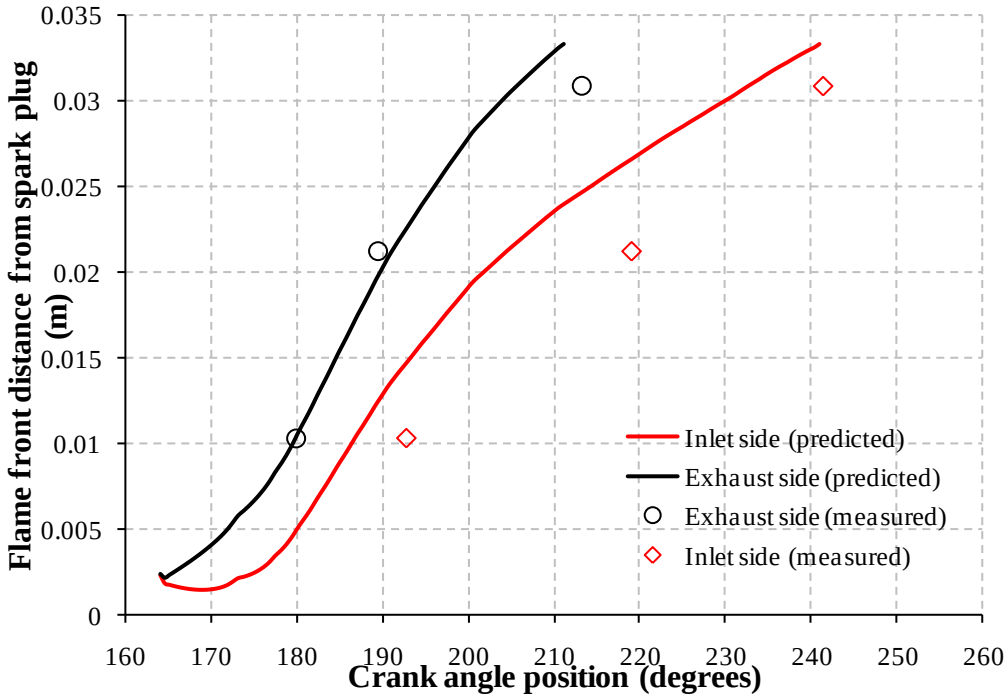

Disc head half throttle 9683 rpm.

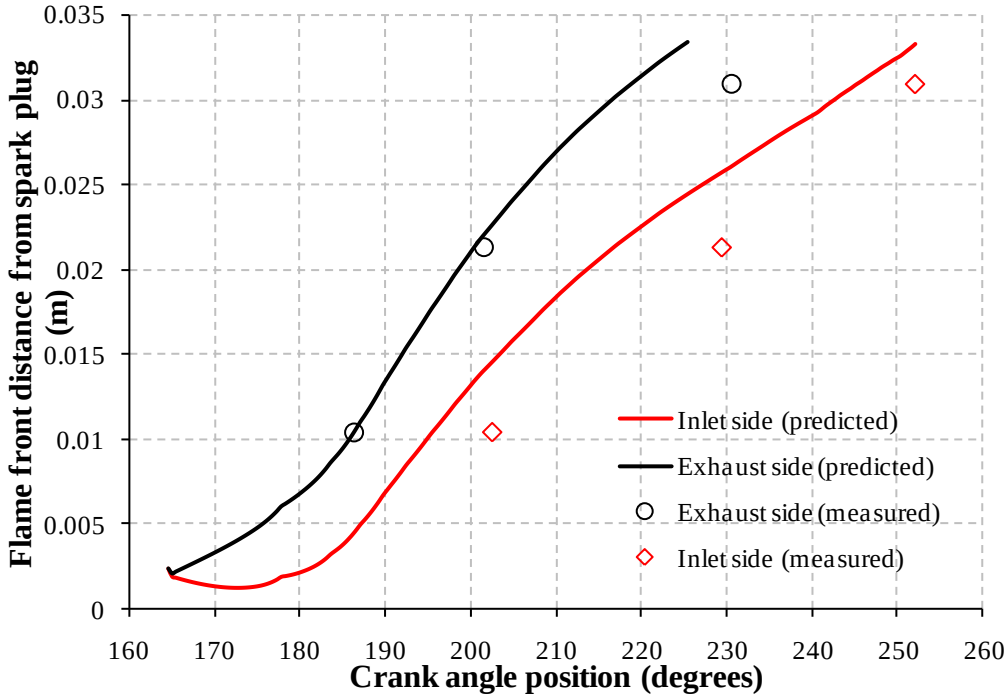

Disc head full throttle 7446 rpm.

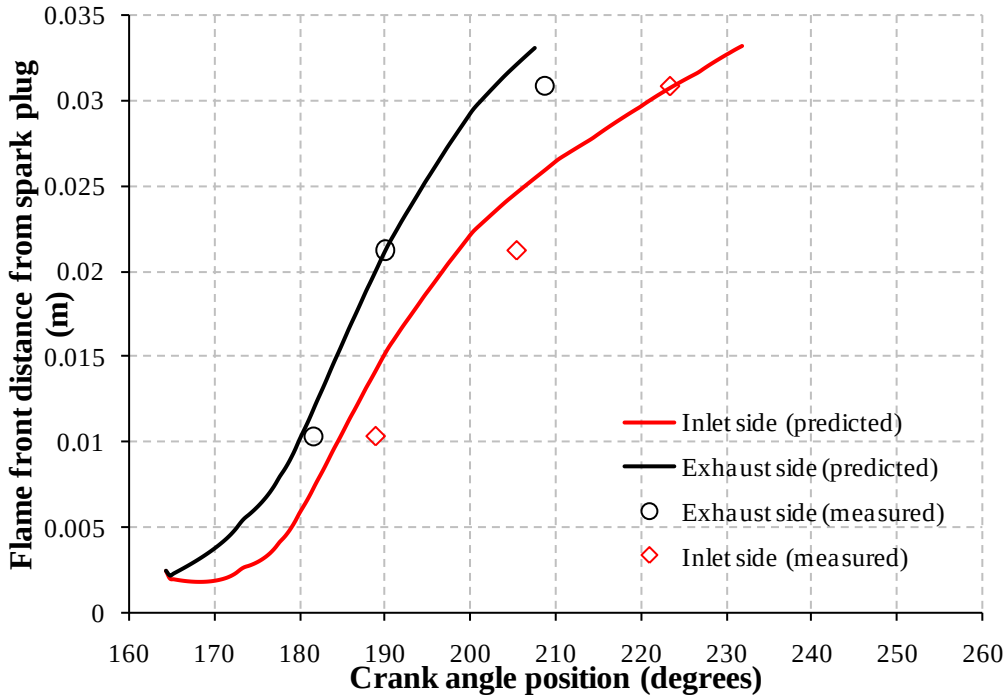

Disc head full throttle 7991 rpm.

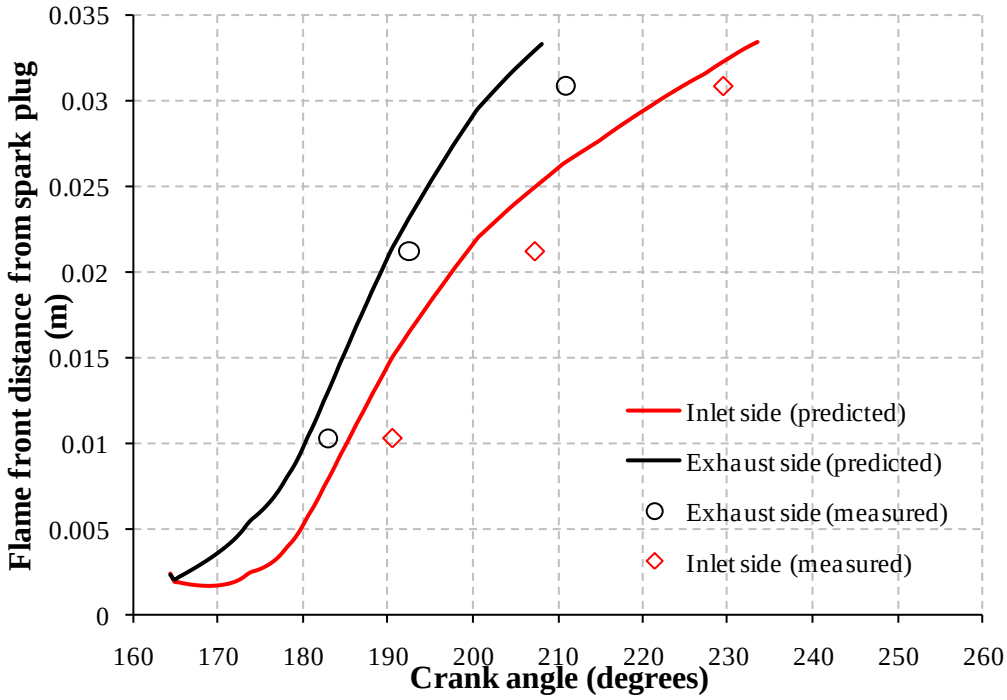

Disc head full throttle 8437 rpm.

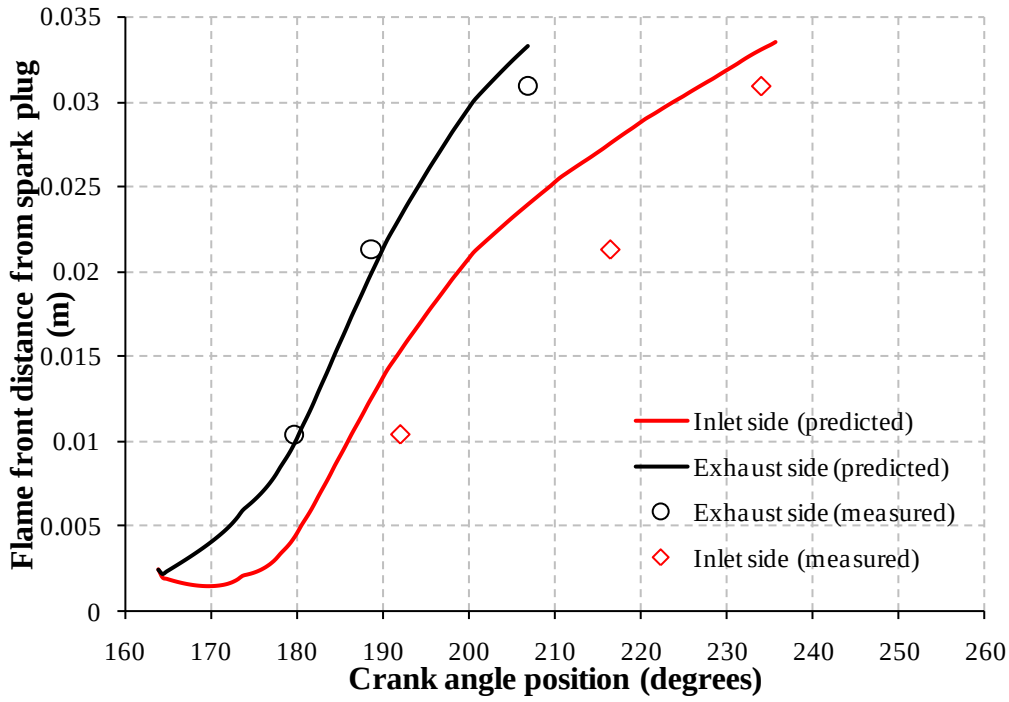

Disc head full throttle 8896 rpm.

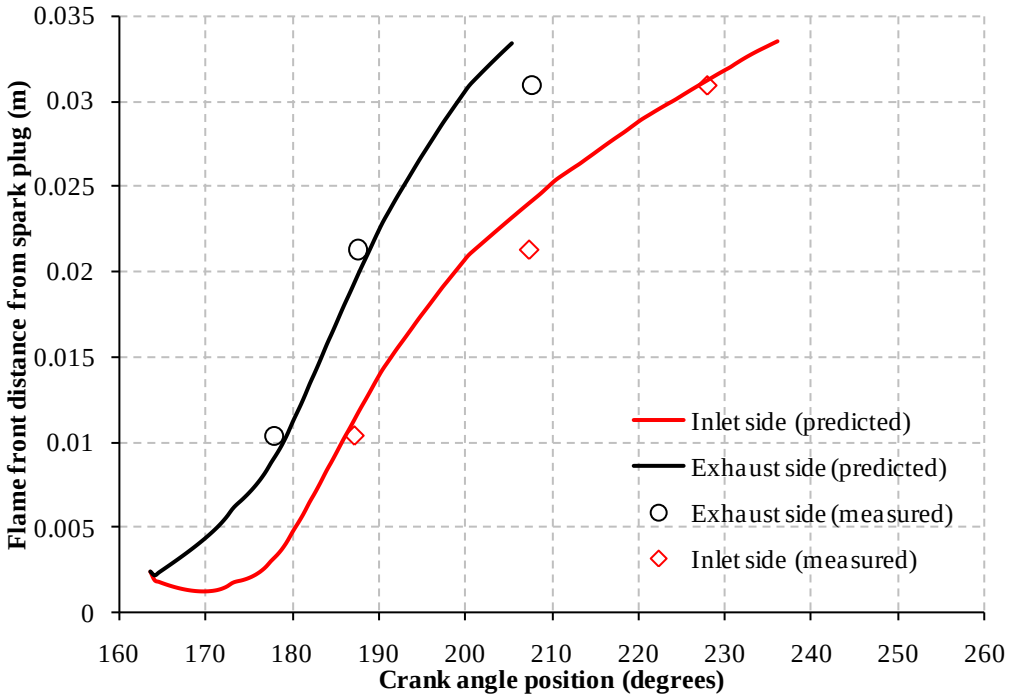

Disc head full throttle 9335 rpm.

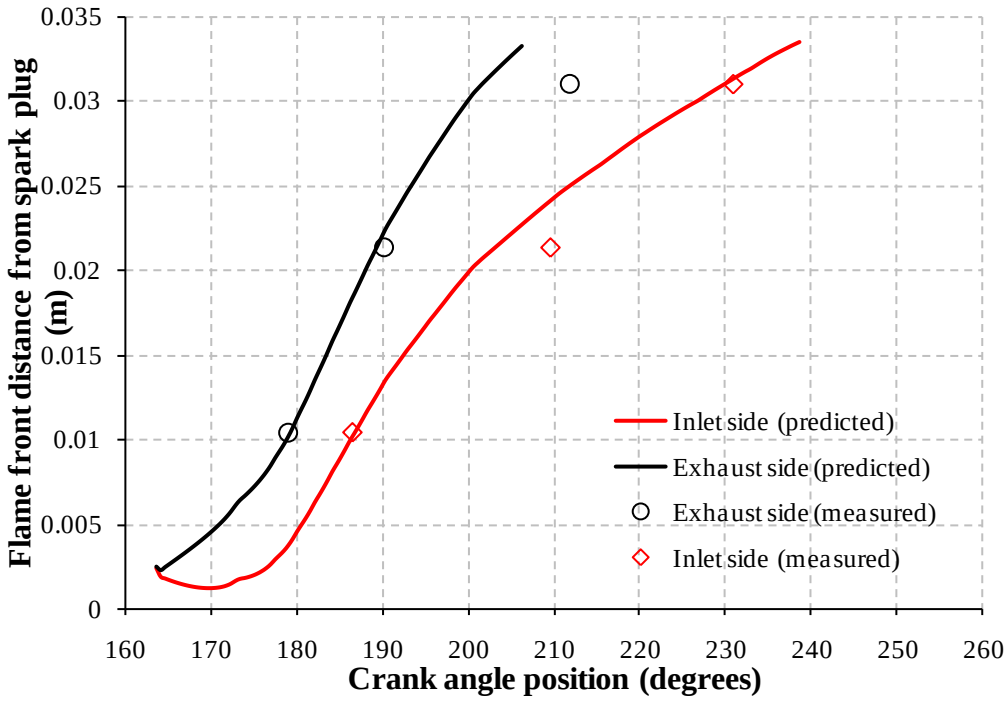

Disc head full throttle 9718 rpm.